Cell-Based Mathematical Models of Small Collections of Excitable Cells

Karoline Horgmo Jæger

Thesis submitted for the degree of Philosophiæ Doctor

Acknowledgements

This is my thesis submitted for the degree of Philosophiae Doctor at the Department of Informatics, University of Oslo. The work has been conducted in the period from June 2016 to March 2019 at Simula Research Laboratory.

I would like to thank my supervisors Aslak Tveito, Molly Maleckar and Tuomo Mäki-Marttunen for their support during this process. In particular, I would like to thank my main supervisor, Aslak Tveito, for his continuous and insightful guidance to all aspects of the work. I am deeply grateful for all the time he has invested and for the excellent help and advice he has given me throughout the process. His extraordinary patience, encouraging enthusiasm and considerate support have meant so much to me.

I also wish to express my gratitude to the remaining co-authors of the papers of the thesis and the other people that I have worked with at Simula Research Laboratory. Especially, I would like to thank Joakim Sundnes for his input on the EMI model foundations, Andy Edwards and Sam Wall for their explanations of physiological principles, and Marie Rognes and Miro Kuchta for their help with the finite element method and FEniCS. Furthermore, I would like to thank Krissy McLeod, Hermenegild Arevalo, and Siri Kallhovd for their valuable help and encouragement during the first part of the work. I also wish to thank Henrik Finsberg for always being very helpful and kind and for many useful and encouraging discussions throughout the process.

In addition, I would like to thank my little sister, Pernille, for answering numerous stupid biology questions and for her incredibly understandable and fascinating physiology explanations. I also wish to thank my mother for her wise advice about everything and for continuously filling up my supplies of food and candy. Likewise, I wish to thank my father for always being available for helpful discussions about words, sentences or biology. Finally, I would like to thank Pernille and my parents for their invaluable love and support and for always being there for me.

Karoline Horgmo Jæger
Oslo, March 2019

List of papers

Paper I

An Evaluation of the Accuracy of Classical Models for Computing the Membrane Potential and Extracellular Potential for Neurons

Aslak Tveito, Karoline H. Jæger, Glenn T. Lines, Łukasz Paszkowski, Joakim Sundnes, Andrew G. Edwards, Tuomo Mäki-Marttunen, Geir Halnes, and Gaute T. Einevoll

Published in *Frontiers in Computational Neuroscience* 11:27 (2017) doi:10.3389/fncom.2017.00027.

Paper II

A Cell-Based Framework for Numerical Modeling of Electrical Conduction in Cardiac Tissue

Aslak Tveito, Karoline H. Jæger, Miroslav Kuchta, Kent-Andre Mardal, and Marie E. Rognes

Published in *Frontiers in Physics* 5:48 (2017) doi:10.3389/fphy.2017.00048.

Paper III

Properties of Cardiac Conduction in a Cell-Based Computational Model

Karoline H. Jæger, Andrew G. Edwards, Andrew D. McCulloch, and Aslak Tveito

Submitted for publication

Paper IV

Inversion and Computational Maturation of Drug Response Using Human Stem Cell Derived Cardiomyocytes in Microphysiological Systems

Aslak Tveito, Karoline H. Jæger, Nathaniel Huebsch, Bérénice Charrez, Andrew G. Edwards, Samuel Wall, and Kevin E. Healy

Published in *Scientific Reports* 8:17626 (2018)
doi:10.1038/s41598-018-35858-7.

Paper V

Improved Computational Identification of Drug Response Using Optical Measurements of Human Stem Cell Derived Cardiomyocytes in Microphysiological Systems

Karoline H. Jæger, Verena Charwat, Bérénice Charrez, Henrik Finsberg, Samuel Wall, Kevin E. Healy, and Aslak Tveito

Preliminary manuscript, not ready for publication

Paper VI

Detecting Undetectables: Can Conductances of Action Potential Models be Changed Without Appreciable Change in the Transmembrane Potential?

Karoline H. Jæger, Samuel Wall, and Aslak Tveito

Submitted for publication

Contents

Part I

Introduction

Chapter 1

Introduction

Electrical signals play an important role in a number of physiological processes. For example, muscle movement is initiated and coordinated by electrical signals conducted along neurons, and electrical signals transmitted between neurons is an essential part of the complex processes underlying the function of the brain. Furthermore, electrical signals propagating through the cardiac muscle cells enable the cells to contract in synchrony and thereby pump blood through the body.

The study of the electrical properties of biological cells and tissues is called electrophysiology and dates back at least to the 1780s, when Luigi Galvani reported that the leg of a dead frog started to contract when an electrical shock was applied to one of its nerves [1, 2]. About a century later, in 1868, Julius Bernstein was able to describe the electrical signal spreading down a nerve cell as an action potential, i.e. a change in the electrical potential difference between the inside and the outside of the cell [3]. This potential difference is commonly referred to as the membrane potential or the transmembrane potential and is defined as $v = u_i - u_e$, where v denotes the membrane potential, u_i denotes the intracellular potential, and u_e denotes the extracellular potential. Bernstein hypothesised that the cell membrane is selectively permeable to ions and that, at rest, this selective permeability creates a potential difference across the membrane. Furthermore, he hypothesised that the action potential was generated by an increased membrane permeability that reduced the potential difference across the membrane. His theory was further developed by Howard Curtis and Kenneth Cole, who were able to measure a full action potential of a squid giant axon in the 1930s [4]. Their recordings showed that the action potential of the axon consisted of a rapid increase in the membrane potential (depolarization), followed by a subsequent decrease back to rest (repolarization). In 1952, Alan Hodgkin and Andrew Huxley explained the selective membrane permeability by suggesting an ion specific gating mechanism for the exchange of ions over the membrane. This gating mechanism was later believed to be enabled by specialized ion channels located on the cell membrane. In the 1970s, the existence of such specialized ion channels was confirmed, using the so-called patch clamp technique invented by Erwin Neher and Bert Sakmann

[5], and since then, identifying and studying the properties of ion channels have been active fields of research [1].

The knowledge obtained about the electrical properties of biological tissues and cells has helped guide the development of both diagnostic tools and treatments for a number of diseases. Electrocardiography (ECG), electroencephalography (EEG), pacemakers, defibrillation and ablation are a few examples of commonly used diagnostic tools and treatments that benefit from insight about the properties of electrical signals in healthy and diseased hearts and brains[1]. Moreover, it is known that a number of diseases are caused by mutations or toxicological effects on the function of ion channels, and ion channels are therefore common targets for drugs [1]. However, drugs often affect more ion channels than the intended target, and a number of drugs have proven to have dangerous side effects on, for example, the electrical activity of the heart [6, 7]. As more research is conducted aiming to increase our understanding of the electrical properties of cells and tissues, it is hoped that new insights may lead to better diagnostic tools and treatments for patients and aid the development of more effective and safe drugs.

Mathematical models of electrophysiology may be useful tools for gaining more understanding about electrophysiological properties. Already in 1952, Hodgkin and Huxley developed a mathematical model for the action potential of a squid giant axon [8], and this modeling methodology has been continuously developed and now includes models of a large number of different types of excitable cells [9]. As the understanding of electrophysiological properties has developed, mathematical modeling approaches have, for example, helped gain insight into the roles of different ionic currents [10], the effect of a neuron's geometry on the function of the neuron [11] and the extracellular potential measured around the neuron [12], the mechanisms behind arrhythmias [13, 14], and properties of defibrillation [14]. In addition, mathematical modeling has been proposed as a useful tool for drug testing applications [7, 15, 16].

The mathematical models are typically based on the current understanding of and additional assumptions about the principles underlying the electrophysiological processes under consideration. The models are usually expressed as a system of ordinary differential equations (ODEs) or partial differential equations (PDEs) [17]. In some cases, the model equations are simple enough to be solved analytically, but numerical methods are often required, approximating the model equations to a system of equations that may be conveniently solved by a computer.

The mathematical modeling approaches operate on many different spatial scales, from modeling of the function of a single ion channel (e.g., [18]) or modeling of the function of a single cell (e.g., [19]), to modeling of action potential propagation through the entire heart (e.g., [20]) or signalling in a large network of neurons (e.g., [21]). Furthermore, population models may be used to extend these modelling approaches to account for the variability of electrical properties in a population of individuals (e.g., [22, 23]).

[1]The procedures are briefly described in Table 1.1.

Aim of the thesis

The aim of this thesis is to study mathematical models of excitable cells that operate on the scale of a single cell or a small collection of cells. Here, a small collection of cells refers to a collection of about 2–30 cells up to a collection of a few thousand cells, roughly corresponding to the number of human induced pluripotent stem cell-derived cardiomyocytes (hiPSC-CMs) in a microphysiological system used for drug testing applications [24]. The papers of the thesis address a small selection of research questions related to the modelling of the electrical properties of such small cell collections. In short, the questions relate to the accuracy of classical models of computational neuroscience, the numerical challenges associated with a detailed model of cardiac tissue, properties of cardiac conduction, and the identification of drug effects from optical measurements of microphysiological systems of hiPSC-CMs.

Outline of the thesis

The introductory part of the thesis is structured as follows. A brief introduction to some of the mathematical modeling approaches used to study excitable cells is given in Chapter 2, followed in Chapter 3 by a derivation of the EMI model used in the first three research papers of the thesis. Chapter 4 gives an overview of the research questions and research papers of the thesis.

The remaining part of the thesis consists of six research papers. The first paper considers modeling of the membrane potential of neurons and the extracellular potential around neurons. The next two papers consider modeling of small collections of connected cardiac cells. Finally, the last three papers consider identification of drug effects from measurements of the membrane potential and calcium transient of cardiac cells.

Electro-cardiography (ECG)	Diagnostic tool in which electrodes are placed at certain points on the skin of a patient and the electrical potential between the points is measured. The origin of cardiac dysfunction may be identified by interpreting the recorded signals, and the procedure is commonly used for diagnosis of cardiac diseases like cardiac arrhythmias and conduction disturbances [25].
Electroence-phalography (EEG)	Diagnostic tool in which electrodes are placed in different regions of the scalp and the electrical potential between the electrodes are recorded to evaluate the function of the brain. The recorded activity is examined to determine whether the findings are normal or irregular and whether they suggest any particular type of underlying pathological process. The procedure is used in the evaluation of patients with several types of neurological disorders, including seizures, encephalopathy, and focal cerebral abnormalities [26].
Anesthesia	Drug-induced loss of sensation used, e.g., to avoid pain during surgery. Local anesthesia blocks sodium channels on the membrane of neurons in a targeted part of the body or in a region of the central nervous system, hindering the initiation of action potentials and thereby restricting neuronal signalling [27].
Pacemaker	Implantable device with electrodes that provide small electrical stimulus currents to initiate the electrical wave propagation that controls the contraction of the heart in cases when the normal automatic initiation fails [28].
Defibrillation	Treatment for arrhythmias (i.e. irregular heart rhythms caused by abnormal cardiac electrical activity). An electrical shock is delivered to the heart, depolarizing the membrane of all the cardiac muscle cells in an attempt to terminate the arrhythmias [29].
Ablation	Treatment for arrhythmias in which lesions are created in the heart muscle in order to destroy or isolate the areas responsible for the electrical activity triggering the arrhythmias [30].

Table 1.1: A few examples of currently used medical procedures benefiting from insight into electrophysiological processes.

Chapter 2

Mathematical models of electrophysiology

As indicated above, mathematical electrophysiological modeling is an active field of research, focusing of different aspects of the electrical properties of the body. In this thesis, the focus is on mathematical modeling of small collections of excitable cells, and this chapter gives a brief introduction to some of the mathematical modeling approaches used to study action potentials and electrical conduction in biological cells and tissues.

2.1 Single cell action potential models

The aim of this section is to introduce some of the models used to study the action potentials of neurons and cardiac cells. Before introducing the groundbreaking action potential model of Hodgkin and Huxley [8] and the multitude of cardiac action potential models it has inspired, a few of the basic concepts of membrane modeling are introduced. Unless otherwise stated, the theory found in this section is taken from the references [31, 32, 33].

2.1.1 Elements of membrane modeling

In this section, some of the modeling approaches used to model the electrical properties of the cell membrane are described.

The cell membrane

The cell membrane (sarcolemma) is composed of an approximately 5 nm thick lipid bilayer, made up by two layers of lipids with the hydrophilic ends pointing outwards and the hydrophobic ends pointing inwards (see Figure 2.1). The lipid bilayer is virtually impermeable to ions, but ions may cross the membrane through

specialized proteins embedded in the membrane, e.g. ion channels. These proteins are often selective, in the sense that only some types ions may pass through each type of protein. In addition, the ion channels may be gated, meaning that they open and close stochastically according to some open probability. This open probability might, for example, depend on the value of the membrane potential. Channels whose open probability depends on the membrane potential are often referred to as voltage-gated channels.

The Nernst equilibrium potential

The current through an open ion channel is determined by both diffusional and electrical forces. The diffusional forces drive the ions to flow down their concentration gradient. If, for instance, the concentration of K^+-ions is higher in the intracellular space than in the extracellular space, the diffusional flux through an open K^+-channel will be in the direction out of the cell. However, as more K^+-ions flow out of the cell, there will be an accumulation of positive charges on the extracellular side of the membrane and an accumulation of negative charges on the intracellular side of the membrane, assuming that the intracellular and extracellular spaces initially are electrically neutral. The surplus of positive charges in the extracellular space will repel the positive K^+-ions flowing out of the cell and the surplus of negative charges in the intracellular space will similarly attract the K^+-ions. Eventually, the electrical forces driving the K^+-ions into the cell will balance the diffusional forces driving the ions out of the cell, and in this case, the net flow through the channel will be zero. The value of the membrane potential when this occurs is called the Nernst equilibrium potential and is specific for each type of ion.

The Nernst equilibrium potential may be derived by considering the expressions for the diffusional and electrical forces acting on the ions. The diffusional flux of some ion of type P through a one-dimensional channel is given by Fick's law

$$J_d = -D_P \frac{d[P]}{dx},$$

where [P] is the ion concentration (typically in mM), D_P is the diffusion coefficient of the ion (typically in $\mathrm{dm}^2/\mathrm{ms}$), and x denotes a spatial variable along the length of the channel (typically in dm). In addition, electrical forces act on the ions, and the flux of ions due to electrical drift is given by the microscopic version of Ohm's law

$$J_e = -\mu_P \frac{z_P}{|z_P|}[P]\frac{du}{dx},$$

where μ_P is the mobility of the ion P (typically in $\mathrm{dm}^2/(\mathrm{mV\ ms})$), z_P is the (unitless) valence of the ion P, and u is the spatially varying electrical potential in the channel (typically in mV). The diffusion coefficient is related to the ion mobility by

$$D_P = \frac{\mu_P RT}{|z_P|F}, \tag{2.1}$$

Ion type	Intracellular concentration	Extracellular concentration	Nernst equilibrium potential
Ca^{2+}	0.0001 mM	10 mM	145 mV
Na^{+}	50 mM	440 mM	55 mV
Cl^{-}	40 mM	560 mM	-66 mV
K^{+}	400 mM	20 mM	-75 mV

Table 2.1: Typical values of the intracellular and extracellular ionic concentrations and the Nernst equilibrium potential for Ca^{2+}-, Na^{+}-, Cl^{-}- and K^{+}-ions in a squid giant axon at room temperature (20°C, i.e., 293.15 K) [32].

where R is the universal gas constant (typically in mJ/(mol K)), T is the absolute temperature (typically in K) and F is Faraday's constant (typically in C/mol). The total flux due to both diffusional forces and electrical forces is therefore given by

$$J_P = -D_P \left(\frac{d[P]}{dx} + \frac{z_P [P] F}{RT} \frac{du}{dx} \right).$$

Faraday's constant, F, specifies the amount of electrical charge per mole of ions with elementary charge. Therefore, the flux J_P (in mmol/(ms dm^2)) may be converted to a current density I_P (in A/dm^2) by multiplying the flux by the valence of P and Faraday's constant, which yields

$$I_P = -\frac{\mu_P RT z_P}{|z_P|} \left(\frac{d[P]}{dx} + \frac{z_P [P] F}{RT} \frac{du}{dx} \right). \tag{2.2}$$

This is called the Nernst-Planck equation. The Nernst equilibrium potential is defined as the membrane potential for which this total current density is zero, i.e. when the electric field force balances the diffusion force perfectly. From (2.2), we see that this is achieved when

$$\frac{1}{[P]} \frac{d[P]}{dx} = -\frac{z_P F}{RT} \frac{du}{dx}. \tag{2.3}$$

Integrating (2.3) from the extracellular side of the channel to the intracellular side, we get

$$\ln([P]_i) - \ln([P]_e) = -\frac{z_P F}{RT} (u_i - u_e).$$

Recalling that the membrane potential is defined as $v = u_i - u_e$, we obtain the Nernst equilibrium potential for the ion P, $v = E_P$, defined by

$$E_P = \frac{RT}{z_P F} \ln \left(\frac{[P]_e}{[P]_i} \right). \tag{2.4}$$

Models for the current through an open channel

Although the Nernst-Planck equation (2.2) may be used as a model for the current through an open channel, the equation is often approximated to obtain an explicit expression for the current as a function of the membrane potential and the intracellular and extracellular concentrations. The Goldman-Hodgkin-Katz flux, for example, is given by

$$I_P = \frac{D_P}{L}\frac{z_P^2 F^2 v}{RT}\frac{[P]_i - [P]_e \exp\left(\frac{-z_P F v}{RT}\right)}{1 - \exp\left(\frac{-z_P F v}{RT}\right)}, \tag{2.5}$$

and can be derived from the Nernst-Planck equation using some simplifying assumptions (see e.g., Chapter 5.6 of [31]).

Moreover, in many cases, for example in the Hodgkin-Huxley model described below, a linear expression satisfying that the current is zero for the Nernst equilibrium potential is used instead. The current is then given by

$$I_P = g_P(v - E_P), \tag{2.6}$$

where g_P is the conductance of the channel (typically in mS/cm^2), v is the membrane potential (typically in mV) and E_P is the Nernst equilibrium potential (2.4) of the channel (typically in mV).

Modeling the membrane as a capacitor

The lipid bilayer of the cell membrane acts as an electrical insulator and has the ability to separate charge. In this regard, the membrane functions as a capacitor, storing charges of opposite signs on each side. The amount of charge, q, stored by the membrane (typically in nC) and the potential difference between the two sides of the membrane, v, (typically in mV) are related by

$$q = c_m v, \tag{2.7}$$

where c_m is the membrane capacitance (typically in μF)[1]. Assuming that the membrane can be treated as two parallel plates, the membrane capacitance is given by

$$c_m = \frac{\varepsilon_m \varepsilon_0 A}{d},$$

where d is the membrane thickness (typically in cm), A is the membrane area (typically in cm^2), ε_0 is the permittivity of free space (typically in μF/cm), and ε_m is the unitless relative permittivity of the membrane [4]. The specific membrane

[1]Note that since $v = u_i - u_e$, q here by definition denotes the amount of positive charges stored on the intracellular side of the membrane, which equals the amount of negative charges stored on the extracellular side. If the membrane potential is negative, $-q$ likewise denotes the amount of negative charges stored on the intracellular side of the membrane and the amount of positive charges stored on the extracellular side of the membrane.

capacitance C_m (typically in μF/cm^2) is useful for defining current densities and is defined as the capacitance per membrane area, or

$$C_m = \frac{c_m}{A}.$$

If no current flows into or out of the cell (or into or out of the extracellular space), both the amount of charge stored on the membrane and the membrane potential will remain constant. However, if there, for instance, is a flow of positive ions into the cell through an ion channel, the membrane potential and the amount of charge stored on the membrane will change. This is illustrated by a simple example in Figure 2.1. In the upper panel, there is an excess of positive charges on the extracellular side of the membrane and an excess of negative charges on the intracellular side of the membrane, corresponding to a negative membrane potential. In the intracellular space, negative charges are therefore attracted to and stored on the membrane, and positive charges are similarly attracted to and stored on the extracellular side of the membrane. In the lower panel, an ion channel opens and lets positive ions flow from the extracellular space to the intracellular space. This reduces the surplus of negative charges in the intracellular space and the surplus of positive charges in the extracellular space, and attracts some of the charges stored on the cell membrane into the bulk extracellular and intracellular spaces. Thus the amount of charges stored on the membrane, q, and the membrane potential, v, will change.

The charges leaving the membrane can be represented as a current, referred to as the *capacitive current*. The capacitive current density is found by differentiating (2.7) with respect to time and dividing by the membrane area and is given by

$$I_c = \frac{1}{A}\frac{dq}{dt} = C_m \frac{dv}{dt}. \tag{2.8}$$

The capacitive current is positive for a flow of positive charges in the direction along the outward pointing normal vector of the cell[2].

Furthermore, the currents through the ion channels may be collected into a single current density called I_{ion}. By convention, this current is also defined to be positive when positive charges flow out of the cell.

Kirchhoff's current law states that in any point in an electrical circuit, no charge may accumulate, and therefore, the current flowing into a point must equal the current flowing out of the point. In a cell, charges are assumed to only accumulate on the cell membrane, and the charges flowing into the cell must therefore equal the sum of charges flowing out of the cell plus the charges accumulating at the cell membrane (represented by I_c). Since I_{ion} represents the sum of the ionic currents

[2]Since q represents the amount of negative charges stored on the extracellular side of the membrane, we see from (2.8) that I_c represents the accumulation of negative charges on the extracellular side of the membrane, or equivalently, the repulsion of positive charges from the extracellular side of the membrane into the bulk extracellular space. This corresponds to accumulation of positive charges on the intracellular side of the membrane. Therefore, the capacitive current is positive for a flow of positive charges in the direction along the outward pointing normal vector of the cell.

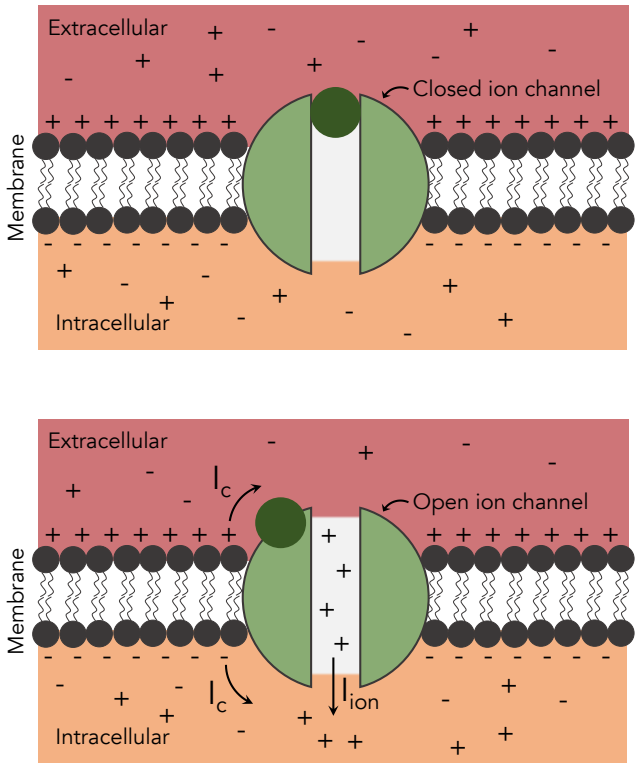

Figure 2.1: Illustration of the capacitive current. In the upper panel, there is an excess of positive charges on the extracellular side of the membrane and an excess of negative charges on the intracellular side of the membrane. Therefore, negative charges are attracted to and stored on the intracellular side of the membrane and positive charges are attracted to and stored on the extracellular side of the membrane. In the lower panel, an ion channel is opened, allowing positive ions to flow from the extracellular to the intracellular space. This reduces the potential difference across the cell membrane and the amount of charges attracted to and stored on the membrane. The capacitive current, I_c, represents the amount of charges being repelled from or attracted to the membrane per time. Note that I_{ion} and I_c are both defined to be positive for a flow of positive charges in the direction along the outward pointing normal vector of the cell.

though the membrane and has positive direction out of the cell, an analogue to Kirchhoff's current law for isolated biological cells may be expressed as

$$I_{\text{ion}} + I_c = 0,$$

or, equivalently,

$$C_m \frac{dv}{dt} = -I_{\text{ion}}. \tag{2.9}$$

2.1.2 The Hodgkin-Huxley model

The Hodgkin-Huxley model [8] from 1952 is commonly recognized as the first mathematical description of the action potential of an excitable cell based on the underlying physiological processes. The model describes the action potential of a squid giant axon, which is a particularly large type of neuron found in squid. In this model, the membrane is treated as a capacitor as explained above, and the dynamics of the membrane potential is governed by (2.9). Moreover, the ionic current density, I_{ion}, is composed of three individual current densities all given on the form (2.6). The model for the membrane potential reads

$$C_m \frac{dv}{dt} = -(I_{\text{Na}} + I_{\text{K}} + I_{\text{L}}),$$

where C_m is the specific membrane capacitance (in $\mu\text{F/cm}^2$), and v is the membrane potential (in mV). Furthermore, I_{Na} represents the current density through sodium channels on the cell membrane, I_{K} represents the current density through potassium channels, and I_{L} is a non-specific passive leak current density. The current densities are all specified in units of $\mu\text{A/cm}^2$ and formulated as:

$$\begin{aligned} I_{\text{Na}} &= g_{\text{Na}}(v - E_{\text{Na}}), \\ I_{\text{K}} &= g_{\text{K}}(v - E_{\text{K}}), \\ I_{\text{L}} &= g_{\text{L}}(v - E_{\text{L}}). \end{aligned}$$

Here, g_{Na}, g_{K}, and g_{L} are conductance densities (in mS/cm^2), and $E_{\text{Na}} = 50$ mV, $E_{\text{K}} = -77$ mV, $E_{\text{L}} = -54.4$ mV are the Nernst equilibrium potentials of the channels. The currents included in the model and the resulting action potential are illustrated in Figure 2.2.

The sodium and potassium channels are assumed to be voltage-gated, while the channels responsible for the leak current are assumed to be open at all times. The conductance density of the leak current is therefore a constant, $g_{\text{L}} = 0.3\ \text{mS/cm}^2$, while the conductance density of the sodium and potassium currents depends on the open probabilities of the channels

$$\begin{aligned} g_{\text{Na}} &= \bar{g}_{\text{Na}} o_{\text{Na}}, \\ g_{\text{K}} &= \bar{g}_{\text{K}} o_{\text{K}}. \end{aligned}$$

Here, o_{Na} and o_{K} are the unitless open probabilities of the sodium and potassium channels, respectively, and $\bar{g}_{\text{Na}} = 120\ \text{mS/cm}^2$, $\bar{g}_{\text{K}} = 36\ \text{mS/cm}^2$ are the maximum

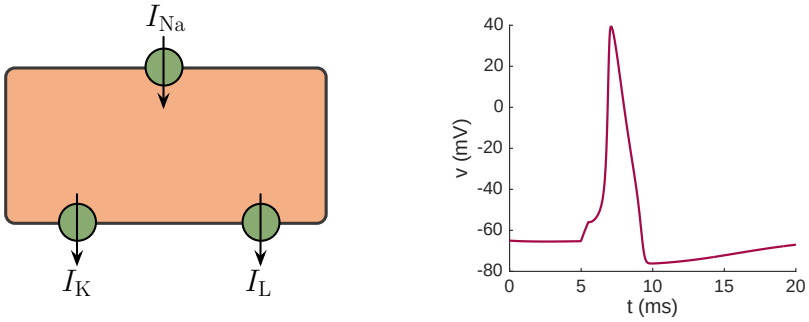

Figure 2.2: Illustration of the currents of the Hodgkin-Huxley model (left) and the action potential produced by the model (right). Note that in the original publication [8], the resting potential of the membrane was set to 0 mV. Here, the resting potential is adjusted to be -65 mV, similar to the actual resting potential in a squid giant axon. The formulation with an adjusted resting potential is taken from [32]. Note also that a stimulus current is applied from $t = 5$ ms to $t = 5.5$ ms, giving rise to the notch in the beginning of the action potential upstroke.

conductance densities. The current densities I_{Na} and I_{K} thus represent the average current densities over a large number of channels, and o_{Na} and o_{K} are assumed to represent the fraction of open channels.

Models for the open probabilities In order to fit the model to measurements of I_{Na} and I_{K}, Hodgkin and Huxley let the open probabilities of the channels be given by the expressions

$$o_{\mathrm{Na}} = m^3 h,$$
$$o_{\mathrm{K}} = n^4,$$

where m, h and n are gating variables that take values between zero and one. The exponent 4 in the expression for the open probability of the potassium channels was chosen to fit recored data of the voltage-dependent activation and deactivation of the potassium channels, and may represent that the channel is open only if four independent gates of the channel are open simultaneously. Similarly, m represents an open gate of the sodium channels and h represents an inactivation gate. The dynamics of the individual gates are explained below.

Dynamics of the gating variables The gating variables are assumed to be governed by a reaction of the form

$$C \underset{\beta}{\overset{\alpha}{\rightleftharpoons}} O,$$

$\alpha_m = \frac{0.1(v+40)}{1-\exp(-(v+40)/10)}$	$\beta_m = 4\exp\left(-(v+65)/18\right)$
$\alpha_h = 0.07\exp\left(-(v+65)/20\right)$	$\beta_h = \frac{1}{1+\exp(-(v+35)/10)}$
$\alpha_n = \frac{0.01(v+55)}{1-\exp(-(v+55)/10)}$	$\beta_n = 0.125\exp\left(-(v+65)/80\right)$

Table 2.2: Expressions for the voltage-dependent opening and closing rates of the gating variables of the Hodgkin-Huxley model [8]. Note that the membrane potential, v, is here assumed to be given in units of mV and inserted into the expressions without unit. The unit of the rates, α_m, β_m, α_h, β_h, α_n, and β_n are ms^{-1}. Furthermore, the expressions are adjusted so that the resting potential is -65 mV and taken from [32].

where C and O denote the closed and open states of the gate, respectively, and α and β are voltage-dependent opening and closing rates for the gate. The law of mass action (see e.g., [34]) gives that the fraction of open gates are given by equations of the form

$$\begin{aligned}\frac{dm}{dt} &= \alpha_m(1-m) - \beta_m m,\\ \frac{dh}{dt} &= \alpha_h(1-h) - \beta_h h,\\ \frac{dn}{dt} &= \alpha_n(1-n) - \beta_n n.\end{aligned}$$

The expressions for the opening and closing rates are given in Table 2.2.

The equations for the gating variables may also be written on the equivalent form

$$\frac{dx}{dt} = \frac{x_\infty - x}{\tau_x}, \tag{2.10}$$

where

$$\begin{aligned}x_\infty &= \frac{\alpha_x}{\alpha_x + \beta_x},\\ \tau_x &= \frac{1}{\alpha_x + \beta_x},\end{aligned}$$

for $x = m, n, h$. Assuming that v, and thereby also α_x and β_x, are constant, (2.10) has the analytical solution

$$x(t) = x_\infty - (x_\infty - x(0))e^{-t/\tau_x}. \tag{2.11}$$

In other words, x approaches the value x_∞ as $t \to \infty$. Furthermore, the smaller the value of τ_x, the faster $x(t)$ approaches x_∞.

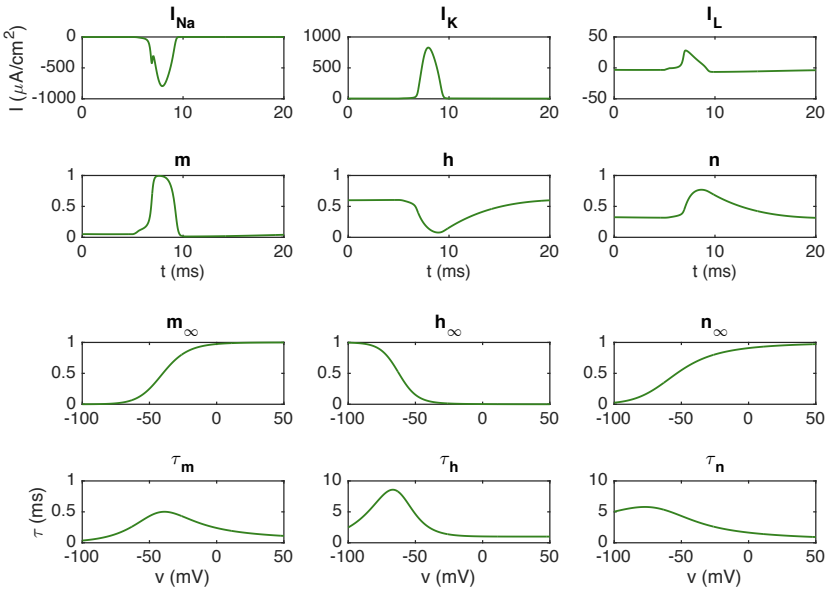

Figure 2.3: Currents and gating variables of the Hodgkin-Huxley model [8]. The upper two panels show the current densities I_{Na}, I_{K} and I_{L} and the gating variables m, h and n as functions of time during the action potential of Figure 2.2. The lower two panels show the steady state values, m_∞, h_∞, n_∞ and time constants, τ_m, τ_h, τ_n, for the gating variables as functions of the membrane potential.

Overview of the action potential dynamics The lower two panels of Figure 2.3 show how the values of x_∞ and τ_x depend on the membrane potential in the Hodgkin-Huxley model. The upper two panels show the currents and the gating variables as functions of time during an action potential.

From Figure 2.3, the dynamics underlying the action potential of the Hodgkin-Huxley model may be examined. For example, we see that for membrane potentials close to the resting potential of -65 mV, m_∞ is close to zero, and thus the open gate m of I_{Na} is close to zero, and I_{Na} is close to zero. The value of n_∞ is larger at potentials close to -65 mV, giving rise to a value of n close to 0.3. However, $o_{\mathrm{K}} = n^4$ gets a value of approximately $0.3^4 \approx 0.01$, so only a small fraction of the total number of potassium channels are open at rest as well. When the cell is stimulated by a small negative stimulus current, the membrane potential is increased. This increases the value of $m_\infty(v)$ and thereby also increases the value of m (see (2.11)). As a result, the I_{Na}-current is activated, allowing positive Na^+-ions to flow into the cell and increase the membrane potential further. This again results in a higher value of $m_\infty(v)$, and thus m and I_{Na} increase. However,

as the membrane potential increases, the value of n_∞ approaches one, activating the I_{K}-current which allows positive K^+-ions to leave the cell and the membrane potential to be reduced. In addition, the value of h_∞ approaches zero as the membrane potential increases, leading to a small value of h and inactivation of the I_{Na}-current. However, because τ_m is much smaller than τ_h and τ_n, the h and n gates approach h_∞ and n_∞ slower than m approaches m_∞, and the I_{Na}-current is therefore allowed enough time to depolarize the membrane. Nevertheless, after the changes to the h and n gates have kicked in, the I_{Na}-current terminates, and the I_{K}-current drives the membrane potential back to rest.

2.1.3 Cardiac action potential models

The cardiac action potential In every heartbeat, the contraction of the heart is synchronized by an action potential being generated in the cardiac muscle cells (cardiomyocytes). Like the neuron action potential shown in Figure 2.2, the action potential of a cardiac cell begins with a rapid depolarization of the cell membrane that is typically caused by a large inward sodium current. The sodium current is activated by an increased membrane potential that is often caused by electrical activity in neighboring cells[3]. After the fast upstroke of the action potential, there is commonly a short period of rapid partial repolarization as potassium currents are activated (see the action potentials of Figures 2.5 and 2.10). The membrane potential then remains quite constant at a depolarized value for several hundred milliseconds. Simplified, this is maintained by a balance between inward calcium currents and outward potassium currents. Finally, the membrane potential returns to rest by inactivation of the calcium channels and increased potassium currents.

Modeling the cardiac action potential In 1962, ten years after the publication of the action potential model by Hodgkin and Huxley for the squid giant axon, the first action potential model for a cardiac cell was introduced by Denis Noble [35]. This was an adjusted version of the Hodgkin-Huxley model, describing the action potential of a Purkinje fibre[4]. After the publication of this first model, cardiac action potential models have been continuously improved and extended. The first models followed the structure of the Hodgkin-Huxley model closely, but the modeling strategy has later been extended to account for components that have been revealed to be important for the electrical properties of cardiac cells [9].

Calcium dynamics The intracellular calcium dynamics play an important role in the function of cardiac cells, since an increased Ca^{2+}-concentration is what makes the cardiac muscle cells contract. When the membrane is depolarized during the upstroke of the action potential, calcium channels on the cell membrane are activated. This allows Ca^{2+}-ions to flow into the cell, particularly into small

[3] Models for the propagation of the action potential from cell to cell will be discussed in Section 2.2.

[4] The Purkinje fibres are large cardiac muscle fibres specialized for fast conduction of electrical signals at the inner layer of the ventricular muscle [36] (see Figure 2.10).

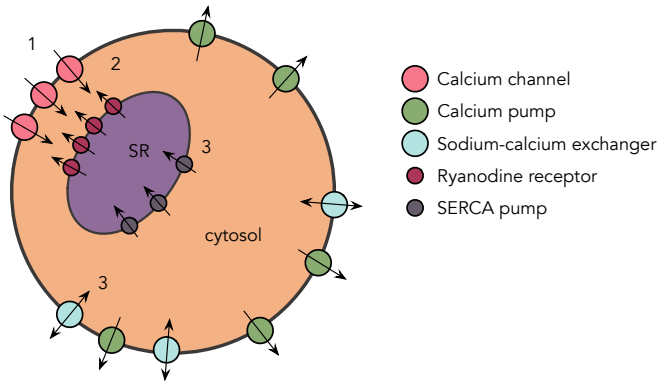

Figure 2.4: Simplified overview of calcium-induced calcium release. (1) Depolarization of the membrane causes Ca^{2+}-channels on the membrane to open and release Ca^{2+}-ions into the cell. (2) The increased Ca^{2+}-concentration triggers further release of Ca^{2+}-ions from the SR through the RyRs. The resulting increased Ca^{2+}-concentration makes the cell contract. (3) The cytosolic Ca^{2+}-concentration returns to a resting level by pumping of Ca^{2+}-ions back to the SR through the SERCA pumps and back to the extracellular space through the sarcolemmal calcium pumps and the sodium-calcium exchangers.

restricted spaces called the dyads. The amount of Ca^{2+}-ions entering the cell through the membrane calcium channels are not alone enough to trigger contraction, but in addition, the increased Ca^{2+}-concentration in the dyads activates channels called ryanodine receptors (RyRs) located on the membrane of an intracellular Ca^{2+}-store called the sarcoplasmic reticulum (SR) (see Figure 2.4). As a result, the RyRs release a large amount of Ca^{2+}-ions from the SR into the bulk cytosol, in a process referred to as calcium-induced calcium release (CICR) [37]. The resulting increased Ca^{2+}-concentration makes the cell contract as the Ca^{2+}-ions bind to the contractile filaments. After contraction, the Ca^{2+}-concentration in the cytosol is returned to the resting level by pumping of Ca^{2+}-ions back to the SR and the extracellular spaces through the SERCA pumps and the sarcolemmal calcium pumps, respectively. In addition, Ca^{2+}-ions leave the cytosol for the extracellular space through the sodium-calcium exchangers on the cell membrane.

Model extensions Because of the important role of the intracellular calcium dynamics, the action potential models for cardiac cells often include equations for the time changes of the intracellular calcium concentration and for the calcium fluxes into and out of the SR. Moreover, a large portion of the calcium ions in the cell is bound to large calcium binding proteins (referred to as calcium buffers), and equations for the reactions between free calcium and calcium buffers are often included in the models. The fact that the calcium concentration may be different

in different parts of the cell, e.g. in the dyad, at other locations close to the membrane and in the bulk cytosolic space, is also accounted for in some of the models, including multiple intracellular compartments. In addition, changes of the intracellular sodium and potassium concentrations might also influence the shape of the action potential, and equations for these concentrations are therefore also sometimes included in the models [38].

Furthermore, the models have been extended to include currents through a large number of different types of ion channels and ionic pumps and exchangers. Such pumps and exchangers include the sarcolemmal calcium pump, the sodium-calcium exchanger and the sodium-potassium exchanger. Markov models with multiple states have also been introduced as an alternative to the gating variables of the Hodgkin-Huxley model (see e.g., [38, 39, 40, 41])

Model variations Today, a large number of different action potential models for cardiac cells exist, and many can be found in the online repository CellML [44] (see also e.g., [9] for an overview of different cardiac action potential models). The models represent different types of cells, for example cells from different locations of the heart (e.g., purkinje fibres [35], atrial cardiomyocytes [45], ventricular cardiomyocytes [19]), cells from different species (e.g., rabbit [46], mouse [47], human [42]) and different levels of maturity (e.g., mature cardiomyocytes [47], neonatal cardiomyocytes [48], cardiomyocytes derived from stem cells [43]).

In addition, the complexity of the models vary greatly — from simple models with just a few currents (e.g., [49, 50]), to detailed models including a large number of currents and intracellular compartments (e.g., [19, 51]). Phenomenological models have also been introduced, replicating properties of an action potential in a simplified manner, without realistic representations of the different ion channel currents (e.g., [52, 53]).

To illustrate some of the variability of the cardiac action potential models, the currents and intracellular compartments of four examples of cardiac action potential models are illustrated in the left panel of Figure 2.5 — the Noble 1962 model for Purkinje fibres [35], the ten Tusscher et al. 2006 model for ventricular cardiomyocytes [42], the Grandi et al. 2010 model for ventricular cardiomyocytes [19], and the Paci et al. 2013 model for ventricular-like human induced pluripotent stem cell-derived cardiomyocytes (hiPSC-CMs) [43]. The right panel shows the action potentials and calcium transients generated by the models. Note that the Noble 1962 model does not include intracellular calcium dynamics, so no calcium transient is shown for that model.

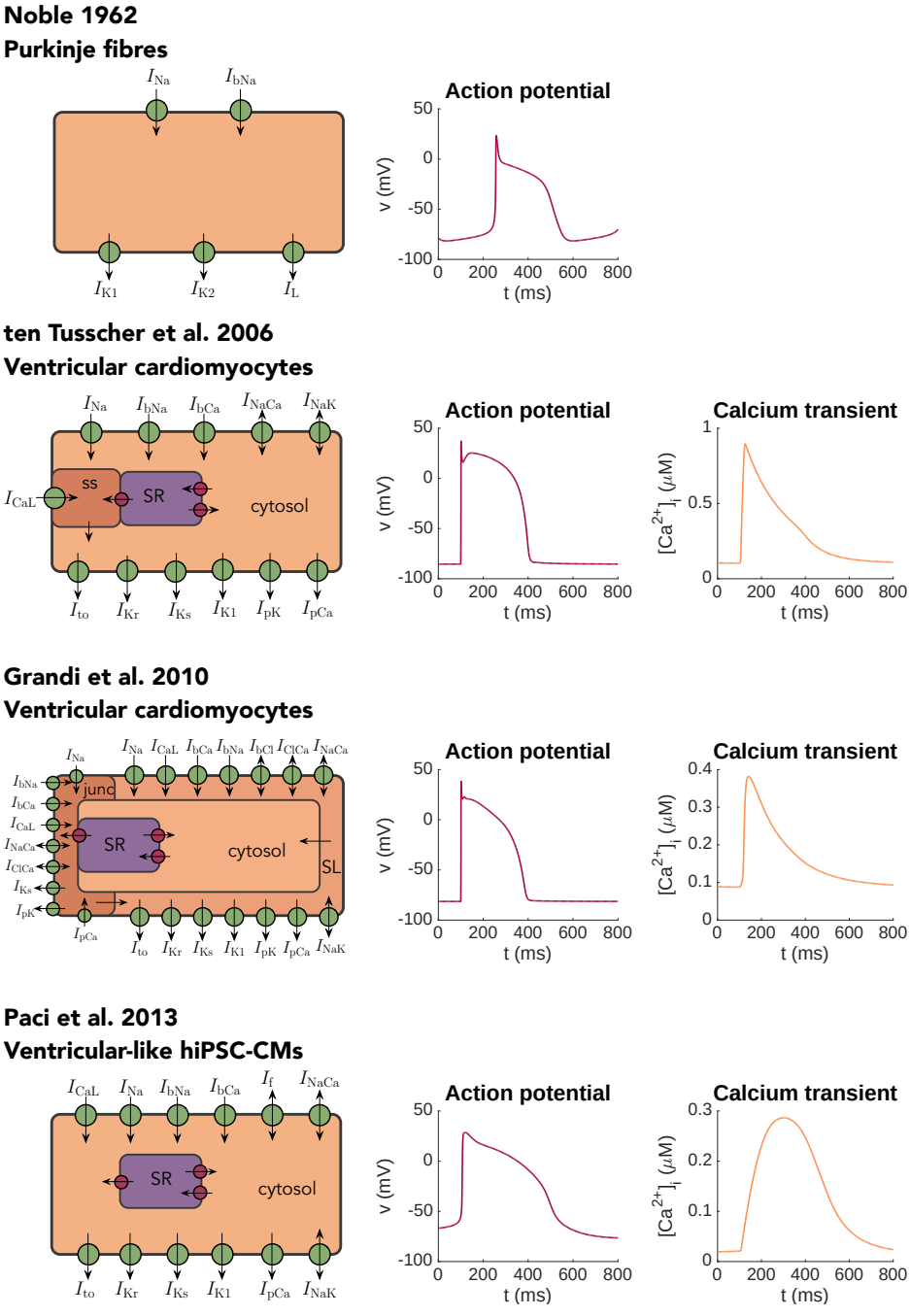

Figure 2.5: Model currents and intracellular compartments (left) and APs and calcium transients (right) of four examples of cardiac AP models [35, 42, 19, 43].

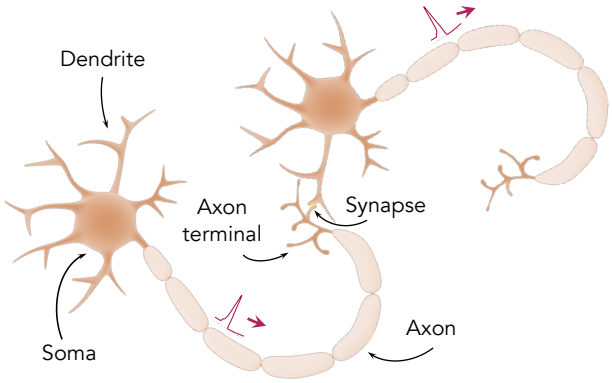

Figure 2.6: Illustration of two neurons, based on [54, 55]. Each neuron consists of the main body, called the soma, and the dendrites and axon extending from the soma. At the end of the axon, it divides into branches that form communication sites to other neurons, called axon terminals. The point where two neurons communicate is referred to as a synapse [56].

2.2 Models of electrical conduction in biological tissues

The action potential models of the previous section describe how the action potential of a neuron or a cardiac cell is generated by ionic currents across the membrane. In this section, models for the spatial propagation of action potentials in a single cell or in a collection of cells are discussed. In addition, the line-source and point-source approximations used to compute the extracellular potential around neurons are described.

2.2.1 The cable equation

This section will introduce the cable equation used to model the spatial conduction of action potentials along an excitable membrane.

Neuron structure Figure 2.6 illustrates the basic structure of two neurons, each consisting of a main body (the *soma*), the *dendrites* and an *axon*. The dendrites are the main apparatus for receiving incoming signals from other neurons, while the axon is the primary pathway for carrying electrical signal to other neurons [56]. In a simplified representation of the neuronal processes, we may say that in order for a neuron to generate an action potential and send a signal to the neurons connected to its axon terminals, a sufficiently large input signal from neighboring neurons must reach the initial segment of the neuron's axon. In other words, the function of complex networks of neurons depends on how the incoming signals of

each neuron spread from the dendrites to the soma and the axon, and how the outgoing signals are propagated down the axon. Therefore, an understanding of the nature of the spread of electrical signals along a cell is an important part of the understanding of the function of a neuron.

The cable equation A commonly used model for the spread of electrical signals along a neuron is called the cable equation. The reason behind the name is that the model was first developed in the 1800s to model the transmission of electrical signals along telegraph cables across the atlantic, before it was adapted to the modeling of signal spread in neurons [57, 58]. In their 1952 paper, Hodgkin and Huxley used the cable equation to model the conduction of an action potential along a squid giant axon [8], and their calculations were able to accurately compute a conduction velocity of 18.8 m/s, about 10% off the experimental value of 21.2 m/s. The same year, Silvio Weidmann demonstrated that propagation of electrical signals in cardiac Purkinje fibres could be described by the same equation [59]. Since then, the cable equation has been used extensively to study electrical conduction in excitable cells (see e.g., [11, 60, 61, 62]).

Derivation of the cable equation The cable equation may be derived by assuming that the cell is shaped like a cylinder with radius r and that the electrical potential only varies in the direction along the long axis of the cylinder (see Figure 2.7). By applying Kirckhoff's current law in every point x along the cylinder and Ohm's law for the current along the cylinder, the following equation is obtained[5]

$$C_m \frac{\partial v}{\partial t} + I_{\text{ion}} = \eta \frac{\partial^2 u_i}{\partial x^2}, \tag{2.12}$$

where

$$\eta = \frac{r\sigma_i}{2}, \tag{2.13}$$

and v is the membrane potential (typically in mV), u_i is the intracellular potential (typically in mV), C_m is the specific membrane capacitance (typically in $\mu\text{F}/\text{cm}^2$), I_{ion} is the total ionic current density out of the cell (typically in $\mu\text{A}/\text{cm}^2$), r is the cell radius (typically in cm), and σ_i is the intracellular conductivity (typically in mS/cm). By using the definition of the membrane potential, $v = u_i - u_e$, and assuming that the extracellular potential, u_e, is constant, we obtain the cable equation [33]:

$$C_m \frac{\partial v}{\partial t} + I_{\text{ion}} = \eta \frac{\partial^2 v}{\partial x^2}. \tag{2.14}$$

[5] See the first paper of the thesis for a derivation of this equation. Note that in that paper, the cell is assumed to be shaped as a rectangular cuboid instead of a cylinder, and η is therefore given by $\frac{h\sigma_i}{4}$, where h is the width of the cell.

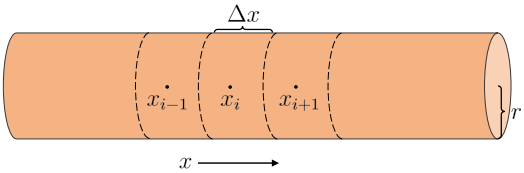

Figure 2.7: A cell represented as a cylinder with radius r.

Alternative derivation of the cable equation Note that an alternative derivation of the cable equation does not rely on the assumption of a constant extracellular potential, but instead assumes that the value of extracellular potential only varies in the direction along the cell (see e.g., [34]). In that case, the Ohmic currents in the extracellular space take a similar form as the intracellular currents, and Kirchhoff's current law applied in the extracellular domain yields

$$C_m \frac{\partial v}{\partial t} + I_{\text{ion}} = -\eta_e \frac{\partial^2 u_e}{\partial x^2}, \tag{2.15}$$

where

$$\eta_e = \frac{\sigma_e A_e}{2\pi r}.$$

Here, σ_e is the extracellular conductivity (in mS/cm) and A_e is the cross-sectional area of the extracellular space (in cm^2). Combining (2.12) and (2.15) gives

$$C_m \frac{\partial v}{\partial t} + I_{\text{ion}} = \eta^* \frac{\partial^2 v}{\partial x^2}, \tag{2.16}$$

where

$$\eta^* = \frac{\eta}{1 + \frac{\eta}{\eta_e}}. \tag{2.17}$$

From this definition of η^*, we see that the model (2.16) is essentially the same as the model (2.14) if η_e is much larger than η. This is true, e.g., if the extracellular conductivity, σ_e, is very large, if the cell radius, r, is very small, or if the extracellular cross-sectional area, A_e, is very large.

Initial and boundary conditions The initial condition for the cable equation can be specified as

$$v(0, x) = v_0(x),$$

where $v_0(x)$ might, for example, be chosen as the resting membrane potential. Furthermore, a set of boundary conditions must be assigned for the start and the end of the cell. For example, one may specify the no-flow boundary conditions

$$\frac{\partial v(t, a)}{\partial x} = \frac{\partial v(t, b)}{\partial x} = 0$$

for a cell defined between $x = a$ and $x = b$, representing that no current flows through the cell ends.

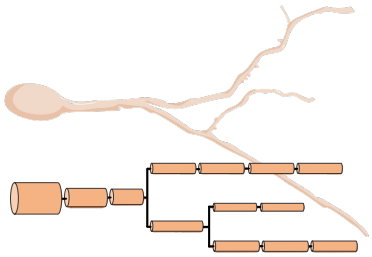

Figure 2.8: Illustration of a compartmental model adjusted to fit a neuron geometry. The illustration is adapted from Figure 4.1 in [33].

Numerical solution Since the ionic current density, I_{ion}, might be given by a complicated mathematical model, it is often most convenient to solve the cable equation using numerical methods. A straightforward approach is to discretize the cell into N small compartments of length Δx (see Figure 2.7), and seek discrete solutions

$$v_i^n \approx v(t_n, x_i), \quad n = 0, ..., N_t, \quad i = 0, ..., N,$$

for the center points x_i of the compartments and the discrete time points given by $t_n = n\Delta t$ for some small time step Δt. The derivatives in (2.14) may then be approximated by the finite differences

$$\frac{\partial v(t,x)}{\partial t} \approx \frac{v(t,x) - v(t-\Delta t, x)}{\Delta t}, \tag{2.18}$$

$$\frac{\partial^2 v(t,x)}{\partial x^2} \approx \frac{v(t, x+\Delta x) - 2v(t,x) + v(t, x-\Delta x)}{\Delta x^2}, \tag{2.19}$$

which yield the following discrete version of the cable equation

$$C_m \frac{v_i^n - v_i^{n-1}}{\Delta t} + I_{\text{ion},i}^n = \eta \frac{v_{i+1}^n - 2v_i^n + v_{i-1}^n}{\Delta x^2}. \tag{2.20}$$

Extensions of the cable equation By specifying different models for the ionic current density, I_{ion}, at different locations of the cell, the cable equation allows for different spatial distributions of ion channels on the cell membrane. For example, the membrane of many dendrites may be assumed not to contain any voltage-gated channels [32], so the model for the current density might be different for parts of the neuron representing the dendrites than for parts representing the axon. Moreover, a network of cells modelled by the cable equation can be connected by distributing a number of synapses between the cells and specifying models for the synapse dynamics. The cable equation framework may also be extended to account for branching and cell parts with different radii like illustrated in Figure 2.8 (see e.g., [33]). In this way, the cable equation can be used to represent neurons with geometries based on reconstructions of realistic neuron morphologies. This type of neuron modeling is often referred to as compartmental modeling [60].

2.2.2 The point-source and line-source approximations

A common approach for measuring neuronal activity is to record the extracellular potential around neurons [63]. The extracellular recordings are typically easier to carry out than intracellular recordings, but the signals may be harder to interpret because they might be generated by a large number of transmembrane currents from different locations [64].

Mathematical modeling can be a useful tool for gaining more insight into the link between the recorded extracellular potentials and the underlying neural activity [65]. For example, mathematical modeling has been used to study how the geometry of the dendrites and the position of the synapses and recording electrodes affects the recorded extracellular potentials from a single neuron (see e.g., [12]) and populations of neurons (see e.g., [66]).

The procedure applied in these studies consist of two steps:

1. First, a numerical simulation of the cable equation is carried out, computing the membrane potential and current densities in every compartment for a number of time steps.

2. Then, the extracellular potential is computed using the membrane currents recorded in Step 1.

To derive the formula typically used to compute the extracellular potential in Step 2, the extracellular space is assumed to be an infinite, homogeneous, isotropic and purely resistive three-dimensional medium. In that case, the extracellular potential u_e in a point $\mathbf{r} = (x, y, z)$ due to a single current source, c_j, located in a point r_j is given by [64]

$$u_e(\mathbf{r}, t) = \frac{1}{4\pi\sigma_e} \frac{c_j(t)}{|\mathbf{r} - \mathbf{r}_j|},$$

where σ_e is the conductivity of the extracellular medium (typically in mS/cm), c_j is the current from the point r_j (typically in μA) and $|\mathbf{r} - \mathbf{r}_j|$ is the distance between $\mathbf{r}$ and $\mathbf{r}_j$ (typically in cm).

When several point sources are present, the contributions to the extracellular potential sums up linearly (see e.g., [67]). Assuming that we have recorded the value of the membrane currents c_j from a number of compartments in a compartmental model and know the location of each compartment, two alternative approximations may be used to calculate the value of u_e from the sum of these sources; the point-source approximation or the line-source approximation [65].

The point-source approximation In the point-source approximation, the membrane currents recorded in a compartment are assumed to enter the extracellular space from a single point located in the center of the compartment. The extracellular potential u_e in a point $\mathbf{r}$ at time t_n can then be computed by [65]

$$u_e(\mathbf{r}, t_n) = \frac{1}{4\pi\sigma_e} \sum_{j=1}^{N} \frac{c_j^n}{|\mathbf{r} - \mathbf{r}_j|}, \tag{2.21}$$

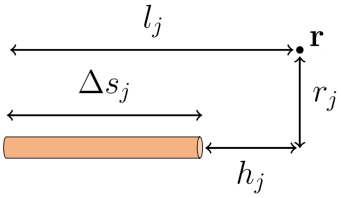

Figure 2.9: Illustration of the lengths used to compute the extracellular potential from the line-source approximation.

where N is the total number of compartments in the model and c_j^n is the total membrane current (including the capacitive current) in compartment j at time t_n. This total current may be computed from the discrete cable equation of the form (2.20) by

$$c_j^n = A_j \left(C_m \frac{v_j^n - v_j^{n-1}}{\Delta t} + I_{\text{ion},j}^n \right), \tag{2.22}$$

where A_j is the membrane area of compartment j.

The line-source approximation In the line-source approximation, the membrane currents of each compartment is assumed to be evenly distributed along a line corresponding to the axis of the compartment. The extracellular potential is then given by [64]

$$u_e(\mathbf{r}, t_n) = \frac{1}{4\pi\sigma_e} \sum_{j=1}^{N} \frac{c_j^n}{\Delta s_j} \log \left| \frac{\sqrt{h_j^2 + r_j^2} - h_j}{\sqrt{l_j^2 + r_j^2} - l_j} \right|, \tag{2.23}$$

where Δs_j is the length of the line segment representing compartment j and r_j is the distance from the point $\mathbf{r}$ to the line segment in the direction perpendicular to the line (i.e., perpendicular to the cylinder axis). Furthermore, h_j is the distance from the end of the line segment to $\mathbf{r}$ in the direction parallel to the line, and $l_j = \Delta s_j + h_j$ is the distance from the start of the line segment to $\mathbf{r}$ in the direction parallel to the line. See Figure 2.9 for an illustration of each of these lengths.

Note that as the compartment length Δs_j approaches 0, h_j approaches l_j, and, using L'Hôpital's rule (see e.g., [68]), we get

$$\lim_{\Delta s_j \to 0} \frac{c_j^n}{\Delta s_j} \log \left| \frac{\sqrt{h_j^2 + r_j^2} - h_j}{\sqrt{l_j^2 + r_j^2} - l_j} \right| = \lim_{\Delta s_j \to 0} \frac{c_j^n}{\sqrt{(h_j + \Delta s_j)^2 + r_j^2}} = \frac{c_j^n}{|\mathbf{r} - \mathbf{r}_j|}.$$

In other words, the difference between the line-source and point-source approximations approaches zero as the length of the compartments approaches zero.

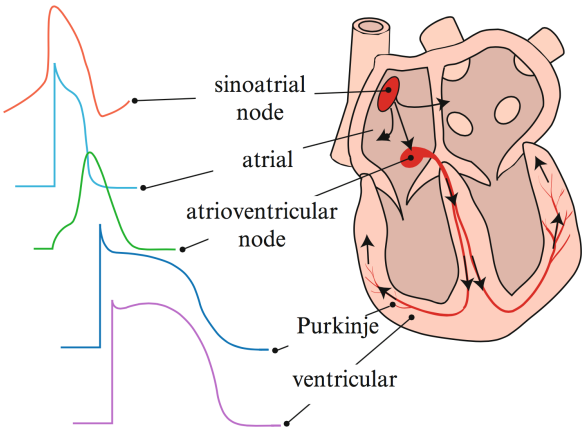

Figure 2.10: Illustration of action potentials in different parts of the heart. The illustration is taken from [54].

2.2.3 The bidomain and monodomain models

In this section, the bidomain and monodomain models for electrical propagation in cardiac tissue will be introduced.

Cardiac propagation The electrical activity of the heart, coordinating the contraction of the heart muscle, is initiated by a collection of pacemaker cells located at the sinoatrial node (see Figure 2.10). The action potential generated here then propagates through the atrial cells and makes the atria contract. At the boundary between the atria and the ventricles, the propagating wave must pass through the slowly conducting atrioventricular node. Afterwards, the wave propagates through a collection of Purkinje fibres, quickly distributing the electrical signals in the ventricles. The wave then spreads through the ventricles, causing ventricular contraction [34].

Tissue structure In order for the action potential to propagate through the heart, the electrical signals must be able to cross from one cell to another. This cell communication is believed to primarily be due to gap junctions allowing for flow of ions between neighboring cells. The left panel of Figure 2.11 illustrates the structure of a small collection of cardiac muscle cells (cardiomyocytes). Each cardiomyocyte is shaped as an irregular cylinder, and the cells may form branches, like illustrated in the figure [69]. The length of each cell is typically in the range

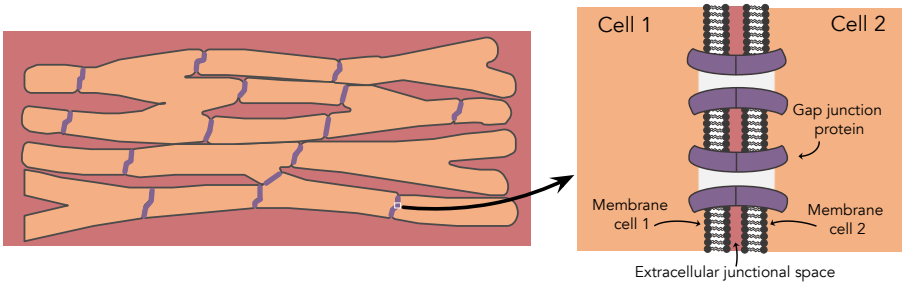

Figure 2.11: Illustration of a small piece of cardiac tissue (left) and a part of an intercalated disc (right). The cells are colored orange and the extracellular space is colored red. In addition, the intercalated discs and the gap junction proteins are colored purple in the left and right panels, respectively.

50–120 μm and the diameter is typically 5–25 μm [69]. Intercalated discs are located at the boundary between adjacent cells. In the figure, these discs are marked with a purple color. The intercalated discs contain specialized proteins that allow ions to flow from one cell to another. A part of an intercalated disc is illustrated in the right panel of Figure 2.11.

Models of cardiac propagation As explained above, the cable equation has been used to study the propagation of electrical signals along a strand of cardiomyocytes (see e.g., [70, 62]). The gap junctions may then be treated as resistive boundaries between the compartments of the cable representing different cells. Moreover, the EMI model described in the next section has been used to study cardiac propagation (see e.g., [71, 72, 73]), in addition to a number of alternative models representing the discrete nature of cardiac tissue (see e.g., [74, 75, 76, 77]).

However, the most commonly used models for the electrical propagation in cardiac tissue is probably the classical bidomain and monodomain models (see e.g., [34]). These models view the tissue in a volume-averaged manner, assuming that, at a length scale significantly larger the cell size, the tissue may be treated as a homogeneous medium with an extracellular space, an intracellular space and a membrane existing everywhere.

The bidomain and monodomain models have been used to study a number of properties of cardiac conduction on tissue level, and the computational costs associated with the models have even allowed for whole heart simulations. For example, the models have been used to study the mechanisms behind arrhythmias and properties of defibrillation (see e.g., [14]).

The bidomain model The bidomain model was introduced in the 1970s [78] and may be derived from the more detailed EMI model described in Section 2.2.4 using mathematical two-scale homogenization (see e.g., [79, 80]). The model takes the form

$$\nabla \cdot (M_i \nabla v) + \nabla \cdot (M_i \nabla u_e) = \chi \left(C_m \frac{\partial v}{\partial t} + I_{\text{ion}} \right), \tag{2.24}$$

$$\nabla \cdot (M_i \nabla v) + \nabla \cdot ((M_i + M_e) \nabla u_e) = 0, \tag{2.25}$$

where v and u_e are the membrane potential and extracellular potential, respectively, (typically in mV), χ is the area of the cell membrane per unit volume (typically in cm^{-1}), C_m is the specific membrane capacitance (typically in $\mu\text{F}/\text{cm}^2$), I_{ion} is the ionic current density across the membrane (typically in $\mu\text{A}/\text{cm}^2$), and M_i and M_e are effective conductivity tensors (typically in mS/cm) for the intracellular and extracellular spaces, respectively.

The values of the conductivity tensors M_i and M_e depend on a number of properties like the cell geometry, the gap junction coupling, the cell orientation, and the cell density. An example of how the conductivity tensors may be set up based on assumptions about the tissue structure is given in [80].

The monodomain model In the more simplified monodomain model, it is assumed that the intracellular and extracellular conductivity tensors are proportional in the sense that

$$M_e = \lambda M_i,$$

for a constant scalar λ. In that case, the bidomain model (2.24)–(2.25) can be reduced to a single equation of the form

$$\frac{\lambda}{1+\lambda} \nabla \cdot (M_i \nabla v) = \chi \left(C_m \frac{\partial v}{\partial t} + I_{\text{ion}} \right). \tag{2.26}$$

This model may be solved more efficiently than the bidomain model and is therefore a common choice of cardiac tissue model [13, 34, 81]. However, in some cases, the full bidomain model might be required to properly represent the electrical properties of the tissue. For example, the bidomain model may be required when strong extracellular stimulations are present, e.g. in studies of defibrillation [13].

Initial and boundary conditions Like for the cable equation, a suitable set of initial conditions and boundary conditions must be specified for the bidomain and monodomain models. In addition, the ionic current density, I_{ion}, will typically be modelled by a cardiac action potential model like described in Section 2.1.3.

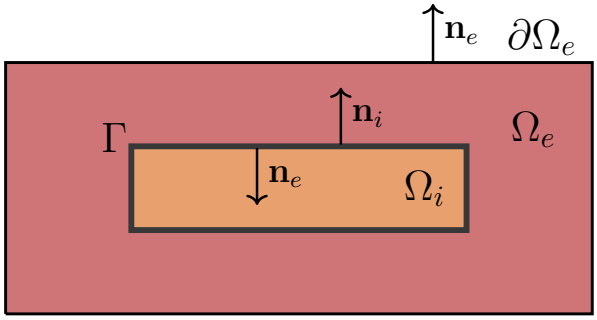

Figure 2.12: Illustration of a 2D version of an EMI model domain for a single cell surrounded by an extracellular space. The intracellular domain, denoted by Ω_i, and the extracellular space, denoted by Ω_e, are treated as separate parts of the domain. The cell membrane, denoted by Γ, represents the boundary between the intracellular and extracellular domains.

2.2.4 The extracellular-membrane-intracellular (EMI) model

In this thesis, an alternative to the above mentioned models of electrical conduction in biological tissues is considered. The model is referred to as the EMI model since the **E**xtracellular space, the cell **M**emebrane and the **I**ntracellular space are all explicitly represented as separate parts of the domain. For a single cell surrounded by an extracellular space, like illustrated in Figure 2.12, the EMI model takes the form

$$\begin{aligned}
\nabla \cdot \sigma_i \nabla u_i &= 0, \text{ in } \Omega_i, && (2.27)\\
\nabla \cdot \sigma_e \nabla u_e &= 0, \text{ in } \Omega_e, && (2.28)\\
\mathbf{n}_e \cdot \sigma_e \nabla u_e &= -\mathbf{n}_i \cdot \sigma_i \nabla u_i, \text{ at } \Gamma, && (2.29)\\
u_i - u_e &= v, \text{ at } \Gamma, && (2.30)\\
I_m &= -\mathbf{n}_i \cdot \sigma_i \nabla u_i, \text{ at } \Gamma, && (2.31)\\
\frac{\partial v}{\partial t} &= \frac{1}{C_m}(I_m - I_{\text{ion}}), \text{ at } \Gamma, && (2.32)
\end{aligned}$$

where u_i, u_e, and v, are the intracellular, extracellular and membrane potentials (typically in mV) defined in Ω_i, Ω_e and at Γ respectively, $\mathbf{n}_i$ and $\mathbf{n}_e$ are the outward pointing normal vectors of the intracellular and extracellular spaces, respectively, C_m is the specific membrane capacitance (typically in $\mu\text{F/cm}^2$), I_{ion} is the ionic current density across the membrane (typically in $\mu\text{A/cm}^2$), I_m the sum of the capacitive and ionic current densities (typically in $\mu\text{A/cm}^2$), and σ_i and σ_e are the

intracellular and extracellular conductivities, respectively (typically in mS/cm). If the value of σ_i and σ_e are assumed to be directionally dependent (i.e., for anisotropic materials), σ_i and σ_e may be represented as tensors, but if the values are assumed to be independent of direction (i.e., for isotropic materials), σ_i and σ_e can be represented as scalars. Furthermore, σ_i and σ_e may vary with position if the intracellular and extracellular spaces are assumed to be inhomogeneous. A derivation of the model equations defined above from Maxwell's equations of electromagnetism is found in Chapter 3.

The EMI model defined above may, for instance, be used as an alternative to the cable equation for computing the membrane potential of neurons without the assumption of a constant extracellular potential. In addition, the EMI model can be used as an alternative to the two-step procedure for computing the extracellular potential around neurons, by computing the membrane currents and the extracellular potential as one coupled system. Furthermore, the model might be used as an alternative to the classical homogenized bidomain and monodomain models for cardiac tissue if the model is extended to include cell connections.

In previous studies, the EMI model has been used to study the electrical properties of both neurons (e.g., [82]) and cardiac tissue (e.g., [83, 71]). For example, the model has been used to study the effect of an external electrical field on an excitable cell [84, 85], the effect of tissue morphology on cardiac propagation [71, 72, 73], and to compute appropriate values for the effective bidomain conductivity tensors, M_i and M_e [86].

Initial and boundary conditions In the EMI model, initial conditions must be specified for the membrane potential and any additional state variables of the model chosen for I_{ion}. In addition, some boundary conditions must be defined at the outer boundary of the extracellular domain, $\partial\Omega_e$. For example, one may assume that the extracellular potential is zero on the outer boundary, expressed as a Dirichlet boundary condition

$$u_e = 0, \quad \text{at } \partial\Omega_e,$$

or that no current flows through the outer boundary, expressed as the Neumann boundary condition

$$\frac{\partial u_e}{\partial \mathbf{n}_e} = 0, \quad \text{at } \partial\Omega_e.$$

Note that if Neumann boundary conditions are applied on the entire $\partial\Omega_e$, the solution of the system (2.27)–(2.32) is not uniquely determined, in the sense that for a given solution (u_e, v, u_i), the solution ($u_e + a$, v, $u_i + a$) will also satisfy the equations for any constant a. Therefore, an additional requirement, e.g.

$$\int_{\Omega_e} u_e dV = 0$$

must be defined to obtain a unique solution.

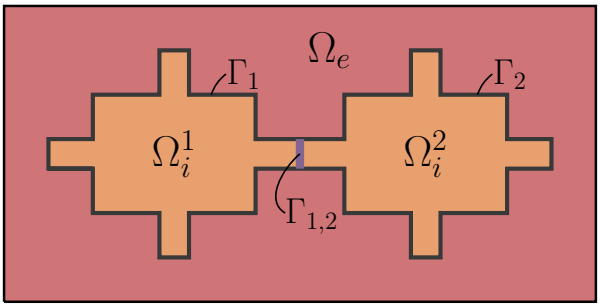

Figure 2.13: Illustration of a 2D version of an EMI model domain for two cells connected by an intercalated disc denoted by $\Gamma_{1,2}$.

Including gap junctions In order to use the EMI model to model collections of connected cardiac cells, models for the currents through the gap junctions connecting neighboring cells should be included. This may be done by treating the boundary between two cells as membranes with embedded gap junction channels and capacitive properties. For two connected cells like illustrated in Figure 2.13, the EMI model can for example be extended to include equations of the form

$$\mathbf{n}_i^2 \cdot \sigma_i \nabla u_i^2 = -\mathbf{n}_i^1 \cdot \sigma_i \nabla u_i^1 \equiv I_{1,2}, \quad \text{at } \Gamma_{1,2}, \tag{2.33}$$

$$u_i^1 - u_i^2 = w, \quad \text{at } \Gamma_{1,2}, \tag{2.34}$$

$$w_t = \frac{1}{C_{1,2}}(I_{1,2} - I_{\text{gap}}), \quad \text{at } \Gamma_{1,2}, \tag{2.35}$$

where $\Gamma_{1,2}$ is the intercalated disc containing the gap junction proteins, u_i^1, u_i^2, $\mathbf{n}_i^1$, and $\mathbf{n}_i^2$, are the intracellular potentials (typically in mV) and the outward pointing normal vectors in the cells denoted by Ω_i^1 and Ω_i^2, respectively, $C_{1,2}$ is the capacitance of the intercalated disc (typically in $\mu\text{F/cm}^2$), I_{gap} is the current density through the gap junction proteins (typically in $\mu\text{A/cm}^2$), and $I_{1,2}$ is the sum of the capacitive current density over the intercalated discs and the current density through the gap junction proteins (typically in $\mu\text{A/cm}^2$).

The current density through a gap junction might for instance be given by a simple passive model of the form

$$I_{\text{gap}} = \frac{w}{R_g}, \tag{2.36}$$

where R_g (typically in $\text{k}\Omega\text{cm}^2$) represents the gap junction resistance. Alternatively, one can use a more detailed model allowing for a voltage-dependent gap junction resistance (see e.g., [87, 88, 89, 90, 91, 92]).

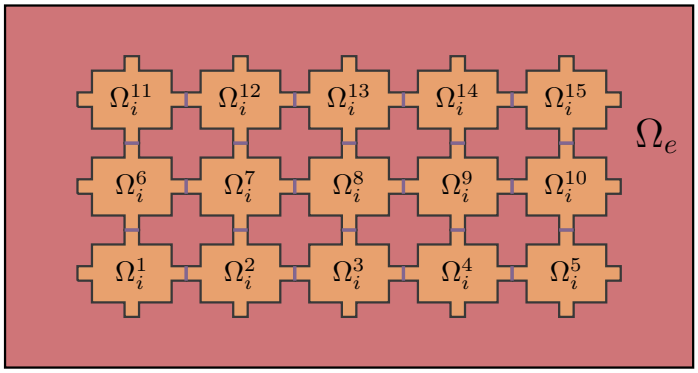

Figure 2.14: EMI model domain for a small collection of connected cells.

Note also that the model for two connected cells outlined above may straightforwardly be extended to models for larger collections of connected cardiac cells like illustrated for a 2D grid structure in Figure 2.14.

Chapter 3

Derivation of the EMI model

In this chapter, the extracellular-membrane-intracellular (EMI) model for the electrical potential in and around biological cells will be derived from Maxwell's macroscopic equations of electromagnetism. The derivation is based on the detailed derivation found in [93].

3.1 Fundamental equations

In this section, Maxwell's macroscopic equations of electromagnetism will be described. In addition, a set of simplifying assumptions will be introduced, leading to the equations that form the foundation of the derivation of the EMI model.

3.1.1 Maxwell's macroscopic equations

Maxwell's equations of electromagnetism relate the electric field, $\mathbf{E}$, and the magnetic field, $\mathbf{H}$, in a region to each other and to the charge and current densities in the region [67]. In Maxwell's *microscopic* equations, the electric and magnetic fields are related to the *total* charge and current densities in the region. The total charge and current densities here refer both to the free charges and currents, and to those bound in atomic and molecular configurations. To study the electrical properties of biological tissues, however, it is more convenient to apply Maxwell's *macroscopic* equations [67]. In these equations, we separate the effects of the free and bound electrical charges, and the equations take the form

$$\nabla \cdot \mathbf{D} = \rho, \tag{3.1}$$

$$\nabla \cdot \mathbf{B} = 0, \tag{3.2}$$

$$\nabla \times \mathbf{E} = -\frac{\partial \mathbf{B}}{\partial t}, \tag{3.3}$$

$$\nabla \times \mathbf{H} = \mathbf{J} + \frac{\partial \mathbf{D}}{\partial t}. \tag{3.4}$$

Here, $\mathbf{E}$ is the net macroscopic electric field (typically in mV/cm), and $\mathbf{D}$ is the electric field due to free charges (typically in nC/cm^2), often called the displacement field [67]. This displacement field is defined as

$$\mathbf{D} = \varepsilon_0 \mathbf{E} + \mathbf{P}, \tag{3.5}$$

where ε_0 is the permittivity of empty space (typically in μF/cm) and $\mathbf{P}$ is the field due to dielectric (bound) charges (typically in nC/cm^2). In other words, the field $\mathbf{P}$ describes the capacitive effects (or polarization) originating from slight separation of bound charge, e.g. resulting from the distortion of the negative cloud of electrons around the positive atomic nuclei or rotation of polar molecules [67]. Consequently, the definition (3.5) shows how the displacement field (due only to free charges) depends on the net macroscopic field $\mathbf{E}$ (due to all charges) and the polarization $\mathbf{P}$ (due to bound charges).

Similarly, $\mathbf{H}$ is the magnetic field (typically in μA/cm) and $\mathbf{B}$ is the corresponding magnetic induction field (typically in pJ/((cm)$^2\mu$A)) defined as

$$\mathbf{B} = \mu_0 \mathbf{H} + \mathbf{M}, \tag{3.6}$$

where μ_0 is the permeability of free space (typically in pJ/((μA)^{2}cm)) and $\mathbf{M}$ is the material magnetization (typically in pJ/((cm)$^2\mu$A)).

Furthermore, ρ is the density of free charge (typically in nC/cm^3) and $\mathbf{J}$ is the free current density, or movement of charge (typically in μA/cm^2). In order to be consistent with the above mentioned units, time is given in ms and length is given in cm.

Assumption of linear materials For biological materials, it is common to introduce the assumption that the fields $\mathbf{P}$ and $\mathbf{M}$ are parallel to $\mathbf{E}$ and $\mathbf{H}$, respectively, so that the equations (3.5) and (3.6) may be rewritten to [94, 67]

$$\mathbf{D} = \varepsilon_r \varepsilon_0 \mathbf{E} = \varepsilon \mathbf{E}, \tag{3.7}$$

$$\mathbf{B} = \mu_r \mu_0 \mathbf{H} = \mu \mathbf{H}, \tag{3.8}$$

where ε_r and μ_r are the unitless relative permittivity and permeability of the material, respectively, and

$$\varepsilon = \varepsilon_r \varepsilon_0, \tag{3.9}$$

$$\mu = \mu_r \mu_0. \tag{3.10}$$

Inserting these assumptions into the system (3.1)–(3.4) give Maxwell's macroscopic equations for linear materials:

$$\nabla \cdot \varepsilon \mathbf{E} = \rho, \tag{3.11}$$

$$\nabla \cdot \mu \mathbf{H} = 0, \tag{3.12}$$

$$\nabla \times \mathbf{E} = -\mu \frac{\partial \mathbf{H}}{\partial t}, \tag{3.13}$$

$$\nabla \times \mathbf{H} = \mathbf{J} + \varepsilon \frac{\partial \mathbf{E}}{\partial t}. \tag{3.14}$$

3.1.2 The quasi-static approximation of Maxwell's equations

For the intracellular and extracellular spaces, we introduce a set of assumptions in order to reduce Maxwell's macroscopic equations for linear materials (3.11)–(3.14) to the so-called *quasi-static approximation* of Maxwell's equations. Justifications and discussions of the quasi-static assumptions are given in e.g., [93, 94, 95].

In short, the first assumption introduced is that the feedback of the magnetic field onto the electric field may be neglected, in the sense that the term $\mu\frac{\partial \mathbf{H}}{\partial t}$ may be set to zero in (3.13). The second assumption is that free unbalanced charges is instantly balanced in the intracellular and extracellular spaces, implying that the free charges ρ in (3.11) and the term $\varepsilon\frac{\partial \mathbf{E}}{\partial t}$ in (3.14) may be neglected.

Introducing these two assumptions, Maxwell's macroscopic equations for linear materials (3.11)–(3.14) take the quasi-static form:

$$\nabla \cdot \varepsilon\mathbf{E} = 0, \tag{3.15}$$

$$\nabla \cdot \mu\mathbf{H} = 0, \tag{3.16}$$

$$\nabla \times \mathbf{E} = 0, \tag{3.17}$$

$$\nabla \times \mathbf{H} = \mathbf{J}. \tag{3.18}$$

3.1.3 Ohm's law

Ohm's law is a commonly used assumption to describe the relationship between the current density and the electric field. It assumes that the current density $\mathbf{J}$ is related to the electric field $\mathbf{E}$ by [67]

$$\mathbf{J} = \sigma\mathbf{E}. \tag{3.19}$$

Here, σ is defined as the conductivity of the medium (typically in mS/cm).

Note here that Ohm's law does not account for currents due to diffusional forces. In order to account for the diffusional forces, the flux could instead be described by the Nernst-Planck equation of the form

$$\mathbf{J} = \sigma\mathbf{E} - \sum_i D_i \nabla \rho_i,$$

where D_i are the diffusion coefficients for the different types of ions (typically in $\mathrm{cm}^2/\mathrm{ms}$) and ρ_i are the corresponding charge densities (typically in $\mathrm{nC}/\mathrm{cm}^3$) [67]. However, in the derivation of the EMI model, the currents due to diffusional forces in the intracellular and extracellular spaces are assumed to be negligible. On the other hand, the diffusional forces due to differences in ion concentrations between the intracellular and extracellular spaces are often accounted for in the models used for the currents across the membrane, termed I_{ion} in the derivation below (see Section 2.1 in Chapter 2).

3.1.4 Foundations for the EMI model derivation

We are now ready to sum up the equations forming the foundation of the derivation of the EMI model.

Locations where the quasi-static approximation is assumed to hold: the extracellular and intracellular domains

In the intracellular and extracellular spaces, we assume that the quasi-static approximation of Maxwell's equations (3.15)–(3.18) as well as Ohm's law (3.19) hold. From (3.17),

$$\nabla \times \mathbf{E} = 0,$$

we know that the electric field $\mathbf{E}$ is a conservative vector field and may therefore be defined as the gradient of a scalar field (see e.g., [96]), like

$$\mathbf{E} = -\nabla u, \tag{3.20}$$

where u is defined as the scalar electrical potential (typically in mV). Furthermore, taking the divergence of both sides of (3.18),

$$\nabla \times \mathbf{H} = \mathbf{J},$$

yields

$$\nabla \cdot (\nabla \times \mathbf{H}) = \nabla \cdot \mathbf{J}.$$

and applying the identity

$$\nabla \cdot (\nabla \times \mathbf{H}) = 0 \tag{3.21}$$

(see e.g., [96]), which holds for any vector $\mathbf{H}$, we get

$$\nabla \cdot \mathbf{J} = 0.$$

Inserting Ohm's law (3.19), $\mathbf{J} = \sigma\mathbf{E}$, we obtain

$$\nabla \cdot \sigma\mathbf{E} = 0, \tag{3.22}$$

and inserting (3.20), we get the Laplace equation

$$\nabla \cdot \sigma\nabla u = 0. \tag{3.23}$$

Locations where the quasi-static approximation is not assumed to hold: the cell membrane and intercalated discs

We assume that charges may accumulate at the membrane and on the intercalated discs between neighboring cells. Therefore the quasi-static approximation of Maxwell's equations (3.15)–(3.18) is not assumed to hold on these domain boundaries. In particular, this concerns the assumption that any free charges are instantly balanced, so that ρ in (3.11) and the term $\varepsilon \frac{\partial \mathbf{E}}{\partial t}$ in (3.14) may be neglected.

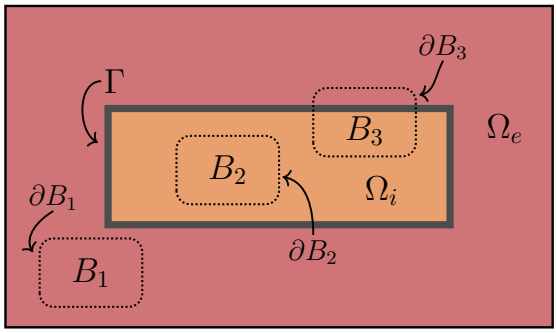

Figure 3.1: Illustration of a domain consisting of an intracellular domain, Ω_i, surrounded by an extracellular domain, Ω_e. The intracellular and extracellular domains are separated by the membrane, denoted by Γ. In addition, examples of volume elements B_1, B_2, B_3 are illustrated. The volume element B_1 exists entirely in the extracellular domain, B_2 exists entirely in the intracellular domain, and B_3 intersects the membrane. The boundary of the volume elements are denoted by ∂B_1, ∂B_2, and ∂B_3, respectively.

Instead of considering the quasi-static equation (3.18), we therefore consider the full form (3.14),

$$\nabla \times \mathbf{H} = \mathbf{J} + \varepsilon \frac{\partial \mathbf{E}}{\partial t}$$

on these boundaries. Taking the divergence of both sides of the equation and applying the vector identity (3.21), we obtain

$$\begin{aligned} \nabla \cdot (\nabla \times \mathbf{H}) &= \nabla \cdot \left(\mathbf{J} + \varepsilon \frac{\partial \mathbf{E}}{\partial t} \right) \\ \nabla \cdot \mathbf{J} &= -\nabla \cdot \varepsilon \frac{\partial \mathbf{E}}{\partial t}. \end{aligned} \tag{3.24}$$

Note here that, following [93], the assumption that the feedback of the magnetic field onto the electric field may be neglected, in the sense that the term $\mu \frac{\partial \mathbf{H}}{\partial t}$ may be set to zero in (3.13), is assumed to hold also at the cell membrane and the intercalated discs. In other words, we assume that (3.17) and consequently (3.20) hold, i.e. that we have $\mathbf{E} = -\nabla u$ across the membrane or an intercalated disc.

3.2 Derivation of the model equations

The equations defined above form the foundations of the derivation of the EMI model. In the remaining part of the derivation, we will consider the equations that are assumed to hold in small volume elements of the tissue (see Figure 3.1).

We will consider some volume elements existing entirely in the intracellular or extracellular domains like B_1 and B_2 in Figure 3.1 and some volume elements intersecting the membrane like B_3. Similarly, we will consider volume elements intersecting the boundary between two cells for situations where several cells are coupled by gap junctions (see Figure 3.4).

3.2.1 Model for the extracellular and intracellular domains

We start by considering volume elements existing entirely in the intracellular or extracellular domains. For these volume elements (3.23) hold in the entire element, and we obtain

$$\nabla \cdot \sigma_i \nabla u_i = 0 \quad \text{in } \Omega_i, \tag{3.25}$$

$$\nabla \cdot \sigma_e \nabla u_e = 0 \quad \text{in } \Omega_e. \tag{3.26}$$

Here, σ_i and σ_e are the intracellular and extracellular conductivities, respectively, and u_i and u_e are the electrical potentials in the intracellular and extracellular domains, respectively.

3.2.2 Model for the membrane

Next, we consider volume elements intersected by the membrane like B_3 in Figure 3.1. For these volume elements, we do not assume that (3.23) holds in the entire element. Furthermore, for any such volume element, B, we may divide the volume into an extracellular part, B_e, and an intracellular part, B_i, such that $B_e \cup B_i = B$ and $B_e \cap B_i = \emptyset$ as illustrated in Figure 3.2. The equation (3.24) is assumed to hold in both of these parts. Integrating (3.24) over each of the volume elements, we obtain

$$\int_{B_i} \nabla \cdot \mathbf{J} dV = -\int_{B_i} \nabla \cdot \varepsilon \frac{\partial \mathbf{E}}{\partial t} dV,$$

$$\int_{B_e} \nabla \cdot \mathbf{J} dV = -\int_{B_e} \nabla \cdot \varepsilon \frac{\partial \mathbf{E}}{\partial t} dV.$$

Applying the divergence theorem (see e.g., [96]) gives

$$\int_{\partial B_i} \mathbf{J} \cdot \mathbf{n}_{B_i} dS = -\int_{\partial B_i} \varepsilon \frac{\partial \mathbf{E}}{\partial t} \cdot \mathbf{n}_{B_i} \, dS, \tag{3.27}$$

$$\int_{\partial B_e} \mathbf{J} \cdot \mathbf{n}_{B_e} dS = -\int_{\partial B_e} \varepsilon \frac{\partial \mathbf{E}}{\partial t} \cdot \mathbf{n}_{B_e} \, dS, \tag{3.28}$$

where $\mathbf{n}_{B_i}$ and $\mathbf{n}_{B_e}$ are the outward pointing normal vectors of B_i and B_e, respectively. Here each side of the equations (3.27)–(3.28) represents a different type of current. The left-hand side terms represent the (free) ionic currents through the membrane and the remaining part of the boundary of B, whereas the right-hand side terms represent the capacitive (bound) effects. These two types of currents will be considered in the following two subsections.

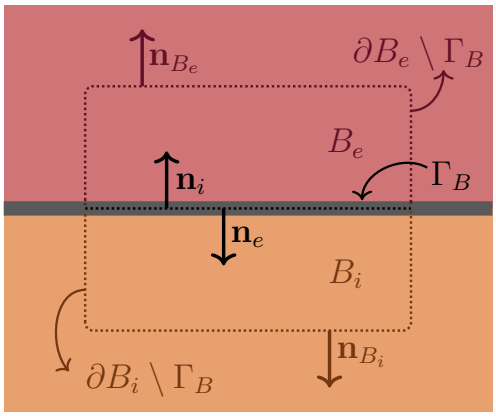

Figure 3.2: Illustration of a volume element, B, intersected by the membrane. The volume element is separated into an intracellular part, B_i, and an extracellular part, B_e. The boundary of B_i is denoted by ∂B_i and consists of one membrane part, Γ_B, and the remaining part, $\partial B_e \setminus \Gamma_B$. Similarly, the boundary of B_e consists of Γ_B and $\partial B_i \setminus \Gamma_B$.

Ionic current

We start by considering the term $\int_{\partial B_i} \mathbf{J} \cdot \mathbf{n}_{B_i} \, dS$ in (3.27). Separating the boundary ∂B_i into one part, Γ_B, that coincides with the membrane and one part, $\partial B_i \setminus \Gamma_B$, separate from the membrane, this term may be written as

$$\int_{\partial B_i} \mathbf{J} \cdot \mathbf{n}_{B_i} dS = \int_{\partial B_i \setminus \Gamma_B} \mathbf{J} \cdot \mathbf{n}_{B_i} dS + \int_{\Gamma_B} \mathbf{J} \cdot \mathbf{n}_i dS. \tag{3.29}$$

Here, $\mathbf{n}_i$ is the outward pointing normal vector of the membrane and $\mathbf{n}_{B_i}$ is the normal vector of the remaining part of B_i (see Figure 3.2). On the membrane, the ionic current density $\mathbf{J}$ is given by the currents through the different types of ion channels, pumps and exchangers located on the cell membrane. This current is typically given in units of $\mu\text{A}/\text{cm}^2$ and is denoted by I_{ion}. By convention I_{ion} is defined to be positive for a flux of positive ions out of the cell (i.e., in the direction of $\mathbf{n}_i$). Therefore,

$$\int_{\Gamma_B} \mathbf{J} \cdot \mathbf{n}_i dS = \int_{\Gamma_B} I_{\text{ion}} dS.$$

The remaining part of the boundary of B_i, $\partial B_i \setminus \Gamma_B$, is located in the intracellular domain, and the ionic flux is assumed to be given by Ohm's law (3.19), which yields

$$\int_{\partial B_i \setminus \Gamma_B} \mathbf{J} \cdot \mathbf{n}_{B_i} dS = \int_{\partial B_i \setminus \Gamma_B} \sigma_i \mathbf{E} \cdot \mathbf{n}_{B_i} dS.$$

Collecting the two terms, we have

$$\int_{\partial B_i} \mathbf{J} \cdot \mathbf{n}_{B_i} dS = \int_{\partial B_i \setminus \Gamma_B} \sigma_i \mathbf{E} \cdot \mathbf{n}_{B_i} dS + \int_{\Gamma_B} I_{\text{ion}} dS. \tag{3.30}$$

Following the same arguments for the extracellular side, the term $\int_{\partial B_e} \mathbf{J} \cdot \mathbf{n}_{B_e} dS$ may be written as

$$\int_{\partial B_e} \mathbf{J} \cdot \mathbf{n}_{B_e} dS = \int_{\partial B_e \setminus \Gamma_B} \sigma_e \mathbf{E} \cdot \mathbf{n}_{B_e} dS - \int_{\Gamma_B} I_{\text{ion}} dS. \tag{3.31}$$

Note that the negative sign in front of the last term is due to the fact that $\mathbf{n}_e = -\mathbf{n}_i$.

Capacitive current

For the term $\int_{\partial B_i} \varepsilon \frac{\partial \mathbf{E}}{\partial t} \cdot \mathbf{n}_{B_i} \, dS$ on the right-hand side of (3.27), we again split the integral into two parts, which yields

$$\int_{\partial B_i} \varepsilon \frac{\partial \mathbf{E}}{\partial t} \cdot \mathbf{n}_{B_i} \, dS = \int_{\partial B_i \setminus \Gamma_B} \varepsilon \frac{\partial \mathbf{E}}{\partial t} \cdot \mathbf{n}_{B_i} \, dS + \int_{\Gamma_B} \varepsilon_\Gamma \frac{\partial \mathbf{E}}{\partial t} \cdot \mathbf{n}_i \, dS.$$

Here, $\varepsilon_\Gamma = \varepsilon_0 \varepsilon_m$ is the membrane permittivity (ε_0 is the permittivity of empty space and ε_m is the relative membrane permittivity, see (3.9)). Following the quasi-static assumptions, we assume that $\varepsilon \frac{\partial \mathbf{E}}{\partial t}$ is negligible for the part of the boundary that does not coincide with the membrane. Therefore,

$$\int_{\partial B_i} \varepsilon \frac{\partial \mathbf{E}}{\partial t} \cdot \mathbf{n}_{B_i} \, dS = \int_{\Gamma_B} \varepsilon_\Gamma \frac{\partial \mathbf{E}}{\partial t} \cdot \mathbf{n}_i \, dS.$$

As explained in Section 3.1.4, we assume that $\mathbf{E} = -\nabla u$ across the membrane. Therefore, we may set $\mathbf{E} \cdot \mathbf{n}_i = -\nabla u \cdot \mathbf{n}_i$, where $-\nabla u \cdot \mathbf{n}_i$ may be approximated by

$$-\nabla u \cdot \mathbf{n}_i = \frac{v}{d}, \tag{3.32}$$

if v is the membrane potential defined as

$$v = u_i - u_e \quad \text{on } \Gamma, \tag{3.33}$$

and d is the thickness of the membrane. Assuming that the membrane can be treated as a capacitor formed by two parallel plates separated by an insulator, the membrane capacitance per area is given by [4]

$$C_m = \frac{\varepsilon_\Gamma}{d}. \tag{3.34}$$

Therefore,

$$\varepsilon_\Gamma \frac{\partial \mathbf{E}}{\partial t} \cdot \mathbf{n}_i = \frac{\varepsilon_\Gamma}{d} \frac{\partial v}{\partial t} = C_m \frac{\partial v}{\partial t},$$

and

$$\int_{\partial B_i} \varepsilon \frac{\partial \mathbf{E}}{\partial t} \cdot \mathbf{n}_{B_i}\, dS = \int_{\Gamma_B} C_m \frac{\partial v}{\partial t} dS. \tag{3.35}$$

Following the same arguments for the extracellular side,

$$\int_{\partial B_e} \varepsilon \frac{\partial \mathbf{E}}{\partial t} \cdot \mathbf{n}_{B_e}\, dS = -\int_{\Gamma_B} C_m \frac{\partial v}{\partial t} dS. \tag{3.36}$$

Again, the change of sign is due to the opposite directions of $\mathbf{n}_i$ and $\mathbf{n}_e$.

Collecting the ionic and capacitive currents

Inserting (3.30)–(3.31) and (3.35)–(3.36) into (3.27)–(3.28), we obtain

$$\int_{\partial B_i \setminus \Gamma_B} \sigma_i \mathbf{E} \cdot \mathbf{n}_{B_i} dS + \int_{\Gamma_B} I_{\text{ion}} dS = -\int_{\Gamma_B} C_m \frac{\partial v}{\partial t} dS,$$
$$\int_{\partial B_e \setminus \Gamma_B} \sigma_e \mathbf{E} \cdot \mathbf{n}_{B_e} dS - \int_{\Gamma_B} I_{\text{ion}} dS = \int_{\Gamma_B} C_m \frac{\partial v}{\partial t}\, dS,$$

which can be rewritten to

$$\int_{\partial B_i \setminus \Gamma_B} \sigma_i \mathbf{E} \cdot \mathbf{n}_{B_i} dS = -\int_{\Gamma_B} I_m\, dS, \tag{3.37}$$
$$\int_{\partial B_e \setminus \Gamma_B} \sigma_e \mathbf{E} \cdot \mathbf{n}_{B_e} dS = \int_{\Gamma_B} I_m\, dS, \tag{3.38}$$

where I_m is defined as

$$I_m = C_m \frac{\partial v}{\partial t} + I_{\text{ion}}. \tag{3.39}$$

We now wish to rewrite (3.37)–(3.38) to a differential form. Since any volume element intersecting the membrane may be divided into a purely intracellular, a purely extracellular, and a membrane intersecting part, and we know that (3.25)–(3.26) hold in the purely intracellular and extracellular parts, we consider the equations (3.37)–(3.38) as the size of the volume element B approaches zero. For example, we may consider a small extracellular volume element shaped as a cylinder located on top of the membrane, as illustrated in Figure 3.3.

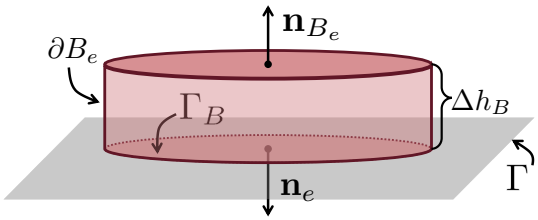

Figure 3.3: Illustration of a small volume element B located on the extracellular part of the membrane.

For this volume element, we see that as the height of the cylinder Δh_B approaches zero, the integral over $\partial B_e \setminus \Gamma_B$ approaches the integral over Γ_B, and for a very small volume element located on top of the membrane, the integral over the two parts of the membrane may be assumed to be the same. Therefore,

$$\int_{\partial B_e \setminus \Gamma_B} \sigma_e \mathbf{E} \cdot \mathbf{n}_{B_e} dS \approx \int_{\Gamma_B} \sigma_e \mathbf{E} \cdot \mathbf{n}_{B_e} \, dS$$

and (3.38) may be rewritten as

$$\int_{\Gamma_B} \sigma_e \mathbf{E} \cdot \mathbf{n}_{B_e} dS = \int_{\Gamma_B} I_m \, dS,$$

implying that

$$\sigma_e \mathbf{E} \cdot \mathbf{n}_{B_e} = I_m.$$

The normal vector $\mathbf{n}_{B_e}$ points in the direction out of the cell, while $\mathbf{n}_e$ points in the direction into the cell. Substituting $\mathbf{n}_e$ for $\mathbf{n}_{B_e}$, and using that $\mathbf{E} \cdot \mathbf{n} = -\nabla u \cdot \mathbf{n}$ (see Section 3.1.4), we obtain

$$\sigma_e \nabla u_e \cdot \mathbf{n}_e = I_m, \tag{3.40}$$

Applying a similar argument for the intracellular part of the membrane, we obtain

$$-\sigma_i \nabla u_i \cdot \mathbf{n}_i = I_m. \tag{3.41}$$

Note that the reason for the negative sign on the left-hand side of (3.41) is the opposite signs in (3.37) and (3.38).

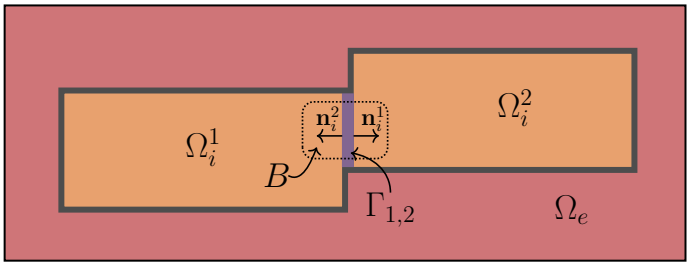

Figure 3.4: Illustration of two cells denoted by Ω_i^1 and Ω_i^2 surrounded by an extracellular domain, Ω_e. The boundary between the two intracellular domains is represented by the intercalated disc denoted by $\Gamma_{1,2}$. A volume element, B, intersects the intercalated disc.

3.2.3 Model for the intercalated discs

In some cases, we wish to model cells that are connected by gap junctions, as illustrated in Figure 3.4. We let the intercalated discs connecting the cells be represented as boundaries between the intracellular domains, like the membrane is a boundary between an intracellular domain and the extracellular domain. The derivation of equations for volume elements intersecting an intercalated disc therefore follows the exact same lines as the derivation of the membrane equations. In other words, for a case with two connected cells, as illustrated in Figure 3.4, we define an intercalated disc potential, w, by

$$w = u_i^1 - u_i^2, \tag{3.42}$$

where u_i^1 and u_i^2 are the electrical potentials in Ω_i^1 and Ω_i^2, respectively. Furthermore, the total intercalated disc current is defined as the sum of the capacitive current and the current through the gap junction proteins,

$$I_{1,2} = C_{1,2}\frac{\partial w}{\partial t} + I_{\text{gap}}, \tag{3.43}$$

where I_{gap} is the current through the gap junctions with positive direction in the direction from Ω_i^1 to Ω_i^2. Furthermore, $C_{1,2}$ is the capacitance of the intercalated disc. Following the same arguments as for the derivation of the membrane equations, we end up with equations similar to (3.40) and (3.41),

$$\sigma_i^2 \nabla u_i^2 \cdot \mathbf{n}_i^2 = I_{1,2} \tag{3.44}$$

$$-\sigma_i^1 \nabla u_i^1 \cdot \mathbf{n}_i^1 = I_{1,2}. \tag{3.45}$$

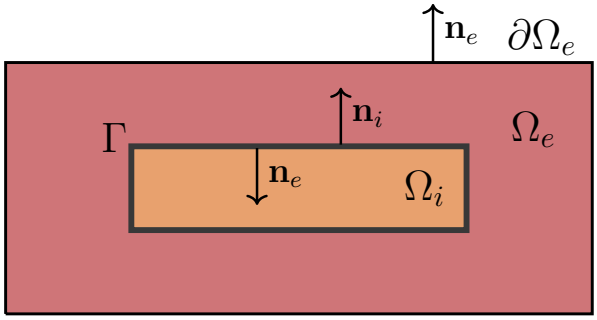

Figure 3.5: Illustration of a 2D version of an EMI model domain for a single cell, Ω_i, surrounded by an extracellular space, Ω_e. The cell membrane separates Ω_i and Ω_e and is denoted by Γ.

3.3 Summary of the model equations

Summing up the equations of the EMI model, we have that in the intracellular and extracellular domains, Ω_i and Ω_e, the equations (3.25) and (3.26) apply. This means that

$$\nabla \cdot \sigma_i \nabla u_i = 0 \quad \text{in } \Omega_i, \tag{3.46}$$

$$\nabla \cdot \sigma_e \nabla u_e = 0 \quad \text{in } \Omega_e, \tag{3.47}$$

where u_i and u_e are the electrical potentials (typically in mV) in the intracellular and extracellular domains, respectively, and σ_i and σ_e (typically in mS/cm) are the conductivities of the two domains.

On the membrane, equations (3.40) and (3.41) imply that

$$I_m = -\sigma_i \nabla u_i \cdot \mathbf{n}_i \quad \text{at } \Gamma, \tag{3.48}$$

$$\sigma_e \nabla u_e \cdot \mathbf{n}_e = -\sigma_i \nabla u_i \cdot \mathbf{n}_i \quad \text{at } \Gamma. \tag{3.49}$$

Here, I_m (typically in μA/cm^2) is defined by (3.39)

$$I_m = C_m \frac{\partial v}{\partial t} + I_{\text{ion}} \quad \text{at } \Gamma,$$

which imply that

$$\frac{\partial v}{\partial t} = \frac{1}{C_m}(I_m - I_{\text{ion}}) \quad \text{at } \Gamma. \tag{3.50}$$

Furthermore, C_m is the specific membrane capacitance (typically in μF/cm^2), and v (typically in mV) is defined in (3.33) as

$$v = u_i - u_e \quad \text{at } \Gamma. \tag{3.51}$$

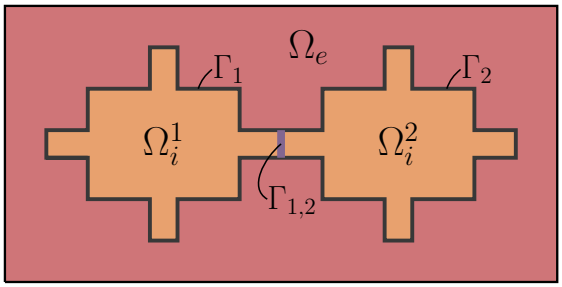

Figure 3.6: Illustration of a 2D version of an EMI model domain for two cells connected by an intercalated disc denoted by $\Gamma_{1,2}$.

For a single cell surrounded by an extracellular domain, as illustrated in Figure 3.5, the EMI model is given by the system (3.46)–(3.51). If several cells are connected by gap junctions, the system is extended to include equations of the form (3.48)–(3.51) also at the intercalated discs connecting the cells. For example, for two connected cells like illustrated in Figure 3.6, the model is extended to include the equations

$$I_{1,2} = -\sigma_i \nabla u_i^1 \cdot \mathbf{n}_i^1 \qquad \text{at } \Gamma_{1,2}, \tag{3.52}$$

$$\sigma_i \nabla u_i^2 \cdot \mathbf{n}_i^2 = -\sigma_i \nabla u_i^1 \cdot \mathbf{n}_i^1 \qquad \text{at } \Gamma_{1,2}, \tag{3.53}$$

$$u_i^1 - u_i^2 = w \qquad \text{at } \Gamma_{1,2}, \tag{3.54}$$

$$w_t = \frac{1}{C_{1,2}}(I_{1,2} - I_{\text{gap}}) \qquad \text{at } \Gamma_{1,2}, \tag{3.55}$$

where $\Gamma_{1,2}$ is the intercalated disc, $\mathbf{n}_i^1$ is the outward pointing normal vector of the cell represented by the domain Ω_i^1, $\mathbf{n}_i^2$ is the outward pointing normal vector of the cell represented by the domain Ω_i^2, and u_i^1 and u_i^2 are the intracellular potentials (typically in mV) of the two cells. Furthermore, $C_{1,2}$ is the capacitance of the intercalated disc (typically in μF/cm^2), and I_{gap} is the current through the gap junctions (typically in μA/cm^2).

Chapter 4

Thesis overview

The aim of this chapter is to give an overview of the research papers of the thesis. First, in Section 4.1, the research questions addressed in the thesis will be introduced. Next, in Section 4.2, the research papers of the thesis will be summarized. Finally, the results of the thesis will be summarized and a few suggestions for future work will be provided in Section 4.3.

4.1 Research questions of the thesis

As mentioned above, the overall aim of the thesis is to study mathematical models of small collections of excitable cells. The thesis addresses questions related to the modeling of both neurons and cardiomyocytes. Some of the research questions relate to the models themselves, and consider their accuracy and computational challenges, while other questions relate to the application of the models for gaining electrophysiological insight. In particular, the conduction properties of cardiac tissue and the effect of drugs on the action potential of cardiac cells are considered.

Accuracy of classical models of neuroscience

The first research questions addressed in the thesis regard the accuracy of the classical cable equation and point-source approximation used to model the membrane potential of and the extracellular potential around neurons. Specifically, the consequences of some of the models' underlying assumptions are investigated by comparing the solution of the cable equation and point-source approximation to the solution of the EMI model, which does not rely on all of the same simplifying assumptions. In particular, the consequences of the assumption of a constant extracellular potential in the derivation of the cable equation and the assumption of the membrane currents acting as point sources located at the center of the compartments in the point-source approximation are investigated.

Using the EMI model to study cardiac conduction

Since many of the electrophysiological principles governing the electrical activity of neurons are the same as those governing the electrical activity of cardiomyocytes, the same EMI model framework used to model the electrical properties of neurons in the first research paper may also be used to study collections of cardiomyocytes. This is the focus of the next set of research questions of the thesis.

First, in the second paper, the feasibility of using such a detailed model for cardiac tissue is investigated by studying the computational challenges associated with the EMI model and attempting to find efficient numerical solution methods for the model. This is motivated by the fact that the homogenization assumptions underlying the classical bidomain and monodomain models commonly used to study cardiac conduction make the models unsuitable to study certain properties related to the discontinuous nature of cardiac tissue, and more detailed models (like the EMI model) might be necessary to study such properties. However, the homogenized models may be solved much more efficiently than the EMI model because they do not require a resolution small enough to represent the individual cells. Therefore, efficient solution methods are required in order to be able to fully use the EMI model as an alternative to the homogenized models. This research question also relates to the first set of research questions of the thesis, because a major motivation for using the classical cable equation and point-source approximation instead of a detailed model like the EMI model is that the simplified models are associated with significantly smaller computational costs than the EMI model.

In the third research paper of the thesis, the numerical methods for the EMI model investigated in the second paper are applied to examine questions about the conduction properties of cardiac tissue. For example, the effect of a non-uniform distribution of sodium channels on the cell membrane is studied. This is motivated by the fact that a number of studies have demonstrated that sodium channels highly localize at the intercalated discs between cells (see e.g., [97, 98, 99]). This question is also considered in the second research paper, as an example of an application of the EMI model, but it is studied in more detail in the third paper. Another property studied in the third research paper is ephaptic coupling between cells. This is a mechanism for cell-to-cell communication through the extracellular potential proposed as a possible alternative or supplement to gap junction coupling (see e.g., [100]).

Identification of drug effects from microphysiological systems of hiPSC-CMs

As investigated in the second and third research papers, computational challenges currently limit the size of the cell collections that may be readily modeled by the EMI model. A suitable application of the model could therefore be modeling of small collections of human induced pluripotent stem cell-derived cardiomyocytes (hiPSC-CMs), for example organized in a microphysiological system or *chip* (see [24]). The hiPSC-CMs chips show great promise for drug testing applications, but

their applicability is limited by the fact that the electrophysiological properties of the hiPSC-CMs are different from those of the mature cardiomyocytes found in the adult heart, and therefore, their drug response might be different [101].

The final three research papers of the thesis investigate whether mathematical modeling might help improve the applicability of this technology. Specifically, the models might help estimating the drug effects on mature cardiomyocytes based on measurements of hiPSC-CMs. Initially, we conducted the mathematical modeling using the EMI model applied in the remaining papers of the thesis. However, the optical measurements of the action potential and calcium transient obtained from the chips showed relatively small spatial variations across the chip. It was therefore concluded that, at least in these initial stages of the project, the spatial variation could be ignored, and a single action potential model like the ones described in Section 2.1 (Chapter 2) would be sufficient for modeling the electrical activity of the chip.

The fourth and fifth research papers of the thesis therefore investigate how measurements of the action potential and calcium transient obtained from the hiPSC-CMs chips may be inverted to parameterize action potential models for the hiPSC-CMs. Furthermore, it is examined how this inversion procedure may be applied to identify the effect of a drug on the hiPSC-CMs and how this drug effect may be mapped to estimate the drug effect on mature cardiomyocytes.

An important element to consider when optical measurements of the action potential are used to parameterize action potential models, like in the fourth and fifth research papers, is whether the parameterization of the model is unique, or whether other choices of parameter values might result in the same action potential. For example, if we identify that blocking of a specific channel in the model gives a change in the action potential similar to what is measured for the application of a drug, it is very useful to know whether other model adjustments could equally well give rise to the same change. In the sixth research paper, we therefore consider this question and investigate an approach for identifying unidentifiable model currents based on singular value decomposition (see e.g., [102, 103]).

Summary of research questions

In short, the research questions described above may be summarized as

- What are the consequences of the assumptions underlying the derivation of the cable equation and the point-source approximation?
- How can the EMI model be efficiently solved numerically?
- What is the effect of a non-uniform distribution of sodium channels on the cell membrane in simulations of the EMI model?
- How can electrophysiological models of small collections of hiPSC-CMs be parameterized based on optical measurements of the membrane potential and the intracellular calcium transient?

- How can the drug effect on hiPSC-CMs be identified and mapped to drug effects on mature cardiomyocytes?

- Which currents in mathematical action potential models are identifiable from measurements of the action potential?

4.2 Summary of research papers

In this section, the motivation and results for each of the research papers of the thesis are summarized.

Paper I: An Evaluation of the Accuracy of Classical Models for Computing the Membrane Potential and Extracellular Potential for Neurons

The purpose of the first paper of the thesis is to evaluate the consequences of some of the underlying assumptions of two classical models of computational neuroscience. The first model considered is the cable equation, used to model the conduction of electrical signals along a cell. A common derivation of this model relies on the assumption that the extracellular potential is essentially constant in space (see Section 2.2.1 of Chapter 2), and one of the main problems of this paper is to investigate the consequences of this assumption. This is done by setting up a simple test case and comparing the solution of the cable equation to the solution of a model that does not rely on the assumption of a constant extracellular potential. This alternative model is referred to as the EMI model because it models the electrical potential in both the extracellular space, the membrane and the intracellular space as a coupled system (see Section 2.2.4 of Chapter 2).

In our simple test case with a neuron with a passive membrane model, we observe that the difference between the solution of the EMI model and the cable equation depends on the value of the model parameters. Specifically, we find that the difference increases as the cell width or the intracellular conductivity increases, or as the conductance of the passive membrane channels or the extracellular conductivity decreases. Moreover, we find that in some cases, the difference between the solution of the cable equation and the EMI model is several millivolts.

The second classical model considered in Paper I is the point-source approximation, used to compute the extracellular potential around neurons. A commonly used procedure for computing the extracellular potential around neurons consists of two steps [65]: First, the membrane potential and membrane currents are computed using the cable equation, and then the extracellular potential is calculated from this solution using, for example, the point-source approximation (see Section 2.2.2 of Chapter 2). This approximation relies on the assumptions that the extracellular space is infinite and that the membrane currents from a compartment in the cable equation may be defined as a single point-source located in the center of the compartment. In that case, the extracellular potential may be found by an explicit formula.

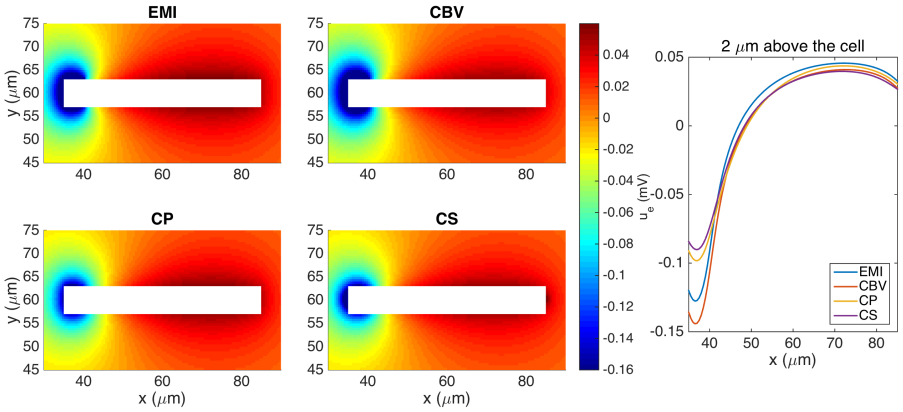

Figure 4.1: Extracellular potential computed using four different approaches from Paper I. See Paper I for more details.

In this paper, we evaluate the accuracy of this approach by comparing the extracellular potential computed by the classical two-step method (referred to as the CS method) and the solution of the EMI model, which models the potentials in the intracellular space, the membrane and the extracellular space as a coupled system. In order to get an impression of the reason for the difference between the methods, we also consider two intermediate methods for computing the extracellular potential; referred to as the CBV and CP methods. In the CBV method, we first solve the cable equation and collect the membrane currents from the solution. Then, the extracellular potential is computed by solving the Poisson equation (2.28) with an inner boundary condition on the membrane defined by the membrane currents computed in the cable equation. In the CP method, this is simplified further by distributing the membrane currents uniformly in each of the intracellular compartments.

The extracellular potential computed for each of the methods in a simple test case is illustrated in Figure 4.1. We observe that there is a small difference between the solution of the EMI model and the CBV method, resulting from the different approaches for computing the membrane currents (i.e., the EMI model or the cable equation). The difference is larger between the EMI model and the CP and CS methods, which assume that the membrane currents are distributed in the intracellular compartments or collected in the center of the compartments, respectively. The relative maximum difference between each of the simplified models and the EMI model for this example was 11% for the CBV method, 30% for the CP method, and 54% for the CS method.

Cells	System size	T_{ODE} (s)	T_{PDE} (s)	T (s)	T/cell (s)
1	14 609	2.9	0.7	3.6	3.6
4	42 563	7.6	4.5	12.1	3.0
16	141 179	23.9	12.7	36.5	2.3
64	509 243	85.1	41.5	126.6	2.0
256	1 928 699	351.9	109.8	461.7	1.8
1 024	7 500 923	1 256.0	442.6	1 698.6	1.7
4 096	29 578 619	4 512.8	1 515.8	6 028.6	1.5
16 384	117 467 003	17 594.6	6 171.9	23 766.5	1.5

Table 4.1: CPU times for a single time step of size 0.1 ms using the finite difference method to solve the EMI model. Here, $T = T_{\text{ODE}} + T_{\text{PDE}}$, where T_{ODE} is the time spent on the ODE part of the time step, and T_{PDE} is the time spent on the PDE part. For more details, see Paper II.

Paper II: A Cell-Based Framework for Numerical Modeling of Electrical Conduction in Cardiac Tissue

In the second paper, we address the computational challenges associated with the EMI model used in the first research paper. In particular, we investigate the feasibility of using the model to study electrical propagation in collections of cardiac cells. Electrical propagation in cardiac tissue is commonly modeled using the classical bidomain or monodomain models, but these models rely on homogenization assumptions and might therefore be insufficient for studying questions related to the discontinuous nature of cardiac tissue. For example, since the geometry of the individual cells is not defined in the models, it is hard to study the effect of a non-uniform distribution of ion channels on the cell membrane. To study these questions, the EMI model might be more appropriate, because the geometry of each cell is explicitly represented. However, in order to represent the geometry of each cell, a detailed spatial resolution is required, potentially leading to dramatically increased computational costs.

The aim of the second paper is therefore to consider a few numerical solution methods for the EMI model in order to examine whether the EMI model can be solved efficiently enough to be used to study collections of cardiac cells. We solve the EMI model numerically using an operator splitting procedure where we for every time step update the solution of the model in two steps. In the first (ODE) step, we update the membrane potential and the remaining state variables of the action potential model for the ionic currents, I_{ion}. Then, in the second (PDE) step, the remaining part of the EMI model is solved using one of three alternative discretization techniques; a finite difference method, an H(div)-based finite element method, and a Mortar-based finite element method.

The investigations of the paper show that the finite element methods provide the most accurate solutions, but that they at the current state are associated with relatively long solution times. For the finite difference method, however, the

solution times appear to be manageable, at least for small cell collections. In addition, the solution time per cell appears to be bounded, indicating that the solution time will not grow uncontrollably as the number of cells increases. The solution times for a single time step for cell collections of different sizes using the finite difference method is given in Table 4.1.

Paper III: Properties of Cardiac Conduction in a Cell-Based Computational Model

In the third research paper, we utilize the results from the second paper and apply the finite difference discretization of the EMI model to study properties of cardiac conduction in small collections of cardiomyocytes. Properties of cardiac conduction are classical questions that have been extensively studied, but a number of questions related to these properties still remain unresolved (see e.g., [104]). For example, it is not completely understood how the size and shape of the cells and the distribution ion channels and gap junctions affect conduction properties.

The main question investigated in this paper is the effect of a non-uniform distribution of sodium channels on the cell membrane. This is motivated by the fact that a number of studies have shown that the sodium channels highly localize at the intercalated discs between cells (e.g., [97, 98, 99]), but the effect of this non-uniform distribution is still not well understood [105]. In this paper, we therefore investigate this question by comparing conduction properties in simulations of a uniform and non-uniform distribution of sodium channels on the cell membrane, while holding the total number of sodium channels constant. A few of the results from the paper are shown in Figure 4.2. In Panel A, we observe that as a larger percentage of the sodium channels are moved to the cell ends, the conduction velocity of the cell collection increases. Moreover, in Panel B, we observe that the time delays across gap junctions of reduced coupling are larger for a uniform (U) distribution of sodium channels than for a non-uniform (NU) distribution with all sodium channel located close to the cell ends.

In addition to investigating the effect of a non-uniform distribution of sodium channels, we also consider the possibility of ephaptic coupling (i.e., coupling through the extracellular potential) acting as an alternative to gap junction coupling. This is investigated by recording the extracellular potential in the space between two cells with a closed gap junction for different distances between the cells and a non-uniform distribution of sodium channels. Figure 4.2C illustrates that as the cell distance is decreased, the magnitude of the extracellular potential between the cells increases significantly, and for the smallest distance considered (5 nm), the extracellular potential reaches a value of about -30 mV. This leads to a corresponding increase in the membrane potential, $v = u_i - u_e$, of the cell after the closed gap junction. However, this is not sufficient to generate an action potential in the second cell. In other words, the results support the potential of ephaptic coupling acting as a mechanism of conduction, but we do not achieve cell-to-cell communication of an action potential through ephaptic coupling alone in this case. However, this conclusion is expected to depend on the choice of parameters used

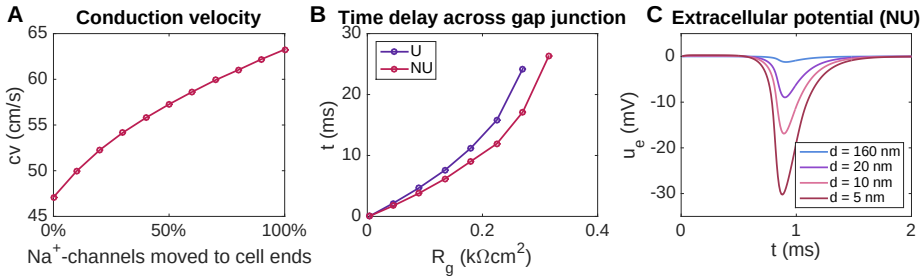

Figure 4.2: A few results from Paper IV, investigating properties of cardiac conduction using the EMI model. **A**: The conduction velocity increases as a larger percentage of the sodium channels is moved to the cell ends. **B**: The time delays across gap junctions of reduced coupling (increased R_g) are shorter for a non-uniform distribution of sodium channels (NU) than for a uniform distribution (U). **C**: The magnitude of the extracellular potential between cells increases significantly as the distance d between the cells is reduced for a non-uniform distribution of sodium channels. For more details, see Paper III.

in the simulations. If we, for example, decrease the value of the extracellular conductivity, we find that the extracellular potential increases enough to trigger an action potential in the second cell. In addition, we investigate ephaptic effects on the sodium channels in the case of an open gap junction. In this case, we observe that for a non-uniform distribution of sodium channels, ephaptic effects alter the dynamics of the sodium channels in the sense that as the cell distance is decreased (and the magnitude of the extracellular potential between the cells is increased), the sodium channels are activated at an earlier point in time and for a lower intracellular potential. In other words, the ephaptic effects seem to have a significant effect of the properties of conduction.

Paper IV: Inversion and Computational Maturation of Drug Response using hiPSC-derived Cardiomyocytes in Microphysiological Systems

In the forth research paper, we consider the identification of drug effects using measurements from microphysiological systems of hiPSC-CMs. The hiPSC-CMs are cardiomyocytes derived from human induced pluripotent stem cells. This means that the stem cells that the cardiomyocytes are derived from are induced stem cells generated from, e.g., a person's skin cells [101]. Such cells show great promise for drug screening applications, because they are relatively easily obtained human cardiac cells. However, their applicability is limited by the fact that a number of electrophysiological properties differ between the hiPSC-CMs and the mature cardiomyocytes found in the adult heart. Specifically, the hiPSC-CMs are more similar to immature cardiomyocytes [101]. Therefore, the drug effects observed for the hiPSC-CMs might not match the drug effect that would be observed for the

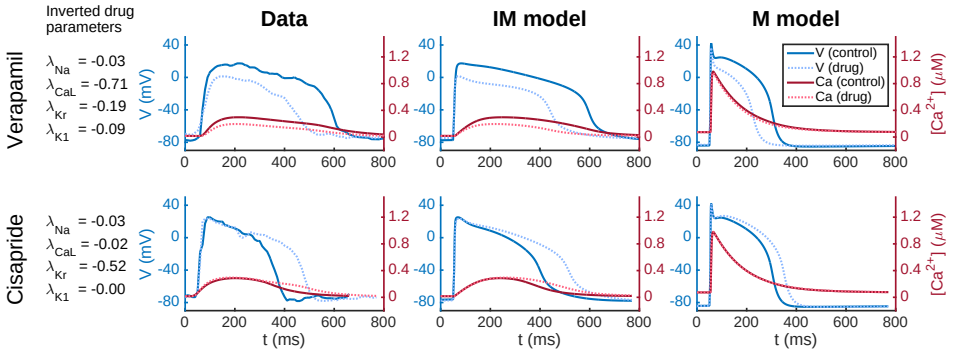

Figure 4.3: Identification of the effect of the drugs Verapamil and Cisapride from Paper IV. The left panel shows the data obtained from optical measurements of hiPSC-CMs. The second panel shows the action potential and calcium transient resulting from the models adjusted to fit the data. The identified drug effects are given by the parameters on the left-hand side. The right panel shows the estimated drug effect for a mature cardiomyocyte. For more information, see Paper IV.

mature cardiomyocytes in the heart.

In this paper, we address this problem using mathematical modeling. In particular, we consider a possible framework for identifying drug effects based on optical measurements from microphysiological systems of hiPSC-CMs and estimating the corresponding drug effects for mature cardiomyocytes. The procedure is based on two main steps. First, the drug effect on the hiPSC-CMs is identified by inversion of optical measurements of the action potential and calcium transient obtained using voltage- and calcium sensitive dyes. The measurements are conducted both when no drug is present (control) and when a drug is introduced in the microphysiological system. Two examples of such measurements are given in the left panel of Figure 4.3[1]. The second panel shows the action potential and calcium transient of the models adjusted to fit the data. The parameters of a default base model are first adjusted to fit the control data, and then adjusted to fit the drug data by minimizing a cost function set up to measure the difference between the model and the data. This cost function is given by a number of terms measuring various differences between the data and the model, for example the difference in the action potential duration.

The effect of the drug is estimated by comparing the parameters of the model adjusted to fit the control data and the model adjusted to fit the drug data. The estimated effects of the two drugs in Figure 4.3 are given by the parameters on the left-hand side of the plots. Here, each λ_x represents the adjustment of the current

[1]Note that the values obtained from the optical measurements are only relative values, and the specific values for the membrane potential and the calcium concentration are adjusted so that they match the maximum and minimum values of the adjusted model in the second panel.

through the channels of type x, in the sense that the conductance of the channel in the drug case is given by $g_x^{\text{drug}} = (1+\lambda_x)g_x^{\text{control}}$, where g_x^{control} is the conductance in the control case. In other word, the inversion procedure suggests that Verapamil primarily blocks I_{CaL}, and also to some extent I_{Kr}, whereas Cisapride primarily blocks I_{Kr}. This is in rough agreement with the expected effect of these drugs (see e.g., [106]).

The second step of the procedure consists of mapping the identified drug effect for hiPSC-CMs to the corresponding effect for mature cardiomyocytes. This mapping relies on the assumption that what makes the immature and mature cells different is a difference in the cell geometry and the density of different proteins on the cell membrane, but that the function of the individual proteins, e.g. the ion channels, stays the same during maturation. Therefore, the drug is assumed to affect a protein of a mature cell in exactly the same manner as a protein of an immature cell, and the drug effect for a mature cell may be estimated by introducing the same scaling factors λ_x in a mature version of the model, parameterized to represent the protein density and cell geometry of a mature cell. The estimated effects of the two drugs in Figure 4.3 on a mature action potential and calcium transient are illustrated in the right panel of the figure.

Paper V: Improved Identification of Drug Response Using Optical Measurements of Human Stem Cell Derived Cardiomyocytes in Microphysiological Systems

The aim of the fifth research paper is to improve some of the elements of the procedure used in the fourth paper. For example, the AP model forming the basis of the inversion is changed considerably. A few additional membrane currents are included, and the model for the intracellular calcium dynamics is reformulated. A schematic illustration of the model is shown in Figure 4.4.

The new model for the intracellular calcium dynamics is set up to be both stable with respect to adjustments of the model parameters and to exhibit *high gain* and *graded release*. High gain means that for a small amount of calcium entering the cell through the L-type calcium channels on the cell membrane, a larger amount of calcium is released into the cytosol from the intracellular calcium storage of the SR. Graded release means that the amount of calcium released from the SR depends upon the amount of calcium entering the cell through the L-type calcium channels. In order to achieve this, the reformulated model deviates from common modeling of calcium dynamics in AP models in two main ways. First, even though the calcium released from the SR is activated by an increased calcium concentration in the dyad (see Section 2.1.3 in Chapter 2), the calcium is not released into the dyad, but is instead directed into the so-called subsarcolemmal space. This is done in order to achieve a stable graded release mechanism in the model. Second, the release of calcium from the SR through the RyRs is often inactivated by a decreased SR calcium concentration, but because the SR concentration could potentially vary significantly for different parameter combinations, we instead inactivate the release by introducing an assumption that each RyR protein is only able to carry a given

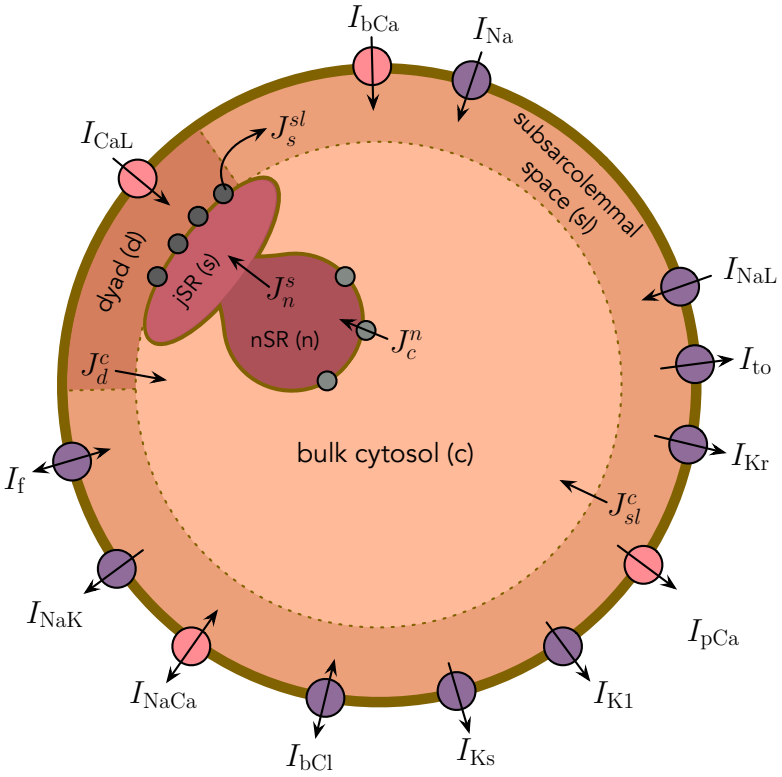

Figure 4.4: Membrane currents, intracellular calcium fluxes and intracellular compartment of the base model introduced in Paper V. For more details, see Paper V.

amount of calcium in each AP cycle.

In addition, a new minimization method is introduced in the inversion procedure. In the fourth paper, we applied an algorithm where we searched for the optimal parameters by randomly drawing parameters in bounding boxes of decreasing size and choosing the parameters that gave the smallest value of a given cost function, measuring the difference between the model solution and the data. In the fifth paper, we replace this procedure by a continuation-based method, where we search for the optimal parameters for some data that is gradually evolving from the starting point of the inversion to the data we are trying to invert. In addition, we introduce an assumption about the dose-dependent effect of a drug based on IC50-values, and we run the inversion of the measurements for the control case and for several drug doses simultaneously in a coupled manner.

Using the updated methodology, we show some preliminary results for simulated and measured data for five drugs; Nifedipine, Lidocaine, Cisapride, Flecainide, and Verapamil. However, before the paper is ready to be submitted for publication, we plan to refine both the base model and the inversion procedure. In addition, we plan to test the procedure using more drugs than the five drugs currently included in the paper.

Paper VI: Detecting Undetectables: Can Conductances of Action Potential Models be Changed Without Appreciable Change in the Transmembrane Potential?

The sixth research paper of the thesis considers the question of which of the maximum conductances of the currents in an action potential model can be changed without any noticeable effect on the action potential. For the inversion procedure in the fourth and fifth research papers, this is an important question to consider in order to know whether we can assume that the identified model parameters are unique or whether other parameter combinations might result in almost exactly the same action potential. The method considered in the sixth research paper is based on a singular value decomposition of the model currents, and an advantage of the approach is that the method, in addition to identifying single currents that are very small, also has the potential of identifying that certain perturbations of combinations of currents could result in virtually identical action potentials.

Specifically, the method consists of recording each of the model currents for a number of time steps during the action potential and collecting them in a matrix. A singular value decomposition of the matrix is then computed, giving rise to a set of singular values and singular vectors. From the properties of the singular value decomposition, it is shown that perturbations along singular vectors associated with large singular values are expected to result in large changes in the resulting action potential, whereas perturbations along singular vectors associated with small singular values are expected to result in small changes in the action potential.

In the paper, we show that this expected result seems to hold for three well-known AP models of human mature ventricular cardiomyocytes – the ten Tusscher

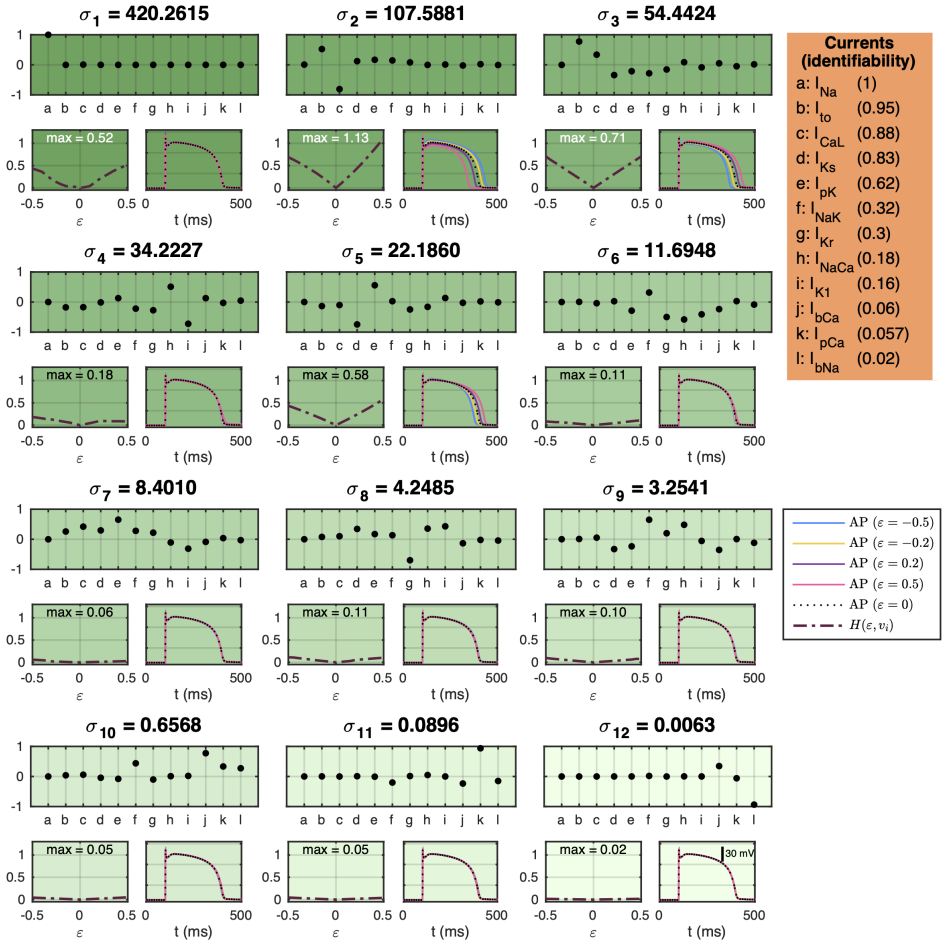

Figure 4.5: Singular value decomposition analysis of the model currents in the ten Tusscher et al. 2006 model [42]. For details, see Paper VI.

et al. model [42], the Grandi et al. model [19], and the O'Hara-Rudy et al. model [51]. The results for the ten Tusscher et al. model is shown in Figure 4.5. Below each singular value σ_1, ..., σ_{12}, the components for each membrane current of the corresponding singular vector are shown as black circles. In the below left plot, a cost function is evaluated, measuring the change in the action potential resulting from perturbations along the singular vector. Moreover, the right plots show some examples of action potentials resulting from different perturbations along the singular vectors. We observe that the action potential is clearly most affected by perturbations corresponding to large singular values and that a number of singular vectors result in nearly indistinguishable changes in the action potential. The singular value decomposition analysis therefore seem to be a useful tool for identifying unidentifiable model currents in action potential models.

4.3 Conclusions and future directions

In this final section of the introduction, the conclusions from the research papers will be summarized and a few directions for further investigation will be suggested.

Accuracy of classical models of neuroscience

In the first paper of the thesis, we investigate the accuracy of some of the assumptions underlying some of the classical models of computational neuroscience. We find that in some cases there may be considerable differences between the solution of the detailed EMI model and the more simplified cable equation and point-source approximation.

Applying a detailed model like the EMI model as an alternative to the classical models might help improve the accuracy of the computations, but is still much too computationally demanding for many applications. However, as the available computing power continues to grow, possibilities open up for using more detailed and accurate models. This has the potential of greatly improving the accuracy and reliability of the models used to investigate electrophysiological questions. On the other hand, as the models become more detailed and complex, valuable intuitive understanding of the underlying mechanisms, for example in the form of analytical solutions, is harder to obtain. In addition, more complex mathematical models might introduce more free parameters for which it might be hard to determine appropriate values. Ultimately, the question of choosing an appropriate level of modeling complexity will probably always be both an essential and challenging part of mathematical modeling of biological processes.

In order to make informed decisions about an appropriate level of modeling complexity, knowledge about the type of errors introduced by different modeling assumptions is useful. This type of investigation is conducted in the first paper of the thesis, but a number of additional investigations may help provide more understanding of the consequences of the assumptions underlying the classical models. For example, it might be useful to compare the solution of the EMI

model and the cable equation and point-source approximation for more realistic neuron geometries. In addition, it could be useful to consider non-linear membrane models including voltage-gated ion channels. In that case, ephaptic effects between neurons might, for example, affect whether neighboring neurons fires an action potential or not. Note also that some simplifying assumptions, like ignoring the effect of diffusion of ions, underly both the classical models and the EMI model. Therefore, alternative models would be necessary to evaluate the accuracy of these assumptions (see e.g., [107]).

Moreover, a further aspect related to the accuracy of the classical models of computational neuroscience is investigated using the EMI model in [108]. The question considered is whether the presence of the probe may be neglected when mathematical models are used to interpret recordings of the extracellular potential. As mentioned above, one of the assumptions underlying the classical two-step approach for computing the extracellular potential is that the extracellular space is an infinite and homogeneously conducting medium. However, when measurements of the extracellular potential is conducted, the probe used to measure the potential is present in the extracellular space around the neurons, violating these assumptions. In [108], it is shown using the EMI model that the presence of the probe in some cases significantly affects the measured extracellular potential, indicating that the classical two-step approach might not be sufficient for interpreting recorded extracellular potentials in all situations.

Using the EMI model to study cardiac conduction

The second and third papers of the thesis use the same detailed EMI model to study collections of connected cardiac cells. Cardiac tissue is commonly modeled using the classical bidomain or monodomain models, but the homogenization assumptions underlying these models might render them insufficient to study properties related to the discontinuous nature cardiac conduction. Therefore, more detailed models, like the EMI model, may be useful.

The second research paper investigates the computational challenges associated with the EMI model and demonstrates that the computational demands are manageable for small cell collections, but that the possible applications of the model are limited by computational costs. This includes limitations of, for instance, the possible number of cells included in the simulations and the spatial resolution of the domain. Therefore, further studies for obtaining more efficient numerical strategies might be helpful. For example, improvements of the solution time associated with the finite element method might be useful for studying more realistic cell geometries. Moreover, meshes with varying spatial resolutions and efficient parallel algorithms might help improve the simulation time and open up for more possible applications of the model.

In the third research paper, we use the EMI model to study properties of cardiac conduction and find, for example, that the distribution of sodium channels on the cell membrane has a significant effect on the properties of conduction. However, if more efficient numerical solution methods for the EMI model is obtained, a number

of additional questions may be studied. For example, in the simulations conducted in the third paper, the distance between the cells is generally much larger than what is physiologically realistic (see e.g., [76]). The reasons for this is the large computational costs associated with a resolution fine enough to represent realistic cell distances. Consequently, the study of ephaptic effects between cells is limited to simulations of just two connected cells. In order to study these effects in more detail, for example to investigate the ephaptic effects on the conduction velocity or directional differences of the ephaptic effects, it would be beneficial to include more cells in the simulations.

Furthermore, since the computational challenges associated with the EMI model still limit the possible applications, a useful application of the model might be to investigate the accuracy of alternative, simpler models of cardiac conduction. A number of less computationally expensive models representing the discontinuous nature of cardiac tissue have been proposed (e.g., [62, 74, 75, 76, 77]), and the EMI model might be a useful tool for investigating their accuracy.

Identification of drug effects from microphysiological systems of hiPSC-CMs

The fourth and fifth papers of the thesis focus on using mathematical modeling to aid the usefulness of microphysiological systems of hiPSC-CMs for drug testing applications. The approach consists of two main steps. The first step is an inversion procedure for inverting calcium and voltage traces to parameterize a mathematical action potential model, and the second step is a maturation map for mapping drug effects for immature cells to drug effects for mature cells. In the papers, the approach seems to give results similar to what would be expected for some drugs with known effects, but the procedure is still far from being fully developed. In the fifth research paper, several aspects of the approach used in the fourth paper is improved, but a number of further improvements might be considered regarding both the inversion procedure, the base model formulation and the definition of the maturation map.

For example, more efficient inversion methods and cost function definitions might be obtained. In addition, the base model currently used in the inversion might be improved by, for instance, reducing the drift of the intracellular calcium concentrations. The maturation map could also be extended to allow for possible known functional differences of the membrane proteins during maturation. This could, for example, be represented by adjustments of the dynamics of the gating variables of the ion channel currents of the model, in addition to the adjustments of the maximal conductances currently used. The construction of the maturation map might also be improved by a more detailed investigation of known differences of the individual currents and properties between immature and mature cells.

More detailed representations of drug effects may also be considered by, for example, representing the drug effects by adjustments of the gating dynamics of the ion channels instead of simply adjusting the channels' maximum conductances. Moreover, further investigations of the accuracy of the procedure, for instance by

comparing the drug responses estimated by the procedure to known drug responses for additional drugs would probably be useful. Furthermore, the accuracy might be investigated further by comparing the currents in an adjusted model to measurements of individual currents conducted on the cells the model was adjusted to represent.

In addition, the sixth research paper of the thesis investigates a possible approach for identifying which parameters are identifiable in an AP model. The approach is based on singular value decomposition of a matrix consisting of the model currents. The approach seems to be useful for identifying how some model currents could be perturbed without any noticeable change in the resulting AP, both for well-known AP models of human mature cardiomyocytes and for the base model introduced in the fifth paper. This approach could possibly be further developed to identify the identifiability of more model parameters than the maximum conductances of the membrane currents. For instance, the analysis could be extended to include other model variables than the membrane potential, for example the intracellular calcium concentrations. In addition, other methods for identifying unidentifiable model parameters might also be considered as alternatives or supplements to the singular value decomposition analysis.

Furthermore, the overall modeling approach could also be extended in various directions. For example, the concept of representing different cell types using the same base model could be extended from maps between cells of different maturity levels to maps between cells of different species. The framework may also be extended to modeling of, for example, a gradual maturation process. The approach could also be applied to study other properties than the effect of a drug. For instance, in [109], the inversion procedure of the fourth and fifth papers is applied to explain differences in the electrophysiological properties of hiPSC-CMs exposed to different culturing conditions.

Bibliography

[1] Hussein Nori Rubaiy. A short guide to electrophysiology and ion channels. *Journal of Pharmacy & Pharmaceutical Sciences*, 20:48–67, 2017.

[2] Marco Piccolino. Animal electricity and the birth of electrophysiology: the legacy of Luigi Galvani. *Brain Research Bulletin*, 46(5):381–407, 1998.

[3] Ernst-August Seyfarth. Julius Bernstein (1839–1917): pioneer neurobiologist and biophysicist. *Biological Cybernetics*, 94(1):2–8, 2006.

[4] Bertil Hille. *Ion channels of excitable membranes*, volume 507. Sinauer Sunderland, MA, 2001.

[5] Erwin Neher, Bert Sakmann, and Joe Henry Steinbach. The extracellular patch clamp: a method for resolving currents through individual open channels in biological membranes. *Pflügers Archiv*, 375(2):219–228, 1978.

[6] Dan M Roden. Cellular basis of drug-induced torsades de pointes. *British Journal of Pharmacology*, 154(7):1502–1507, 2008.

[7] Gary R Mirams, Yi Cui, Anna Sher, Martin Fink, Jonathan Cooper, Bronagh M Heath, Nick C McMahon, David J Gavaghan, and Denis Noble. Simulation of multiple ion channel block provides improved early prediction of compounds' clinical torsadogenic risk. *Cardiovascular Research*, 91(1):53–61, 2011.

[8] Alan L Hodgkin and Andrew F Huxley. A quantitative description of membrane current and its application to conduction and excitation in nerve. *The Journal of Physiology*, 117(4):500–544, 1952.

[9] Denis Noble, Alan Garny, and Penelope J Noble. How the Hodgkin–Huxley equations inspired the cardiac physiome project. *The Journal of Physiology*, 590(11):2613–2628, 2012.

[10] Denis Noble. Successes and failures in modeling heart cell electrophysiology. *Heart Rhythm*, 8(11):1798–1803, 2011.

[11] Andreas VM Herz, Tim Gollisch, Christian K Machens, and Dieter Jaeger. Modeling single-neuron dynamics and computations: a balance of detail and abstraction. *Science*, 314(5796):80–85, 2006.

[12] Henrik Lindén, Klas H Pettersen, and Gaute T Einevoll. Intrinsic dendritic filtering gives low-pass power spectra of local field potentials. *Journal of Computational Neuroscience*, 29(3):423–444, 2010.

[13] Zhilin Qu, Gang Hu, Alan Garfinkel, and James N Weiss. Nonlinear and stochastic dynamics in the heart. *Physics Reports*, 543(2):61–162, 2014.

[14] Natalia A Trayanova. Whole-heart modeling: applications to cardiac electrophysiology and electromechanics. *Circulation Research*, 108(1):113–128, 2011.

[15] Lucia Romero, Jordi Cano, Julio Gomis-Tena, Beatriz Trenor, Ferran Sanz, Manuel Pastor, and Javier Saiz. In silico QT and APD prolongation assay for early screening of drug-induced proarrhythmic risk. *Journal of Chemical Information and Modeling*, 58(4):867–878, 2018.

[16] Mark R Davies, Ken Wang, Gary R Mirams, Antonello Caruso, Denis Noble, Antje Walz, Thierry Lavé, Franz Schuler, Thomas Singer, and Liudmila Polonchuk. Recent developments in using mechanistic cardiac modelling for drug safety evaluation. *Drug Discovery Today*, 21(6):924–938, 2016.

[17] Annamaria Carusi, Kevin Burrage, and Blanca Rodríguez. Bridging experiments, models and simulations: an integrative approach to validation in computational cardiac electrophysiology. *American Journal of Physiology-Heart and Circulatory Physiology*, 303(2):H144–H155, 2012.

[18] Indira H Shrivastava and Mark SP Sansom. Simulations of ion permeation through a potassium channel: molecular dynamics of KcsA in a phospholipid bilayer. *Biophysical Journal*, 78(2):557–570, 2000.

[19] Eleonora Grandi, Francesco S Pasqualini, and Donald M Bers. A novel computational model of the human ventricular action potential and Ca transient. *Journal of Molecular and Cellular Cardiology*, 48(1):112–121, 2010.

[20] Hermenegild J Arevalo, Fijoy Vadakkumpadan, Eliseo Guallar, Alexander Jebb, Peter Malamas, Katherine C Wu, and Natalia A Trayanova. Arrhythmia risk stratification of patients after myocardial infarction using personalized heart models. *Nature Communications*, 7:11437, 2016.

[21] Henry Markram, Eilif Muller, Srikanth Ramaswamy, Michael W Reimann, Marwan Abdellah, Carlos Aguado Sanchez, Anastasia Ailamaki, Lidia Alonso-Nanclares, Nicolas Antille, Selim Arsever, et al. Reconstruction and simulation of neocortical microcircuitry. *Cell*, 163(2):456–492, 2015.

[22] Oliver J Britton, Alfonso Bueno-Orovio, Karel Van Ammel, Hua Rong Lu, Rob Towart, David J Gallacher, and Blanca Rodriguez. Experimentally calibrated population of models predicts and explains intersubject variability in cardiac cellular electrophysiology. *Proceedings of the National Academy of Sciences*, 110(23):E2098–E2105, 2013.

[23] Carlos Sanchez, Alfonso Bueno-Orovio, Erich Wettwer, Simone Loose, Jana Simon, Ursula Ravens, Esther Pueyo, and Blanca Rodriguez. Inter-subject variability in human atrial action potential in sinus rhythm versus chronic atrial fibrillation. *PloS one*, 9(8):e105897, 2014.

[24] Anurag Mathur, Peter Loskill, Kaifeng Shao, Nathaniel Huebsch, SoonGweon Hong, Sivan G Marcus, Natalie Marks, Mohammad Mandegar, Bruce R Conklin, Luke P Lee, and Kevin E Healy. Human iPSC-based cardiac microphysiological system for drug screening applications. *Scientific Reports*, 5:8883, 2015.

[25] Antoni Bayés de Luna. *Basic electrocardiography: normal and abnormal ECG patterns*. John Wiley & Sons, 2007.

[26] Michael J Aminoff. Electrophysiology. In *Textbook of Clinical Neurology (Third Edition)*, pages 477–497. Elsevier, 2007.

[27] Harry A Fozzard, Michael F Sheets, and Dorothy Hanck. The sodium channel as a target for local anesthetic drugs. *Frontiers in Pharmacology*, 2:68, 2011.

[28] Siva K Mulpuru, Malini Madhavan, Christopher J McLeod, Yong-Mei Cha, and Paul A Friedman. Cardiac pacemakers: function, troubleshooting, and management: part 1 of a 2-part series. *Journal of the American College of Cardiology*, 69(2):189–210, 2017.

[29] Natalia Trayanova. Defibrillation of the heart: insights into mechanisms from modelling studies. *Experimental Physiology*, 91(2):323–337, 2006.

[30] Hugh Calkins, Gerhard Hindricks, Riccardo Cappato, Young-Hoon Kim, Eduardo B Saad, Luis Aguinaga, Joseph G Akar, Vinay Badhwar, Josep Brugada, John Camm, et al. 2017 HRS/EHRA/ECAS/APHRS/SOLAECE expert consensus statement on catheter and surgical ablation of atrial fibrillation. *Ep Europace*, 20(1):e1–e160, 2017.

[31] Robert Plonsey and Roger C Barr. *Bioelectricity: a quantitative approach*. Springer Science & Business Media, 2007.

[32] G Bard Ermentrout and David H Terman. *Mathematical foundations of neuroscience*, volume 35. Springer Science & Business Media, 2010.

[33] David Sterratt, Bruce Graham, Andrew Gillies, and David Willshaw. *Principles of computational modelling in neuroscience*. Cambridge University Press, 2011.

[34] James Keener and James Sneyd. *Mathematical physiology*. Springer Science & Business Media, 2010.

[35] Denis Noble. A modification of the Hodgkin–Huxley equations applicable to purkinje fibre action and pacemaker potentials. *The Journal of Physiology*, 160(2):317–352, 1962.

[36] Raymond E Ideker, Wei Kong, and Steven Pogwizd. Purkinje fibers and arrhythmias. *Pacing and Clinical Electrophysiology*, 32(3):283–285, 2009.

[37] Donald M Bers. Calcium cycling and signaling in cardiac myocytes. *Annual Review of Physiology*, 70:23–49, 2008.

[38] Yoram Rudy and Jonathan R Silva. Computational biology in the study of cardiac ion channels and cell electrophysiology. *Quarterly Reviews of Biophysics*, 39(1):57–116, 2006.

[39] Aslak Tveito and Glenn T Lines. *Computing characterizations of drugs for ion channels and receptors using Markov models*, volume 111 of *Lecture Notes in Computational Science and Engineering*. Springer, 2016.

[40] Raimond L Winslow, Jeremy Rice, Saleet Jafri, Eduardo Marban, and Brian O'Rourke. Mechanisms of altered excitation-contraction coupling in canine tachycardia-induced heart failure, II: Model studies. *Circulation Research*, 84(5):571–586, 1999.

[41] Colleen E Clancy and Yoram Rudy. Na^+ channel mutation that causes both brugada and long-QT syndrome phenotypes: A simulation study of mechanism. *Circulation*, 105(10):1208–1213, 2002.

[42] Kirsten HWJ ten Tusscher and Alexander V Panfilov. Alternans and spiral breakup in a human ventricular tissue model. *American Journal of Physiology-Heart and Circulatory Physiology*, 291(3):H1088–H1100, 2006.

[43] Michelangelo Paci, Jari Hyttinen, Katriina Aalto-Setälä, and Stefano Severi. Computational models of ventricular-and atrial-like human induced pluripotent stem cell derived cardiomyocytes. *Annals of Biomedical Engineering*, 41(11):2334–2348, 2013.

[44] Autumn A Cuellar, Catherine M Lloyd, Poul F Nielsen, David P Bullivant, David P Nickerson, and Peter J Hunter. An overview of CellML 1.1, a biological model description language. *Simulation*, 79(12):740–747, 2003.

[45] Anders Nygren, Céline Fiset, Ludwik Firek, John W Clark, Douglas S Lindblad, Robert B Clark, and Wayne R Giles. Mathematical model of an adult human atrial cell: the role of K+ currents in repolarization. *Circulation Research*, 82(1):63–81, 1998.

[46] Thomas R Shannon, Fei Wang, José Puglisi, Christopher Weber, and Donald M Bers. A mathematical treatment of integrated Ca dynamics within the ventricular myocyte. *Biophysical Journal*, 87(5):3351–3371, 2004.

[47] Vladimir E Bondarenko, Gyula P Szigeti, Glenna CL Bett, Song-Jung Kim, and Randall L Rasmusson. Computer model of action potential of mouse ventricular myocytes. *American Journal of Physiology-Heart and Circulatory Physiology*, 287(3):H1378–H1403, 2004.

[48] Linda J Wang and Eric A Sobie. Mathematical model of the neonatal mouse ventricular action potential. *American Journal of Physiology-Heart and Circulatory Physiology*, 294(6):H2565–H2575, 2008.

[49] George W Beeler and Harald Reuter. Reconstruction of the action potential of ventricular myocardial fibres. *The Journal of Physiology*, 268(1):177–210, 1977.

[50] Richard A Gray and Pras Pathmanathan. A parsimonious model of the rabbit action potential elucidates the minimal physiological requirements for alternans and spiral wave breakup. *PLoS Computational Biology*, 12(10):e1005087, 2016.

[51] Thomas O'Hara, László Virág, András Varró, and Yoram Rudy. Simulation of the undiseased human cardiac ventricular action potential: model formulation and experimental validation. *PLoS Computational Biology*, 7(5):e1002061, 2011.

[52] Flavio Fenton and Alain Karma. Vortex dynamics in three-dimensional continuous myocardium with fiber rotation: Filament instability and fibrillation. *Chaos: An Interdisciplinary Journal of Nonlinear Science*, 8(1):20–47, 1998.

[53] Rubin R Aliev and Alexander V Panfilov. A simple two-variable model of cardiac excitation. *Chaos, Solitons & Fractals*, 7(3):293–301, 1996.

[54] Shinji Doi, Junko Inoue, Zhenxing Pan, and Kunichika Tsumoto. *Computational electrophysiology*, volume 2. Springer Science & Business Media, 2010.

[55] Library of science & medical illustrations. `http://www.somersault1824.com/science-illustrations`.

[56] Eric R Kandel, James H Schwartz, Thomas M Jessell, Steven A Siegelbaum, and AJ Hudspeth. *Principles of Neural Science*, volume 5. McGraw-Hill books, 2000.

[57] William Thomson. On the theory of the electric telegraph. *Proceedings of the Royal Society of London*, 7:382–399, 1856.

[58] Alan L Hodgkin and William AH Rushton. The electrical constants of a crustacean nerve fibre. *Proceedings of the Royal Society of London*, 133(873):444–479, 1946.

[59] Silvio Weidmann. The electrical constants of purkinje fibres. *The Journal of Physiology*, 118(3):348–360, 1952.

[60] Gaute T Einevoll. Mathematical modeling of neural activity. In *Dynamics of Complex Interconnected Systems: Networks and Bioprocesses*, pages 127–145. Springer, 2006.

[61] Andreas T Schaefer, Matthew E Larkum, Bert Sakmann, and Arnd Roth. Coincidence detection in pyramidal neurons is tuned by their dendritic branching pattern. *Journal of Neurophysiology*, 89(6):3143–3154, 2003.

[62] Robin M Shaw and Yoram Rudy. Ionic mechanisms of propagation in cardiac tissue: roles of the sodium and L-type calcium currents during reduced excitability and decreased gap junction coupling. *Circulation Research*, 81(5):727–741, 1997.

[63] Marie Engelene J Obien, Kosmas Deligkaris, Torsten Bullmann, Douglas J Bakkum, and Urs Frey. Revealing neuronal function through microelectrode array recordings. *Frontiers in Neuroscience*, 8:423, 2015.

[64] Klas H Pettersen and Gaute T Einevoll. Amplitude variability and extracellular low-pass filtering of neuronal spikes. *Biophysical Journal*, 94(3):784–802, 2008.

[65] Gaute T Einevoll, Christoph Kayser, Nikos K Logothetis, and Stefano Panzeri. Modelling and analysis of local field potentials for studying the function of cortical circuits. *Nature Reviews Neuroscience*, 14(11):770, 2013.

[66] Henrik Lindén, Tom Tetzlaff, Tobias C Potjans, Klas H Pettersen, Sonja Grün, Markus Diesmann, and Gaute T Einevoll. Modeling the spatial reach of the LFP. *Neuron*, 72(5):859–872, 2011.

[67] Paul L Nunez and Ramesh Srinivasan. *Electric fields of the brain: the neurophysics of EEG*. Oxford University Press, USA, 2nd edition, 2006. Chapter 3.

[68] Walter Rudin et al. *Principles of mathematical analysis*, volume 3. McGraw-hill New York, 1964.

[69] Frank B. Sachse. *Computational cardiology. Modeling of anatomy, electrophysiology, and mechanics*. Springer-Verlag, 2004.

[70] Pedro J Diaz, Yoram Rudy, and Robert Plonsey. Intercalated discs as a cause for discontinuous propagation in cardiac muscle: A theoretical simulation. *Annals of Biomedical Engineering*, 11(3-4):177–189, 1983.

[71] Jeroen G Stinstra, Sarah F Roberts, John B Pormann, Rob S MacLeod, and Craig S Henriquez. A model of 3D propagation in discrete cardiac tissue. In *Computers in Cardiology, 2006*, pages 41–44. IEEE, 2006.

[72] Sarah F Roberts, Jeroen G Stinstra, and Craig S Henriquez. Effect of nonuniform interstitial space properties on impulse propagation: a discrete multidomain model. *Biophysical Journal*, 95(8):3724–3737, 2008.

[73] Jeroen Stinstra, Rob MacLeod, and Craig Henriquez. Incorporating histology into a 3D microscopic computer model of myocardium to study propagation at a cellular level. *Annals of biomedical engineering*, 38(4):1399–1414, 2010.

[74] Madison S Spach, J Francis Heidlage, Roger C Barr, and Paul C Dolber. Cell size and communication: role in structural and electrical development and remodeling of the heart. *Heart Rhythm*, 1(4):500–515, 2004.

[75] Marjorie L Hubbard and Craig S Henriquez. A microstructural model of reentry arising from focal breakthrough at sites of source-load mismatch in a central region of slow conduction. *American Journal of Physiology-Heart and Circulatory Physiology*, 306(9):H1341–H1352, 2014.

[76] Joyce Lin and James P Keener. Modeling electrical activity of myocardial cells incorporating the effects of ephaptic coupling. *Proceedings of the National Academy of Sciences*, 107(49):20935–20940, 2010.

[77] Joyce Lin and James P Keener. Microdomain effects on transverse cardiac propagation. *Biophysical Journal*, 106(4):925–931, 2014.

[78] Leslie Tung. *A bi-domain model for describing ischemic myocardial dc potentials.* PhD thesis, Massachusetts Institute of Technology, 1978.

[79] Piero Colli Franzone, Luca Franco Pavarino, and Simone Scacchi. *Mathematical cardiac electrophysiology*, volume 13. Springer, 2014.

[80] Craig S Henriquez and Wenjun Ying. The bidomain model of cardiac tissue: from microscale to macroscale. In *Cardiac Bioelectric Therapy*, pages 401–421. Springer, 2009.

[81] Joakim Sundnes, Bjørn Fredrik Nielsen, Kent-Andre Mardal, Xing Cai, Glenn Terje Lines, and Aslak Tveito. On the computational complexity of the bidomain and the monodomain models of electrophysiology. *Annals of Biomedical Engineering*, 34(7):1088–1097, 2006.

[82] Andres Agudelo-Toro and Andreas Neef. Computationally efficient simulation of electrical activity at cell membranes interacting with self-generated and externally imposed electric fields. *Journal of Neural Engineering*, 10(2):026019, 2013.

[83] Jeroen G Stinstra, Craig S Henriquez, and Rob S MacLeod. Comparison of microscopic and bidomain models of anisotropic conduction. In *Computers in Cardiology, 2009*, pages 657–660. IEEE, 2009.

[84] Wanda Krassowska and John C Neu. Response of a single cell to an external electric field. *Biophysical Journal*, 66(6):1768–1776, 1994.

[85] Wenjun Ying and Craig S Henriquez. Hybrid finite element method for describing the electrical response of biological cells to applied fields. *IEEE Transactions on Biomedical Engineering*, 54(4):611–620, 2007.

[86] Jeroen G Stinstra, Bruce Hopenfeld, and Rob S MacLeod. On the passive cardiac conductivity. *Annals of Biomedical Engineering*, 33(12):1743–1751, 2005.

[87] Rolf Vogel and Robert Weingart. Mathematical model of vertebrate gap junctions derived from electrical measurements on homotypic and heterotypic channels. *The Journal of Physiology*, 510(1):177–189, 1998.

[88] Alexandra P Henriquez, Rolf Vogel, Barbara J Muller-Borer, Craig S Henriquez, Robert Weingart, and Wayne E Cascio. Influence of dynamic gap junction resistance on impulse propagation in ventricular myocardium: a computer simulation study. *Biophysical Journal*, 81(4):2112–2121, 2001.

[89] Xianming Lin, Joanna Gemel, Eric C Beyer, and Richard D Veenstra. Dynamic model for ventricular junctional conductance during the cardiac action potential. *American Journal of Physiology-Heart and Circulatory Physiology*, 288(3):H1113–H1123, 2005.

[90] Nerijus Paulauskas, Henrikas Pranevicius, Jonas Mockus, and Feliksas F Bukauskas. Stochastic 16-state model of voltage gating of gap-junction channels enclosing fast and slow gates. *Biophysical Journal*, 102(11):2471–2480, 2012.

[91] Mindaugas Snipas, Tadas Kraujalis, Nerijus Paulauskas, Kestutis Maciunas, and Feliksas F Bukauskas. Stochastic model of gap junctions exhibiting rectification and multiple closed states of slow gates. *Biophysical Journal*, 110(6):1322–1333, 2016.

[92] Seth H Weinberg. Ephaptic coupling rescues conduction failure in weakly coupled cardiac tissue with voltage-gated gap junctions. *Chaos: An Interdisciplinary Journal of Nonlinear Science*, 27(9):093908, 2017.

[93] Andres Agudelo-Toro. *Numerical simulations on the biophysical foundations of the neuronal extracellular space*. PhD thesis, Niedersächsische Staats-und Universitätsbibliothek Göttingen, 2012.

[94] Kenneth A Lindsay, Jay R Rosenberg, and Gayle Tucker. From Maxwell's equations to the cable equation and beyond. *Progress in Biophysics and Molecular Biology*, 85(1):71–116, 2004.

[95] Robert Plonsey and Dennis B. Heppner. Considerations of quasi-stationarity in electrophysiological systems. *Bulletin of Mathematical Biology*, 29(4):657–664, 1967.

[96] David J Griffiths. *Introduction to electrodynamics*. Prentice Hall, 2nd edition, 1989.

[97] Jan P Kucera, Stephan Rohr, and Yoram Rudy. Localization of sodium channels in intercalated disks modulates cardiac conduction. *Circulation Research*, 91(12):1176–1182, 2002.

[98] Rengasayee Veeraraghavan, Joyce Lin, Gregory S Hoeker, James P Keener, Robert G Gourdie, and Steven Poelzing. Sodium channels in the Cx43 gap junction perinexus may constitute a cardiac ephapse: an experimental and modeling study. *Pflügers Archiv-European Journal of Physiology*, 467(10):2093–2105, 2015.

[99] Ruth E Westenbroek, Sebastian Bischoff, Ying Fu, Sebastian KG Maier, William A Catterall, and Todd Scheuer. Localization of sodium channel subtypes in mouse ventricular myocytes using quantitative immunocytochemistry. *Journal of Molecular and Cellular Cardiology*, 64:69–78, 2013.

[100] Nicholas Sperelakis and Keith McConnell. Electric field interactions between closely abutting excitable cells. *IEEE Engineering in Medicine and Biology Magazine*, 21(1):77–89, 2002.

[101] Priyanka Garg, Vivek Garg, Rajani Shrestha, Michael C Sanguinetti, Timothy J Kamp, and Joseph C Wu. Human induced pluripotent stem cell–derived cardiomyocytes as models for cardiac channelopathies: A primer for non-electrophysiologists. *Circulation Research*, 123(2):224–243, 2018.

[102] Jörg Liesen and Volker Mehrmann. *Linear Algebra*. Springer, 2015.

[103] Tom Lyche. *Numerical Linear Algebra and Matrix Factorizations*. University of Oslo, lecture notes, 2017.

[104] Rengasayee Veeraraghavan, Robert G Gourdie, and Steven Poelzing. Mechanisms of cardiac conduction: a history of revisions. *American Journal of Physiology-Heart and Circulatory Physiology*, 306(5):H619–H627, 2014.

[105] Jan P Kucera, Stephan Rohr, and Andre G Kleber. Microstructure, cell-to-cell coupling, and ion currents as determinants of electrical propagation and arrhythmogenesis. *Circulation: Arrhythmia and Electrophysiology*, 10(9):e004665, 2017.

[106] William J Crumb, Jose Vicente, Lars Johannesen, and David G Strauss. An evaluation of 30 clinical drugs against the comprehensive in vitro proarrhythmia assay (CiPA) proposed ion channel panel. *Journal of Pharmacological and Toxicological Methods*, 81:251–262, 2016.

[107] Jurgis Pods. A comparison of computational models for the extracellular potential of neurons. *Journal of Integrative Neuroscience*, 16(1):19–32, 2017.

[108] Alessio Buccino, Miroslav Kuchta, Karoline H Jæger, Torbjorn Ness, Pierre Berthet, Kent-Andre Mardal, Gert Cauwenberghs, and Aslak Tveito. How does the presence of neural probes affect extracellular potentials? *Journal of Neural Engineering*, 16:026030, 2019.

[109] Nathaniel Huebsch, Berenice Charrez, Brian Siemons, Steven C Boggess, Sam Wall, Verena Charwat, Karoline H Jæger, Felipe T Lee-Montiel, Nicholas C Jeffreys, Nikhil Deveshwar, Andrew Edwards, Jonathan Serrano, Matija Snuderl, Andreas Stahl, Aslak Tveito, Evan W Miller, and Kevin E Healy. Metabolically-driven maturation of hiPSC-cell derived heart-on-a-chip. *bioRxiv*, 2018. preprint.

Part II

Research papers

Paper I

An Evaluation of the Accuracy of Classical Models for Computing the Membrane Potential and Extracellular Potential for Neurons

Aslak Tveito, Karoline H. Jæger, Glenn T. Lines,
Łukasz Paszkowski, Joakim Sundnes, Andrew G. Edwards,
Tuomo Mäki-Marttunen, Geir Halnes, and Gaute T. Einevoll

Frontiers in Computational Neuroscience 11:27, 2017.

An Evaluation of the Accuracy of Classical Models for Computing the Membrane Potential and Extracellular Potential for Neurons

Aslak Tveito[1,2], Karoline H. Jæger[1], Glenn T. Lines[1], Łukasz Paszkowski[3], Joakim Sundnes[1,2], Andrew G. Edwards[1,4], Tuomo Mäki-Marttunen[5], Geir Halnes[6], and Gaute T. Einevoll[6,7]

[1]Simula Research Laboratory, Center for Biomedical Computing, Norway
[2]Department of Informatics, University of Oslo, Norway
[3]Radytek, Wrocław, Poland
[4]Department of Biosciences, University of Oslo, Oslo, Norway
[5]NORMENT, KG Jebsen Center for Psychosis Research, Institute of Clinical Medicine, University of Oslo, Oslo, Norway
[6]Department of Mathematical Sciences and Technology, Norwegian University of Life Sciences, Ås, Norway
[7]Department of Physics, University of Oslo, Oslo, Norway

Abstract

Two mathematical models are part of the foundation of Computational neurophysiology; a) the Cable equation is used to compute the membrane potential of neurons, and, b) volume-conductor theory describes the extracellular potential around neurons. In the standard procedure for computing extracellular potentials, the transmembrane currents are computed by means of a) and the extracellular potentials are computed using an explicit sum over analytical point-current source solutions as prescribed by volume conductor theory. Both models are extremely useful as they allow huge simplifications of the computational efforts involved in computing extracellular potentials. However, there are more accurate, though computationally very expensive, models available where the potentials inside and outside the neurons are computed simultaneously in a self-consistent scheme. In the present work we explore the accuracy of the classical models a) and b) by comparing them to these more accurate schemes.

The main assumption of a) is that the ephaptic current can be ignored in the derivation of the Cable equation. We find, however, for our examples with stylized neurons, that the ephaptic current is comparable in magnitude to other currents involved in the computations, suggesting that it may be significant – at least in parts of the simulation. The magnitude of the error introduced in the membrane potential is several millivolts, and this error also translates into errors

in the predicted extracellular potentials. While the error becomes negligible if we assume the extracellular conductivity to be very large, this assumption is, unfortunately, not easy to justify *a priori* for all situations of interest.

1 Introduction

Computational modeling in neurophysiology is a rapidly developing field taking on problems of enormous complexity. This is illustrated in the recent paper by Markram et al. [1] where the authors present results of amazingly detailed digital algorithmic reconstruction of a neocortical volume segment (about 0.29 mm^3) of rat cortex, containing ∼31,000 neurons with ∼37 million synapses. The complexity of the project is astonishing, and it opens amazing perspectives for insight in the complexities of the brain. The paper also raises questions of more philosophical nature brilliantly examined in the accompanying perspective by Koch and Buice [2].

The development of enormously complex computational models motivates closer examination of the basis of the mathematical models underpinning the computations. It is the purpose of this study to evaluate the accuracy of two basic models extensively used throughout the field of computational neurophysiology, and our main question is whether the popularity of these models is warranted by their accuracy.

The first model we consider is the celebrated Cable equation used to compute membrane potentials and transmembrane currents. This model is absolutely essential in computational neurophysiology, and is used in numerous papers every year. The derivation of the model is classical and can be found in any introduction to computational neurophysiology; see e.g. [3, 4, 5, 6, 7]. An important assumption in the most common derivation of the Cable equation is that the extracellular conductivity is very large, and that consequently the extracellular potential can be assumed to be constant. This assumption represents a major simplification of the model since the extracellular field does not have to be represented in the model, which means that a costly solution of a Poisson equation in the extracellular domain is avoided.

One way of interpreting the effect of ignoring the coupling to the extracellular potential is that (as we shall see below) we disregard the so-called ephaptic current; see e.g. [8]. It is well known that neglecting this current represents a key assumption, and the validity of the assumption, and also the effect of ephaptic coupling, have previously been discussed by several authors; see e.g. [9, 10, 11, 12, 13, 14]. An analytical treatment of the effect of ephaptic currents on nerve pulses in parallel nerve fibers is given in Chapter 8 of Scott [5]. That exposition is motived by classical experiments performed by Katz and Schmitt (see e.g. [15]) and analyzed by an extension of the scalar Cable equation to a 2×2 system of partial differential equations governing the membrane potential of the neighboring nerve fibers. This work is followed up by Shneider and Pekker [16] who suggest that the ephaptic current acts as a synchronization mechanism for action potentials along bundles

of neurons. For axons, the coupling is particularly important in the unmyelinated case; see Bokil et al. [14] for an analysis of bundles of olfactory nerve axons. Furthermore, Goldwyn and Rinzel [11] recently studied ephaptic interactions in a bundle of neurons and found that the effects of the ephaptic currents were small but not negligible.

The question of ephaptic coupling between cells has been studied for a long time; 75 years ago Arvanitaki [17] stated that *there is no doubt that the activity of an element in the midst of a cell agglomeration can influence that of its neighbors, even when specialized contact surfaces for transmission, i.e. those loci traditionally known as synapses and which have been endowed with particular properties are lacking.* In [8], Holt and Koch analyse the magnitude and possible consequences of ephaptic coupling. They observe that spikes from a neuron can cause an extracellular potential of a few mV near the cell body, and they analyse the effect of this on nearby cells. The impact of ephaptic coupling remains uncertain [12, 13], but it seems to be acknowledged that ephaptic currents *may* be significant. However, it is usually not taken into account in most computational analyses of neurons, and the reason for this is clearly to improve computational efficiency. In this paper we will quantify the error introduced by this assumption. We will compare the results of the Cable equation to those of an accurate mathematical model which includes the ephaptic current. The more accurate model will be referred to as the **EMI** model since it builds on detailed representation of both the **E**xtracellular space surrounding the neuron, the **M**embrane of the neuron and the **I**ntracellular space of the neuron. EMI computations are typically *much* more CPU demanding than solving the Cable equation, but the model faithfully represents the physics of the neuron and its surroundings. Variants of the EMI model have been studied previously by e.g. Krassowska and Neu [18], Ying and Henriquez [19], Henriquez et al. [20], Agudelo-Toro and Neef [21], and Agudelo-Toro [22]. For linear membrane currents and specialized geometries, analytical solutions are available; see e.g. [23, 24, 25, 18, 19, 21].

The second model we consider is the standard formalism for computing the extracellular potential based on solutions of the Cable equation. It is well known that if the current sources are given by Dirac delta functions, the solution of the Poisson equation, defined on an infinite domain, can be computed by an explicit formula, see e.g. [26]. Based on the solution of the Cable equation, the current sources can be defined for each compartment in the numerical solution, and the solution of the Poisson equation can (due to linearity) be given as the sum of contributions from all compartments. Note that in practice the so-called *line-source approximation* [8] where the current sources are assumed to be evenly distributed along cylindrical axes of dendritic compartments, is commonly used rather than the point-source approximation built on solutions of the Dirac delta functions. However, these two methods are directly related as a line source can be arbitrarily accurately approximated by a line of delta-function sources.

The combined use of the two models a) and b) in computing extracellular potentials is especially intriguing since a) is solved based on the assumption that the extracellular field is *constant*, and then b) is used to compute the *non-constant*

extracellular potential.

We have evaluated the accuracy of these two basic models by comparing the results with the results obtained by solving the EMI model. Our findings can be summarized as follows:

1. We find that the membrane potential computed by the Cable equation qualitatively resembles the solution of the EMI model but may differ quantitatively (several millivolts) from the solution of the EMI model.

2. We find, using reasonable parameters, that the magnitude of the ephaptic current is comparable to the other currents in our example model, so that its omission is, in general, difficult to justify.

3. For our example application the error in neglecting the ephaptic effect when computing the extracellular potentials is found to be 10 % or more, and stem from the inaccurate computation of the transmembrane currents when the extracellular potentials are assumed to be constant.

We have found the EMI model to be a useful framework for assessing the accuracy of the classical models. The EMI model is, however, *much more computationally demanding*, it is much more difficult to implement correctly, and therefore very challenging to apply to problems of greater complexity than the simple problems addressed in the present report.

The rest of this report is organized as follows: In the Methods section, we derive the classical Cable equation and highlight what assumptions are needed to remove the extracellular potential from the model. Given the solution of the Cable equation, we show how to compute the extracellular potential by solving a boundary value problem, how to approximate the solution by solving a Poisson equation, and how to approximate the solution of the extracellular potential using a classical summation formula. Finally, we introduce the EMI model where the dynamics of the extracellular space, the cell membrane and the intracellular space are fully coupled, and we show how the EMI model can be solved numerically. In the Results section, we study the error introduced in the model by ignoring the ephaptic currents and how the ephaptic current depends on the extracellular conductivity. Furthermore, we compare the extracellular potential around a single simplified neuron computed by various approximate models, and we also compare the extracellular potential between two simplified neurons. Finally, we show that the numerical solutions seem to converge under mesh refinement and that infinite domains can be reasonably well represented using large extracellular domains. Implications and relevance of the results are examined in the Discussion section. In an appendix we give a theoretical estimate of the error introduced by removing the ephaptic current.

2 Methods

The standard way of computing the extracellular potential surrounding a neuron is a two-step process: a) solve the Cable equation, and b) use the transmembrane currents defined by step a) to compute the extracellular potential. Our aim is to assess the accuracy of the solution of these two steps. For comparison we will use an accurate model combining the Extracellular domain, the Membrane, and the Intracellular domain, referred to as the EMI model. Below, the EMI solution will be regarded as the reference solution, and therefore solutions computed by all other methods (derived below) will be compared to the EMI solution.

We will take care to try to explain exactly how the EMI model and the two-step models are defined and solved although the derivations presented here can, at least in part, be found elsewhere. The derivations will also help us clarify what assumptions underlie the various models.

2.1 The classical two-step method

We start by describing the two steps of the classical approach of computing the extracellular potential [8, 27]. The first step is to compute the membrane potential and transmembrane currents. In the classical approach this problem is solved assuming a constant extracellular potential. We briefly review the derivation of the Cable equation in order to clarify exactly what assumption is made in order to remove the extracellular potential from the equation defining the membrane potential. By identifying what term is ignored in the equation, this term can be evaluated and used to illuminate the accuracy of the Cable equation.

The second step is to compute the extracellular potential by using the solution of the Cable equation to define the transmembrane current sources. This step can be done in numerous ways, and we will derive alternative methods starting with the approach considered to most faithfully represent the physics involved, and then derive simpler and more efficient methods in order to end up with the classical summation formula defining the extracellular potential.

2.1.1 The Cable equation

Consider a simplified neuron geometry illustrated in Figure 1. The intracellular space of the neuron is denoted by Ω_{i} and the boundary of Ω_{i} is the membrane of the neuron, denoted by Γ. The size of Ω_{i} is given by l_x, l_y, and l_z. In the derivation of the Cable equation, the neuron is divided into compartments, see e.g. [3, 5, 4], and it is assumed that the variations in the y- and z-directions are small and can be ignored. Our derivation is based on the version of the Cable equation used in [8]. The compartments are denoted by $\Omega_{\mathrm{i},k}$, and have length Δx. For the k-th compartment, the transmembrane current density (positive outward) is given by (see e.g. [3])

$$I_{\mathrm{m}}^k = C_{\mathrm{m}} \frac{dv^k}{dt} + I_{\mathrm{ion}}^k, \tag{1}$$

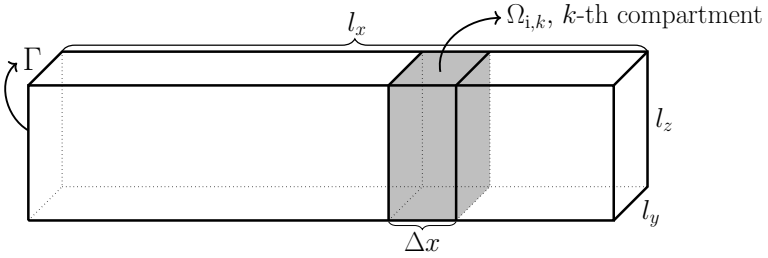

Figure 1: Sketch of a simplified neuron of rectangular cuboid shape with dimensions l_x, l_y, and l_z. The intracellular domain is denoted Ω_{i}, the boundary is Γ, and the compartments of length Δx are denoted by $\Omega_{\mathrm{i},k}$.

where v is the membrane potential, C_{m} is the cell membrane capacitance and I_{ion} is the ionic current density out of the cell. Furthermore, assuming ohmic resistance along the length of the neuron, we have

$$\Delta x I_{k+1/2} = \sigma_{\mathrm{i}}(u_{\mathrm{i}}^k - u_{\mathrm{i}}^{k+1}), \tag{2}$$

where u_{i}^k is the intracellular potential in compartment k, σ_{i} is the intracellular conductivity, and $I_{k+1/2}$ is the intracellular current density from compartment k to compartment $k+1$. Applying Kirchhoff's current law, the sum of the currents flowing out of a compartment must equal the sum of currents flowing into a compartment, i.e.

$$|\Gamma^k| I_{\mathrm{m}}^k = l_y l_z (I_{k-1/2} - I_{k+1/2}), \tag{3}$$

where $|\Gamma^k|$ is the membrane area associated with $\Omega_{\mathrm{i},k}$. Therefore,

$$|\Gamma^k| \left(C_{\mathrm{m}} \frac{dv^k}{dt} + I_{\mathrm{ion}}^k \right) = \frac{\sigma_{\mathrm{i}} l_y l_z}{\Delta x} \left(u_{\mathrm{i}}^{k-1} - 2u_{\mathrm{i}}^k + u_{\mathrm{i}}^{k+1} \right). \tag{4}$$

To simplify notations, we assume that $l_y = l_z := h$, and we have

$$C_{\mathrm{m}} \frac{dv^k}{dt} + I_{\mathrm{ion}}^k = \frac{\sigma_{\mathrm{i}}}{4} \frac{h}{\Delta x^2} \left(u_{\mathrm{i}}^{k-1} - 2u_{\mathrm{i}}^k + u_{\mathrm{i}}^{k+1} \right). \tag{5}$$

Certainly, in the limit of small compartments ($\Delta x \to 0$), we have

$$C_{\mathrm{m}} \frac{\partial v}{\partial t} + I_{\mathrm{ion}} = \eta \frac{\partial^2 u_{\mathrm{i}}}{\partial x^2}, \tag{6}$$

where we have introduced the conductance

$$\eta = \frac{h \sigma_{\mathrm{i}}}{4}. \tag{7}$$

The membrane potential is defined as

$$v = u_{\mathrm{i}} - u_{\mathrm{e}}, \tag{8}$$

where u_{e} denotes the extracellular potential. Therefore, we can replace the intracellular potential u_{i} in (6) by $v + u_{\mathrm{e}}$ to get

$$C_{\mathrm{m}} \frac{\partial v}{\partial t} + I_{\mathrm{ion}} = \eta \left(\frac{\partial^2 v}{\partial x^2} + \frac{\partial^2 u_{\mathrm{e}}}{\partial x^2} \right). \tag{9}$$

At this point a major assumption is introduced; it is assumed that the extracellular potential varies so little that it can be taken to be a constant (see e.g. [3])[1];

$$u_{\mathrm{e}} \approx \text{const.} \tag{10}$$

Building on this assumption we arrive at the classical Cable equation

$$C_{\mathrm{m}} \frac{\partial v}{\partial t} + I_{\mathrm{ion}} = \eta \frac{\partial^2 v}{\partial x^2}. \tag{11}$$

Note that the term we ignored in the derivation of the Cable equation is

$$I_{\mathrm{eph}} = \eta \frac{\partial^2 u_{\mathrm{e}}}{\partial x^2}, \tag{12}$$

which is referred to as the *ephaptic* current density [8]. In the computations below we will compute this current using the EMI model and use it to quantify the effect of the assumption underlying the classical Cable equation.

2.1.2 Computing the transmembrane current based on the solution of the Cable equation

Next we address the problem of computing the transmembrane current based on the solution of the Cable equation. Suppose that the Cable equation is solved numerically using an implicit finite difference scheme of the form

$$C_{\mathrm{m}} \frac{v_{n,k} - v_{n-1,k}}{\Delta t} + I_{\mathrm{ion},n,k} = \eta \frac{v_{n,k-1} - 2v_{n,k} + v_{n,k+1}}{\Delta x^2}, \tag{13}$$

where, as above, Δx denotes the spatial discretization in form of compartments, Δt denotes the time-step, and n is used to enumerate the time steps. Then, the associated transmembrane current density is given by

$$I_{\mathrm{m}}^{k,n} = \eta \frac{v_{n,k-1} - 2v_{n,k} + v_{n,k+1}}{\Delta x^2}. \tag{14}$$

All the methods discussed below for computing the extracellular potential rely on an approximation of this current density, but the methods differ in how the current is approximated and in the assumptions made on the extracellular domain.

[1] Assuming that the extracellular potential is a linear function of position would result in the same simplified model.

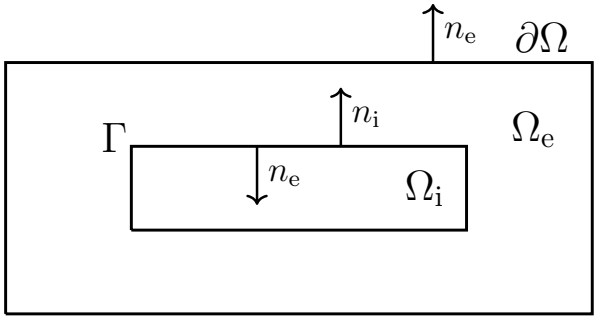

Figure 2: Sketch of a simplified neuron geometry and its surroundings; the extracellular domain Ω_e, the cell membrane Γ, and the intracellular domain Ω_i. The normal vector pointing out of Ω_i, is denoted by n_i and, similarly, n_e denotes the normal vector pointing out of Ω_e.

2.1.3 Computing the extracellular potential in terms of solving a boundary value problem; the CBV method

Consider the simplified 2D geometry illustrated in Figure 2. Our aim is now to compute the extracellular potential in Ω_e for the given transmembrane currents computed as explained above. The problem we have to solve is given by

$$\nabla^2 u_e = 0, \text{ in } \Omega_e, \tag{15}$$

$$\sigma_e \frac{\partial u_e}{\partial n_e} = I_m, \text{ at } \Gamma, \tag{16}$$

where I_m is computed by (14) and n_e is the outward pointing normal vector of Ω_e. The boundary condition at the outer boundary of Ω_e will be described for the simulations presented below.

In our computations, the Laplace equation (15) together with the boundary condition (16) is solved numerically using straightforward finite difference approximations leading to a linear system of algebraic equations. The finite difference stencil used for (15) will be described below.

We will refer to this method for computing the extracellular potential as the CBV-method since it comprises the solution of the Cable equation (C) and the solution of a boundary value (BV) problem.

2.1.4 Computing the extracellular potential by solving the Poisson equation; the CP method

In the CBV method the transmembrane currents setting up the extracellular potential are positioned at the interface between the intracellular and extracellular

domains. In the standard method for computing extracellular potentials (referred to as the CS method below), the transmembrane currents are instead assumed to be positioned at the points (or lines) at the centre of the intracellular domain [8]. One step in this direction is to replace the boundary value problem (15, 16) of the CBV method with a Poisson equation of the form

$$\nabla \cdot (\sigma \nabla u) = -C, \text{ in } \Omega, \tag{17}$$

where $\Omega = \Omega_\mathrm{e} \cup \Omega_\mathrm{i}$. Here σ equals σ_i and σ_e in Ω_i and Ω_e, respectively, and u equals u_i and u_e in Ω_i and Ω_e, respectively. The problem now is how to define the current source density C. In order to define C, we start by recalling that integration by parts gives

$$\int_\Omega \nabla \cdot (\sigma \nabla u)\phi \, dV = \int_\Gamma \sigma \frac{\partial u}{\partial n}\phi \, ds - \int_\Omega \nabla \phi \cdot (\sigma \nabla u) \, dV \tag{18}$$

for any smooth functions u and ϕ, see e.g. [28] page 140. By choosing $\phi = 1$, and using this identity, it follows from (17) that the integral of C must be given by

$$\int_{\Omega_\mathrm{i}} C dV = -\int_{\Omega_\mathrm{i}} \nabla \cdot (\sigma_\mathrm{i} \nabla u_\mathrm{i}) dV = -\int_\Gamma \sigma_\mathrm{i} \frac{\partial u_\mathrm{i}}{\partial n_\mathrm{i}} ds = \int_\Gamma I_\mathrm{m} ds, \tag{19}$$

where n_i is the outward pointing normal vector of Ω_i. We now want to define the source term C such that the identity (19) holds. To this end, we define the constants[2]

$$C_k = \frac{|\Gamma_k|}{|\Omega_{\mathrm{i},k}|} I_{\mathrm{m},k}, \tag{20}$$

for every compartment $\Omega_{\mathrm{i},k}$, where

$$I_{\mathrm{m},k} = \frac{1}{|\Gamma_k|} \int_{\Gamma_k} I_\mathrm{m} ds \tag{21}$$

is the average transmembrane current density of the compartment. Based on these constants, we can define the source term

$$C = C_k \text{ for } x \in \Omega_{\mathrm{i},k}. \tag{22}$$

With this definition of the source term, we have

$$\int_{\Omega_\mathrm{i}} C dx = \int_\Gamma I_\mathrm{m} ds$$

and therefore (19) holds provided that the current source density C is defined by (22).

We can now approximate the solution of the boundary value problem (15,16) defined on Ω_e with the Poisson problem (17) defined on the entire $\Omega = \Omega_\mathrm{e} \cup \Omega_\mathrm{i}$.

[2]Note that C_k is a constant defined on the compartment $\Omega_{\mathrm{i},k}$; it is constant in space but varies in time.

It remains to be seen that the current flowing into the extracellular domain Ω_e defined by boundary condition (16) is the same as the amount of current flowing out of the intracellular domain Ω_i in the solution of the Poisson equation (17). This holds, since by the definition of C we have

$$\int_\Gamma \sigma_e \frac{\partial u_e}{\partial n_e} ds = \int_\Gamma I_m ds = -\int_\Gamma \sigma_i \frac{\partial u_i}{\partial n_i} ds. \tag{23}$$

Note that this method effectively assumes the transmembrane current to be homogeneously distributed in the intracellular domain in the computation of the extracellular potential. Again, the numerical solution of (22) is obtained by the finite difference method where the right-hand side of the equation is evaluated in the mesh points. This leads to a linear system of algebraic equations.

The method of computing the extracellular potential by solving the Cable equation (11), using the result to define the source term C by (22), and then solving the Poisson equation (17), will be referred to as the CP method (C is for Cable and P is for Poisson).

2.1.5 Computing the extracellular potential by the point source method; the CS method

The final method for computing the extracellular potential based on the solution of the Cable equation we will consider is the point source method. This method relies on two basic assumptions; first it is assumed that all the current can be gathered in the center of each compartment; and second, it is assumed that the extracellular space is infinite. Under these assumptions, the Poisson equation can be solved analytically, see e.g. [29, 8, 30, 26]. This dramatically increases computational efficiency and thus this approach is extremely popular and completely dominates computations of extracellular potentials around neurons. Again, our aim is to assess the accuracy of this method.

By using the notation introduced above, we define current sources for each compartment by

$$c_k = |\Omega_{i,k}| C_k, \tag{24}$$

and define the associated Poisson problems

$$\sigma_e \nabla^2 u_{e,k} = -c_k \delta(r - r_k), \tag{25}$$

where $r = (x, y, z)$ and r_k is the center of the $k-$th compartment. The solution of this problem reads

$$u_{e,k} = \frac{c_k}{4\pi\sigma_e |r - r_k|}, \tag{26}$$

and therefore, by linearity, the extracellular potential is given by

$$u_e = \sum_k u_{e,k} = \frac{1}{4\pi\sigma_e} \sum_k \frac{c_k}{|r - r_k|}. \tag{27}$$

Note that $|r - r_k|$ denotes the Euclidean distance for r to the point r_k. In the computations below we will refer to this method of computing the extracellular potential as the CS-method (where C is for Cable and S is for sum).

2.2 The extracellular-membrane-intracellular (EMI) model

The dynamics of a neuron and its extracellular surroundings can be accurately modeled by explicitly considering the Extracellular space (Ω_e), the Membrane (Γ) and the Intracellular domain (Ω_i); as mentioned above we call this the EMI model. Analytical examples of solutions are given by Krassowska and Neu [18], finite element formulations are provided by Ying and Henriquez [19], Henriquez et al. [20] and Agudelo-Toro and Neef [21]; see also Agudelo-Toro [22] for a detailed derivation of the model.

The main elements of the model are sketched in Figure 2. Note that $\Omega = \Omega_\mathrm{i} \cup \Omega_\mathrm{e}$ contains a single cell, where Ω_i is the intracellular domain of the cell and Ω_e is the extracellular space surrounding the cell. We let u_i and u_e denote the intra- and extracellular potentials, and at the interface between the intracellular and extracellular domains, given by Γ, we define the membrane potential by $v = u_\mathrm{i} - u_\mathrm{e}$. Then the electrical potential defined in $\Omega = \Omega_\mathrm{i} \cup \Omega_\mathrm{e}$ is governed by the system

$$
\begin{aligned}
\nabla \cdot \sigma_\mathrm{i} \nabla u_\mathrm{i} &= 0, \text{ in } \Omega_\mathrm{i}, && (28)\\
\nabla \cdot \sigma_\mathrm{e} \nabla u_\mathrm{e} &= 0, \text{ in } \Omega_\mathrm{e}, && (29)\\
u_\mathrm{e} &= 0, \text{ at } \partial\Omega_\mathrm{e}, && (30)\\
n_\mathrm{e} \cdot \sigma_\mathrm{e} \nabla u_\mathrm{e} &= -n_\mathrm{i} \cdot \sigma_\mathrm{i} \nabla u_\mathrm{i}, \text{ at } \Gamma, && (31)\\
u_\mathrm{i} - u_\mathrm{e} &= v, \text{ at } \Gamma, && (32)\\
I_\mathrm{m} &= -n_\mathrm{i} \cdot \sigma_\mathrm{i} \nabla u_\mathrm{i}, \text{ at } \Gamma, && (33)\\
\frac{\partial v}{\partial t} &= \frac{1}{C_\mathrm{m}}(I_\mathrm{m} - I_\mathrm{ion}), \text{ at } \Gamma, && (34)
\end{aligned}
$$

where σ_i and σ_e are intra- and extracellular conductivities, n_i and n_e are the normal vectors of Ω_i and Ω_e, C_m is the cell membrane capacitance, and the ion current density is given by I_ion.

2.2.1 Numerical methods

We describe the finite difference scheme for solving the system (28)-(34) in the case of passive ion currents; i.e. for a case where I_ion is linear. In this case the problem (28)-(34) is linear and it is straightforward to define a fully implicit finite difference scheme. In the description of the solution method, we will consider the 2D case illustrated in Figure 3. The extension to 3D is notationally messy but conceptually straightforward.

The system (28)-(34) can be triggered in several different ways. Since we want to compare results using the Cable equation and the EMI model, we will apply an initial condition that can be used in an identical manner for both methods. This is achieved by assuming that the membrane potential is given at time $t = 0$, and by adding a one dimensional synaptic input current.

We let $(u_\mathrm{e}^{n,j,k}, v^{n,j,k}, u_\mathrm{i}^{n,j,k})$ denote finite difference approximations of $(u_\mathrm{e}, v, u_\mathrm{i})$ at $(t_n, x_j, y_k) = (n\Delta t, j\Delta x, k\Delta y)$ for given mesh parameters Δt, Δx and Δy. The computational nodes used for the discrete version of the system are shown in the

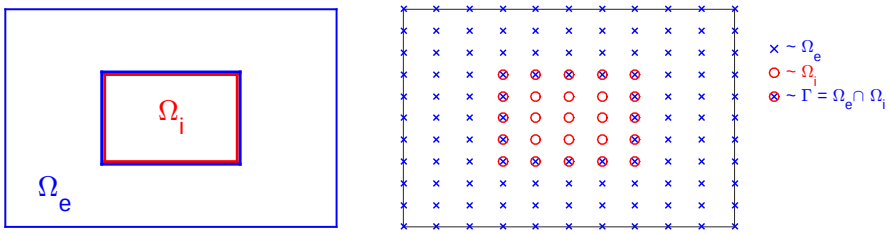

Figure 3: Sketch of the computational mesh for Ω_e and Ω_i; the nodes of Ω_e are marked by '$\times$', the nodes of Ω_i are marked by '$\circ$', and the membrane is defined as the intersection of Ω_e and Ω_i marked by '$\otimes$'.

right panel of Figure 3; nodes of the extracellular domain are marked by $'\times'$, the intracellular nodes are marked by '$\circ$', and the nodes on the membrane are marked by '$\otimes$'.

Suppose that $v = v^{n-1}$ is known at time $t = t_{n-1}$. The update from t_{n-1} to t_n is computed by solving a coupled linear system defined by a finite difference version of the system (28)-(34). In each node of the extracellular domain the elliptic equation (29) is replaced by a finite difference scheme of the form

$$\frac{\sigma_e^{j+1/2,k}(u_e^{n,j+1,k} - u_e^{n,j,k}) - \sigma_e^{j-1/2,k}(u_e^{n,j,k} - u_e^{n,j-1,k})}{\Delta x^2} + \frac{\sigma_e^{j,k+1/2}(u_e^{n,j,k+1} - u_e^{n,j,k}) - \sigma_e^{j,k-1/2}(u_e^{n,j,k} - u_e^{n,j,k-1})}{\Delta y^2} = 0, \qquad (35)$$

where $\sigma_e^{j+1/2,k} = \sigma_e((j+1/2)\Delta x, k\Delta y)$. Likewise, the elliptic equation (28) is replaced by a finite difference scheme of similar form (u_e replaced by u_i and σ_e replaced by σ_i). The numerical scheme given by (35) provides one equation for all nodes in the domain $\Omega_e \backslash \Gamma$ and (as explained above) for all nodes in the domain $\Omega_i \backslash \Gamma$.

It remains to specify three equations for all nodes on the membrane Γ since there are three unknowns, (u_e, v, u_i), in each of the membrane nodes. One equation is clearly given by (32); i.e. $u_i^{n,j,k} - u_e^{n,j,k} = v^{n,j,k}$ for all nodes (x_j, y_k) on the membrane Γ. The second equation is provided by replacing the flux-equality (31) by a finite difference equation, and the third equation is the discrete version of (34) in terms of an implicit scheme;

$$v^{n,j,k} - \frac{\Delta t}{C_m}(I_m^{n,j,k} - I_{ion}^{n,j,k}) = v^{n-1,j,k}. \qquad (36)$$

Here, I_m is defined as a discrete version of (33). Furthermore, in the passive case, the function I_{ion} is linear with respect to v and therefore the entire system is linear.

The four corners of the membrane mesh need special attention. In these nodes we define two extracellular and two intracellular flux terms; one term from the

Abbreviation	Explanation	Method
CBV	Cable equation, Boundary Value problem	(11), (15)–(16)
CP	Cable equation, Poisson equation	(11), (17)
CS	Cable equation, solution given by a Sum	(11), (27)
EMI	Extracellular Membrane Intracellular	(28)–(34)

Table 1: Definition of the methods used to compute the extracellular potential.

normal derivative in the x-direction and one from the normal derivative in the y-direction. Furthermore, we let the sum of the two intracellular fluxes equal the sum of the two extracellular fluxes in the flux-equality (31) and let $I_{\mathrm{m}}^{n,j,k}$ in (36) be the mean of the two intracellular fluxes. In the 3D extension we similarly define three extracellular and three intracellular flux terms for the corner nodes where three membrane planes intersect, and two extracellular and two intracellular flux terms for the edge nodes where two membrane planes intersect.

In the case of simple, rectangular geometries, this numerical strategy is straightforward. However, for more complex geometries, finite element or finite volume methods should be used.

3 Results

In this section we will report results using the methods described above. We will start the section by investigating the error in the membrane potential introduced by ignoring the ephaptic current (12).

Secondly, we will compare the extracellular potential computed by the CBV, CP and CS methods with the solution of the EMI model. Clearly, there are a set of different assumptions underlying these methods: The CS method is unique in assuming the extracellular domain to be infinite. In order to be able to compare the results of the CS method with the other methods, we have used large extracellular domains. In order to estimate how large the domain must be, we have systematically increased the size of the extracellular space until convergence of the EMI solutions and then used the largest domain for our comparisons.

For the CS method the transmembrane currents are gathered in the center of each compartment thus giving rise to the classical formula of the solution, whereas for the CP method the transmembrane currents are distributed over each compartment, and numerical methods are used to compute the solution of the associated Poisson equation. In contrast, in the CBV and EMI methods the transmembrane currents setting up the extracellular potentials are placed at the interface between the intracellular and extracellular domains. The CBV and EMI methods are thus defined on the same domain, and the only difference lies in the proper self-consistent modeling of ephaptic effects in the EMI method.

For convenience, the abbreviations (CBV, CP, CS and EMI) and references to the methods are summarized in Table 1.

Parameter	Value	Parameter	Value
L_x	60 μm	g_L	$6 \cdot 10^{-7}$ μS/μm^2
L_y	20 μm	g_{syn}	$1.25 \cdot 10^{-3}$ μS/μm^2
L_z	20 μm	v_{rest}	-90 mV
l_x	50 μm	v_{eq}	0 mV
h, l_y, l_z	6 μm	t_0	0 ms
Δx, Δy, Δz	0.5 μm	α	2 ms
Δt	0.02 ms	σ_{i}	0.7 μS/μm
C_{m}	$2 \cdot 10^{-5}$ nF/μm^2	σ_{e}	0.3 μS/μm

Table 2: Parameters used in the computations of the Cable equation and the EMI model.

3.1 Model parameters

We consider the Cable equation and the EMI model using the parameters given in Table 2 (unless otherwise stated). The domain $\Omega = \Omega_{\text{i}} \cup \Omega_{\text{e}}$ is defined as

$$\Omega = [0, L_x] \times [0, L_y] \times [0, L_z], \tag{37}$$

and the intracellular domain, Ω_{i}, is shaped as a rectangular cuboid of size $l_x \times l_y \times l_z$ located in the center of Ω. The ionic current density I_{ion} is defined as

$$I_{\text{ion}} = I_{\text{leak}} + I_{\text{syn}}, \tag{38}$$

where I_{leak} is the leak current density given by

$$I_{\text{leak}} = g_L(v - v_{\text{rest}}), \tag{39}$$

and I_{syn} is the conductance-based synaptic current density with single-exponential dynamics (see [31]) given by

$$I_{\text{syn}} = g_s(x) e^{-\frac{t-t_0}{\alpha}} (v - v_{\text{eq}}). \tag{40}$$

For the first 10 % of the cell in the x-direction, $g_s(x)$ is given by the value g_{syn} in Table 2. On the remaining part of the membrane $g_s(x)$ is set to zero.

We use the initial condition $v = v_{\text{rest}} = -90$ mV for the membrane potential. In addition, we apply the boundary condition $\frac{\partial v}{\partial x} = 0$ at the start and the end of the cell in the Cable equation and the boundary condition $u_{\text{e}} = 0$ on the outer boundary of Ω_{e} in the EMI, CBV and CP methods unless otherwise stated.

3.2 Numerical assessment of the error in membrane potential introduced by ignoring the ephaptic current

In Figure 4 we show the membrane potential computed by solving the Cable equation and the EMI model for different values of h, σ_{i}, σ_{e} and g_L. The solutions

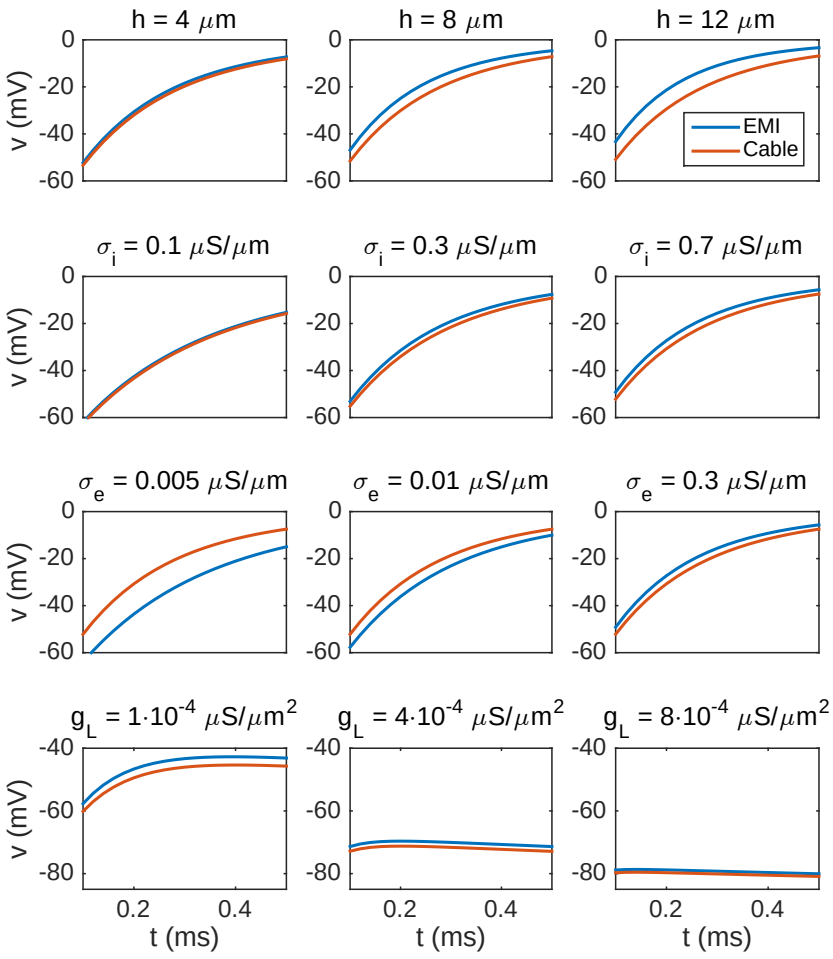

Figure 4: Comparison of the membrane potential computed by solving the Cable equation (red) and the EMI model (blue) for some different values of h, σ_{i}, σ_{e} and g_L, where we recall that $h = l_y = l_z$ (the width of the neuron). The plots show how the membrane potential in the compartment 25 μm from the start of the cell changes with time from t = 0.1 ms to t = 0.5 ms. The parameters used in the computations are given in Table 2 except for the values given above each plot. We observe that the difference between the two solutions increases when the value of h or σ_{i} is increased, and the difference decreases when the value of σ_{e} or g_L is increased. Note that in order to observe any effect of changing the value of g_L, we increase the default value by a factor of order 100–1000 in the lower panel of the figure.

σ_{e} (μS/μm)	$I_{\mathrm{eph}}^{\mathrm{max}}$ (nA/μm^2)	$\sigma_{\mathrm{e}} \cdot I_{\mathrm{eph}}^{\mathrm{max}}$ (nAμS/μm^3)
0.1	0.616	0.0616
0.3	0.208	0.0623
0.6	0.104	0.0625
1.5	0.042	0.0626
3.0	0.021	0.0627

Table 3: Maximum absolute values of I_{eph} from time t = 0.02 ms to t = 1 ms as a function of σ_{e} as computed by the EMI method. We observe that $\sigma_{\mathrm{e}} \cdot I_{\mathrm{eph}}^{\mathrm{max}}$ is close to constant for the different values of σ_{e}. The parameters used in the computations are given in Table 2.

are compared in the compartment 25 μm from the start of the cell (i.e. in the center of the cell in the x-direction). The difference is several millivolts, but it is reduced as the intracellular conductivity σ_{i} is reduced or the size h (recall that $h = l_y = l_z$) of the neuron is reduced. Furthermore, we observe that the difference is reduced as the extracellular conductivity, σ_{e}, or g_L is increased. These observations are consistent with our theoretical finding in an appendix given below where we show that, under reasonable assumptions, the error introduced in the transmembrane potential by removing the ephaptic current goes like

$$O\left(\frac{h\sigma_{\mathrm{i}}}{g_L\sigma_{\mathrm{e}}}\right). \tag{41}$$

To summarize, the error increases when h or σ_{i} are increased, and the error decreases if g_L or σ_{e} are increased.

3.3 The magnitude of the ephaptic current decreases as the extracellular conductivity is increased

As mentioned above, the derivation of the Cable equation relies on the assumption that the extracellular potential is constant, and under that assumption, the ephaptic current defined by (12) can be ignored. This can also be understood on biophysical grounds as a high extracellular conductivity implies a low extracellular resistance so that potential drops due to extracellular currents driven through the extracellular medium will be small. In the limit of very large extracellular conductivities these potential drops will become negligible, i.e., the assumption of constant extracellular potentials in the standard Cable equation will become fulfilled.

In Table 3 the maximum magnitude (absolute value) of the ephaptic current (computed by solving the EMI model) is given as a function of the extracellular conductivity σ_{e}, and we note that the magnitude decreases as σ_{e} is increased. In addition, we report the value of the maximum ephaptic current multiplied by the

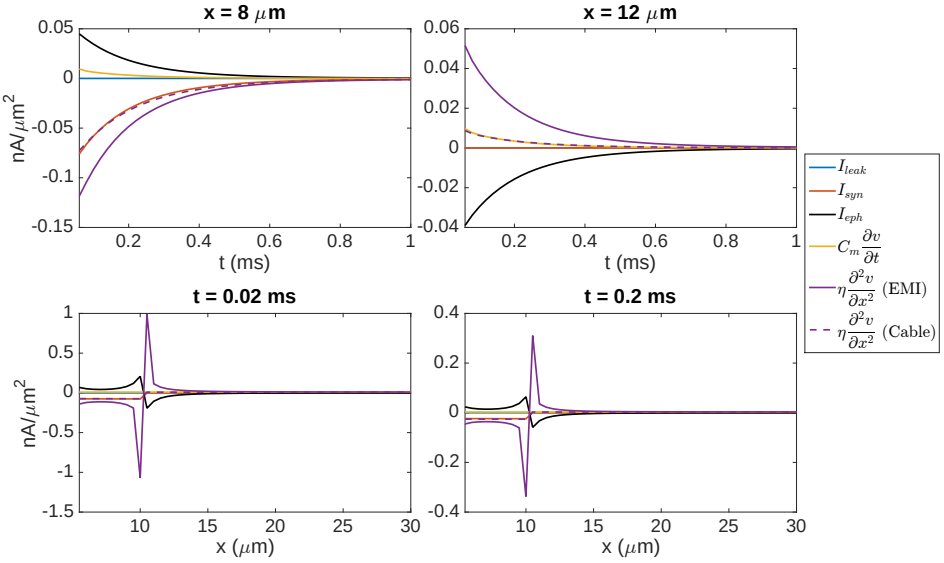

Figure 5: Values of each of the terms in Equation (9). In the upper panel, we show the time evolution of the terms in the point (8 μm, 10 μm, 7 μm) inside the synaptic input zone and the point (12 μm, 10 μm, 7 μm) outside the synaptic input zone. In the lower panel, we show the values of the terms for $y = 10$ μm, $z = 7$ μm and $x \in [5\ \mu\text{m}, 30\ \mu\text{m}]$ at time $t = 0.02$ ms (left) and $t = 0.2$ ms (right). The solution of the EMI model is used to compute each of the terms. In addition, we show $\eta \frac{\partial^2 v}{\partial x^2}$ for the corresponding solution of the Cable equation, where I_{eph} is assumed to be zero. We observe that the size of I_{eph} is comparable to the size of the other terms in (9) and that neglecting I_{eph} leads to a considerable difference in the value of the term $\eta \frac{\partial^2 v}{\partial x^2}$. The parameters used in the computations are given in Table 2.

value of σ_{e} and observe that this value is close to a constant, so we have

$$I_{\text{eph}} \sim O\left(1/\sigma_{\text{e}}\right). \tag{42}$$

Therefore, for very large values of σ_{e}, the ephaptic current can be ignored, but the reported values of σ_{e} are in general not so large that this assumption can be generally trusted.

It is also interesting to compare the size of the ephaptic current with the size of the other currents involved in the dynamics of the model neuron. Figure 5 shows the time evolution of each of the terms in Equation (9) and we observe that the size of the ephaptic current is comparable to the size of the other terms in the equation. The peak of the ephaptic current is located at the jump in the synaptic input.

3.4 Comparing the extracellular potential computed by the CBV, CP, CS and EMI methods

In this section we will compare the extracellular potentials (EPs) computed by the EMI, CBV, CP and CS methods described above (see Table 1 for definitions of the abbreviations). When comparing the predicted extracellular potentials for the various methods, observed differences will expectedly have different model origins. For the EMI and CBV methods the key physical difference is in the lack of inclusion of ephaptic effects in the CBV method. Compared to EMI and CBV where the transmembrane currents setting up the EP are at the true membrane interface between the intracellular and extracellular domains, the CP and CS methods assume that the EP-generating currents are defined as the right-hand side of the Poisson equation (17). For the CS method the current source density is gathered in a single point in the center of the neuronal compartment, whereas for the CP method the current density is evenly distributed over the entire compartment (See Figure 1).

3.4.1 Convergence under mesh refinements

In Figure 6 we show the extracellular potential computed by the EMI method for four different values of the discretization parameter $\Delta x = \Delta y = \Delta z$. The solutions for the 0.5 μm resolution and the 0.25 μm resolution appear to be similar and we use a spatial discretization of $\Delta x = \Delta y = \Delta z = 0.5$ μm for the rest of our computations.

To reduce the computational cost in this case, we consider the stationary version of the model, i.e. we set the time derivative in (34) to zero. We use the parameter values given in Table 2, except for an increased value of $g_L = 3 \cdot 10^{-5}$ $\mu\text{S}/\mu\text{m}^2$ and a domain of size 60 μm $\times$ 60 μm $\times$ 60 μm. We again let $g_s(x)$ be g_{syn} for the first 10 % of the cell in the x-direction and zero elsewhere and apply the boundary condition $u_{\text{e}} = 0$ on the outer boundary of the extracellular domain.

3.4.2 Convergence of the EMI solution as the domain size is increased

In the derivation of the CS method, the extracellular domain is assumed to be infinite (see Section 2.1.5). When comparing CS and EMI results, we therefore wish to compare the solution of the CS method to the solution of the EMI model as the size of the extracellular domain approaches infinity.

We again consider the stationary version of the model with the parameter values given in Table 2, except for an increased value of $g_L = 3 \cdot 10^{-5}$ $\mu\text{S}/\mu\text{m}^2$ and an increased domain size.

Figure 7 shows the stationary solution of the EMI model for four different sizes of the extracellular domain. We observe that as the size of the extracellular domain increases, the solution of the EMI model appears to converge, and we assume that the solution for a domain of size 120 μm $\times$ 120 μm $\times$ 120 μm is sufficiently large to represent the EMI solution of an infinite domain.

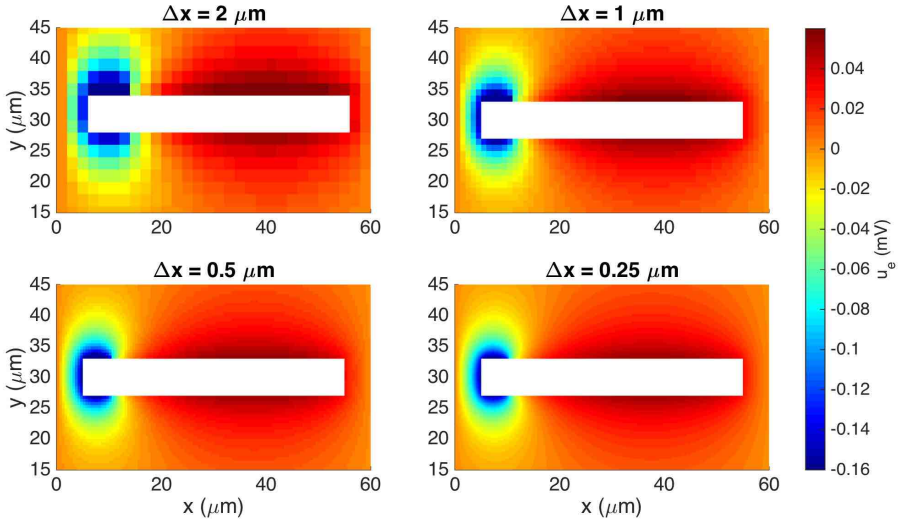

Figure 6: Extracellular potential computed by the stationary EMI model for four different values of $\Delta x = \Delta y = \Delta z$. We show the solution in a rectangle of size 60 μm $\times$ 30 μm on the plane in the center of the domain in the z-direction. The white area represents the cell. We use the parameters given in Table 2 except for an increased value of $g_L = 3 \cdot 10^{-5}$ μS/μm^2 and a domain of size 60 μm $\times$ 60 μm $\times$ 60 μm.

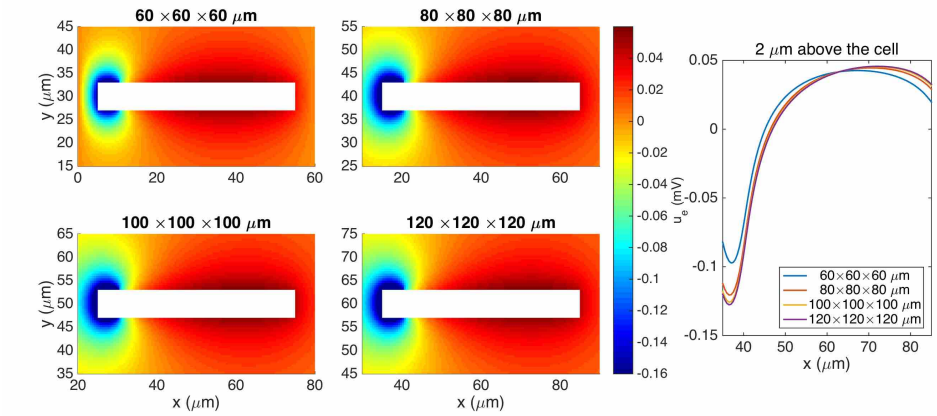

Figure 7: Comparison of the extracellular potential around a neuron computed by the stationary EMI model for four different sizes of the extracellular domain. The plots to the left show the solution in a rectangle of size 60 μm $\times$ 30 μm on the plane in the center of the domain in the z-direction. The white area represents the neuron. The plot to the right shows the extracellular potential along a line 2 μm above the neuron in the y-direction and in the center of the domain in the z-direction. The parameters used in the computations are given in Table 2 except for L_x, L_y and L_z, which are specified for each simulation, and g_L, which is set to $3 \cdot 10^{-5}$ μS/μm^2.

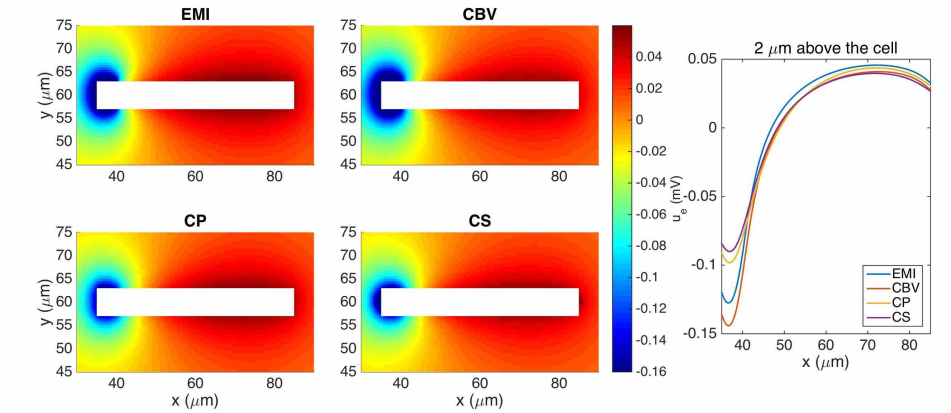

Figure 8: The extracellular potential around a neuron shaped as a rectangular cuboid computed by the stationary versions of the EMI, CBV, CP and CS methods. The plots to the left show the solution in a rectangle of size 60 μm $\times$ 30 μm on the plane in the center of the domain in the z-direction. The white area represents the neuron. The plot to the right shows the extracellular potential along a line 2 μm above the neuron in the y-direction and in the center of the domain in the z-direction. We use the parameters specified in Table 2 except for $L_x = L_y = L_z = 120$ μm and $g_L = 3 \cdot 10^{-5}$ μS/μm^2. The abbreviations (EMI, CBV, CP and CS) are summarized in Table 1.

3.4.3 One single simplified neuron

Our first test case for comparing the methods for computing the extracellular potential is a single neuron of the form given above. The extracellular potential computed by the CBV, CP, CS and EMI methods are presented in Figure 8 (see Table 1 for definitions of the abbreviations). In Table 4 we report the maximum difference between the extracellular potential computed by the EMI model and the extracellular potential computed by each of the other methods. The deviation of the CBV result from the EMI result is smaller than the difference to the CP and CS results. Thus the largest differences appear to come from the different assumptions of placement of the transmembrane currents in the EP-generating step (compare CBV vs. CP and CS). The effect of the ephaptic current (CBV vs. EMI) is smaller.

3.4.4 Two simplified neurons

In Figure 9 we show the extracellular potential around two neurons of the form given above computed by the CBV, CP, CS and EMI methods. In the upper part of the figure the neurons are separated by a distance of 10 μm in the y-direction and in the lower part the neurons are separated by a distance of 4 μm. In Table 5 we report the maximum difference between the extracellular potential computed

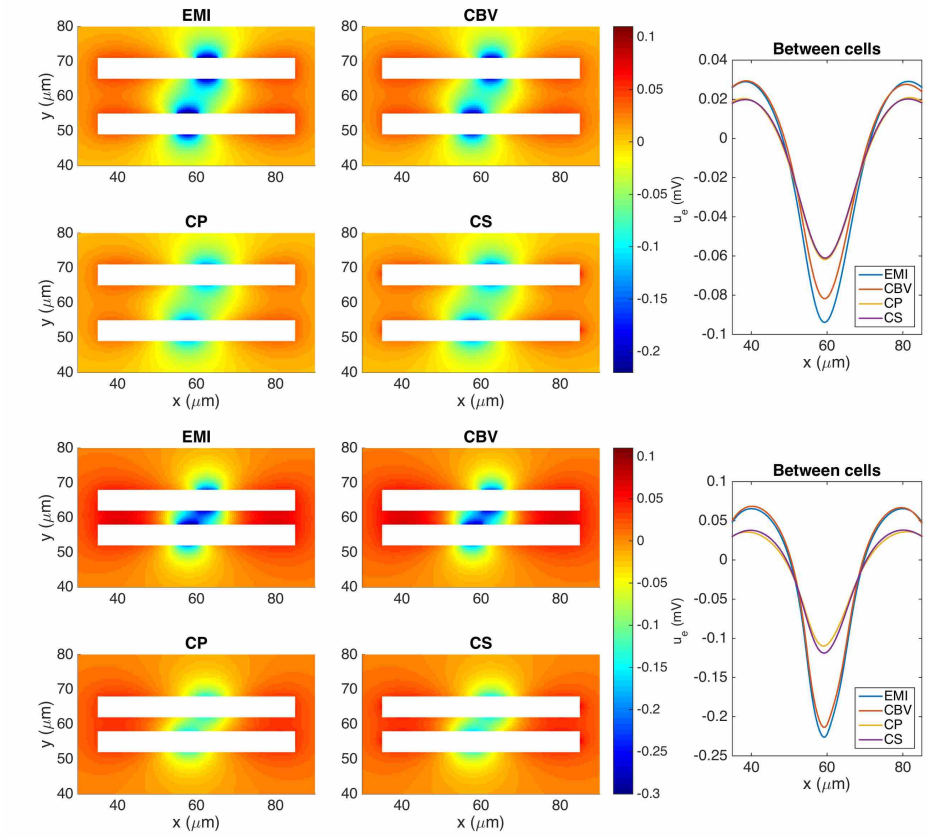

Figure 9: The extracellular potential around two neurons computed by the stationary versions of the EMI, CBV, CP and CS methods. The plots to the left show the solution in a rectangle of size 60 μm $\times$ 40 μm on the plane in the center of the domain in the z-direction. The white areas represent the neurons. The plots to the right show the extracellular potential along the line in the center of the space between the two neurons. In the upper five plots, the neurons are separated by a distance of 10 μm in the y-direction, and in the lower five plots the neurons are separated by a distance of 4 μm. In all plots $g_s(x)$ is given by g_{syn} for $x \in [55$ μm, 60 μm] and is zero on the rest of the membrane for the lower neuron. For the upper neuron $g_s(x)$ is given by g_{syn} for $x \in [60$ μm, 65 μm]. We use the parameters specified in Table 2 except for $L_x = L_y = L_z = 120$ μm and $g_L = 3 \cdot 10^{-5}$ μS/μm^2. The abbreviations (EMI, CBV, CP and CS) are summarized in Table 1.

Method	Maximum difference (mV)	Relative maximum difference
CBV	0.024	11.3 %
CP	0.058	27.7 %
CS	0.113	53.7 %

Table 4: Maximum difference between the solution for the extracellular potential in $\Omega_e \setminus \Gamma$ computed by the EMI method and each of the other methods for the test case in Figure 8. The relative maximum differences are computed as the maximum difference divided by the maximum absolute value of the extracellular potential computed by the EMI method. The abbreviations (EMI, CBV, CP and CS) are summarized in Table 1.

by the EMI method and each of the other methods for the two test cases.

As for the case with a single simplified neuron above, the deviation of the CBV result from the EMI result is seen to be smaller than the difference to the CP and CS results. Interestingly, in the lower part of Figure 9 where the distance between the two neurons is very small (4 μm), the EMI and CBV results are essentially identical in the space between the cells.

3.4.5 Confined extracellular space

Figure 10 shows the extracellular potential around a neuron in a domain of size 60 μm$\times$20 μm$\times$20 μm computed by the EMI, CBV, CP and CS methods. The left panel shows the solution for a homogeneous Dirichlet boundary condition, and the right panel shows the solution for a homogeneous Neumann boundary condition on the outer boundary of the extracellular space.

As explained above, the CS method is founded on the assumption of an infinite extracellular space. We have therefore focused on a very large computational domain mimicking the properties of an infinite domain. Certainly, also limited domains are of interests and simulation results are given in Figure 10 using both Dirichlet and Neumann type boundary conditions. Although we present results for all four models, it is important to keep in mind that a confined domain breaks a basic assumption underlying the CS method and consequently we get very large errors, especially in the case of Neumann type boundary conditions.

Note that in the case of Neumann boundary conditions, the solution is not uniquely determined by the systems defining the EMI, CBV and CP methods, and we expand the systems with the additional constraint

$$\int_{\Omega_e} u_e \, dV = 0 \tag{43}$$

in order to obtain unique solutions of the methods.

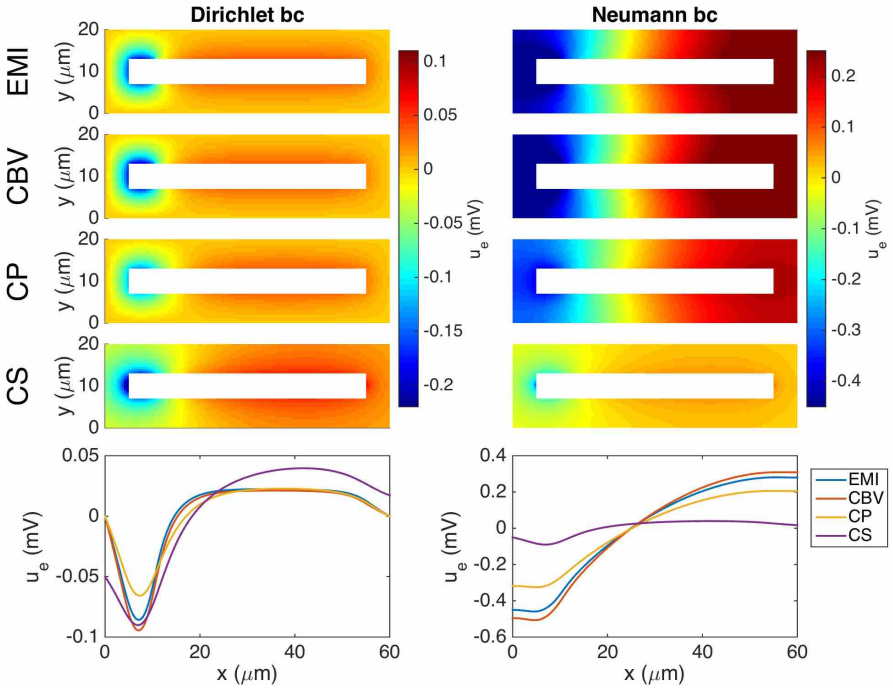

Figure 10: Extracellular potential around a neuron computed by the EMI, CBV, CP and CS methods. We consider the stationary version of the models and the parameter values given in Table 2 except for an increased value of $g_L = 3{\cdot}10^{-5}$ μm. A Dirichlet boundary condition, $u_\mathrm{e} = 0$, is applied in the simulation in the left panel and a Neumann boundary condition, $\frac{\partial u_\mathrm{e}}{\partial n_\mathrm{e}} = 0$, is applied in the right panel. The upper panels show the extracellular potential in the plane in the center of the domain in the z-direction for each of the methods. The lower panel shows the solution along a line 2 μm above the cell in the y-direction and in the center of the domain in the z-direction. Note that in the case of Neumann boundary conditions, we include the additional constraint $\int_{\Omega_\mathrm{e}} u_\mathrm{e}\, dV = 0$ for the EMI, CBV and CP methods in order to obtain unique solutions. The abbreviations (EMI, CBV, CP and CS) are summarized in Table 1.

Method	Maximum difference (mV)	Relative maximum difference
CBV	0.025	12.6 %
CP	0.087	43.2 %
CS	0.086	42.4 %

(a) Neurons separated by 10 μm.

Method	Maximum difference (mV)	Relative maximum difference
CBV	0.014	5.2 %
CP	0.141	52.9 %
CS	0.128	48.3 %

(b) Neurons separated by 4 μm.

Table 5: Maximum difference between the solution for the extracellular potential in $\Omega_e \setminus \Gamma$ computed by the EMI method and each of the other methods for the test cases in Figure 9. The relative maximum differences are computed as the maximum difference divided by the maximum absolute value of the extracellular potential computed by the EMI method. The abbreviations (EMI, CBV, CP and CS) are summarized in Table 1.

3.4.6 Effects of the size of the synaptic input area

In Figure 11 we show the extracellular potential surrounding a neuron for four different sizes of the synaptic input area. The upper panel shows the extracellular potential computed by the EMI method, and the lower panel shows a comparison of the extracellular potentials computed by each of the methods along a line above the neuron. We note from the simulations that the results are qualitatively similar for all different sizes of the synaptic input region. Therefore, we choose to focus on the 10 % synaptic input region as the base case for our simulations.

3.4.7 Simulation time

Table 6 shows the CPU time for the simulations shown in the left panel of Figure 10 using a direct and an iterative solver.

The EMI model is clearly much more computationally expensive than the classical CS method. This is expected because the EMI model involves solving a large coupled system of equations, whereas the CS method only requires solving the Cable equation which involves a much smaller number of unknowns. After solving the Cable equation, the CS methods assumes that the extracellular potential may be found directly by the explicit formula (27), so no further equations has to be solved.

Moreover, in the computations reported in the table, the extracellular potential is computed for all nodes in the mesh. In the CS method this is not necessary, and the CPU time for the CS method could possibly be further reduced by only computing the values for the points of interest. This is not possible for the EMI

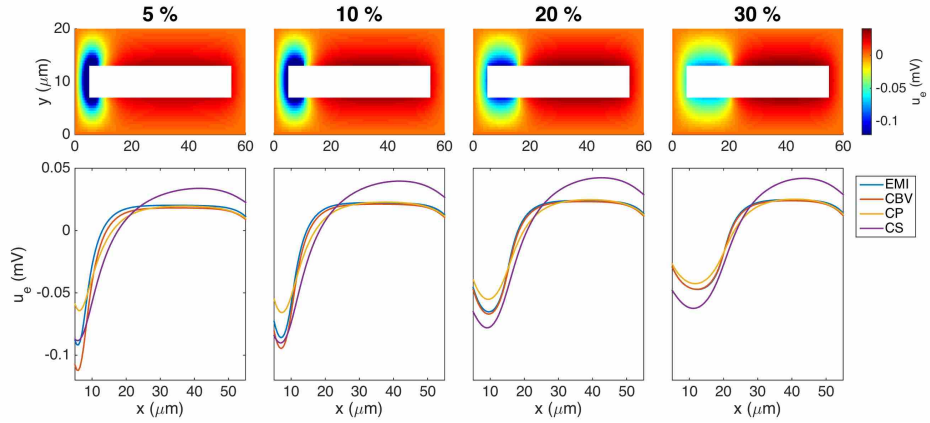

Figure 11: Extracellular potential around a neuron with a synaptic input area of length 5 %, 10 %, 20 % and 30 % of the total cell length. The upper panel shows the extracellular potential computed by the EMI method in the plane in the center of the domain in the z-direction. The lower panel shows the solution for each of the methods along a line 2 μm above the cell in the y-direction and in the center of the domain in the z-direction. The figure shows the solution of the stationary version of the models using the parameter values given in Table 2 except for an increased value of $g_L = 3 \cdot 10^{-5}$ μm. We apply a homogeneous Dirichlet boundary condition on the outer boundary of the extracellular domain. The abbreviations (EMI, CBV, CP and CS) are summarized in Table 1.

	System size	CPU time (s) Direct solver	CPU time (s) Iterative solver
EMI	208 491	34.9	15.5
CBV	101 + 191 422	29.6	1.9
CP	101 + 203 401	35.2	3.3
CS	101 + 0	1.0	1.0

Table 6: CPU time in seconds for the EMI, CBV, CP and CS methods. In the third column the linear systems of the EMI, CBV and CP methods are solved using direct Gaussian elimination, and in the fourth column the linear systems are solved using the bistable conjugate gradient stabilized method with an incomplete LU preconditioner and a relative tolerance of 10^{-5}. The second column reports the number of unknowns in the linear systems to be solved in each of the methods. In the EMI model, we solve a coupled system for the extracellular, membrane and intracellular potentials simultaneously. In the CBV, CP and CS methods, on the other hand, we first find the membrane potential by solving the Cable equation consisting of 101 compartments. Then, we find the extracellular potential by solving an equation for each node in the extracellular or entire domain, for the CP and CBV methods, respectively. In the CS method, the extracellular potential is given directly from the solution of the Cable equation by an explicit formula. The parameters used in the simulation are given in Table 2 except for an increased value of $g_L = 3 \cdot 10^{-5}$ μm. The table reports the solution time for the stationary versions of the models with homogeneous Dirichlet boundary conditions.

method (or the CBV or CP methods) because the systems of equations has to be solved for all nodes in order to find the solution in a single point.

In contrast, the simulation time for the CBV and CP methods are more comparable to that of the EMI model, at least for the direct solver. This is because these methods also rely on solving a linear system of equations for all nodes in the extracellular domain or the entire domain for the CVB and CP methods, respectively.

The extra complexity introduced in the EMI model by solving for the membrane, intracellular and extracellular potentials simultaneously is apparent, however, when an iterative method is applied to solve the linear system. The fourth column of Table 6 shows the solution time for each of the methods using the bistable conjugate gradient stabilized method with an incomplete LU preconditioner. In this case, the CBV and CP methods are much faster than the EMI method.

4 Discussion

In the present paper we have compared four different methods for computing neural dynamics. In the numerically comprehensive EMI model the intracellular and extracellular dynamics are solved self-consistently and the membrane potentials and extracellular potential are computed simultaneously. For the other methods (CBV, CP, CS; see Table 1 for definitions of abbreviations) the membrane potential is first computed using the Cable equation, and the resulting transmembrane currents are used in a second step to compute the extracellular potential.

In the CBV method the transmembrane currents are placed on the interface between the intracellular and extracellular domains, and the only difference with the EMI model is the lack of self-consistency in the two-step computational scheme inherent in the CBV scheme, that is, the transmembrane currents are first computed using the Cable equation assuming a constant extracellular potential, while a non-constant potential (both in space and time) is computed in the second step.

For the CP and CS methods an additional assumption is made in the second step, namely that the effect of the transmembrane currents are assumed to be represented in terms of currents source densities. Specifically, for the CP method, the current source density is distributed evenly over a neuronal compartment and a numerical scheme is used to solve the resulting Poisson equation (17), and for the CS method the source density is concentrated in a single point and thus the classical sum formula (27) of the solution can be applied.

4.1 Ignoring the ephaptic current

4.1.1 Error in membrane potential introduced by ignoring the ephaptic current

To study the error introduced by ignoring the ephaptic current in the Cable equation, we compared the membrane potential computed by solving the Cable equation to the corresponding solution of the EMI model. In our simple test case, we found that the membrane potential computed by the Cable equation could differ several millivolts from the solution of the EMI model and that the magnitude of the error seems to decrease with the value of the intracellular conductivity, σ_{i}, and the cell width, h. This suggests that the Cable equation is applicable for computing the membrane potential for sufficiently thin dendrites.

4.1.2 Ephaptic current decreases with increasing extracellular conductivity

In the derivation of the Cable equation, it is assumed that the extracellular conductivity σ_{e} is so large that the extracellular potential varies very little in space and can be assumed to be a constant. As a result, the ephaptic current I_{eph} will be zero and may be removed from the model. In our numerical simulations of the EMI model, we confirmed that the size of I_{eph} decreases when the value of σ_{e} is increased (see Table 3). In fact, we found that the maximum absolute value of

I_{eph} appeared to be inversely proportional to the value of σ_{e}. However, we also observed that the magnitude of I_{eph} was similar in size to the other currents involved in the model (see Figure 5). This suggests that I_{eph} is not negligible for the stylized neuron geometries and model parameters chosen here.

4.2 Error in neglecting ephaptic currents

The CBV and EMI methods are defined on identical domains, and the key physical difference between the methods is the absence of ephaptic effects in the CBV method. Comparisons of computed extracellular potentials indeed show such ephaptic effects of varying magnitudes, both for the extracellular potential outside a single activated neuron (Figure 8) and between two activated neurons (Figure 9).

4.3 Effects of position of transmembrane currents

To explore the effects of assumed positions of transmembrane currents, it is easiest to compare results from the three methods, i.e., CBV, CP and CS, where the transmembrane currents in all cases are found from the Cable equation. Here effects from the ephaptic current are in all cases absent. For the present examples we observe that CS and CP results are typically quite similar, but both quite different from the CBV results (Figures 8 and 9). From the point-source formula in (27) we see that the contribution to the extracellular potential from a point current source is inversely proportional to distance, and it is thus not surprising that this difference in assumed source positions has a sizeable effect on the predicted extracellular potentials.

4.4 Effects of size of extracellular domain

Both in the CP and CBV methods (as well as in the EMI model) the extracellular domain is finite, while in the CS method the extracellular domain is infinite so that the solution of the Poisson equation can be given as an explicit sum. With a very small extracellular domain, corresponding to a small piece of brain tissue embedded in an insulator, large deviations from the infinite-domain results will be observed (Figure 7; see also Figure 10).

In order to compare results with the CS method, we here computed the EMI solution for gradually larger domains until the solutions appeared to converge. Further, we regarded the converged solution as the solution of the EMI problem for an infinite extracellular space, i.e., we estimated that the difference of the results for the largest considered domain and a (hypothetical) infinite domain was negligible for the present purposes. Roughly speaking, convergence was obtained for an extracellular space extending twice the length of the cable in every direction.

4.5 The simplified geometry

Today, simulations of neurons typically use much more complex and realistic geometries than what has been applied here. Already in 1968, Clark and Plonsey

[32] were able to analytically evaluate the extracellular potential of a cylindrical neuron, and it is certainly of interest to evaluate the models and methods discussed here in more realistic geometries. The generic limitation of the finite difference method used here is that it is hard to apply, correctly, to non-rectangular geometries. In [21], the finite element method is used and this gives much more freedom to represent realistic geometries. However, the code used in [21] required extremely fine times steps and we therefore focused on simplified geometries where the problem could be solved using a reasonable number of time steps. The solution of the EMI model using an implicit formulation will likely reduce the time step restrictions and this is subject for ongoing investigations.

Another limitation in the present study is the size of the extracellular space. This space is actually quite limited (see e.g. [33]), but the assumption of an infinite extracellular space is necessary for the application of the classical CS method (summation method), and thus we have used very large extracellular domains in order to provide fair comparisons with the classical model at the cost of simulating more realistic volumes.

4.6 Neural tissue

The EMI model provides a useful framework for accurate computations of the electrophysiology of a small number of cells and their surroundings. It is, however, very hard to apply this methodology to neural tissue consisting of huge numbers of cells. In simulations of cardiac tissue, the Bidomain approach has successfully been applied to simulate the electrophysiology, see e.g. [34, 35, 36, 37, 38]. Recently, a similar approach has been applied to neural tissue, see [39, 40]. Most likely, some form of homogenization process is needed to derive tractable mathematical models for neural tissue.

4.7 Possible additive effects for non-linear membrane dynamics

We have focused on a linear membrane model in order to highlight the effect of removing the ephaptic current in the simplest possible case. More generally, the question is whether *ephaptic coupling would constitute a 'feedback' mechanism with electric fields altering the activity of the same neural elements that gave rise to them in the first place,* see [13]. For a linear model, this feedback mechanism was recently found to be the *small but not negligible*, see [11], which clearly is consistent with our findings. However, the effect may very well be larger for non-linear models of the membrane dynamics; small electric fields can be amplified by non-linear effects, see [41]. At present, we have not conducted systematic simulations using a non-linear membrane model.

4.8 Other assumptions

We note also that the current study was limited to standard simulation frameworks in neuroscience, where intra- and extracellular currents are assumed to be purely Ohmic, so that equations (28) and (29) apply in the bulk solutions. That is, we did not include possible contributions from advective currents, displacement currents and ionic diffusion currents. These currents are typically neglected, as they are believed to play negligible roles for the system electrodynamics under most biophysically relevant conditions. However, computational studies have indicated that at least ionic diffusion could, in some scenarios, influence electrical potentials (see e.g., [42, 43, 44, 45, 46, 47]). These effects were not accounted for in the current study. We also confined our simulations to linear, passive membranes even if it known that active voltage-gated channels affect the extracellular potential; see e.g. [48].

5 Conclusion

We have compared various methods for computing membrane potentials and extracellular potentials. For the simple test cases considered here, non-negligible errors were observed when neglecting ephaptic effects, i.e., when comparing results from the EMI model with the CBV model building on results from the Cable equation. Further, substantial differences in the predicted extracellular potentials were observed depending on whether transmembrane current sources were assumed to be placed in the center of the neural compartment or at the membrane interfaces. This study motivates further analysis of the errors for computations based on more realistic representations of the geometry and dynamics of the neurons using the EMI model.

References

[1] Henry Markram, Eilif Muller, Srikanth Ramaswamy, Michael W Reimann, Marwan Abdellah, Carlos Aguado Sanchez, Anastasia Ailamaki, Lidia Alonso-Nanclares, Nicolas Antille, Selim Arsever, et al. Reconstruction and simulation of neocortical microcircuitry. *Cell*, 163(2):456–492, 2015.

[2] Christof Koch and Michael A Buice. A biological imitation game. *Cell*, 163(2):277–280, 2015.

[3] David Sterratt, Bruce Graham, Andrew Gillies, and David Willshaw. *Principles of computational modelling in neuroscience*. Cambridge U. Press, 2011.

[4] G Bard Ermentrout and David H Terman. *Mathematical foundations of neuroscience*, volume 35. Springer Science & Business Media, 2010.

[5] Alwyn Scott. *Neuroscience: A mathematical primer*. Springer Science & Business Media, 2002.

[6] Peter Dayan and Laurence F Abbott. *Theoretical neuroscience*. MIT Press, 2001.

[7] Christof Koch. *Biophysics of Computation*. Oxford University Press, 1999.

[8] Gary R Holt and Christof Koch. Electrical interactions via the extracellular potential near cell bodies. *Journal of Computational Neuroscience*, 6(2):169–184, 1999.

[9] György Buzsáki, Costas A Anastassiou, and Christof Koch. The origin of extracellular fields and currents – EEG, ECoG, LFP and spikes. *Nature Reviews Neuroscience*, 13(6):407–420, 2012.

[10] Upinder S Bhalla. Multi-compartmental models of neurons. In *Computational Systems Neurobiology*, pages 193–225. Springer, 2012.

[11] Joshua H Goldwyn and John Rinzel. Neuronal coupling by endogenous electric fields: cable theory and applications to coincidence detector neurons in the auditory brain stem. *Journal of Neurophysiology*, 115(4):2033–2051, 2016.

[12] Costas A Anastassiou, Rodrigo Perin, Henry Markram, and Christof Koch. Ephaptic coupling of cortical neurons. *Nature Neuroscience*, 14(2):217–223, 2011.

[13] Costas A Anastassiou and Christof Koch. Ephaptic coupling to endogenous electric field activity: why bother? *Current opinion in neurobiology*, 31:95–103, 2015.

[14] Hemant Bokil, Nora Laaris, Karen Blinder, Mathew Ennis, and Asaf Keller. Ephaptic interactions in the mammalian olfactory system. *J Neurosci*, 21:1–5, 2001.

[15] Bernhard Katz and Otto H Schmitt. Electric interaction between two adjacent nerve fibres. *The Journal of physiology*, 97(4):471, 1940.

[16] Mikhail N Shneider and Mikhail Pekker. Correlation of action potentials in adjacent neurons. *Physical biology*, 12(6):066009, 2015.

[17] A Arvanitaki. Effects evoked in an axon by the activity of a contiguous one. *Journal of Neurophysiology*, 5(2):89–108, 1942.

[18] Wanda Krassowska and John C Neu. Response of a single cell to an external electric field. *Biophysical Journal*, 66(6):1768, 1994.

[19] Wenjun Ying and Craig S Henriquez. Hybrid finite element method for describing the electrical response of biological cells to applied fields. *IEEE Transactions on Biomedical Engineering*, 54(4):611–620, 2007.

[20] Fernando Henríquez, Carlos Jerez-Hanckes, and MD Fernando R Altermatt. Dynamic finite-element model of axon extracellular stimulation. In *2013 6th International IEEE/EMBS Conference on Neural Engineering (NER)*, pages 589–592. IEEE, 2013.

[21] Andres Agudelo-Toro and Andreas Neef. Computationally efficient simulation of electrical activity at cell membranes interacting with self-generated and externally imposed electric fields. *Journal of Neural Engineering*, 10(2):026019, 2013.

[22] Andres Agudelo-Toro. *Numerical Simulations on the Biophysical Foundations of the Neuronal Extracellular Space*. PhD thesis, Niedersächsische Staats-und Universitätsbibliothek Göttingen, 2012.

[23] Wilfrid Rall. Electrophysiology of a dendritic neuron model. *Biophysical Journal*, 2(2):145–167, 1962.

[24] Wilfrid Rall. Time constants and electrotonic length of membrane cylinders and neurons. *Biophysical Journal*, 9(12):1483–1508, 1969.

[25] Maurice Klee and Wilfrid Rall. Computed potentials of cortically arranged populations of neurons. *Journal of Neurophysiology*, 40(3):647–666, 1977.

[26] Gaute T Einevoll, Christoph Kayser, Nikos K Logothetis, and Stefano Panzeri. Modelling and analysis of local field potentials for studying the function of cortical circuits. *Nature Reviews Neuroscience*, 14(11):770–785, 2013.

[27] Henrik Lindén, Espen Hagen, Szymon Leski, Eivind S Norheim, Klas H Pettersen, and Gaute T Einevoll. LFPy: A tool for biophysical simulation of extracellular potentials generated by detailed model neurons. *Frontiers in Neuroinformatics*, 7(41), 2014.

[28] Christian Grossmann, Hans-Görg Roos, and Martin Stynes. *Numerical treatment of partial differential equations*. Springer, 2007.

[29] Gary R Holt. *A critical reexamination of some assumptions and implications of cable theory in neurobiology*. PhD thesis, California Institute of Technology, 1998.

[30] Carl Gold, Darrell A Henze, Christof Koch, and György Buzsáki. On the origin of the extracellular action potential waveform: a modeling study. *Journal of Neurophysiology*, 95(5):3113–3128, 2006.

[31] Wulfram Gerstner, Werner M Kistler, Richard Naud, and Liam Paninski. *Neuronal dynamics: From single neurons to networks and models of cognition*. Cambridge University Press, 2014.

[32] John Clark and Robert Plonsey. The extracellular potential field of the single active nerve fiber in a volume conductor. *Biophysical Journal*, 8(7):842–864, 1968.

[33] Eva Syková and Charles Nicholson. Diffusion in brain extracellular space. *Physiological Reviews*, 88(4):1277–1340, 2008.

[34] James P Keener and James Sneyd. *Mathematical Physiology*. Springer, 2009.

[35] Piero Colli Franzone, Luca F Pavarino, and Simone Scacchi. *Mathematical Cardiac Electrophysiology*. Springer International Publishing, 2014.

[36] Joakim Sundnes, Glenn T Lines, Xing Cai, Bjørn F Nielsen, Kent-Andre Mardal, and Aslak Tveito. *Computing the Electrical Activity of the Heart*. Springer, 2006.

[37] Bradley J Roth. Bidomain simulations of defibrillation: 20 years of progress. *Heart Rhythm*, 10(8):1218–1219, 2013.

[38] Natalia A Trayanova. Whole-heart modeling: applications to cardiac electrophysiology and electromechanics. *Circulation Research*, 108(1):113–28, 2011.

[39] Hamish Meffin, Bahman Tahayori, Evgeni N Sergeev, Iven MY Mareels, David B Grayden, and Anthony N Burkitt. Modelling extracellular electrical stimulation: III. Derivation and interpretation of neural tissue equations. *Journal of neural engineering*, 11(6):065004, 2014.

[40] Bahman Tahayori, Hamish Meffin, Evgeni N Sergeev, Iven MY Mareels, Anthony N Burkitt, and David B Grayden. Modelling extracellular electrical stimulation: IV. Effect of the cellular composition of neural tissue on its spatio-temporal filtering properties. *Journal of Neural Engineering*, 11(6):065005, 2014.

[41] Thomas Radman, Yuzhuo Su, Je Hi An, Lucas C Parra, and Marom Bikson. Spike timing amplifies the effect of electric fields on neurons: implications for endogenous field effects. *Journal of Neuroscience*, 27(11):3030–3036, 2007.

[42] Ning Qian and TJ Sejnowski. An electro-diffusion model for computing membrane potentials and ionic concentrations in branching dendrites, spines and axons. *Biological Cybernetics*, 62(1):1–15, 1989.

[43] Claude Bédard and Alain Destexhe. Generalized cable theory for neurons in complex and heterogeneous media. *Physical Review E*, 88(2):022709, 2013.

[44] Jurgis Pods, Johannes Schönke, and Peter Bastian. Electrodiffusion models of neurons and extracellular space using the Poisson-Nernst-Planck equations – numerical simulation of the intra- and extracellular potential for an axon model. *Biophysical Journal*, 105(1):242–254, 2013.

[45] Geir Halnes, Ivar Østby, Klas H Pettersen, Stig W Omholt, and Gaute T Einevoll. Electrodiffusive model for astrocytic and neuronal ion concentration dynamics. *PLoS Computational Biology*, 9(12):e1003386, 2013.

[46] Geir Halnes, Tuomo Mäki-Marttunen, Daniel Keller, Klas H Pettersen, Ole A Andreassen, and Gaute T Einevoll. Effect of ionic diffusion on extracellular potentials in neural tissue. *PLoS Computational Biology*, 12(11):1–38, 11 2016.

[47] Jurgis Pods. A comparison of computational models for the extracellular potential of neurons. *Journal of Integrative Neuroscience*, 16:19–32, 2017.

[48] Torbjørn V Ness, Michiel WH Remme, and Gaute T Einevoll. Active subthreshold dendritic conductances shape the local field potential. *The Journal of Physiology*, 594(13):3809–3825, 2016.

Appendix: Theoretical considerations concerning the effect of removing the ephaptic current

In this appendix, we will provide theoretical arguments indicating the asymptotic nature of the errors introduced by removing the ephaptic current. These arguments are founded on strong assumptions on the analytical properties of the solutions and rigorous mathematical arguments would require *a priori* proofs of these properties. We therefore emphasize that the arguments provided here just indicate relations and it is an open problem to rigorously prove these relations mathematically.

As discussed above, the key step in deriving the classical Cable model is to remove the ephaptic current, I_{eph}. We have given computational evidence indicating that

$$I_{\text{eph}} \sim O\left(1/\sigma_{\text{e}}\right).$$

This relation can also be derived from the classical summation formula (see Equation (27) in the paper). If we assume that (27) holds and assume that $\frac{\partial^2 u_{\text{e}}}{\partial x^2}$ is uniformly bounded, we find that

$$I_{\text{eph}} = \eta \frac{\partial^2 u_{\text{e}}}{\partial x^2} = O\left(\frac{h\sigma_{\text{i}}}{\sigma_{\text{e}}}\right),$$

where we have used that $\eta = \frac{h\sigma_{\text{i}}}{4}$; recall that $h = l_y = l_z$ (the width of the neuron).

Next, our aim in this appendix is to provide a rough estimate of the error introduced in the membrane potential by removing the ephaptic current given by (12) in the paper. The theoretical bound will be based on the assumption that the term $\frac{\partial^2 u_{\text{e}}}{\partial x^2}$ in (12) is bounded independently of the parameter η.

In order to derive the bound, we compare the two models given by

$$C_{\text{m}} v_t + I_{\text{ion}}(v, x, t) = \eta \left(v_{xx} + u^e_{xx}\right), \tag{1}$$

and

$$C_{\text{m}} \bar{v}_t + I_{\text{ion}}(\bar{v}, x, t) = \eta \bar{v}_{xx}. \tag{2}$$

Here subscript t represents the derivative with respect to t and subscript xx represents the double derivative with respect to x. For simplicity, we assume that both models are equipped with the boundary condition $v = v_{\text{rest}}$ at $x = 0$ and $x = l_x$.

By subtracting (1) from (2), we find that the error

$$e = \bar{v} - v$$

is governed by

$$C_{\mathrm{m}} e_t + g(x,t)e = \eta e_{xx} - \eta u^e_{xx}, \tag{3}$$

with the boundary condition $e(0,t) = e(l_x,t) = 0$, initial condition $e(\cdot,0) = 0$, and where

$$g(x,t) = g_L + g_s(x)e^{-\frac{t-t_0}{\alpha}}.$$

By multiplying (3) by e and integrating over the length of the neuron, we get

$$\frac{1}{2}C_{\mathrm{m}}\frac{d}{dt}\int_0^{l_x} e^2 dx + \int_0^{l_x} g(x,t)e^2 dx = -\eta\int_0^{l_x} e_x^2 dx - \eta\int_0^{l_x} e u^e_{xx} dx. \tag{4}$$

First, we note that

$$\int_0^{l_x} g(x,t)e^2 dx \geqslant g_L \int_0^{l_x} e^2 dx, \tag{5}$$

and secondly, we use the Poincaré inequality (see e.g. [1]) to find that

$$\frac{l_x^2}{2}\int_0^{l_x} e_x^2 dx \geqslant \int_0^{l_x} e^2 dx. \tag{6}$$

In order to estimate the last term of (4), we note that, for any a, b and $\varepsilon \neq 0$, we have

$$0 \leqslant \left(\varepsilon a - \frac{b}{\varepsilon}\right)^2 = (\varepsilon a)^2 - 2ab + \left(\frac{b}{\varepsilon}\right)^2$$

and therefore

$$ab \leqslant \frac{1}{2}\left((\varepsilon a)^2 + \left(\frac{b}{\varepsilon}\right)^2\right).$$

By using this inequality with $a = e$, and $b = u^e_{xx}$, we find that

$$-\int_0^{l_x} e u^e_{xx} dx \leqslant \int_0^{l_x} |e u^e_{xx}|\, dx \leqslant \frac{1}{2}\left(\int_0^{l_x} (\varepsilon e)^2\, dx + \int_0^{l_x}\left(\frac{u^e_{xx}}{\varepsilon}\right)^2 dx\right). \tag{7}$$

We define

$$E(t) = \int_0^{l_x} e^2 dx,$$

and note that, by $(4, 5, 6, 7)$, we have

$$\frac{1}{2}C_{\mathrm{m}}E' \leqslant -\frac{2}{l_x^2}\eta E - g_L E + \frac{\eta\varepsilon^2}{2}E + \frac{\eta}{2\varepsilon^2}F_0, \tag{8}$$

where we have introduced

$$F_0 = \max_t \int_0^{l_x} (u^e_{xx})^2\, dx.$$

Again, if we assume that the extracellular potential is faithfully represented by the classical summation formula (27), we have

$$F_0 = O(1/\sigma_{\mathrm{e}}^2).$$

Equation (8) can be written as

$$\frac{1}{2}C_{\mathrm{m}}E' \leqslant (A\varepsilon^2 - B)E + C/\varepsilon^2$$

with $A = \eta/2, B = 2\eta/l_x^2 + g_L$ and $C = \eta F_0/2$. Provided that $B > A\varepsilon^2$ this ODE will be bounded by the steady state

$$E^*(\varepsilon^2) = \frac{C}{\varepsilon^2(B - A\varepsilon^2)}.$$

Choosing $\varepsilon^2 = B/2A$ in order to minize this upper bound, it follows that

$$E(t) \leqslant E^*\left(\frac{B}{2A}\right) = \frac{4AC}{B^2} = \frac{\eta^2}{(\frac{2\eta}{l_x^2} + g_L)^2}F_0.$$

Since, $F_0 = O(1/\sigma_{\mathrm{e}}^2)$, we find that for small values of η we have

$$E(t) \leqslant O\left(\frac{\eta^2}{g_L^2\sigma_{\mathrm{e}}^2}\right) = O\left(\frac{h\sigma_{\mathrm{i}}}{g_L\sigma_{\mathrm{e}}}\right)^2,$$

where we recall that $h = l_y = l_z$ represents the width of the neuron. Finally, we conclude that

$$\|e(t)\| = E^{1/2}(t) = O\left(\frac{h\sigma_{\mathrm{i}}}{g_L\sigma_{\mathrm{e}}}\right).$$

This estimate indicates that the error introduced by removing the ephaptic current is reduced as h or σ_{i} are reduced, and it is reduced if σ_{e} or g_L is increased.

References

[1] Aslak Tveito and Ragnar Winther. *Introduction to Partial Differential Equations; a Computational Approach*, volume 29. Springer-Verlag, second edition, 2009. 392 pages.

II

Paper II

A Cell-Based Framework for Numerical Modeling of Electrical Conduction in Cardiac Tissue

Aslak Tveito, Karoline H. Jæger, Miroslav Kuchta,
Kent-Andre Mardal, and Marie E. Rognes

Frontiers in Physics 5:48 (2017)

A Cell-Based Framework for Numerical Modeling of Electrical Conduction in Cardiac Tissue

Aslak Tveito[1,2], Karoline H. Jæger[1], Miroslav Kuchta[1,3], Kent-Andre Mardal[1,3], and Marie E. Rognes[1]

[1]Simula Research Laboratory, Center for Biomedical Computing, Norway
[2]Department of Informatics, University of Oslo, Norway
[3]Department of Mathematics, University of Oslo, Norway

Abstract

In this paper, we study a mathematical model of cardiac tissue based on explicit representation of individual cells. In this EMI model, the extracellular (E) space, the cell membrane (M) and the intracellular (I) space are represented as separate geometrical domains. This representation introduces modelling flexibility needed for detailed representation of the properties of cardiac cells including their membrane. In particular, we will show that the model allows ion channels to be non-uniformly distributed along the membrane of the cell. Such features are difficult to include in classical homogenized models like the monodomain and bidomain models frequently used in computational analyses of cardiac electrophysiology. The EMI model is solved using a finite difference method (FDM) and two variants of the finite element method (FEM). We compare the three schemes numerically, reporting on CPU-efforts and convergence rates. Finally, we illustrate the distinctive capabilities of the EMI model compared to classical models by simulating monolayers of cardiac cells with heterogeneous distributions of ionic channels along the cell membrane.

Because of the detailed representation of every cell, the computational problems that result from using the EMI model are much larger than for the classical homogenized models, and thus represent a computational challenge. However, our numerical simulations indicate that the FDM scheme is optimal in the sense that the computational complexity increases proportionally to the number of cardiac cells in the model. Moreover, we present simulations, based on systems of equations involving ~ 117 million unknowns, representing up to ~ 16000 cells.

We conclude that collections of cardiac cells can be simulated using the EMI model, and that the EMI model enable greater modeling flexibility than the classical monodomain and bidomain models.

1 Introduction

The pumping function of the heart is governed by an electrochemical wave traversing the entire cardiac muscle resulting in the muscle's synchronized contraction. This electrochemical wave has been subject to intense study over many decades and mathematical models have played an essential role in understanding its properties. However, these models are based on homogenization of the cardiac tissue, which imposes limitations on the level of detail that can be studied by the models. For instance, the details of the dynamics surrounding a single cell are difficult to study using classical homogenized models simply because the single cell is not present in such models.

In this paper, we consider an emerging mathematical modeling framework for representing and simulating excitable cells in general and cardiac cells in particular. In this framework, the extracellular space, the cell membranes, and the intracellular spaces are explicitly represented as separate physical and geometrical objects. The state variables are the extracellular, membrane, and intracellular potentials defined over the corresponding domains. We refer to this framework as the EMI (Extracellular-Membrane-Intracellular) model. This approach has been applied in several earlier papers (e.g., [1, 2, 3, 4, 5, 6, 7]), which used the EMI framework (or related approaches) for detailed simulations of a single cell or a small number of cells. Indeed, the presentation here is very much motivated by the formulation presented by [5] and by [4]. Furthermore, the EMI approach was used to study the effect of the ephaptic coupling of neurons in [8].

The EMI framework represents an alternative to the classical and more common bidomain or monodomain models. These latter models are based on homogenization of the cardiac tissue and the extracellular space, the intracellular space, and the cell membrane are all assumed to exist everywhere (e.g., [9, 10, 11, 12, 13]). In the following, when we refer to homogenized models, we will refer to models of the monodomain or bidomain type. In contrast, the EMI approach avoids this full homogenization at the tissue level. Note however, that homogenization is also used in the EMI approach to formulate equations for the intracellular domain and the extracellular domain.

The classical models (monodomain, bidomain) have been successfully used to study the propagation of the electrochemical wave in cardiac tissue (e.g., [14, 15, 16]), the initiation of excitation waves (e.g., [17, 18, 19, 20, 21]), the development of cardiac arrhythmias (e.g., [14, 17, 18]), the effect of defibrillation (e.g., [22, 23, 24, 25, 26, 27, 28]), and the effect of various drugs (e.g., [29, 30, 31, 32]).

Despite the many successful applications of the monodomain and bidomain models, there are a number of motivating factors for introducing a more explicit, more accurate, and more detailed framework for modeling cardiac tissue. We address some of these factors in the following paragraphs.

Homogenized models may be insufficient to represent details of the remodeling of the heart Although classical models represent the big picture of the electrochemical wave traversing cardiac tissue well, they may fail to reveal the finer details of cardiac conduction. For example, it is well established that local perturbations to the conduction velocity may be arrhythmogenic; in particular, slowed conduction will increase the risk of arrhythmias [33]. It is therefore essential to understand how various remodelings of the heart affect the conduction velocity. Individual perturbations of the size and shape of the cardiac cells clearly affect the conduction velocity (e.g., [34]), but such changes are very hard to represent in a classical homogenized model, since a detailed representation of the individual cells in the tissue is needed. Furthermore, local density distributions of ion channels on the cell membrane will affect local conduction properties and such effects are also very hard, if even possible, to represent in the classical models.

Homogenized models are unsuitable for addressing the ephaptic coupling of cardiac cells The electrical conduction of the heart is believed to depend on direct cell-to-cell contact realized in terms of gap junctions (e.g., [35, 36, 37]). These connections are reduced under heart failure, resulting in impaired conduction velocity that may in turn increase the probability of arrhythmias (e.g., [38, 37]). However, even when conduction through gap junctions is significantly reduced, electrical signals are still conducted (e.g., [39]). This conduction is believed to rely on ephaptic coupling between neighboring cells via the extracellular space. The effect depends on the shape and size of the extracellular space and is thus not directly amenable to analysis via the homogenized bidomain or monodomain models.

Simulating cell monolayers is of increasing significance The number of cardiomyocytes in the human ventricles can be estimated to be around 8 billion (e.g., [40]), and the number is close to 4 million for the mouse heart (e.g., [41]). In both cases, a homogenized model may be justified by the large number of cells involved. However, for experimental setups with monolayers of cardiac cells, the number of cells is much lower (hundreds or a few thousands) and the validity of the homogenized continuum approach becomes questionable. The EMI model, on the other hand, is very well suited, since it represents every individual cell. The ability to faithfully simulate monolayers of cardiac cells has become very important since it has become possible to simultaneously measure the transmembrane potential and the intracellular calcium concentration (e.g., [42]). Therefore, at least in principle, the inversion of spatial models of monolayers may be applied to characterize properties of single cells using monolayer experiments. This is particularly important because of the development of human induced pluripotent stem cells (hi-PSC). Based on skin samples, such cells can be used to derive cardiac cells with certain properties identical to a patient's cardiac cells. Therefore, this technology is believed to have great potential in the development of personalized drugs for rare diseases (e.g., [43, 44, 45]).

Available computational power allows for cell size resolution Twenty-five years ago, the best mathematical model of cardiac tissue was solved using 257 computational nodes [12, 46]. At that time, an accurate representation of cardiac tissue in terms of the representation of individual cells was inconceivable for reasons of both storage and computing time. This has changed dramatically; in recent computational studies, 29 million computational nodes were used to represent cardiac tissue [27, 47]. The computational mesh size in these simulations was about 59 μm, which should be compared with 100 μm, the typical length of a cardiac cell. This means that current simulators of the electrophysiology of the heart are, at least in principle, able to resolve features at the individual cell level.

The main purpose of the present paper is to assess the computational challenges of the EMI modeling framework. We will show how the model's complexity increases as the number of cardiac cells in the simulations increases and how the complexity of the membrane model affects the overall CPU demands. Furthermore, we will demonstrate that the EMI framework opens the possibility of simulating local properties of the cell that are hard to represent in homogenized models.

We introduce an operator splitting scheme for the EMI model and propose and compare three numerical schemes for the discretization of the resulting partial differential equations (PDEs): one finite difference-based (FDM) and two finite element-based (FEM) schemes of various degrees of complexity, computational cost, and accuracy. We compare the three schemes numerically in terms of convergence rates and computational cost. Moreover, to illustrate the distinctive capabilities of the EMI model, we present new results for simulating monolayers of cardiac cells with spatially heterogeneous distributions of ionic channels across the cell membrane.

Our results demonstrate that the EMI approach is computationally feasible: We can solve systems relevant for simulating monolayers of cardiac cells with sufficient resolution. Moreover, we show, using numerical computations based on the FDM code, that the computational effort per cell is bounded independently of the number of cardiac cells, and thus that the effort increases at most linearly with the number of cells.

Outline In the next section, we will present the EMI model and three numerical methods used to solve the model. Next, we will discuss the numerical accuracy of the solutions, show convergence under mesh refinements, and assess the methods' CPU demands. To illustrate the ability to model local properties of individual cells, we present an example showing the difference in the conduction velocity of cells with uniform and non-uniform distributions of sodium channels. In the final sections, the results will be summarized and discussed.

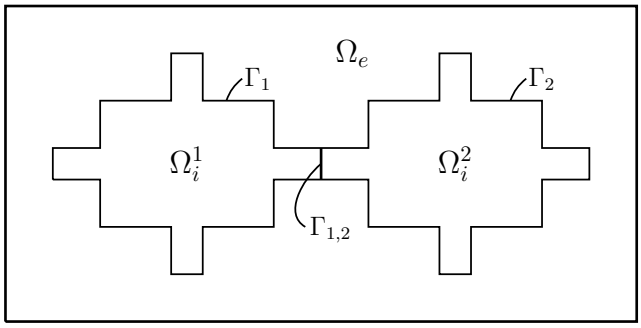

Figure 1: Illustration of an idealized computational domain: two idealized cells Ω_i^1 and Ω_i^2 connected by a gap junction $\Gamma_{1,2}$ and the surrounding extracellular domain Ω_e.

2 Models and methods

In this section, we present the EMI model and numerical methods for solving the corresponding set of equations.

2.1 The EMI model

We will use the EMI model to simulate collections of cardiac cells. However, to present the model, it is sufficient to consider the case of two coupled cells.

We assume that the complete computational domain consists of intracellular spaces Ω_i^k, with $k = 1, 2$ in the case of two cells, that are connected by gap junctions $\Gamma_{1,2}$ and surrounded by a connected extracellular space Ω_e. The membrane is defined to be the intersection between each intracellular domain Ω_i^k and the extracellular domain and is denoted by Γ_k, while the remaining boundary of the extracellular domain is denoted by $\partial\Omega_e$. Figure 1 illustrates a two-dimensional (2D) version of this setup, showing two connected cells surrounded by extracellular space. In our computations (except in the first simple test case with an analytical solution) all cells are 3D and the cells can be connected in one-, two- or three-dimensional collections. In one-dimensional strands of cells, the cell coupling is as illustrated in Figure 1; for two and three-dimensional collections of cells, the coupling in the y- and z-directions are similar to the x-coupling illustrated in the figure.

For the case illustrated in Figure 1, the EMI model can be formulated as follows: Find the extracellular potential u_e defined over Ω_e, the intracellular potentials u_i^k defined over Ω_i^k, and the transmembrane potentials v^k defined over Γ_k for $k = 1, 2$

and w defined over $\Gamma_{1,2}$ satisfying

$$\begin{aligned}
\nabla \cdot \sigma_e \nabla u_e &= 0 && \text{in } \Omega_e, && (1)\\
\nabla \cdot \sigma_i \nabla u_i^k &= 0 && \text{in } \Omega_i^k, && (2)\\
u_e &= 0 && \text{at } \partial\Omega_e, && (3)\\
n_e \cdot \sigma_e \nabla u_e &= -n_i^k \cdot \sigma_i \nabla u_i^k \equiv I_m^k && \text{at } \Gamma_k, && (4)\\
u_i^k - u_e &= v^k && \text{at } \Gamma_k, && (5)\\
v_t^k &= \frac{1}{C_m}(I_m^k - I_{\text{ion}}^k) && \text{at } \Gamma_k, && (6)\\
n_i^2 \cdot \sigma_i \nabla u_i^2 &= -n_i^1 \cdot \sigma_i \nabla u_i^1 \equiv I_{1,2} && \text{at } \Gamma_{1,2}, && (7)\\
u_i^1 - u_i^2 &= w && \text{at } \Gamma_{1,2}, && (8)\\
w_t &= \frac{1}{C_{1,2}}(I_{1,2} - I_{\text{gap}}) && \text{at } \Gamma_{1,2}, && (9)
\end{aligned}$$

for $k = 1, 2$. Here, n_e is the normal pointing out from Ω_e and n_i^k is the (outward) normal pointing out from Ω_i^k for $k = 1, 2$; σ_i and σ_e are the intracellular and extracellular conductivities, respectively; I_{ion}^k represents the ionic current density, which typically depends on additional state variables such as ionic concentrations; and I_{gap} represents the gap junction current density. In terms of units, the potentials u_e, u_i^k, v^k and w are given in mV; the current densities I_m^k, I_{ion}^k, $I_{1,2}$ and I_{gap} are given in μA/cm^2; the conductivities σ_i and σ_e are given in mS/cm; the capacitances C_m and $C_{1,2}$ are given in μF/cm^2; length is given in cm; and time is given in ms. In the following, we will refer to (1)–(9) as the EMI model. For brevity, we will write u_i in place of u_i^k, v in place of v^k, I_{ion} in place of I_{ion}^k and Γ in place of Γ_k for $k = 1, 2$ when context allows.

2.2 Membrane model

In our computations, we will consider both a passive and an active model for the dynamics on the cell membrane between the intracellular and extracellular spaces. In the passive model, I_{ion} is given by the linear model

$$I_{\text{ion}}(v) = \frac{1}{R_m}(v - v_{\text{rest}}), \tag{10}$$

where R_m represents the resistance of the passive membrane (in kΩcm^2) and v_{rest} denotes the resting potential of the membrane. In the active model, we let I_{ion} be represented by the action potential (AP) model of Grandi et al. [48]. In this case, equation (6) is replaced by a system of the form

$$\begin{aligned}
v_t &= \frac{1}{C_m}(I_m - I_{\text{ion}}(v, s)), && (11)\\
s_t &= F(v, s), && (12)
\end{aligned}$$

where v represents the membrane potential and s represents a collection of additional state variables introduced in the AP model. Furthermore, I_{ion} represents the sum of the ionic current densities across the membrane through a number of different types of ion channels, pumps, and exchangers and $F(v, s)$ represents the ordinary differential equations (ODEs) describing the dynamics of the additional state variables. The Grandi model is implemented by defining a membrane potential v and a set of state variables s for each of the membrane nodes of the mesh. We let all state variables of the Grandi model, including the intracellular ionic concentrations, be defined only on the mesh nodes located on the cell membrane, and we allow the value of these variables to vary for different membrane nodes located on the same cell. The values of the state variables are updated in each time step using an operator splitting scheme described below. Intracellular and extracellular gradients of the ionic concentrations are ignored (see comment in Discussion).

Finally, we represent the gap junction between neighboring cells by a passive membrane:

$$I_{\text{gap}}(w) = \frac{1}{R_{\text{gap}}} w, \tag{13}$$

where R_{gap} represents the resistance of the passive membrane (in $\text{k}\Omega\text{cm}^2$). A discussion of the modeling of the gap-junctions is given in [1] where a boundary element method is used to solve a model similar to the system (1)–(9).

2.3 Operator splitting scheme

The ionic current density I_{ion} entering the EMI model through (6) typically introduce a significant number of additional states (e.g. as in (11)). For this reason, we consider an operator splitting approach to solve the EMI model defined by (1)–(9).

The system (1)–(9) is solved by first applying given initial conditions for v and w. Then, for each time step n, we assume that the solutions v^{n-1} and w^{n-1} are known for $t = t_{n-1}$ on Γ and $\Gamma_{1,2}$ respectively. We then find the solutions at $t = t_n$ using a two-step (first-order) operator splitting procedure, but note that a three-step (second-order) operator splitting could equally well be used (e.g., [11]).

In the first step, we update the solutions for the membrane potential by solving a system of ODEs of the form (11) and (12) over Γ with I_m set equal to zero. In the following numerical experiments, the ODE system (11) and (12) is solved by taking m forward Euler steps of size $\Delta t^* = \Delta t/m$ for each global time step, though any other suitable ODE scheme could be used.

In the second (PDE) step of the operator splitting procedure, we solve the linear system arising from an implicit discretization in time and space of (1)–(9) with I^1_{ion} and I^2_{ion} set to zero. For the discretization in time of (6) and (9), we use an implicit Euler scheme using the solution from the first (ODE) step of the operator splitting scheme as the previous state.

When a linear model for I_{ion} is considered, the first (ODE) step of the splitting scheme is redundant and thus omitted, and I^k_{ion} for $k = 1, 2$ is kept in the PDE step, altering the linear system to be solved.

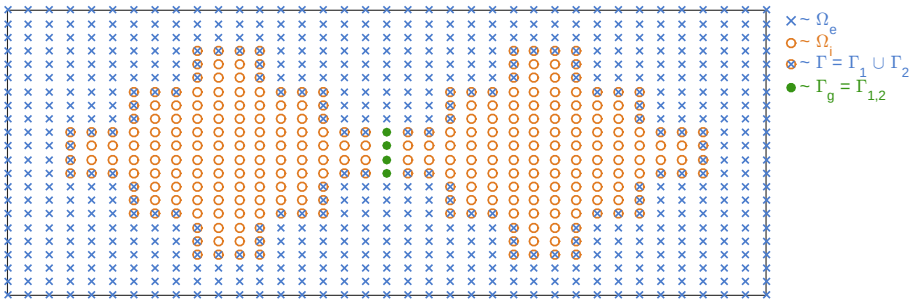

Figure 2: Sketch of the computational mesh used for the FDM. Nodes in Ω_e are marked by $\times$, nodes in $\Omega_i = \Omega_i^1 \cup \Omega_i^2$ are marked by $\circ$, nodes on the membrane between the intracellular and the extracellular space ($\Gamma = \Gamma_1 \cup \Gamma_2$) are marked by $\otimes$, and nodes on the membrane between two cells ($\Gamma_{1,2}$) are marked by $\bullet$.

We propose and compare three different approaches for the spatial discretization of the PDE step in this study, each presented in the following sections. For the numerical experiments, the finite difference method (FDM) was implemented directly in MATLAB, while the finite element methods (FEMs) were implemented using the FEniCS finite element library [49, 50]. All computations were run on a Dell PowerEdge R430 with dual Intel Xeon processors (E5-2623 v4 2.60 GHz) and 12x32GB RDIMM; each processor runs four kernels with two threads each.

2.3.1 Finite difference method for solving the EMI PDEs

We first consider a finite difference scheme for solving the PDE step of the EMI model as defined above. To simplify the notation, we describe here the 2D case only; the extension to three dimensions is immediate. The spatial discretization employed here is taken from [8].

Figure 2 shows the four different types of nodes used in the computations. Nodes marked by $\times$ represent the extracellular domain. In these nodes, we define a single unknown, u_e. Similarly, nodes marked by $\circ$ represent the intracellular domain (either Ω_i^1 or Ω_i^2) and we define a single unknown u_i for these nodes. Nodes marked by $\otimes$ represent the membrane between the intracellular and the extracellular space ($\Gamma = \Gamma_1 \cup \Gamma_2$). For these nodes, we define three unknowns: u_e, u_i, and v, with $v = u_i - u_e$. Similarly, nodes marked by $\bullet$ represent the membrane between two cells and, for these nodes, we define the three unknowns u_i^1, u_i^2, and w, with $w = u_i^1 - u_i^2$.

We use the notation $u_e^{n,j,k}$ for the numerical solution of the extracellular potential, u_e, at the point $(x_j, y_k) = (j\Delta x, k\Delta y)$ at time $t_n = n\Delta t$ and use an analogous notation for the numerical solution of the remaining variables.

We discretize (1) using the finite difference scheme

$$\frac{\sigma_e^{j+1/2,k}(u_e^{n,j+1,k} - u_e^{n,j,k}) - \sigma_e^{j-1/2,k}(u_e^{n,j,k} - u_e^{n,j-1,k})}{\Delta x^2}$$
$$+ \quad \frac{\sigma_e^{j,k+1/2}(u_e^{n,j,k+1} - u_e^{n,j,k}) - \sigma_e^{j,k-1/2}(u_e^{n,j,k} - u_e^{n,j,k-1})}{\Delta y^2} = 0, \qquad (14)$$

where $\sigma_e^{j+1/2,k} = \sigma_e((j+1/2)\Delta x, k\Delta y)$. Equation (2) is discretized similarly, with σ_e replaced by σ_i and u_e replaced by u_i.

On the membrane between the intracellular and extracellular domains, there are three unknowns and three equations. The first equation is given directly by (5) and the second equation is given by a first-order finite difference discretization of (4). Finally, the third equation is given by an implicit discretization of (6) of the form

$$\frac{v^{n,j,k} - v^{n-1/2,j,k}}{\Delta t} = \frac{1}{C_m} I_m^{n,j,k}, \qquad (15)$$

where $I_m^{n,j,k}$ is a discrete version of the term $n_e \cdot \sigma_e \nabla u_e$ from (4) and $v^{n-1/2,j,k}$ is the solution of the membrane potential from the first step of the operator splitting procedure.

Similarly, for the nodes on the membrane between the cells, there are three unknowns and three equations. The first equation is given directly by (8), the second is a first-order finite difference discretization of (7), and the third is an implicit discretization of (9) of the form

$$\frac{w^{n,j,k} - w^{n-1,j,k}}{\Delta t} = \frac{1}{C_{1,2}} \left(I_{1,2}^{n,j,k} - I_{\text{gap}}(w^{n,j,k}) \right), \qquad (16)$$

where $I_{1,2}^{n,j,k}$ is a discrete version of the term $n_i^2 \cdot \sigma_i \nabla u_i^2$ from (7) and $I_{\text{gap}}(w^{n,j,k})$ is a linear function of $w^{n,j,k}$ given by (13). It is worth mentioning here that if the gap junction dynamics is modeled using a non-linear model, operator splitting can be applied as was done for the membrane model.

Two special types of nodes require some special treatment. The first type is the nodes on the corners of the membrane. For these nodes, we define two flux terms $I_m^{n,j,k} = n_e \cdot \sigma_e \nabla u_e$, one for the normal derivative in the x direction and one for the normal derivative in the y direction, and we use the mean of these two terms in the equation of the form (15). Furthermore, in the flux equality equation (4), we also define two intracellular flux terms, one for each direction, and let the sum of the two intracellular flux terms equal the sum of the two extracellular flux terms.

The second special node type is the extracellular nodes located next to a node on the membrane between two cells. In Figure 2, these are the two extracellular nodes just above or below $\Gamma_{1,2}$. For these nodes, we define a no-flux boundary condition between the extracellular node and the adjacent node on $\Gamma_{1,2}$. This is implemented by defining an extracellular potential for the node on the end of $\Gamma_{1,2}$ with a value equal to the extracellular potential in the node just outside $\Gamma_{1,2}$.

When considering a linear model for I_{ion}, we skip the first step of the operator splitting procedure and replace the equation of the form (15) in the finite difference scheme by

$$\frac{v^{n,j,k} - v^{n-1,j,k}}{\Delta t} = \frac{1}{C_m}\left(I_m^{n,j,k} - I_{\text{ion}}(v^{n,j,k})\right). \tag{17}$$

A major drawback of the finite difference discretization is the fact that actual cell geometries are quite complex and virtually impossible to handle with this method. However, complex geometries can be resolved by the finite element method. In the following, we shall propose two different FEM formulations of the EMI equations (1)–(9): the mortar finite element formulation, where the primary unknowns are the intra/extracellular potentials, and the H(div)-based finite element formulation, where the currents are the primary unknowns in the cells/tissue.

2.3.2 Mortar finite element method for solving the EMI PDEs

Mortar finite element methods ([51]; see also [4] for the application of the method in simulations of cell membranes) allow for the coupling of different types of variational problems posed over non-overlapping domains by weakly (in an integral sense) enforcing interface conditions on common boundaries. For the EMI system, the Poisson problems (1) and (2) are coupled by the conditions (4) and (5) and the conditions (7) and (8).

Let V_e and V_i^k be spaces of functions over Ω_e and Ω_i^k for $k = 1, 2$, and let Q be a function space defined over $\Gamma = \Gamma_1 \cup \Gamma_2 \cup \Gamma_{1,2}$, to be precisely defined below. For any $\psi \in Q$, we denote by ψ^1, ψ^2 and $\psi^{1,2}$ the restriction of ψ to Γ_1, Γ_2, and $\Gamma_{1,2}$, respectively. With this notation, given $(v^k)^n$ and w^n at time level n, at each time level $n+1$ of the temporal discretization, we aim to find the membrane current density $J \in Q$, defined such that $J^k = I_m^k$ and $J^{1,2} = I_{1,2}$ and the extracellular and intracellular potentials $u_e \in V_e$ and $u_i^i \in V_i^k$ such that:

$$\begin{aligned}
\int_{\Omega_i^1} \sigma_i \nabla u_i^1 \cdot \nabla \phi_i^1 \,\mathrm{d}x + \int_{\Gamma_1} J^1 \phi_i^1 \,\mathrm{d}s + \int_{\Gamma_{1,2}} J^{1,2} \phi_i^1 \,\mathrm{d}s = 0 && \forall\, \phi_i^1 \in V_i^1,\\
\int_{\Omega_i^2} \sigma_i \nabla u_i^2 \cdot \nabla \phi_i^2 \,\mathrm{d}x + \int_{\Gamma_2} J^2 \phi_i^2 \,\mathrm{d}s - \int_{\Gamma_{1,2}} J^{1,2} \phi_i^2 \,\mathrm{d}s = 0 && \forall \phi_i^2 \in V_i^2,\\
\int_{\Omega_e} \sigma_e \nabla u_e \cdot \nabla \phi_e \,\mathrm{d}x - \int_{\Gamma_1} J^1 \phi_e \,\mathrm{d}s - \int_{\Gamma_2} J^2 \phi_e \,\mathrm{d}s = 0 && \forall\, \phi_e \in V_e,\\
\int_{\Gamma_1} (u_i^1 - u_e)\psi^1 \,\mathrm{d}s - \frac{\Delta t}{C_m} \int_{\Gamma_1} J^1 \psi^1 \,\mathrm{d}s = \int_{\Gamma_1} (v^1)^n \psi^1 \,\mathrm{d}s && \forall \psi \in Q,\\
\int_{\Gamma_2} (u_i^2 - u_e)\psi^2 \,\mathrm{d}s - \frac{\Delta t}{C_m} \int_{\Gamma_2} J^2 \psi^2 \,\mathrm{d}s = \int_{\Gamma_1} (v^2)^n \psi^2 \,\mathrm{d}s && \forall \psi \in Q,\\
\int_{\Gamma_{1,2}} (u_i^1 - u_i^2)\psi^{1,2} \,\mathrm{d}s - \frac{\Delta t}{C_{1,2}} \int_{\Gamma_{1,2}} J^{1,2} \psi^{1,2} \,\mathrm{d}s = \int_{\Gamma_{1,2}} w^n \psi^{1,2} \,\mathrm{d}s && \forall \psi \in Q.
\end{aligned} \tag{18}$$

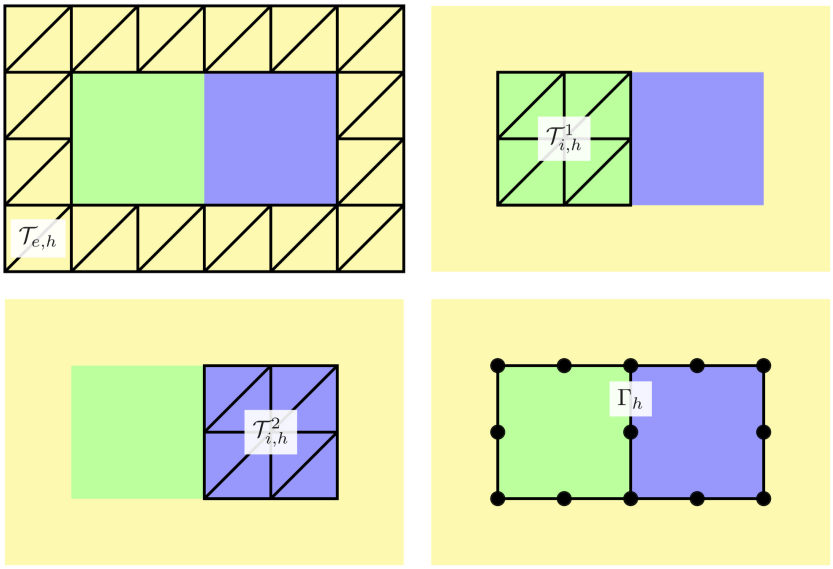

Figure 3: Schematic representation of finite element meshes considered with the mortar element method: (upper left) the tesselation $\mathcal{T}_{e,h}$ of the extracellular domain, (upper right and bottom left) the tessellations $\mathcal{T}^1_{i,h}$ and $\mathcal{T}^2_{i,h}$ of the intracellular domains, and (bottom right) the membrane discretization Γ_h. In our implementation, $\mathcal{T}_{e,h}$ and $\mathcal{T}^k_{i,h}$ have identical facets on Γ and the facets define the finite element cells of Γ_h, see the location of the vertices of the 1D mesh depicted by black circles.

Here, the first three equations of the variational problem are obtained by multiplying (1) and (2) by test functions ϕ_e and ϕ_i^k and integrating over the associated domains while using conditions (4) and (7) in the integration by parts. The final three equations are then weakly enforcing the constraints

$$u_i^k - u_e - \frac{\Delta t}{C_m} I_m^k = (v^k)^n \text{ on } \Gamma_i^k, \quad u_i^1 - u_i^2 - \frac{\Delta t}{C_{1,2}} I_{1,2} = w^n \text{ on } \Gamma_{1,2} \tag{19}$$

which are obtained by a backward Euler discretization of (6) and (9) (cf. equations (15) and (16)) while expanding the transmembrane potentials of Γ_i^k and $\Gamma_{1,2}$ at the $(n+1)$th temporal level using definitions (5) and (8), respectively. We note that the definitions of the transmembrane potentials enter the variational problem only via (19). Moreover, the membrane current density J can be interpreted as the multiplier of the augmented Lagrangian associated with these constraints.

System (18) is the linear part of the operator splitting procedure described above. The well-posedness of the system (18) was established in [52] or [53] for the stationary case, where it was shown that a unique solution exists in the Sobolev spaces $V_e = H^1_{0,\partial\Omega_e}(\Omega_e)$, $V_i^k = H^1(\Omega_i^k)$ and $Q = H^{-1/2}(\Gamma)$.

To discuss the finite element discretization of the well-posed problem (18), we denote by $\mathcal{T}_{e,h}$ and $\mathcal{T}_{i,h}^k$ simplicial meshes of the domains Ω_e and Ω_i^k, respectively. Generally, the mortar finite element approach allows the tessellations to be independent of one another and the elements of Γ_h, the triangulation of Γ, are defined in terms of facets of one of the sharing tessellations. For simplicity, we opt here for meshes such that they share facets on Γ (see Figure 3). In particular, the neighboring tessellations define identical meshes Γ_h.

In the following, the discrete finite element subspaces of V_e, V_i^k, and Q will be constructed from continuous piecewise linear Lagrange elements. More precisely, we let

$$\begin{aligned} V_{e,h} &= \left\{ v \in C(\mathcal{T}_{e,h}); v|_K = P^1(K) \, \forall K \in \mathcal{T}_{e,h} \right\}, \\ V_{i,h}^k &= \left\{ v \in C(\mathcal{T}_{i,h}^k); v|_K = P^1(K) \, \forall K \in \mathcal{T}_{i,h}^k \right\}, \\ Q_h &= \left\{ v \in C(\Gamma_h); v|_K = P^1(K) \, \forall K \in \Gamma_h \right\} \end{aligned}$$

and thus the space Q_h is the trace space of the functions in $V_{e,h}$ and $V_{i,h}^k$. We refer to [54] and references therein for proof of the numerical stability of this choice of discretization. We also note that the choice of element for the space Q_h simplifies the implementation, however, dual Lagrange multipliers (see [53, 54]), though more involved, are more suitable if static condensation is employed to solve the linear system arising from (18). Finally, in the numerical experiments, the scheme was implemented using the $\text{FEniCS}_{\text{ii}}$ extension [55] of the FEniCS finite element library [49, 50].

2.3.3 H(div)-based finite element method for solving the EMI PDEs

The mortar finite element formulation defined above introduces separate function spaces for each of the intracellular domains Ω_i^k, which adds implementational complexity. As an alternative approach, we also consider an H(div)-based finite

element method (e.g., [56]) for solving the PDE step of the operator splitting scheme. This scheme relaxes the continuity constraint for the potentials throughout the domain Ω and introduces *potential gradients* as additional variables with the appropriate normal continuity regularity for the associated currents. Therefore, the interface continuity conditions for the currents can be handled seamlessly.

To this end, we use the intracellular current density vector $\hat{J}_i$ and the extracellular current density vector $\hat{J}_e$ as additional vector fields defined over Ω_i and Ω_e, respectively:

$$\hat{J}_i = -\sigma_i \nabla u_i, \quad \hat{J}_e = -\sigma_e \nabla u_e. \tag{20}$$

We let $\hat{J}$ denote the extension of $\hat{J}_i$ and $\hat{J}_e$ to Ω, and assume that $\hat{J}$ is in the space H(div, Ω), that is, $\hat{J}$ is a square-integrable vector field with square-integrable divergence. Furthermore, denote by u the extension of u_i and u_e to Ω, and analogously for σ. In addition, we define $\hat{v}$ as the extension of the transmembrane potential v and the transcellular potential w and we let $\hat{I}$ denote the extension of I_{ion} and I_{gap}. Thus the variable u is defined over Ω while $\hat{v}$ and $\hat{I}$ are defined over the whole interior membrane $\hat{\Gamma} = \Gamma_1 \cup \Gamma_2 \cup \Gamma_{1,2}$.

Let n_i denote the outward normal, from the intracellular domains to the extracellular domain, on Γ_k for $k = 1, 2$ and from Ω_i^1 to Ω_i^2 on $\Gamma_{1,2}$ and, analogously, let n_e denote the outward normal from the extracellular to the intracellular domains. By the flux continuity conditions (4) and (7), we require that $\hat{J}_i \cdot n_i = -\hat{J}_e \cdot n_e$ on Γ_k $(k = 1, 2)$ and analogously on $\Gamma_{1,2}$. Let $\hat{v}^{n,*}$ denote the membrane potential solution from the ODE step in the nonlinear case or the membrane solution $\hat{v}^{n,*} = \hat{v}_h^{n-1}$ at the previous time in the linear (no ODE) case.

With this notation and after an implicit Euler discretization in time, our H(div)-based finite element scheme at each time step n reads as follows: For given $v^{n,*}$, f^n, and g^n, find $u_h^n \in U_h$, $\hat{J}_h^n \in S_h$ and $\hat{v}_h^n \in V_h$ such that

$$-\int_\Omega \nabla \cdot \hat{J}_h^n \, \phi \, \mathrm{d}x = \int_\Omega f^n \phi \, \mathrm{d}x \; \forall \, \phi \in U_h, \tag{21}$$

$$\int_\Omega \left(\sigma^{-1} \hat{J}_h^n \cdot \tau - \nabla \cdot \tau \, u_h^n \right) \mathrm{d}x + \int_{\hat{\Gamma}} \tau \cdot n_i \, \hat{v}_h^n \, \mathrm{d}s = \int_\Omega g^n \cdot \tau \, \mathrm{d}x \; \forall \, \tau \in S_h, \tag{22}$$

$$\int_{\hat{\Gamma}} \left(C_m \hat{v}_h^n + \Delta t(-\hat{J}_h^n \cdot n_i + \alpha \hat{I}(\hat{v}_h^n)) \right) \beta \, \mathrm{d}s = \int_{\hat{\Gamma}} C_m \hat{v}^{n,*} \beta \, \mathrm{d}s \; \forall \, \beta \in V_h. \tag{23}$$

In the case of a nonlinear I_{ion}, we set $\alpha = 0$ and treat the non-linear term by operator splitting as outlined above.

In the numerical experiments, as for the mortar finite element method described in Section 2.3.2, we let $\mathcal{T}_h$ denote a simplicial mesh of Ω conforming to Ω_i^k $(k = 1, 2)$ and Ω_e such that $\hat{\Gamma}_h$, the restriction of $\mathcal{T}_h$ to $\hat{\Gamma}$, defines a conforming mesh of $\hat{\Gamma}$ (of one topological dimension lower). Relative to these meshes, we define the spaces S_h as the lowest-order Raviart–Thomas elements defined over $\mathcal{T}_h$ and U_h as the space of (discontinuous) piecewise constants defined over $\mathcal{T}_h$, and V_h as the space of (discontinuous) piecewise constants defined over $\hat{\Gamma}_h$. The Raviart–Thomas elements are, by definition, such that the normal components of the vector

fields are continuous across cell facets (edges in 2D, faces in 3D) and thus the flux continuity conditions (4) and (7) hold by construction [56].

This mixed finite element combination is conforming and our numerical experiments indicate that the element pairing is stable and convergent. The scheme can also be compared to the schemes discussed by [57]. Based on the interpolation properties of the lowest-order finite element spaces as described above, we expect to observe first-order convergence for u, $\hat{J}$, and $\hat{v}$ in the respective L^2 norms, and first-order convergence for $\hat{J}$ in the H(div) norm. Higher-order convergence in the L^2 norm of $\hat{J}$ can be recovered by using the Brezzi–Douglas–Marini [58] H(div) elements instead of the Raviart–Thomas family.

In the numerical experiments, this scheme was implemented using the FEniCS finite element library [49, 50].

2.4 Optimal solvers

A common problem in scientific computing is to solve a linear PDE defined on a certain geometry. After applying some sort of discretization characterized by a mesh parameter h, the remaining problem is to solve a linear system of algebraic equations. The linear solution process is usually said to be order optimal provided that the number of floating point operations (FLOPs) required to solve the problem grows linearly in the number of unknowns as h decreases. For self-adjoint, linear PDEs, optimal solvers are well understood (e.g., see the review papers [59, 60] for the theory of saddle point problems). In simulating cardiac tissue, optimal solvers exist for both the monodomain model and the bidomain model (e.g., [61, 62, 11]).

Feynman [63] suggested an alternative, but related, definition of order optimality: Suppose a numerical method is used to simulate a small space–time volume of a physical process and the mesh is refined to convergence. Then computational complexity should only grow linearly as the space–time volume is increased. For our application, this definition is very well suited; we consider a single cell surrounded by an extracellular space, and we carry out numerical simulations to find the mesh resolution in time and space necessary to obtain convergence. Then we define a numerical solution as being order optimal provided that the CPU efforts only increase linearly in the number of biological cells in the computation.

3 Results

In this section, we present applications of the methods introduced above. We start by assessing the accuracy of the numerical methods for a very simple unitless test problem where an analytical solution can be enforced using the method of manufactured solutions. For non-linear membrane dynamics, we explore convergence under mesh refinements. Next, we consider the CPU efforts needed to solve the numerical problems arising from the EMI model and we are particularly interested in the CPU effort per physical cell to understand the scalability of the EMI approach. For the FEM, we also show results for cylindrical geometries. Finally, we

Parameter	Value	Ref.
C_m	1 μF/cm^2	[64]
$C_{1,2}$	1 μF/cm^2	
σ_i	5 mS/cm	[65]
σ_e	20 mS/cm	[7]
v_{rest}	-85 mV	[66]
R_m	10 kΩcm^2	[64]
R_g	0.0015 kΩcm^2	[7]
Δx, Δy, Δz	2 μm	
Δt (PDE part)	0.1 ms	
Δt^* (ODE part)	0.001 ms	

Table 1: Default parameter values used in the simulations. For the parameters used in the Grandi model, we refer to [48].

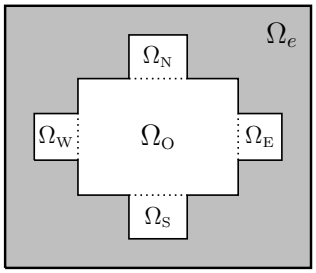

Figure 4: Sketch of the 2D version of a domain in the case of a single cell. Here, $\Omega_i = \Omega_{\text{O}} \cup \Omega_{\text{W}} \cup \Omega_{\text{E}} \cup \Omega_{\text{S}} \cup \Omega_{\text{N}}$.

investigate the effect of non-uniform distributions of sodium channels along the cell membrane.

3.1 Model parameters

In the first unitless test problem we consider a 2D domain consisting of an extracellular domain and a single cell. In the remaining simulations, we consider 3D domains consisting of a number of connected cells and the surrounding extracellular space. The coupled cells are organized as a single layer where the cells are connected to each other in a grid in the x and y directions by gap junctions. The shape and size of the cells and the extracellular domain will be specified for each simulation below. We primarily consider cells of the shape illustrated in Figure 4, where each part of the intracellular domain, $\Omega_{\text{O}}, \Omega_{\text{W}}, \Omega_{\text{E}}, \Omega_{\text{S}}$, and Ω_{N}, is shaped as a rectangular cuboid.

The parameter values used in the simulations are given in Table 1 unless otherwise specified. Moreover, we use the initial condition $w = 0$ in all the simulations of connected cells. When the Grandi model is used to model I_{ion}, we mainly use the default initial conditions of the Grandi model for v and the remaining state variables. When a passive model is used for I_{ion}, we primarily use the initial condition $v = v_{\text{rest}}$.

3.2 Numerical verification and accuracy

3.2.1 Linear ionic current: Method of manufactured solutions

To evaluate the accuracy of the numerical methods, we construct an analytical solution for a 2D single-cell version of the EMI model with the passive model $I_{\text{ion}} = v$. The analytical solution of this simple example is constructed using the method of manufactured solutions (e.g., [67]). We consider a single cell surrounded by extracellular space:

$$\nabla \cdot \sigma_i \nabla u_i = f, \text{ in } \Omega_i, \tag{24}$$
$$\nabla \cdot \sigma_e \nabla u_e = g, \text{ in } \Omega_e, \tag{25}$$
$$u_e = 0, \text{ at } \partial\Omega_e, \tag{26}$$
$$n_e \cdot \sigma_e \nabla u_e = -n_i \cdot \sigma_i \nabla u_i, \text{ at } \Gamma, \tag{27}$$
$$u_i - u_e = v, \text{ at } \Gamma, \tag{28}$$
$$I_m = -n_i \cdot \sigma_i \nabla u_i, \text{ at } \Gamma, \tag{29}$$
$$v_t = \frac{1}{C_m}(I_m - I_{\text{ion}}), \text{ at } \Gamma. \tag{30}$$

For this case, we assume that the model is unitless with parameters $\sigma_i = \sigma_e = C_m = 1$, and we define the domain $\Omega = \Omega_i \cup \Omega_e = [0,1] \times [0,1]$, where $\Omega_i = [0.25, 0.75] \times [0.25, 0.75]$.

We let

$$f = f(x,y,t) = -8\pi^2 \sin(2\pi x)\sin(2\pi y)(1 + e^{-t}), \tag{31}$$
$$g = g(x,y,t) = -8\pi^2 \sin(2\pi x)\sin(2\pi y) \tag{32}$$

and the analytical solution of (24)–(30) is then given by

$$u_i(x,y,t) = (1 + e^{-t})\sin(2\pi x)\sin(2\pi y), \tag{33}$$
$$u_e(x,y,t) = \sin(2\pi x)\sin(2\pi y), \tag{34}$$
$$v(x,y,t) = e^{-t}\sin(2\pi x)\sin(2\pi y). \tag{35}$$

In the numerical experiments of this test case, we use $\Delta t = 0.01/n$, where for the FDM, n equals the number of intervals in each direction of the spatial discretization of the domain. In the FEM case, $2n^2$ is the number of triangles that constitute the uniformly discretized mesh. We note that the chosen time step criterion is not necessary for numerical stability of any of the methods. Rather, it

n	$\|u-u_h\|_\infty$	$\|v-v_h\|_\infty$
16	3.24E-01(--)	1.21E-01(--)
32	1.73E-01(0.91)	7.24E-02(0.75)
64	9.32E-02(0.89)	3.98E-02(0.86)
128	4.80E-02(0.96)	2.09E-02(0.93)
256	2.43E-02(0.98)	1.07E-02(0.96)
512	1.22E-02(0.99)	5.44E-03(0.98)

Table 2: Convergence of the finite difference method for the manufactured test problem with convergence rates in parentheses. The convergence rates in row i are computed by $r = \frac{\log(E_i/E_{i-1})}{\log(h_i/h_{i-1})}$, where E_i is the maximum error of u or v in row i and h_i is the value of $h = \Delta x = \Delta y = 100\Delta t$ used in the simulation in row i.

was selected to yield more stable convergence rates. For this test case, the linear systems arising in the experiments are solved by direct solvers (LU factorization), and the errors are computed at time $t = 0.1$.

Table 2 shows the maximum error of the finite difference method as the discretization parameters are refined. We observe that the convergence rates of the intracellular and extracellular potentials u_h and the membrane potential v_h are both close to one, indicating that the maximum (L^∞) error of the FDM is $O(h)$.

In Table 3, we report the results obtained with the mortar FEM. The error of the potentials u_h is reported in the broken H^1 norm $\|u-u_h\|_1$, which is natural for the problem [53], the L^2 norm $\|u-u_h\|_0$ to enable comparison with the H(div) FEM, and the supremum norm $\|u-u_h\|_\infty$ to allow for comparison across different numerical methods. The error in the current density J_h is measured in the L^2 norm rather than the natural but more involved $H^{-1/2}$ norm. Finally, we report convergence of the membrane potential difference $\|v-v_h\|_\infty$, where v_h is obtained from the definition $u_{i,h} - u_{e,h} = v_h$ using the computed potentials. We note that the integral norms are evaluated by first interpolating the error in the space of discontinuous fourth-order polynomials. The supremum norms are then computed using linear polynomials.

Using piecewise linear elements, the observed convergence rates in the integral norms (see the first three columns of Table 3), are 1.0 (optimal) and 1.73 (slightly suboptimal) for the broken H^1 norm and the L^2 norm of potentials, respectively, while order 2 can be seen in the L^2 norm of the current density. We note that the suboptimal rate of convergence is due to the error being dominated by the temporal discretization and decreasing the time step restores the optimal quadratic convergence. Let us also note that the quadratic convergence of the current density is likely related to the fact that $I_m = 0$ in the test case. The observed order of convergence in the supremum norms is 1.59 and 1.56 for u_h and v_h, respectively. However, the error here seems again to be dominated by temporal discretization, since using $\Delta t = 10^{-3}/n$ improves the rates towards 2.0.

n	$\|u-u_h\|_1$	$\|u-u_h\|_0$	$\|J-J_h\|_0$	$\|u-u_h\|_\infty$	$\|v-v_h\|_\infty$
16	1.11E+00(--)	2.85E-02(--)	1.45E-01(--)	6.36E-02(--)	5.03E-02(--)
32	5.59E-01(0.98)	7.37E-03(1.95)	4.01E-02(1.86)	2.09E-02(1.60)	1.82E-02(1.47)
64	2.80E-01(1.00)	1.90E-03(1.96)	1.05E-02(1.94)	6.73E-03(1.64)	6.22E-03(1.54)
128	1.40E-01(1.00)	4.99E-04(1.93)	2.65E-03(1.98)	2.15E-03(1.65)	2.08E-03(1.58)
256	7.02E-02(1.00)	1.38E-04(1.86)	6.66E-04(1.99)	6.93E-04(1.63)	6.90E-04(1.59)
512	3.51E-02(1.00)	4.16E-05(1.73)	1.66E-04(2.00)	2.31E-04(1.59)	2.34E-04(1.56)

Table 3: Convergence of the mortar finite element method for the manufactured test problem with convergence rates in parentheses.

n	$\|u-u_h\|_0$	$\|\hat{J}-\hat{J}_h\|_0$	$\|\hat{J}-\hat{J}_h\|_{\text{div}}$	$\|v-v_h\|_0$	$\|u-u_h\|_\infty$	$\|v-v_h\|_\infty$
16	8.41E-02(--)	6.49E-01(--)	6.62E+00(--)	1.02E-01(--)	2.73E-02(--)	2.53E-03(--)
32	4.21E-02(1.00)	3.24E-01(1.00)	3.32E+00(0.99)	5.13E-02(1.00)	6.87E-03(1.99)	6.36E-04(1.99)
64	2.11E-02(1.00)	1.62E-01(1.00)	1.66E+00(1.00)	2.56E-02(1.00)	1.72E-03(2.00)	1.57E-04(2.02)
128	1.05E-02(1.00)	8.10E-02(1.00)	8.31E-01(1.00)	1.28E-02(1.00)	4.30E-04(2.00)	3.76E-05(2.06)
256	5.27E-03(1.00)	4.05E-02(1.00)	4.16E-01(1.00)	6.41E-03(1.00)	1.08E-04(2.00)	8.63E-06(2.12)
512	2.63E-03(1.00)	2.03E-02(1.00)	2.08E-01(1.00)	3.21E-03(1.00)	2.69E-05(2.00)	1.77E-06(2.29)

Table 4: Convergence of the H(div) finite element method for the manufactured test problem, with convergence rates in parentheses.

Domain	Size
Ω_{O}	36 μm $\times$ 16 μm $\times$ 16 μm
$\Omega_{\mathrm{W}}, \Omega_{\mathrm{E}}$	8 μm $\times$ 8 μm $\times$ 8 μm
$\Omega_{\mathrm{S}}, \Omega_{\mathrm{N}}$	20 μm $\times$ 8 μm $\times$ 8 μm
$\Omega_i \cup \Omega_e$	120 μm $\times$ 48 μm $\times$ 32 μm

Table 5: The cell and domain sizes used in the simulations reported in Figure 5. The intracellular domain consists of two connected cells, where each cell is a composition of the domains $\Omega_{\mathrm{O}}, \Omega_{\mathrm{W}}, \Omega_{\mathrm{E}}, \Omega_{\mathrm{S}}$, and Ω_{N} (see Figure 4). Note that the geometry used in the remaining 3D simulations is specified in Tables 6 and 10.

Table 4 reports the errors and convergence rates for the H(div)-based FEM. The error in the computed intracellular and extracellular potentials u_h and the error in the membrane potential v_h are reported in the L^2 norm and in the supremum norm. Furthermore, the error in the computed potential gradient $\hat{J}_h$ is reported in the L^2 and H(div) norms. We observe that the convergence rate is one both for the error in the L^2 norm for u_h and v_h and for the H(div) and L^2 norms for $\hat{J}_h$. These rates are in complete agreement with the theoretical expectations. In addition, we observe that the convergence of the supremum norm of u_h and v_h, computed after a projection onto continuous piecewise linears, appears to be close to quadratic.

3.2.2 Nonlinear ionic current: Mesh refinement

To investigate the accuracy of the numerical methods using the Grandi AP model, we compare the solutions obtained from the numerical methods using different spatial resolutions.

Figure 5 shows the solution of the membrane potential in a single point on the membrane for the FDM and the H(div)-based FEM for a number of resolutions. We consider the solution for two connected cells; and the sizes of the cells and the domain used in the simulations are given in Table 5.

In the upper panel of Figure 5, the solutions for different resolutions are almost indistinguishable, but in the lower panel we focus on a small part of the solution and a difference is visible for the different resolutions of the FDM. The H(div) FEM solutions are very similar for different resolutions, indicating that the method is more accurate than the FDM in this case as well.

3.3 CPU requirements

As mentioned in the Introduction, simulation of the electrophysiology of cardiac tissue is usually based on homogenized models such as the monodomain model or the bidomain model. The motivation for this is certainly that it requires considerably less computing power than the EMI approach considered here. Therefore, it

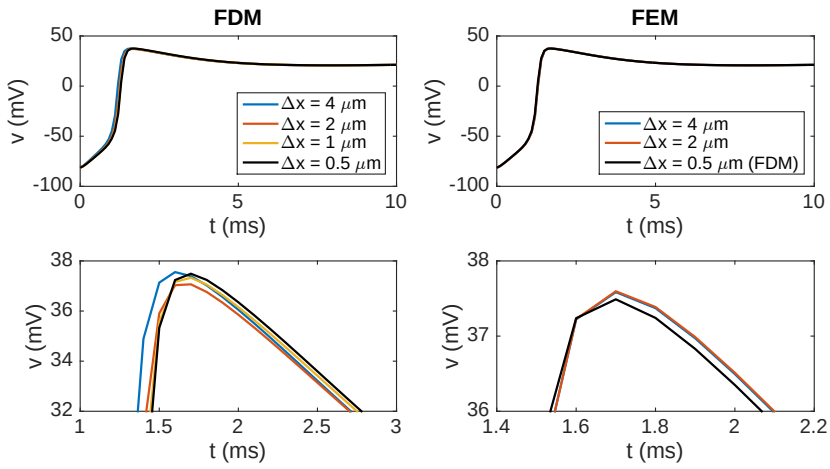

Figure 5: Membrane potential at the point (112 μm, 24 μm, 16 μm) for the finite difference and the finite element methods for two connected cells for some different values of $\Delta x = \Delta y = \Delta z$. The upper panel shows the solution from $t = 0$ ms to $t = 10$ ms. In the lower panel, we zoom in on the peak to observe a difference between the solutions. Note that the scaling of the y axis is different for the two plots in the lower panel and that the FEM solutions for $\Delta x = 4$ μm and $\Delta x = 2$ μm are almost indistinguishable in the lower right plot. The parameter values used in the simulations are given in Tables 1 and 5, and we apply a 1-ms-long stimulus current of 120 μA/μF for the first 24 μm of the first cell.

is very important to understand the computational complexity of the EMI model to appreciate the applications in which this approach can be used.

3.3.1 Finite difference method

Tables 7 and 8 report the CPU times, number of iterations, and system size for the FDM as the number of cells included in the simulation is increased. In Table 7, we use the passive model (10) for I_{ion}, and in Table 8, we use the Grandi AP model. The linear systems are solved using the BiCGStab method (see [68, 69]) with an incomplete LU preconditioner (e.g., [68]) and relative tolerance of 10^{-5} for the *true/unpreconditioned* (l^2) norm of the residuum. The computations are performed using MATLAB. The last column of the tables reports the simulation time per cell for a single time step and we observe that the simulation time *per physical cell* appears to be bounded as the number of cells is increased.

Domain	Size
Ω_{O}	100 μm $\times$ 12 μm $\times$ 12 μm
$\Omega_{\mathrm{W}}, \Omega_{\mathrm{E}}$	4 μm $\times$ 8 μm $\times$ 8 μm
$\Omega_{\mathrm{S}}, \Omega_{\mathrm{N}}$	60 μm $\times$ 4 μm $\times$ 8 μm

Table 6: Cell sizes used in the simulations reported in Figures 7, 8 and 9 and Tables 7, 8, and 9. The intracellular domain consists of a number of connected cells where each cell is a composition of the domains $\Omega_{\mathrm{O}}, \Omega_{\mathrm{W}}, \Omega_{\mathrm{E}}, \Omega_{\mathrm{S}}$, and Ω_{N} (see Figure 4). The size of $\Omega = \Omega_i \cup \Omega_e$ is $L_x \times L_y \times L_z$, where $L_z = 20$ μm and L_x and L_y depend on the number of cells in the simulation. The minimal distance between the intracellular domain and the boundary of the extracellular domain is 8 μm in both the x and y directions.

Cells	Grid points	System size	n_{it}	T (s)	T/cell (s)
1	13 167	14 609	44	0.5	0.5
4	37 323	42 563	122	3.9	1.0
16	121 275	141 179	146	7.2	0.5
64	431 739	509 243	198	24.3	0.4
256	1 622 907	1 928 699	256	86.4	0.3
1 024	6 286 203	7 500 923	258	328.7	0.3
4 096	24 736 635	29 578 619	250	1 195.9	0.3
16 384	98 132 859	117 467 003	209	3 696.8	0.2

Table 7: CPU times for the finite difference method for a passive membrane model. Here, n_{it} is the number of iterations in the fourth time step of size $\Delta t = 0.1$ ms and T is the solution time for the fourth time step. The parameters used in the computations are given in Table 1 and the domain sizes are specified in Table 6. For the 25% of the cells at the center of the domain, we use the initial condition $v = 10$ mV and, for the remaining cells, we use the initial condition $v = v_{\mathrm{rest}}$.

Cells	Grid points	System size	n_{it}	T_{ODE} (s)	T_{PDE} (s)	T (s)	T/cell (s)
1	13 167	14 609	64	2.9	0.7	3.6	3.6
4	37 323	42 563	150	7.6	4.5	12.1	3.0
16	121 275	141 179	210	23.9	12.7	36.5	2.3
64	431 739	509 243	260	85.1	41.5	126.6	2.0
256	1 622 907	1 928 699	318	351.9	109.8	461.7	1.8
1 024	6 286 203	7 500 923	338	1 256.0	442.6	1 698.6	1.7
4 096	24 736 635	29 578 619	322	4 512.8	1 515.8	6 028.6	1.5
16 384	98 132 859	117 467 003	360	17 594.6	6 171.9	23 766.5	1.5

Table 8: CPU times for the finite difference method using the Grandi membrane model for I_{ion}. Here, $T = T_{\mathrm{ODE}} + T_{\mathrm{PDE}}$ is the solution time for the fourth time step of size $\Delta t = 0.1$ ms, where T_{ODE} is the solution time for the first (ODE) part of the operator splitting procedure and T_{PDE} is the solution time for the second (PDE) part of the procedure. Furthermore, n_{it} is the number of iterations needed to achieve convergence of the BiCGStab method used in the PDE part of the procedure. The parameters used in the computations are given in Tables 1 and 6. For the 25% of the cells at the center of the domain, we replace the default initial conditions of the Grandi model with the values of the state variables obtained when the membrane potential first reached $v = -10$ mV during the upstroke of the AP in a single-cell simulation of the model. For the remaining cells, we use the default initial conditions of the Grandi model.

Cells	$\dim(S_h)$	$\dim(U_h)$	$\dim(V_h\|_{\Gamma_h})$	$\dim(M_h)$	n_{it}	T (s)	T/cell (s)
1	137 752	66 960	3 216	342 464	74	6.1	6.1
4	399 136	194 880	12 320	993 152	220	49.8	12.5
16	1 317 184	645 120	48 192	3 279 488	458	337.6	21.1
64	4 734 400	2 323 200	190 592	11 792 000	637	1 684.8	26.3

Table 9: CPU times for the H(div) finite element method for a passive membrane model. Here, n_{it} is the number of iterations in the fourth time step of size $\Delta t = 0.1$ ms and T is the solution time for the fourth time step. Furthermore, T/cell is the solution time per cell for the fourth time step. The second to fifth columns give the dimensions of the various finite element spaces (see Section 2.3.3). Note that $V_h|_{\Gamma_h}$ refers to the space V_h restricted to the membrane Γ_h but that V_h is defined in the entire domain in the computations reported in the table. Note also that $\dim(M_h)$ refers to the dimension of the total mixed space $U_h \times S_h \times V_h$. The parameters used in the computations are given in Tables 1 and 6. For the 25% of the cells at the center of the domain, we use the initial condition $v = 10$ mV and, for the remaining cells, we use the initial condition $v = v_{\text{rest}}$.

3.3.2 Finite element method

Because of the complexity of the mortar FEM, which introduces a separate function space for the potential of each cell[1] Ω_i^k, we shall focus on the H(div) FEM in the following.

Table 9 shows the CPU time, the number of iterations, and the dimensions of the finite element spaces for a number of simulations using the H(div) FEM described in Section 2.3.3 with an increasing number of cells and a passive membrane model. The linear systems are again solved using the biconjugate gradient stabilized method with an incomplete LU preconditioner and a convergence criterion as in the FDM case. The linear solver and the preconditioner were provided by the PETSc library [70], while the system was assembled using FEniCS [49, 50].

Since the definition of the H(div)-based variational problem (21) in FEniCS is not immediately obvious, we briefly comment on some implementational aspects. Recall that the solution is sought in the space $U_h \times S_h \times V_h$, where the functions in V_h are defined over $\hat{\Gamma}_h$, the discretization of the cell mebranes Γ. However, FEniCS (version 2017.1) does not currently support mixed spaces with components defined over different meshes, such as over $\mathcal{T}_h$ and $\hat{\Gamma}_h$. To bypass this restriction, we construct the space V_h over all the facets of $\mathcal{T}_h$ and the excess degrees of freedom are set to zero in the assembled linear system. As illustrated above the construction yields the correct numerical solution. However, the additional degrees of freedom naturally affect the performance of the linear solvers, since they increase the computational cost of the matrix–vector product significantly. FEniCS support for mixed finite element spaces with components defined over different meshes is currently under development and we thus expect this issue to be resolved in future FEniCS releases.

Comparing the results of Table 9 with those of the FDM (see Table 7), we observe that the CPU times for the FEM are considerably larger (by a factor of $\sim$70). While the longer solution times for the FEM are expected due to the larger linear systems stemming from the method (with factors of $\sim$23 and $\sim$14 for the system with or without the additional degrees of freedom introduced in V_h, respectively), the results also point out that the iterative solver does not perform as well as in the FDM case. More efficient solution strategies for the system are currently being investigated.

3.4 Cylindrical geometry

The somewhat clunky geometry of the cells used above does not reflect reality very well. Indeed, cardiac cells have cylindrical shapes, but such shapes are inconvenient to address using FDMs, and we therefore apply the FEM. Figure 6 shows the membrane potential and surrounding extracellular potential for a simulation of two connected cylinders using the parameters given in Tables 1 and 10. We note that the FEM is well suited for handling cylindrical geometry, and we expect that

[1] The space for intracellular potentials for the case considered with FDM in the section 3.3.1 would be $V_i^1 \times V_i^2 \times \cdots \times V_i^n$ where $n = 16384$.

Length of Ω_{O}	100 μm
Radius of Ω_{O}	10 μm
Length of Ω_{W} and Ω_{E}	4 μm
Radius of Ω_{W} and Ω_{E}	8 μm
Domain $(\Omega_i \cup \Omega_e)$	228 μm $\times$ 40 μm $\times$ 40 μm

Table 10: Cell and domain sizes used in the simulations of the two connected cylinders in Figure 6. The intracellular domain consists of two cells, where each cell is a composition of three cylinders Ω_{W}, Ω_{O}, and Ω_{E}.

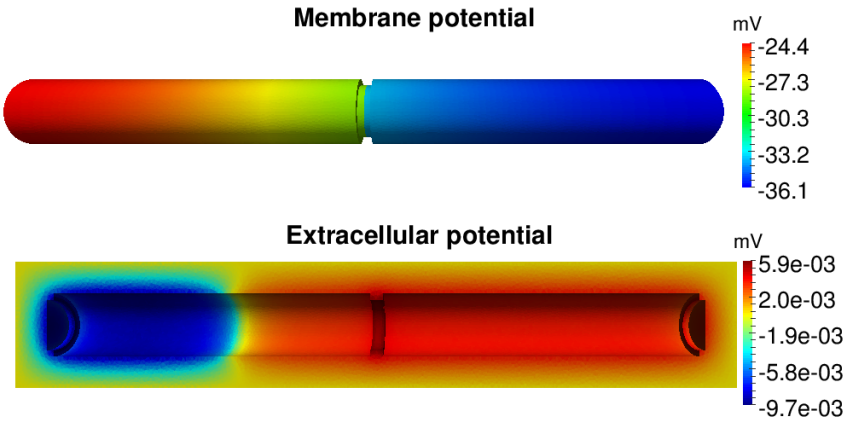

Figure 6: Membrane potential and the surrounding extracellular potential of two connected cylinders at time $t = 1$ ms computed by the H(div) FEM. The parameters used in the simulations are given in Tables 1 and 10 and we apply a stimulus current of 120 μA/μF for the first half of the first cell in the x direction.

the method can also be used to handle the even more complex geometries that will arise when the T-tubules of ventricular cells (e.g., [71]) are incorporated in the model.

3.5 Ion channel density distribution affects conduction velocity

As mentioned in the Introduction, it is difficult to represent a non-uniform distribution of ion channels along the cell membrane using classical homogenized models. This is an important shortcoming of the classical methods, because a non-uniform distribution of sodium channels is believed to affect the conduction velocity. In the EMI modeling framework, the representation of non-uniform distributions of ion channels is straightforward.

Figure 7 shows the solutions of two simulations of a collection of 30 $\times$ 5 cells

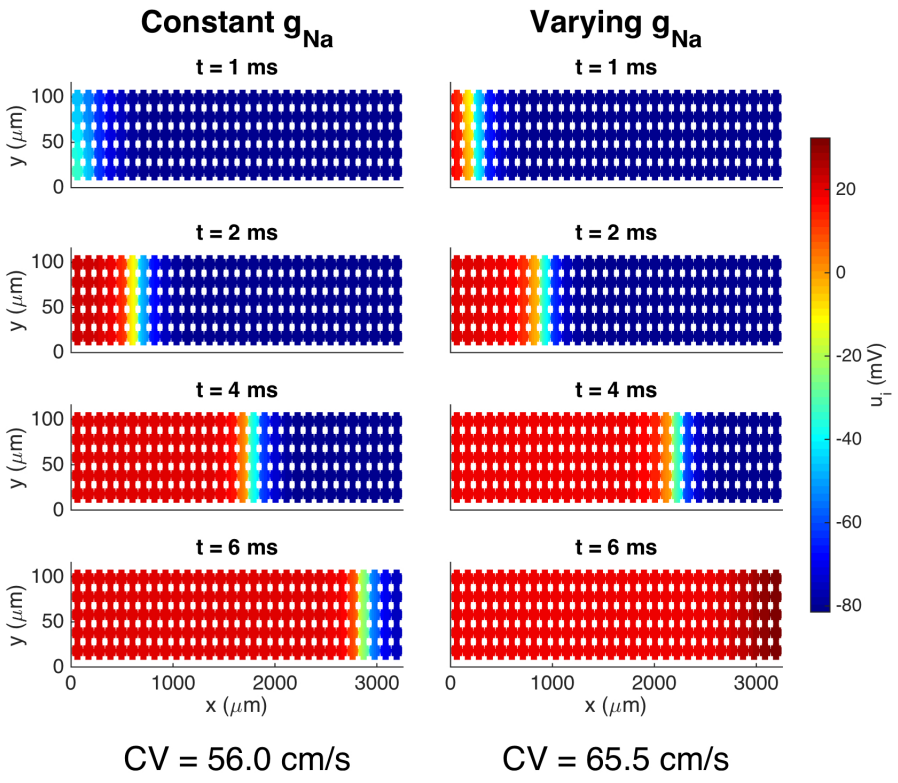

Figure 7: Intracellular potential at four points in time for a collection of cells with two different distributions of the sodium channel conductance. In the case of a constant g_{Na}, the value is $g_{\mathrm{Na}} = 23$ mS/μF on the entire membrane, and in the case of a varying g_{Na}, the value is $g_{\mathrm{Na}} = 783$ mS/μF on Ω_{W} and Ω_{E} and zero elsewhere. The solutions are obtained using the FDM and the parameters used in the simulations are given in Tables 1 and 6, except that we use $\Delta t = 0.01$ ms. We apply a 1-ms-long stimulus current of 120 μA/μF for the 2×2 cells in the lower left corner of the domain.

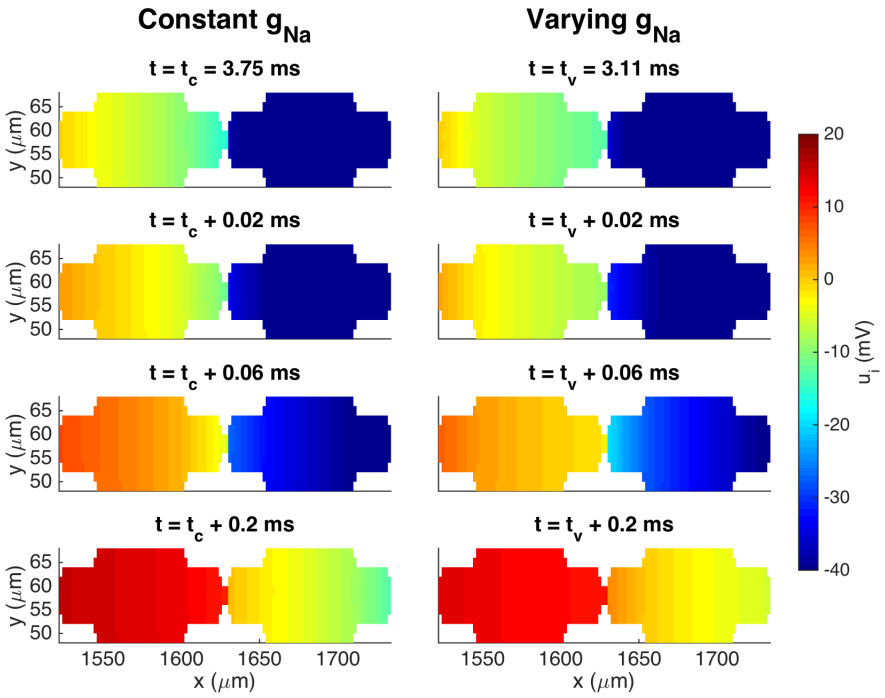

Figure 8: Intracellular potentials at four points in time for the two cells at the center of the domain from the simulation in Figure 7. The plots in the upper panel show the solutions at the last point in time before the intracellular potential at the start of the first cell is first positive. Because the conduction velocity is different in the two cases, this occurs at two different points in time, t_c and t_v, for the cases with a constant g_{Na} and a varying g_{Na}, respectively. The next plots show the solutions at times 0.02 ms, 0.06 ms, and 0.2 ms after t_c and t_v.

with different distributions of the sodium channel conductance, g_{Na}. In the left panel the value of g_{Na} is constant on the entire membrane, while, in the right panel, g_{Na} is zero over a large part of the membrane and only non-zero on Ω_{W} and Ω_{E}, that is, near the ends of the cell in the x direction. The mean value of g_{Na} over the cells is the same in the two simulations. We observe that the conduction velocity is increased for the case with a varying value of g_{Na} compared to the case with a constant value. The conduction velocities reported in the figure are computed from the 10th and 20th cells in the third row in the y direction, and are defined as the distance between the cell centers divided by the time between each of the two cell centers reaches a membrane potential of $v = 0$ mV.

Figure 8 shows a more detailed view of the two cells at the center of the domain. Here, we observe that the conduction velocity across the first part of the cell appears to be higher for the case with a constant value of g_{Na} than for

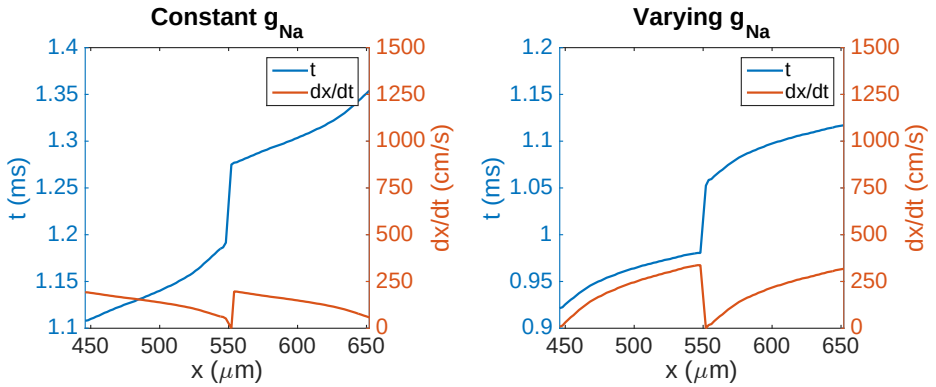

Figure 9: Activation times and conduction velocities along the length of two cells in a simulation of 10 $\times$ 1 cells with different distributions of g_{Na}, similar to the simulations shown in Figure 7. The blue line shows the points in time when the membrane nodes corresponding to each x-value along cells number five and six first reach a membrane potential of 0 mV. The orange line shows the corresponding conduction velocity along the two cells, computed from a piecewise second order polynomial approximation of the activation curves. The parameters used in the simulations are given in Tables 1 and 6, except that we use $\Delta t = 0.0005$ ms. Note that the values of the left y-axis (representing activation time) is different in the two plots, but that the scaling of the axis is the same in both plots.

the varying case, but that the traveling wave moves faster across the gap junction for the case with a varying g_{Na} than for the constant case, leading to an overall increased conduction velocity for the varying case.

This effect is studied more closely in Figure 9, which shows the activation times and conduction velocities along the length of two cells in a similar pair of simulations. The gap junction between the two cells is located at $x = 548$ μm, and we observe that there is a delay of about 0.1 ms between when the membrane on each side of the gap junction is activated. The delay appears to be slightly longer for the case with a constant g_{Na} compared to the varying case. We also observe that, overall, the wave uses less time to activate the two cells for the case with a varying g_{Na} than for the constant case, consistent with the results of Figures 7 and 8. In addition, we observe that the shape of the activation curve is different in the two cases. In the case with a constant g_{Na} distribution, the activation curve becomes steeper towards the end of the cells, corresponding to a decreasing conduction velocity along the cell lengths. For the varying case, however, the activation curve flattens out towards the end of the cells, corresponding to an increased conduction velocity towards the cell ends.

4 Discussion

As described above, the classical models of cardiac tissue are founded on homogenization of the tissue and the resulting models therefore assume that the extracellular space, the cell membrane, and the intracellular space exist everywhere. This leads to tractable computing problems that have provided insights into important applications such as the propagation of an electrochemical wave, cardiac arrhythmias, the effect of defibrillation, the onset of cardiac waves, and the effect of diverse drugs. However, in some cases, it is of interest to see the dynamics surrounding individual cells as part of the tissue, which is hard to do using homogenized models. It is also of interest to be able to change local properties of the tissue that are difficult to represent in homogenized models.

In the present report, we focused on the computational challenges of a different approach in which separate geometrical domains for the extracellular space, the cell membrane, and the intracellular domain represent the tissue; we refer to this as the EMI model. Clearly, the computational problems arising from the EMI model are much more challenging than for traditional models, but we have shown that, for some applications, the more detailed model is feasible. In particular, we have shown that the EMI model is suitable for monolayers of cells. Furthermore, we have demonstrated that the EMI framework allows the representation of local properties of cells that are hard to represent in classical homogenized models of cardiac tissue.

4.1 Membrane dynamics

The dynamics of the cell membrane are absolutely critical for the functioning of the cell and have been subject to intense studies for centuries. A wide variety of models are available through the open CellML library [72]. In our computations, we have used the ventricular cell model by Grandi et al. [48]. That model consists of a system of 39 ODEs defined on every computational node of the cell membrane and is believed to provide an accurate representation of the cell's action potential. From a computational point of view, we could have used numerous other models (e.g., [73, 74, 75, 76, 77, 78, 79, 80]) with comparable complexity of the membrane computations. Common to all these models is that the ion currents are represented using models where the ion channel density must be specified. When the models are used as part of a monodomain or bidomain model, the channel density is most conveniently treated as a constant for each cell, but in the EMI model, the ion channel density associated with any of the currents can be specified as a function of space on the cell membrane. We noted in Figure 7 that a non-uniform distribution of sodium channels significantly affects the tissue's conduction velocity.

4.2 Numerical accuracy

The numerical accuracy of the discretizations considered was assessed using a single-cell problem (24)–(30) and the method of manufactured solutions. As seen

in Tables 2, 3 and 4, all the discretizations provide converging numerical solutions. However, taking the L^∞ norms of the computed potentials for comparison, there are considerable differences in the convergence properties of the methods.

The convergence of the FDM discretization is linear and this method is the least accurate. The first order convergence of the FDM is to be expected, since all internal boundary conditions are approximated using first-order finite differences. Compared to the FDM, the mortar FEM yields solutions with considerably smaller error and the observed rates are about 1.5. It should be noted that, on a given grid, the methods lead to identical numbers of unknowns. The H(div) FEM is the most accurate among the methods considered with errors much smaller than those of the mortar FEM. As noted in Section 3.3, the H(div) FEM leads to larger linear systems than the other two methods do (see Tables 7 and 9). Finally, let us note that the manufactured solution employed was particularly simple and thus the numerical results obtained may not be universally valid.

4.3 CPU requirements

The CPU efforts needed to solve the system (1)–(9) using the FDM or the FEM are given in Table 7 (FDM, passive membrane dynamics), Table 8 (FDM, membrane dynamics given by the Grandi model), and Table 9 (H(div) FEM, passive membrane dynamics). We observe that, for the FDM, the CPU efforts per cell seem to be bounded independently of the number of cardiac cells. This result implies that the solver is optimal in the sense defined above. When the Grandi model is used for the membrane dynamics, the CPU efforts per time step per cell are around 1.5 second. This enables us to simulate 16,384 cells, which defines a linear system with over 117 million unknowns. Since the CPU efforts per cell seem to be bounded independent of the number of cells, the CPU efforts will not explode as more cells are added to the computations. With proper parallelization strategies, it should be possible to simulate huge numbers of cells. In fact, the mouse heart, with around 4 million cells, may be within reach; with a computer that is 1000 times faster (for large problems) than the one we used, it would require about one week to perform 100 time steps for 4 million cardiac cells.

We observe from Tables 8 and 9 that the FDM method in the current implementation is significantly faster than the FEM code even though the FDM code is implemented in Matlab. It has proven to be difficult to derive optimal preconditioners to be used for the FEM, but we hope to be able to improve this part of the code in the future.

4.4 Cell geometry

In the present report, we have used very simple geometries to represent the cells. We have assumed that the geometries are simple rectangular cuboids or have cylindrical shapes. However, real cardiac cells have much more complex geometries and future work will investigate the effect of the geometry on the solutions. Of particular importance is the effect of T-tubules in ventricular cells and how they

change during illness (e.g., [81, 71]). The diameter of the T-tubules ranges from 20 nm to 450 nm (see [82]) and therefore a very fine computational mesh would be needed to represent these invaginations. Presently, we have run the FDM code with spatial resolution of 5 nm (in the case of only three coupled cells), so including T-tubules is within reach for the FDM code but not for the FEM code.

4.5 Intracellular calcium dynamics

The focus of the present report has been to show that it is possible to simulate the electrical potential of cardiac cells based on explicit representation of the cells. We have focused on models that represent the membrane dynamics in terms of interchange over the cell membrane and we have ignored the spatial gradients of the ionic concentrations away from the cell membrane. Certainly, this is a major simplification; the intracellular concentration of calcium is essential and can be modelled using partial differential equations defined in the intracellular domain, see e.g. [83, 84, 85, 86]. In [83], a model based on Calcium released units (CRUs) is presented and the number of CRUs for a single cell used in the computations is typically ~ 20.000. In our model, a cardiac cell with a volume of 30 pL and a typical mesh length of 1 μm would consist of 30.000 computational blocks within each cell. A reasonable representation of the CRUs in the EMI model is therefore within reach.

4.6 Conduction velocity

As mentioned above, the conduction velocity is essential for the stability of the electrochemical wave underpinning the rhythmic contraction of the cardiac muscle. In numerical computations, the distribution of ion channels is usually assumed to be constant, but experimental evidence suggests that the ion channel density is non-uniform along the cell membrane. For instance, the density of sodium channels is believed to be much higher closer to the intercalated discs separating individual cells (e.g., [87]). The difference between uniform and non-uniform distributions of sodium channels was addressed in Figures 7–9. We observed that the conduction velocity was significantly lower in the case of a constant distribution of the sodium channels compared to the case of a non-uniform distribution. Interestingly, we also observed (Figure 9) that for the uniform case, the conduction velocity decreased along the cell, whereas it increased in the case of non-uniform distribution. Again, such effects are difficult to observe in the classical models (monodomain, bidomain). This effect deserves closer scrutiny and the EMI model provides a suitable framework for such studies.

5 Conclusion

Local properties of cells and cell membranes are difficult to represent in standard (bidomain, monodomain) models of excitable tissue. In this paper, we have demonstrated that a more accurate model and method can be used. In our approach, every cell is represented in terms of its surrounding extracellular space, the cell membrane, and the intracellular space. The extracellular and intracellular spaces are represented using a mesh of length of 2 μm and the membrane is represented as the intersection of the extracellular and intracellular meshes. We have seen that, with a finite difference method using a very simple geometry, the computations are quite efficient and the computational demands increase linearly in the number of physical cells. We have solved for up to 16,384 cells using this method. More complex geometries must be represented using a method allowing flexible grids and, in the present paper, we have shown the results for two variants of the finite element method. Although, the solution process of the finite element equations is much more time-consuming, the results indicate that more complex cell geometries can, in fact, be handled.

References

[1] Hervé Hogues, L Joshua Leon, and Fernand A Roberge. A model study of electric field interactions between cardiac myocytes. *IEEE transactions on biomedical engineering*, 39(12):1232–1243, 1992.

[2] Wanda Krassowska and John C Neu. Response of a single cell to an external electric field. *Biophysical Journal*, 66(6):1768, 1994.

[3] Wenjun Ying and Craig S Henriquez. Hybrid finite element method for describing the electrical response of biological cells to applied fields. *IEEE Transactions on Biomedical Engineering*, 54(4):611–620, 2007.

[4] Andres Agudelo-Toro and Andreas Neef. Computationally efficient simulation of electrical activity at cell membranes interacting with self-generated and externally imposed electric fields. *Journal of Neural Engineering*, 10(2):026019, 2013.

[5] Jeroen G Stinstra, Craig S Henriquez, and Rob S MacLeod. Comparison of microscopic and bidomain models of anisotropic conduction. In *Computers in Cardiology, 2009*, pages 657–660. IEEE, 2009.

[6] Jeroen G Stinstra, Rob S MacLeod, and Craig S Henriquez. Incorporating histology into a 3D microscopic computer model of myocardium to study propagation at a cellular level. *Annals of Biomedical Engineering*, 38(4):1399–1414, 2010.

[7] Jeroen G Stinstra, Bruce Hopenfeld, and Rob S MacLeod. On the passive cardiac conductivity. *Annals of Biomedical Engineering*, 33(12):1743–1751, 2005.

[8] Aslak Tveito, Karoline Horgmo Jæger, Glenn Terje Lines, Łukasz Paszkowski, Joakim Sundnes, Andrew G Edwards, Tuomo Māki-Marttunen, Geir Halnes, and Gaute T Einevoll. An evaluation of the accuracy of classical models for computing the membrane potential and extracellular potential for neurons. *Frontiers in Computational Neuroscience*, 11:27, 2017.

[9] James P Keener and James Sneyd. *Mathematical Physiology*. Springer, 2009.

[10] Piero Colli Franzone, Luca F Pavarino, and Simone Scacchi. *Mathematical Cardiac Electrophysiology*. Springer International Publishing, 2014.

[11] Joakim Sundnes, Bjørn Fredrik Nielsen, Kent-Andre Mardal, Xing Cai, Glenn Terje Lines, and Aslak Tveito. On the computational complexity of the bidomain and the monodomain models of electrophysiology. *Annals of Biomedical Engineering*, 34(7):1088–1097, 2006.

[12] Bradley J Roth. Bidomain simulations of defibrillation: 20 years of progress. *Heart Rhythm*, 10(8):1218–1219, 2013.

[13] Natalia A Trayanova. Whole-heart modeling: Applications to cardiac electrophysiology and electromechanics. *Circulation Research*, 108(1):113–28, 2011.

[14] Edward Vigmond, Fijoy Vadakkumpadan, Viatcheslav Gurev, Hermenegild Arevalo, Makarand Deo, Gernot Plank, and Natalia A Trayanova. Towards predictive modelling of the electrophysiology of the heart. *Experimental Physiology*, 94(5):563–577, 2009.

[15] Aslak Tveito, Glenn T Lines, Robert Artebrant, Ola Skavhaug, and Mary M Maleckar. Existence of excitation waves for a collection of cardiomyocytes electrically coupled to fibroblasts. *Mathematical Biosciences*, 230(2):79–86, 2011.

[16] Aslak Tveito, Glenn T Lines, Andrew G Edwards, Mary M Maleckar, Anushka Michailova, Johan Hake, and Andrew D McCulloch. Slow calcium–depolarization–calcium waves may initiate fast local depolarization waves in ventricular tissue. *Progress in Biophysics and Molecular Biology*, 110(2–3):295–304, 2012.

[17] Yuanfang Xie, Daisuke Sato, Alan Garfinkel, Zhilin Qu, and James N Weiss. So little source, so much sink: Requirements for afterdepolarizations to propagate in tissue. *Biophysics Journal*, 99(5):1408–1415, Sep 2010.

[18] Yuanfang Xie, Alan Garfinkel, James N Weiss, and Zhilin Qu. Cardiac alternans induced by fibroblast-myocyte coupling: Mechanistic insights from computational models. *Heart Circulation Physiology*, 297(2):H775–84, 2009.

[19] Zhilin Qu and Michael Nivala. Multiscale nonlinear dynamics in cardiac electrophysiology: From sparks to sudden death. *Multiscale Analysis and Nonlinear Dynamics: From Genes to the Brain*, pages 257–275, 2013.

[20] Zhilin Qu, Gang Hu, Alan Garfinkel, and James N Weiss. Nonlinear and stochastic dynamics in the heart. *Physics Reports*, 543(2), 2014.

[21] Aslak Tveito and Glenn T Lines. A condition for setting off ectopic waves in computational models of excitable cells. *Mathematical Biosciences*, 213:141–150, 2008.

[22] James P Keener and Alexander V Panfilov. A Biophysical Model for Defibrillation. *Biophysical Journal*, 71(3):1335–1345, 1996.

[23] Gernot Plank, Edward J Vigmond, and L Joshua Leon. Shock energy for successful defibrillation of atrial tissue during vagal stimulation. *Proceedings of the 25th annual International Conference of the IEEE EMBS*, pages 167–170, 2003.

[24] Gernot Plank, L Joshua Leon, Shane Kimber, and Edward J Vigmond. Defibrillation depends on conductivity fluctuations and the degree of disorganization in reentry patterns. *Journal of Cardiovascular Electrophysiology*, 16:205–216, 2005.

[25] Natalia Trayanova and Ed. Jose Jalife Gernot Plank. *Modeling cardiac defibrillation, In: Cardiac Electrophysiology: From Cell to Bedside*, pages 361–372. WB Saunders, Philadelphia, 2009.

[26] Aslak Tveito, Glenn Lines, Marie E Rognes, and Mary M Maleckar. An analysis of the shock strength needed to achieve defibrillation in a simplified mathematical model of cardiac tissue. *International Journal of Numerical Analysis and Modeling*, 9(3):644–657, 2012.

[27] Lukas J Rantner, Brock M Tice, and Natalia A Trayanova. Terminating ventricular tachyarrhythmias using far-field low-voltage stimuli: mechanisms and delivery protocols. *Heart Rhythm*, 10(8):1209–1217, 2013.

[28] Natalia A Trayanova and Lukas J Rantner. New insights into defibrillation of the heart from realistic simulation studies. *Europace*, 16(5):705–713, 2014.

[29] Jonathan D Moreno, Z Iris Zhu, Pei-Chi Yang, John R Bankston, Mao-Tsuen Jeng, Chaoyi Kang, Lianguo Wang, Jason D Bayer, David J Christini, Natalia A Trayanova, Crystal M Ripplinger, Robert S Kass, and Colleen E Clancy. A computational model to predict the effects of class I anti-arrhythmic drugs on ventricular rhythms. *Science Translational Medicine*, 3(98):1–8, 2011.

[30] Blanca Rodriguez, Kevin Burrage, David Gavaghan, Vicente Grau, Peter Kohl, and Dennis Noble. The systems biology approach to drug development: Application to toxicity assessment of cardiac drugs. *Clinical Pharmacology & Therapeutics*, 88:130–134, 2010.

[31] Aslak Tveito, Glenn T Lines, and Mary M Maleckar. Note on a possible proarrhythmic property of antiarrhythmic drugs aimed at improving gap-junction coupling. *Biophysical Journal*, 102:231–237, 2012.

[32] Aslak Tveito and Glenn T Lines. A note on a method for determining advantageous properties of an anti-arrhythmic drug based on a mathematical model of cardiac cells. *Mathematical Biosciences*, 217(2):167–173, 2009.

[33] Rengasayee Veeraraghavan, Robert G Gourdie, and Steven Poelzing. Mechanisms of cardiac conduction: a history of revisions. *Heart and Circulatory Physiology*, 306(5):H619–H627, 2014.

[34] Madison S Spach, J Francis Heidlage, Roger C Barr, and Paul C Dolber. Cell size and communication: role in structural and electrical development and remodeling of the heart. *Heart Rhythm*, 1(4):500–515, 2004.

[35] Yoram Rudy and WeiLun Quan. A model study of the effects of the discrete cellular structure on electrical propagation in cardiac tissue. *Circulation Research*, 61(6):815–823, 1987.

[36] Robin M Shaw and Yoram Rudy. Ionic mechanisms of propagation in cardiac tissue. *Circulation Research*, 81(5):727–741, 1997.

[37] Ning Wei, Yoichiro Mori, and Elena G Tolkacheva. The dual effect of ephaptic coupling on cardiac conduction with heterogeneous expression of connexin 43. *Journal of Theoretical Biology*, 397:103–114, 2016.

[38] Steven Poelzing and David S Rosenbaum. Altered connexin43 expression produces arrhythmia substrate in heart failure. *Heart and Circulatory Physiology*, 287(4):H1762–H1770, 2004.

[39] Joyce Lin and James P Keener. Ephaptic coupling in cardiac myocytes. *IEEE Transactions on Biomedical Engineering*, 60(2):576–582, 2013.

[40] Giorgio Olivetti, Massimo Melissari, Joseph M Capasso, and Piero Anversa. Cardiomyopathy of the aging human heart. myocyte loss and reactive cellular hypertrophy. *Circulation Research*, 68(6):1560–1568, 1991.

[41] Pieter A Doevendans, Mat J Daemen, Ebo D de Muinck, and Jos F Smits. Cardiovascular phenotyping in mice. *Cardiovascular Research*, 39(1):34–49, 1998.

[42] Peter Lee, Matt Klos, Christian Bollensdorff, Luqia Hou, Paul Ewart, Timothy J Kamp, Jianhua Zhang, Alexandra Bizy, Guadalupe Guerrero-Serna, Peter Kohl, et al. Simultaneous voltage and calcium mapping of genetically purified human induced pluripotent stem cell–derived cardiac myocyte monolayersnovelty and significance. *Circulation Research*, 110(12):1556–1563, 2012.

[43] Marica Grskovic, Ashkan Javaherian, Berta Strulovici, and George Q Daley. Induced pluripotent stem cells – Opportunities for disease modelling and drug discovery. *Nature Reviews Drug Discovery*, 10(12):915–929, 2011.

[44] Elena Matsa, Paul W Burridge, and Joseph C Wu. Human stem cells for modeling heart disease and for drug discovery. *Science Translational Medicine*, 6(239):239ps6–239ps6, 2014.

[45] David G Strauss and Ksenia Blinova. Clinical trials in a dish. *Trends in Pharmacological Sciences*, 38(1):4–7, 2017.

[46] Natalia A Trayanova, Bradley J Roth, and Lisa J Malden. The response of a spherical heart to a uniform electric field: a bidomain analysis of cardiac stimulation. *IEEE Transactions on Biomedical Engineering*, 40(9):899–908, 1993.

[47] Steven Niederer, Lawrence Mitchell, Nicolas Smith, and Gernot Plank. Simulating human cardiac electrophysiology on clinical time-scales. *Frontiers in Physiology*, 2(14):1–7, 2011.

[48] Eleonora Grandi, Francesco S Pasqualini, and Donald M Bers. A novel computational model of the human ventricular action potential and Ca transient. *Journal of Molecular and Cellular Cardiology*, 48:112–121, 2010.

[49] Martin S Alnæs, Jan Blechta, Johan Hake, August Johansson, Benjamin Kehlet, Anders Logg, Chris Richardson, Johannes Ring, Marie E Rognes, and Garth N Wells. The FEniCS Project version 1.5. *Archive of Numerical Software*, 3(100), 2015.

[50] Anders Logg, Kent-Andre Mardal, and Garth N Wells. *Automated Solution of Differential Equations by the Finite Element Method: The FEniCS Book*, volume 84. Springer Science & Business Media, 2012.

[51] Christine Bernardi, Yvon Maday, and Antony T Patera. *Domain Decomposition by the Mortar Element Method*, pages 269–286. Springer Netherlands, Dordrecht, 1993.

[52] Faker Ben Belgacem. The mortar finite element method with Lagrange multipliers. *Numerische Mathematik*, 84(2):173–197, 1999.

[53] Bishnu P Lamichhane and Barbara I Wohlmuth. Mortar finite elements for interface problems. *Computing*, 72(3):333–348, 2004.

[54] Barbara I Wohlmuth. A mortar finite element method using dual spaces for the Lagrange multiplier. *SIAM Journal on Numerical Analysis*, 38(3):989–1012, 2000.

[55] Karl Erik Holter, Miroslav Kuchta, and Kent-Andre Mardal. Trace constrained problems in FEniCS. In J. S. Hale, editor, *Proceedings of the FEniCS Conference 2017.*, Jun 2017.

[56] Pierre-Arnaud Raviart and J M Thomas. A mixed finite element method for 2-nd order elliptic problems. *Mathematical aspects of finite element methods*, pages 292–315, 1977.

[57] Riccardo Sacco. Multiscale modeling of interface phenomena in biology. http://www1.mate.polimi.it/ ricsac/NotesCMElBioMath.pdf.

[58] Franco Brezzi, Jim Douglas, and LD Marini. Two families of mixed finite elements for second order elliptic problems. *Numerische Mathematik*, 47(2):217–235, 1985.

[59] Michele Benzi, Gene H Golub, and Jörg Liesen. Numerical solution of saddle point problems. *Acta Numerica*, 14:1–137, 2005.

[60] Kent-Andre Mardal and Ragnar Winther. Preconditioning discretizations of systems of partial differential equations. *Numerical Linear Algebra with Applications*, 18(1):1–40, 2011.

[61] Kent-Andre Mardal, Bjørn Fredrik Nielsen, Xing Cai, and Aslak Tveito. An order optimal solver for the discretized bidomain equations. *Numerical Linear Algebra with Applications*, 14(2):83–98, 2007.

[62] Svein Linge, Joakim Sundnes, Monica Hanslien, Glenn Terje Lines, and Aslak Tveito. Numerical solution of the bidomain equations. *Philosophical Transactions of the Royal Society of London A: Mathematical, Physical and Engineering Sciences*, 367(1895):1931–1950, 2009.

[63] Richard P Feynman. Simulating physics with computers. *International Journal of Theoretical Physics*, 21(6):467–488, 1982.

[64] Silvio Weidmann. Electrical constants of trabecular muscle from mammalian heart. *The Journal of Physiology*, 210(4):1041, 1970.

[65] Wayne E Cascio, Gan-Xin Yan, and Andre G Kleber. Passive electrical properties, mechanical activity, and extracellular potassium in arterially perfused and ischemic rabbit ventricular muscle. effects of calcium entry blockade or hypocalcemia. *Circulation Research*, 66(6):1461–1473, 1990.

[66] Deborah A Jaye, Yong-Fu Xiao, and Daniel C Sigg. Basic cardiac electrophysiology: Excitable membranes. In *Cardiac Electrophysiology Methods and Models*, chapter 2, pages 41–51. Springer, 2010.

[67] Patrick J Roache. *Verification and Validation in Computational Science and Engineering*. Hermosa Albuquerque, NM, 1998.

[68] Owe Axelsson. *Iterative Solution Methods*. Cambridge University Press, 1996.

[69] Henk A Van der Vorst. Bi-CGSTAB: a fast and smoothly converging variant of Bi-CG for the solution of nonsymmetric linear systems. *SIAM Journal on scientific and Statistical Computing*, 13(2):631–644, 1992.

[70] Satish Balay, Kris Buschelman, DW Gropp, Dinesh Kaushik, GM Knepley, CL Mcinnes, FB Smith, and Hong Zhang. PETSc Web page. 2001.

[71] Alexander R Lyon, Ken T MacLeod, Yanjun Zhang, Edwin Garcia, Gaelle Kikonda Kanda, Yuri E Korchev, Sian E Harding, Julia Gorelik, et al. Loss of T-tubules and other changes to surface topography in ventricular myocytes from failing human and rat heart. *Proceedings of the National Academy of Sciences*, 106(16):6854–6859, 2009.

[72] CellML Model Repository. www.cellml.org/models/.

[73] Denis Noble. Cardiac action and pace-maker potentials based on the Hodgkin–Huxley equations. *Nature*, 188:495–497, 1960.

[74] Ching-Hsing Luo and Yoram Rudy. A model of the ventricular cardiac action potential. depolarization, repolarization, and their interaction. *Circulation Research*, 68(6):1501–1526, 1991.

[75] Ching-Hsing Luo and Yoram Rudy. A dynamic model of the cardiac ventricular action potential. I. Simulations of ionic currents and concentration changes. *Circulation Research*, 74(6):1071–1096, 1994.

[76] Thomas J Hund, Jan P Kucera, Niels F Otani, and Yoram Rudy. Ionic charge conservation and long-term steady state in the Luo–Rudy dynamic cell model. *Biophysical Journal*, 81(6):3324–3331, 2001.

[77] Yoram Rudy and Jonathan R Silva. Computational biology in the study of cardiac ion channels and cell electrophysiology. *Quarterly Reviews of Biophysics*, 39(01):57–116, 2006.

[78] Mary M Maleckar, Joseph L Greenstein, Wayne R Giles, and Natalia A Trayanova. K+ current changes account for the rate dependence of the action potential in the human atrial myocyte. *American Journal of Physiology-Heart and Circulatory Physiology*, 297(4):H1398–H1410, 2009.

[79] Yoram Rudy and Harel Weinstein. From genes and molecules to organs and organisms: Heart. *Comprehensive Biophysics*, pages 268–327, 2012.

[80] Aslak Tveito and Glenn T Lines. *Computing Characterizations of Drugs for Ion Channels and Receptors Using Markov Models*. Springer-Verlag, Lecture Notes, vol. 111, 279 pages, 2016.

[81] William E Louch, Ole M Sejersted, and Fredrik Swift. There goes the neighborhood: Pathological alterations in T-tubule morphology and consequences for cardiomyocyte Ca^{2+} handling. *BioMed Research International*, 2010, 2010.

[82] Christian Soeller and Mark B Cannell. Examination of the transverse tubular system in living cardiac rat myocytes by 2-photon microscopy and digital image–processing techniques. *Circulation research*, 84(3):266–275, 1999.

[83] Michael Nivala, Enno de Lange, Robert Rovetti, and Zhilin Qu. Computational modeling and numerical methods for spatiotemporal calcium cycling in ventricular myocytes. *Frontiers in physiology*, 3, 2012.

[84] Yuhui Cheng, Zeyun Yu, Masahiko Hoshijima, Michael J Holst, Andrew D McCulloch, J Andrew McCammon, and Anushka P Michailova. Numerical analysis of Ca^{2+} signaling in rat ventricular myocytes with realistic transverse-axial tubular geometry and inhibited sarcoplasmic reticulum. *PLoS Computational Biology*, 6(10):e1000972, 2010.

[85] Pawel Swietach, Kenneth W Spitzer, and Richard D Vaughan-Jones. Modeling calcium waves in cardiac myocytes: importance of calcium diffusion. *Frontiers in Bioscience (Landmark edition)*, 15:661, 2010.

[86] Aslak Tveito, Glenn Terje Lines, Johan Hake, and Andrew G Edwards. Instabilities of the resting state in a mathematical model of calcium handling in cardiac myocytes. *Mathematical Biosciences*, 236(2):97–107, 2012.

[87] Jan P Kucera, Stephan Rohr, and Yoram Rudy. Localization of sodium channels in intercalated disks modulates cardiac conduction. *Circulation Research*, 91(12):1176–1182, 2002.

Paper III

Properties of Cardiac Conduction in a Cell-Based Computational Model

III

Karoline H. Jæger, Andrew G. Edwards, Andrew D. McCulloch, and Aslak Tveito

Submitted for publication

Properties of Cardiac Conduction in a Cell-Based Computational Model

Karoline H. Jæger[1], Andrew G. Edwards[1], Andrew McCulloch[2], and Aslak Tveito[1]

[1]Simula Research Laboratory, Norway
[2]Department of Bioengineering, University of California, San Diego, USA

Abstract

The conduction of electrical signals through cardiac tissue is essential for maintaining the function of the heart, and conduction abnormalities are known to potentially lead to life-threatening arrhythmias. The properties of cardiac conduction have therefore been the topic of intense study for decades, but a number of questions related to the mechanisms of conduction still remain unresolved.

In this paper, we demonstrate how the so-called EMI model may be used to study some of these open questions. In the EMI model, the extracellular space, the cell membrane, the intracellular space and the cell connections are all represented as separate parts of the computational domain, and the model therefore allows for study of local properties that are hard to represent in the classical homogenized bidomain or monodomain models commonly used to study cardiac conduction.

We conclude that a non-uniform sodium channel distribution increases the conduction velocity and decreases the time delays over gap junctions of reduced coupling in the EMI model simulations. We also present a theoretical optimal cell length with respect to conduction velocity and consider the possibility of ephaptic coupling (i.e. cell-to-cell coupling through the extracellular potential) acting as an alternative or supporting mechanism to gap junction coupling. We conclude that for a non-uniform distribution of sodium channels and a sufficiently small intercellular distance, ephaptic coupling can influence the dynamics of the sodium channels and potentially provide cell-to-cell coupling when the gap junction connection is absent.

Author summary

The electrochemical wave traversing the heart during every beat is essential for cardiac pumping function and supply of blood to the body. Understanding the stability of this wave is crucial to understanding how lethal arrhythmias are generated. Despite this importance, our knowledge of the physical determinants of wave propagation are still evolving. One particular challenge has been the lack of accurate mathematical models of conduction at the cellular level. Because cardiac muscle is an electrical syncytium, in which direct charge transfer between cells drives wave propagation, classical bidomain and monodomain tissue models employ a homogenized approximation of this process. This approximation is not valid at the length scale of single cells, and prevents any analysis of how cellular structures impact cardiac conduction. Instead, so-called microdomain models must be used for these questions. Here we utilize a recently developed modelling framework that is well suited to represent small collections of cells. By applying this framework, we show that concentration of sodium channels at the longitudinal borders of myocytes accelerates cardiac conduction. We also demonstrate that when juxtaposed cells are sufficiently close, this non-uniform distribution induces large ephaptic currents, which contribute to intercellular coupling.

1 Introduction

The contraction of the heart is initiated by an electrical signal spreading through the cardiac muscle, triggering the cardiomyocytes to contract in synchrony. The conduction of this signal from myocyte to myocyte is therefore essential for maintaining the pumping function of the heart and it is well established that abnormalities in cardiac conduction are associated with an increased risk of life-threatening arrhythmias (see e.g., [1, 2, 3]).

Cardiac conduction was long believed to be continuous in nature, with low resistance gap junctions allowing for a virtually continuous conduction of electrical signals between cells (see e.g., [4]). This view was challenged when experiments in the 1980s revealed that, even though the conduction velocity was faster in the direction along the cardiac fibers than in the transverse direction, the maximal upstroke velocity was higher for transverse propagation than for longitudinal propagation [5, 6]. This observation was not in agreement with the assumption of continuous conduction, because in a continuous medium, the conduction velocity would be expected to directly correspond to the maximal upstroke velocity, in the sense that a fast conduction velocity would be associated with a fast upstroke velocity [7]. The experiments therefore suggested that there might be discontinuities in the intracellular resistivity and it was theorized that these discontinuities might be explained by gap junctions with a considerably higher resistance than previously assumed. Moreover, direct measurements of the gap junction resistance

supported this claim and showed that the resistance at the intercalated discs between adjacent cells was approximately the same as the axial resistance of the cell [8, 9]. Today it is considered well established that cardiac conduction is discontinuous [7], and this raises questions of, for example, how the shape and size of the cardiomyocytes affect the conduction velocity and how this is influenced by the distribution of gap junctions (see e.g., [10, 11, 12, 13, 14, 15, 16]).

Another experimental finding challenging the classical views of cardiac conduction was done in 2012, when it was demonstrated that the conduction velocity decreased as the size of the extracellular space in guinea pig ventricular myocardium was increased [17]. This is the opposite of what is expected from mathematical considerations based on classical cable theory (see e.g., [18]), which predicts that the conduction velocity should increase as the size of the extracellular space increases (see e.g., [2, 14]). In addition, the experiments showed that an increased extracellular volume was associated with an increased sensitivity to gap junction uncoupling [17].

These results seem to support the claim that other mechanisms than the gap junctions might serve as alternative or supporting pathways for spreading the electrical signals from cell to cell (see e.g., [19]). In particular, the results seem to support the hypothesis of ephaptic coupling (i.e. coupling through the extracellular space) acting as a supporting mechanism for cardiac conduction. A number of computational studies have supported the viability of this hypothesis (e.g., [20, 21, 22, 23, 24, 25, 26, 27, 28, 29]), although the effect appears to depend highly on certain parameters. Specifically, the distance between the cells must be relatively small and the sodium channels must be highly localized at the intercalated discs in order for the electrical signal to pass between cells through ephaptic coupling alone. Sodium channels have in fact been demonstrated to highly localize at the intercalated discs (see e.g., [17, 22, 28, 30, 31, 32]) and the precise consequences of such a non-uniform distribution of sodium channels is another open question (see e.g., [20, 22, 33]).

The understanding of cardiac conduction has evolved by both experimental measurements and by theoretical considerations using mathematical models. The mathematical bidomain and monodomain models, for instance, have been used extensively to study propagating waves in cardiac tissue [34], and the models have been incorporated into several major software projects like Chaste, Carp, Continuity, and FEniCS [35, 36, 37, 38]. The bidomain and monodomain models allow for directional intracellular and extracellular resistivities accounting for the anisotropic nature of cardiac conduction. However, the models represent the cardiac tissue in a homogenized manner, and the intracellular space, the extracellular space and the cell membrane are all assumed to exist everywhere in the tissue. Moreover, the resistance of the gap junctions is generally incorporated into the intracellular resistivity in an averaged manner [4]. Consequently, these models might not be sufficient for representing mechanisms related to the discontinuous nature of cardiac conduction. Also, as pointed out in [39], a non-uniform distribution of ion channels is difficult to represent realistically in homogenized models.

In order to study these mechanisms, several alternative models have been in-

troduced, representing the discrete nature of cardiac tissue with different levels of detail and complexity (see e.g., [22, 23, 25, 26, 27, 40, 41]). In this paper, we consider a detailed model which has been applied in several earlier studies of excitable cells, including studies of collections of cardiomyocytes (e.g., [39, 42, 43, 44, 45, 46, 47, 48, 49, 50, 51]). We refer to the model as the EMI model because it includes an explicit representation of the **E**xtracellular space, the cell **M**embrane and the **I**ntracellular space. In addition, the intercalated discs between adjacent cells are incorporated into the model as membranes with capacitive and resistive properties. The model thus allows for a more detailed analysis of the properties of cardiac conduction than the classical bidomain and monodomain models. For example, the possibility to represent the cell connections explicitly allows for investigations of the discontinuous nature of conduction. Similarly, the explicit representation of the extracellular space makes the model applicable for studying the ephaptic coupling between cells and the effect of the size of the extracellular space on the conduction velocity. Furthermore, the EMI model is well-suited for studying non-uniform distributions of ion channels on the cell membrane because the geometry of each cell is explicitly defined in the model.

In our computations, we show that when the sodium channels are located at the cell ends, the conduction velocity increases and the time delays across gap junctions shorten compared to the case of a uniform sodium channel distribution. We also observe that there are large changes in the extracellular potential in the clefts between cells during propagation, leading to changes in the sodium channel dynamics and potentially enabling cell coupling through ephaptic coupling.

2 Methods

In this section, we define the EMI model used in our investigations, as well as the models chosen for the membrane and gap junction dynamics. In addition, we describe the cell geometry and the numerical methods used in our computations.

2.1 The EMI model

The EMI model will be used to simulate small collections of cardiomyocytes. For simplicity, we here describe the EMI model in the case of just two coupled cells. The extension to larger collections of cells follows directly from the two-cell definition.

A two-dimensional (2D) version of the components of the EMI model for two connected cells is illustrated in Figure 1. Note, however, that in all our simulations, we consider a three-dimensional (3D) version of the model. The domain consists of two intracellular domains Ω_i^1 and Ω_i^2 surrounded by an extracellular domain Ω_e. On the interface between the extracellular domain and the intracellular domain Ω_i^k, we define a cell membrane denoted by Γ_k for $k = 1, 2$. Similarly, on the interface between the two intracellular domains Ω_i^1 and Ω_i^2, we define an intercalated disc $\Gamma_{1,2}$. The outer boundary of the extracellular domain is denoted by $\partial\Omega_e$, and

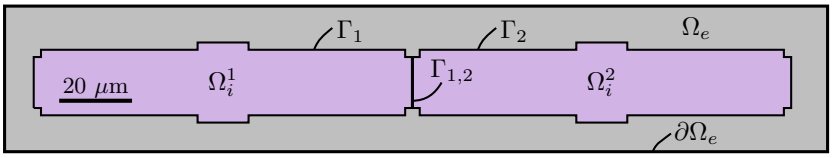

Figure 1: **Illustration of a 2D version of the computational domain for two cells.** The domain consists of an extracellular domain Ω_e and two intracellular domains Ω_i^1 and Ω_i^2 with cell membranes Γ_1 and Γ_2. The intracellular domains are connected by the intercalated disc denoted by $\Gamma_{1,2}$, and the outer boundary of the extracellular domain is denoted by $\partial\Omega_e$.

we separate this boundary into two parts, $\partial\Omega_e = \partial\Omega_e^D \cup \partial\Omega_e^N$, where a Dirichlet boundary condition is applied on Ω_e^D and a Neumann boundary condition is applied on Ω_e^N.

The EMI model describes the electrical potential in these domains and is described in detail in [39], however, for completeness, we repeat the model formulation here. For two connected cells, the EMI model reads

$$\nabla \cdot \sigma_e \nabla u_e = 0 \qquad \text{in } \Omega_e, \tag{1}$$

$$\nabla \cdot \sigma_i \nabla u_i^k = 0 \qquad \text{in } \Omega_i^k, \tag{2}$$

$$u_e = 0 \qquad \text{at } \partial\Omega_e^D, \tag{3}$$

$$\sigma_e \frac{\partial u_e}{\partial n_e} = 0 \qquad \text{at } \partial\Omega_e^N, \tag{4}$$

$$n_e \cdot \sigma_e \nabla u_e = -n_i^k \cdot \sigma_i \nabla u_i^k \equiv I_m^k \qquad \text{at } \Gamma_k, \tag{5}$$

$$u_i^k - u_e = v^k \qquad \text{at } \Gamma_k, \tag{6}$$

$$v_t^k = \frac{1}{C_m}(I_m^k - I_{\text{ion}}^k) \qquad \text{at } \Gamma_k, \tag{7}$$

$$n_i^2 \cdot \sigma_i \nabla u_i^2 = -n_i^1 \cdot \sigma_i \nabla u_i^1 \equiv I_{1,2} \qquad \text{at } \Gamma_{1,2}, \tag{8}$$

$$u_i^1 - u_i^2 = w \qquad \text{at } \Gamma_{1,2}, \tag{9}$$

$$w_t = \frac{1}{C_{1,2}}(I_{1,2} - I_{\text{gap}}) \qquad \text{at } \Gamma_{1,2}, \tag{10}$$

for $k = 1, 2$. Here, the variables of the model are the extracellular potential u_e defined in Ω_e, the intracellular potentials u_i^1 and u_i^2 defined in Ω_i^1 and Ω_i^2, respectively, the membrane potentials v^1 and v^2 defined on the membranes Γ^1 and Γ^2, respectively, and w defined on the intercalated disc, $\Gamma_{1,2}$. All potentials are given in mV. Furthermore, σ_i and σ_e are the intracellular and extracellular conductivities, respectively, given in mS/cm, and n_e and n_i^k, are the outward

Parameter	Value	Ref.
C_m	1 μF/cm^2	[52]
$C_{1,2}$	0.5 μF/cm^2	
σ_i	4 mS/cm	[53], [54]
σ_e	20 mS/cm	[50]
R_g	0.0045 kΩcm^2	
Size Ω_{O}	100 μm $\times$ 18 μm $\times$ 18 μm	
Size $\Omega_{\mathrm{W}}, \Omega_{\mathrm{E}}$	2 μm $\times$ 14 μm $\times$ 14 μm	
Size $\Omega_{\mathrm{S}}, \Omega_{\mathrm{N}}$	14 μm $\times$ 2 μm $\times$ 14 μm	
Δx, Δy	1 μm	
Δz	2 μm	
Δt (PDE part)	0.001 ms	
Δt^* (ODE part)	min(0.001 ms, Δt)	

Table 1: **Default parameter values used in the simulations.** For the parameters used in the Grandi et al. model, we refer to [55].

pointing normal vectors of Ω_e and Ω_i^k, respectively. The current density I_{ion}^k represents the ionic currents across the membrane and I_{gap} represents the ionic current density through the gap junctions. Similarly, I_m^k represents the sum of the ionic and capacitive current densities across the membrane, and $I_{1,2}$ represents the sum of the ionic current density through the gap junctions and the capacitive current density of the intercalated disc. All the current densities I_{ion}^k, I_{gap}, I_m^k and $I_{1,2}$ are given in μA/cm^2. The parameters C_m and $C_{1,2}$ represent the specific capacitance of the cell membrane and the intercalated disc, respectively and are given in μF/cm^2. Moreover, time is given in ms and length is given in cm.

In our simulations, we apply the Dirichlet boundary condition (3) on the outer boundary of the extracellular domain in the x- and y-directions and the Neumann boundary condition (4) in the z-direction. The default parameter values used in the simulations are given in Table 1.

2.2 Membrane dynamics

The ionic current density I_{ion}^k across the membrane between the intracellular and extracellular domains represents the sum of a large number of currents through various ion channels, pumps and exchangers located on the cell membrane. We use the epicardial version of the Grandi et al. action potential model [55] to model these currents. This model includes several state variables in addition to the membrane potential v, representing, for instance, intracellular ionic concentrations and gating variables of the ion channels. In order to account for these additional state variables, the EMI model given by (1)–(10) is extended to include a system of ordinary differential equations of the form

$$s_t = F(v, s) \tag{11}$$

for the dynamics of the state variables. The equations defining the right-hand side $F(v, s)$ is here given directly by the Grandi model. All state variables are defined only on the cell membrane and the value of the state variables is allowed to vary both in time and space. In other words, each state variable may have different values at different locations on the cell membrane.

In our simulations, we use the default initial conditions of the Grandi model for all the state variables governing the membrane dynamics, including the membrane potential v. Unless otherwise stated, we initiate the propagating wave in the simulations by stimulating the first two cells in the x-direction by a 1 ms long stimulus current of 80 A/F.

2.3 Gap junctions

The ionic currents through the gap junctions are modelled by the passive model

$$I_{\text{gap}} = \frac{1}{R_g} w. \tag{12}$$

Here, R_g represents the resistance of the gap junctions (in $\text{k}\Omega\text{cm}^2$), and $G_g = \frac{1}{R_g}$ (in mS/cm^2) is the conductance of the gap junctions. We use the initial condition $w = 0$ mV for the gap junction potential.

2.4 Numerical method

The EMI system (1)–(11) is solved using an operator splitting procedure. This numerical scheme is described in detail in [39]. In short, for every time step $t_n = n\Delta t$, the system (1)–(11) is solved in two steps. First, the system (11) and (7) with I_m^k set to zero is solved by m forward Euler steps of size $\Delta t^* = \Delta t/m$. Then, in the second step of the operator splitting procedure, the system (1)–(10) with I_{ion}^k set to zero is solved by a single step of an implicit finite difference discretization of the linear system.

The default discretization parameters used in the simulations are given in Table 1. Note that for simulations with time steps, Δt, larger than 0.001 ms, the time step $\Delta t^* = 0.001$ ms is still used for the ODE step of the operator splitting procedure, but when values of $\Delta t < 0.001$ ms is used, Δt^* is set equal to this value of $\Delta t < 0.001$ ms.

2.5 Domain and cell geometry

In our computations, we consider a 3D domain consisting of an extracellular space and a single strand of 3D cells. The cells are connected to each other in a single row in the x-direction by gap junctions. Because simple, rectangular geometries are most conveniently handled by the finite difference scheme used in the computations, we consider a very simplified cell geometry. Two- and three-dimensional illustrations of the cell shape used in the simulations are given in the left and

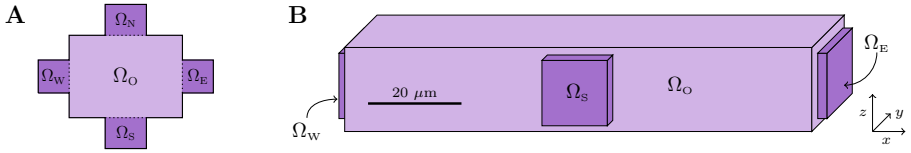

Figure 2: **Cell geometry used in the simulations.** A: Illustration of a two-dimensional version of a single cell. The intracellular domain is composed of the subdomains Ω_O, Ω_W, Ω_E, Ω_S, and Ω_N. B: Three-dimensional illustration of the geometry of a single cell based on the default cell size described in Table 1.

right panels of Figure 2, respectively. Each cell is a composition of the intracellular domains $\Omega_O, \Omega_W, \Omega_E, \Omega_S$, and Ω_N, and each of these domains is shaped as a rectangular cuboid. The cells may connect to each other by gap junctions like illustrated for two cells in Figure 1. The default cell sizes used in our computations are given in Table 1. The minimal distance between the intracellular domain and the outer boundary of the extracellular domain is 10 μm in the x- and y-directions and 4 μm in the z-direction.

2.6 Model parameters

The default parameter values used in the simulation are given in Table 1. The values for the specific membrane capacitance, C_m, and the intracellular and extracellular conductivities, σ_i and σ_e, are taken from literature (see [50, 52, 53, 54]). The value of $C_{1,2}$ is set to $C_m/2$ because the intercalated disc is assumed to be a membrane of thickness twice as large as the cell membrane, and the specific capacitance of a capacitor formed by two parallel plates separated by an insulator may be assumed to be inversely proportional to the thickness of the insulator [56]. The value for R_g was chosen so that the conduction velocity for the uniform distribution of sodium channels (see the next section) was approximately 50 cm/s (in rough agreement with e.g., [57, 58]).

2.7 Distribution of sodium channels

In order to study how the distribution of sodium channels on the cell membrane affects the properties of conduction, we consider both a uniform sodium channel distribution (U) and a non-uniform distribution (NU). In the uniform case, the sodium channels are distributed evenly over the entire membrane. This means that the sodium channel conductance is the same in all computational nodes located on the cell membrane, and this value is set equal to the default value in the Grandi et al. action potential model [55].

In the non-uniform case, some or all of the sodium channels are moved to an area close to the cell ends in the x-direction. For most of the simulations, this area

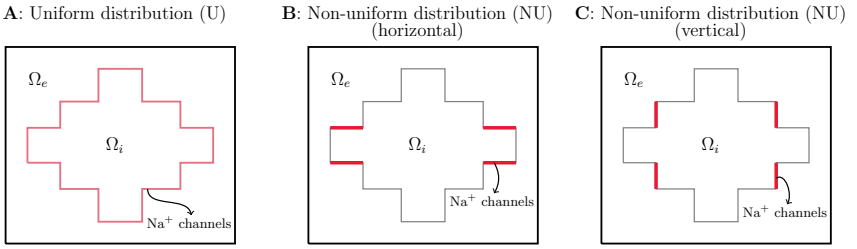

Figure 3: **Illustration of three different spatial distributions of the sodium channels for a 2D single cell case.**

is the membrane of Ω_W and Ω_E (see Figure 3B). However, for the simulations investigating ephaptic coupling, we place the sodium channels on the vertical part of the cell membrane between two cells (see Figure 3C). This is done in order to keep the size of areas with sodium channels constant for different cell distances and because we in these simulations consider much smaller cell distances than in the remaining simulations. In the remaining simulations, the distance between the cells is quite large (4 μm), and the sodium channels are placed on the horizontal part of the cell ends in order to locate the channels as close to the cell connections as possible.

When studying how the conduction properties are affected by different sodium channel distributions, we let the total sodium channel conductance of each cell be the same for the different sodium channel distributions. We define this total sodium channel conductance as

$$G_{\mathrm{Na}} = \int_{\Gamma} g_{\mathrm{Na}} dS, \tag{13}$$

where g_{Na} is the sodium channel conductance density (in mS/cm^2) and Γ is the cell membrane. If $\bar{g}_{\mathrm{Na}}$ is the default value of the sodium channel conductance density used in the uniform case and A_c is the total membrane area of the cell, the total sodium channel conductance in the uniform case is

$$G_{\mathrm{Na,U}} = \int_{\Gamma} \bar{g}_{\mathrm{Na}} dS = A_c \bar{g}_{\mathrm{Na}}. \tag{14}$$

In the non-uniform case, we divide the membrane into a part with an increased sodium channel density, Γ_j, and the remaining part, $\Gamma_r = \Gamma \setminus \Gamma_j$. On Γ_r, we let the sodium channel conductance density be given by

$$g_{\mathrm{Na},r} = (1-p)\bar{g}_{\mathrm{Na}}, \tag{15}$$

where p is the fraction of sodium channels moved to the cell ends. On Γ_j, we let the value be given by

$$g_{\mathrm{Na},j} = g_{\mathrm{Na},r} + p\frac{A_c}{A_j}\bar{g}_{\mathrm{Na}}, \tag{16}$$

where A_j is the area of Γ_j. This way, the total sodium channel conductance in the non-uniform case is

$$G_{\mathrm{Na,NU}} = \int_{\Gamma_r} g_{\mathrm{Na},r} dS + \int_{\Gamma_j} g_{\mathrm{Na},j} dS \tag{17}$$

$$= (A_c - A_j) g_{\mathrm{Na},r} + A_j \left(g_{\mathrm{Na},r} + p \frac{A_c}{A_j} \bar{g}_{\mathrm{Na}} \right) \tag{18}$$

$$= (1-p) A_c \bar{g}_{\mathrm{Na}} + p A_c \bar{g}_{\mathrm{Na}} = A_c \bar{g}_{\mathrm{Na}} \tag{19}$$

$$= G_{\mathrm{Na,U}}. \tag{20}$$

In the case when all the sodium channels are located at the cell ends (i.e., $p = 1$), this means that

$$g_{\mathrm{Na},r} = 0, \tag{21}$$

$$g_{\mathrm{Na},j} = \frac{A_c}{A_j} \bar{g}_{\mathrm{Na}}. \tag{22}$$

2.8 Numerical representation of integrals and areas

The areas A_c and A_j used in the definition (16) are computed by numerical integration over the computational nodes representing the membrane, and the junctional part of the membrane, respectively. More specifically, the areas are computed by

$$A_c = \int_{\Gamma} 1 dS \approx \sum_{i \in I_\Gamma} A_i, \tag{23}$$

$$A_j = \int_{\Gamma_j} 1 dS \approx \sum_{i \in I_{\Gamma_j}} A_i, \tag{24}$$

where I_Γ and I_{Γ_j} denote the collection of the indices of all computational nodes located on the membrane and the junctional part of the membrane, respectively. Furthermore A_i are areas associated with each of the computational membrane nodes i. These areas are defined as

$$A_i = \begin{cases} \Delta x \Delta y, & \text{for nodes on a membrane plane that is constant in the } z\text{-direction,} \\ \Delta x \Delta z, & \text{for nodes on a membrane plane that is constant in the } y\text{-direction,} \\ \Delta y \Delta z, & \text{for nodes on a membrane plane that is constant in the } x\text{-direction,} \\ \frac{1}{2}(\Delta x \Delta y + \Delta x \Delta z), & \text{for nodes at the intersection of membrane planes constant in the } z\text{- and } y\text{-directions,} \\ \frac{1}{2}(\Delta x \Delta y + \Delta y \Delta z), & \text{for nodes at the intersection of membrane planes constant in the } z\text{- and } x\text{-directions,} \\ \frac{1}{2}(\Delta x \Delta z + \Delta y \Delta z), & \text{for nodes at the intersection of membrane planes constant in the } x\text{- and } y\text{-directions,} \\ \frac{1}{3}(\Delta x \Delta y + \Delta x \Delta z + \Delta y \Delta z), & \text{for nodes at the membrane corners.} \end{cases}$$

3 Results

In this section, we demonstrate how the EMI model may be used to investigate properties of cardiac conduction. First, we consider how a non-uniform distribution of sodium channels affects the conduction velocity, the discontinuous nature of conduction and the time delays across gap junctions of reduced coupling. We also consider how the conduction velocity along a strand of cells is affected by the length of the cells. Finally, we use the EMI model to study the possibility of ephaptic coupling acting as an alternative pathway for conduction between cells and investigate how the sodium channel dynamics are affected by ephaptic effects.

3.1 Effect of sodium channel distribution on conduction velocity

As a first example of the application of the EMI model, we will use the model to study how a non-uniform distribution of sodium channels on the cell membrane affects the conduction velocity. In Figure 4, we show the conduction velocity computed in a number of simulations of a strand of 15 cells with an increasing percentages of sodium channels moved to the horizontal parts of the cell ends (see Figure 3B). Here, 0% represents the uniform case, and 100% represents the non-uniform case, when all sodium channels are located close to the cell ends. The total sodium channel conductance of the cell remains the same in each simulation as explained above. We observe that as a larger percentage of the sodium channels are moved to the cell ends, the conduction velocity increases.

Since the largest difference from the uniform case is observed for the case when all sodium channels are moved to the cell ends, we will in the experiments below compare just these two extremes; the uniform case with a constant distribution of sodium channels on the entire membrane and the non-uniform case with all sodium channels located near the cell ends.

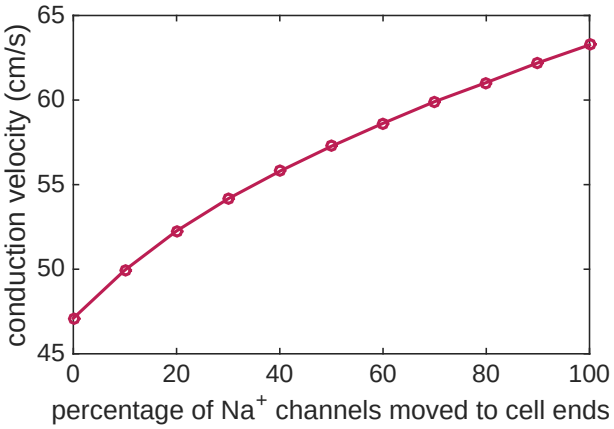

Figure 4: **The conduction velocity increases as a larger percentage of the sodium channels are moved to the cell ends.** The parameters used in the simulations are given in Table 1, and the simulation includes 15 cells. The conduction velocity is computed as the distance between the cell centers of the fifth and tenth cells divided by the time between the two cell centers first reach a membrane potential of $v = 0$ mV.

3.2 Discontinuous conduction

It is considered well-established that the electrical conduction in cardiac tissue is discontinuous with significant conduction delays when the wave crosses the gap junctions [7]. This discontinuous conduction is conveniently studied using the EMI model because the boundaries between cells are explicitly represented in the model. In Figure 5, we consider a single strand of cells and show the points in time when each of the x-values along the cell membranes first reach a membrane potential of $v = 0$ mV. We consider both a uniform and a non-uniform distribution of the sodium channels (see Figure 3A–B), and we consider the case of the default value of R_g in addition to three cases of increased R_g. In the figure, we observe that there are clearly visible gaps in time between each part of the gap junctions reach $v = 0$ mV, and that the size of these gaps increases as the gap junction resistance is increased. In addition, we observe that the gaps in time seem to be longer for the uniform case compared to the non-uniform case, and the overall time spent crossing the five cells is longer for the uniform case for all values of R_g.

3.2.1 Activation times for a single cell

In Figure 6, we focus on the x-values corresponding to a single cell. We observe that the curves for the activation times are not straight lines, but bend along the length of the cell. Moreover, the shape of the curves is clearly different in the uniform and non-uniform cases. In the uniform case, the curves seem to steepen

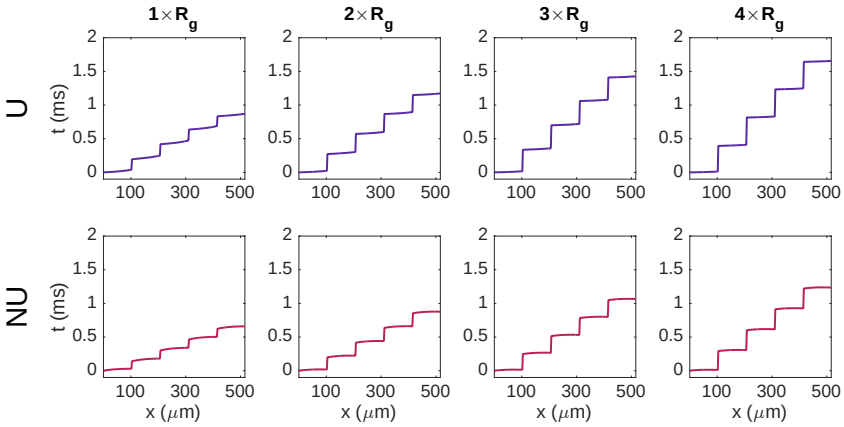

Figure 5: **Illustration of discontinuous conduction for a uniform (U) and a non-uniform (NU) distribution of sodium channels.** The plots show the time at which each of the x-values along the membrane of the five center cells in a simulation of a strand of seven cells first reach a membrane potential of $v = 0$ mV. The title above each panel indicates the factor with which the default value of $R_g = 0.0045$ kΩcm^2 is multiplied in the simulation. The remaining parameter values are specified in Table 1, except that the time step is set to $\Delta t = 0.0005$ ms.

towards the cell end, while for the non-uniform case, the curves seem to flatten out towards the end of the cell. In fact, for the non-uniform case, the activation time is shorter for the far-right part of the cell than at about 80% of the cell length in the cases of increased gap junction resistance.

Furthermore, we observe that for both sodium channel distributions, the time between the start and the end of the cell reaches $v = 0$ mV is shorter for the case with a high gap junction resistance compared to the case with the default value. This means that wave travels faster over a single cell as the gap junction resistance is increased and, as seen in Figure 5, the time delays across the gap junctions are increased.

3.3 Effect of sodium channel distribution on the upstroke velocity

As seen in Figure 4, the conduction velocity is increased for a non-uniform distribution of sodium channels compared to a uniform distribution. To investigate the reason for this effect, we consider the upstroke velocity of the action potential computed for the two sodium channel distributions. In the left panel of Figure 7, we report how the membrane potential changes with time for a grid point located at the beginning of the seventh cell, at the center of the cell and at the end of the cell in the x-direction. In the right panel, we plot the corresponding upstroke velocity (dv/dt) as a function of time. We observe that the upstroke velocity is

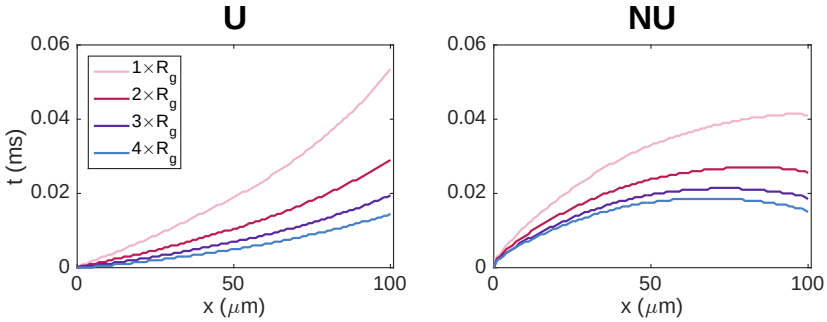

Figure 6: **The intracellular activation times are affected by the sodium channel distribution and gap junction resistance.** The figure shows the results from Figure 5 zoomed in on the x-values corresponding to a single cell in the center of the domain.

quite similar in the three points along the cell, but that the upstroke velocity is clearly increased in the non-uniform case compared to the uniform case. This increased upstroke velocity might explain the increased conduction velocity reported in Figure 4.

Furthermore, in Figures 5 and 6, we observed that the travelling wave spends the majority of the time crossing gap junctions. In Figure 8, we report the time delay across the gap junctions between the sixth and seventh cells as a function of the maximal upstroke velocity for the simulations reported in Figure 4. The maximal upstroke velocity is here defined as the maximal upstroke velocity obtained in the first grid point of the seventh cell. We observe that the time delay across the gap junctions clearly decreases as the maximal upstroke velocity increases.

3.4 Time delays across gap junctions of reduced coupling

In Figure 9, we show how the time delay over the gap junctions increases as the resistance of the gap junctions are increased. We consider both the case of a uniform distribution of sodium channels and the case of a non-uniform distribution with all sodium channels located close to the cell ends. We observe that the time delays across the gap junctions are longer for the uniform case than for the non-uniform case for all values of the gap junction resistance, R_g. Furthermore, the difference between time delays associated with each of the two sodium channel distributions increases as the gap junction resistance is increased. In addition, the value of R_g for which the wave is completely blocked is lower for the uniform case than for the non-uniform case.

Figure 10 illustrates the propagating wave for the uniform and non-uniform cases when the gap junction resistance is increased by a factor of 10 from the default value of 0.0045 kΩcm^2 to 0.045 kΩcm^2. We observe that the wave is delayed by about a millisecond when it reaches the gap junctions of reduced coupling, but that it eventually crosses the gap junctions. This happens faster for the case with

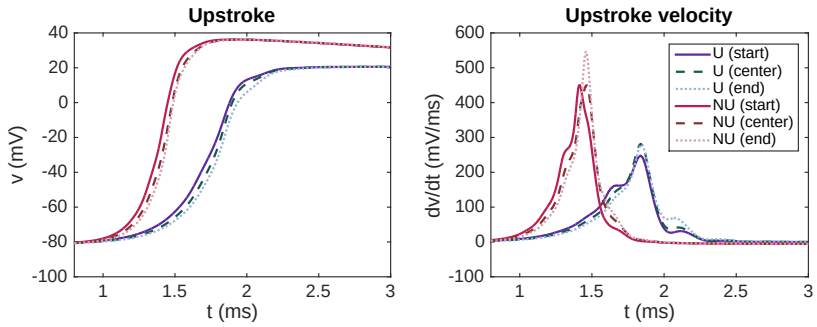

Figure 7: **The upstroke velocity is increased for the NU sodium channel distribution.** The figure shows the action potential upstroke (left) and the corresponding upstroke velocity (right) computed for the NU case with all sodium channels located on the horizontal part of the cell ends and the U case with a uniform distribution of sodium channels. The parameters used in the simulation are given in Table 1, and the simulation includes 15 cells. The membrane potential and upstroke velocities are computed for the first x-value, the center x-value and the last x-value of the seventh cell.

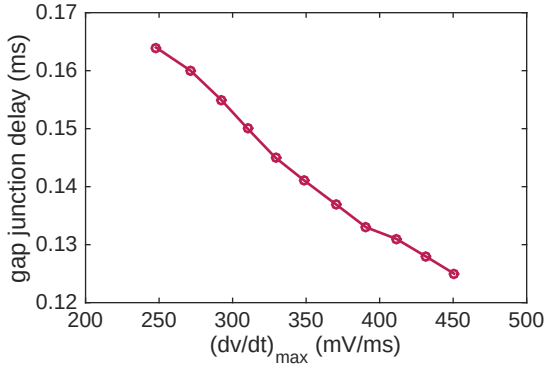

Figure 8: **The time delay across gap junctions is reduced as the maximal upstroke velocity increases.** The time delay is defined as the time between the membrane potential at the last computational node before the gap junctions between the sixth and seventh cells, and the first computational node after the gap junctions reach 0 mV. The upstroke velocity is computed at the first computational node after the gap junctions. The results are computed for the simulations displayed in Figure 4.

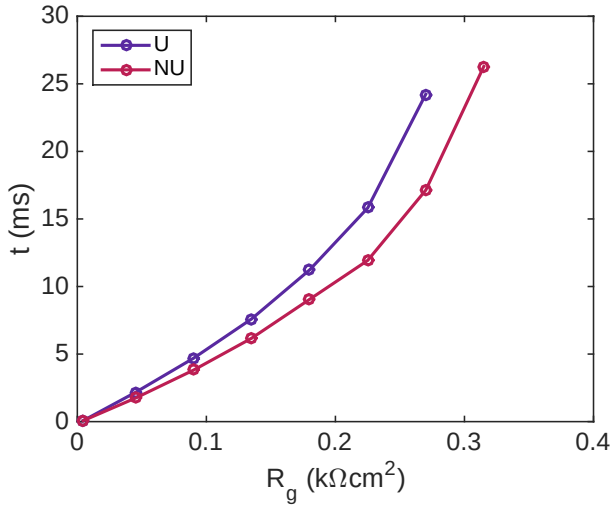

Figure 9: **The time delay across gap junctions of reduced coupling is longer for a uniform (U) distribution than for a non-uniform (NU) distribution of sodium channels.** The simulation includes a row of ten cells and the gap junction resistance between the fifth and sixth cells is increased by a factor of up to 70 from the default value of $R_g = 0.0045$ kΩcm^2. The default value of R_g is used for the remaining gap junctions. The remaining parameters used in the simulations are given in Table 1, except that the time step is set to $\Delta t = 0.01$ ms. The timings reported in the plot are the time between the end of the fifth cell and the start of the sixth cell reach a membrane potential of $v = 0$ mV. In the NU case, all the sodium channels are located on the horizontal part of the cell ends (see Figure 3B).

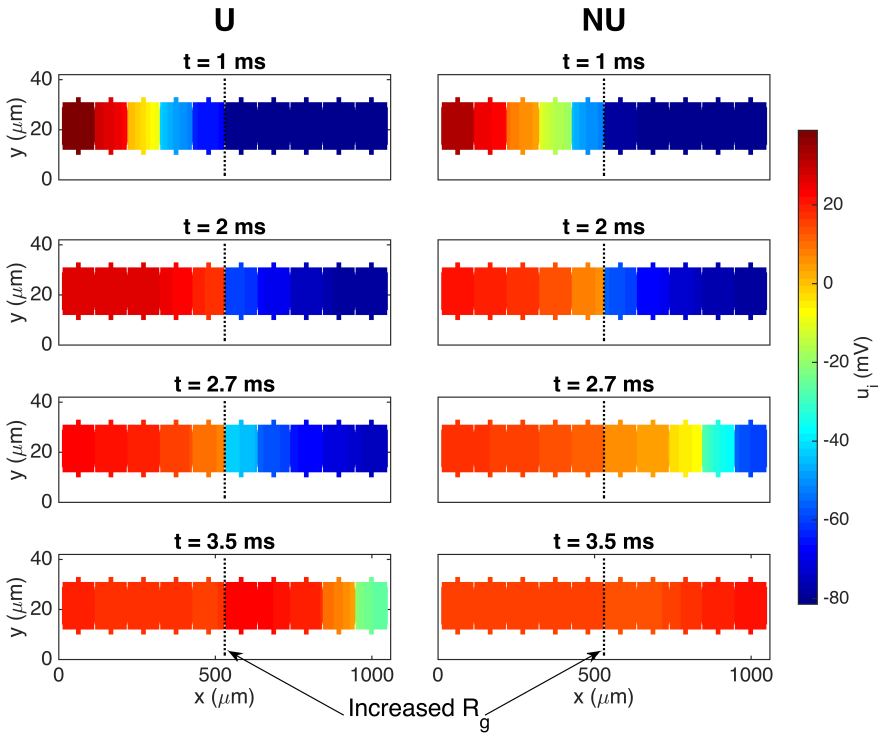

Figure 10: **Illustration of increased gap junction delay for a uniform distribution of sodium channels compared to a non-uniform distribution.** The figure shows the intracellular potential in the plane at the center of the domain in the z-direction at four points in time for the case with a uniform (U) and a non-uniform (NU) distribution of sodium channels. The default gap junction resistance is increased by a factor of 10 from 0.0045 kΩcm^2 to 0.045 kΩcm^2 between the fifth and sixth cells. The remaining parameter values used in the simulations are given in Table 1, except that the time step is set to $\Delta t = 0.01$ ms.

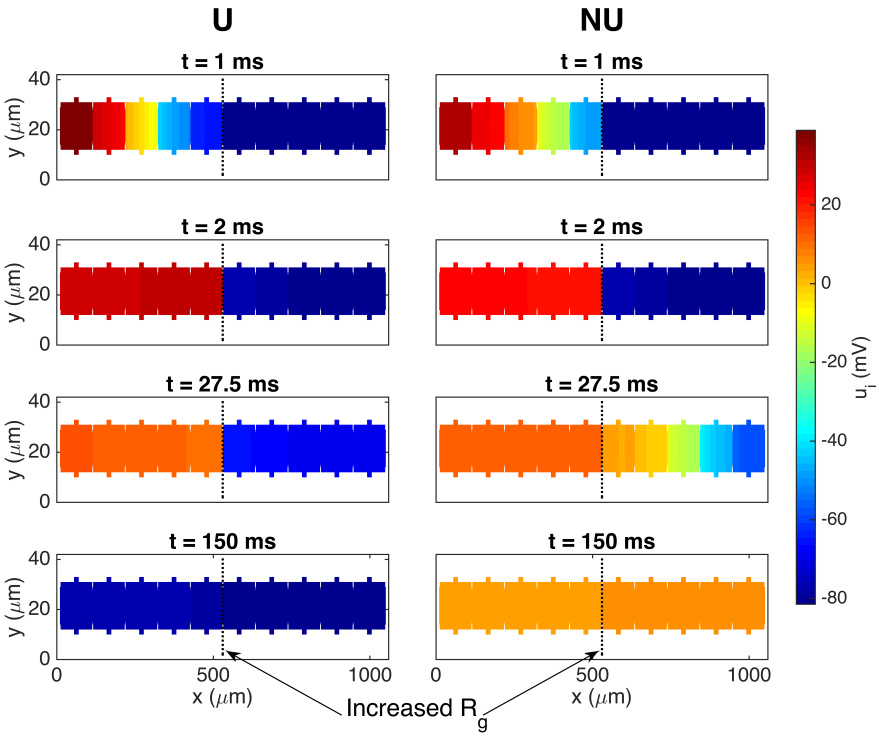

Figure 11: **Illustration of the propagating wave being blocked for the U case but not for the NU case.** The figure shows the intracellular potential in the plane at the center of the domain in the z-direction at four points in time for the case with a uniform (U) and a non-uniform (NU) distribution of sodium channels. The default gap junction resistance is increased by a factor of 70 from 0.0045 kΩcm^2 to 0.315 kΩcm^2 between the fifth and sixth cells. The remaining parameter values used in the simulations are given in Table 1, except that the time step is set to $\Delta t = 0.01$ ms.

a non-uniform distribution of sodium channels than for the uniform case.

Figure 11 similarly illustrates a case in which the propagating wave is only able to cross the gap junctions of increased resistance for a non-uniform distribution of sodium channels. In this example, the gap junction resistance is increased by a factor of 70 compared to the default value on the gap junctions between the fifth and sixth cells. We observe that the propagating wave is able to cross the gap junctions of increased resistance after a long time delay for the non-uniform case, but is completely blocked in the uniform case. Also, it is worth observing that the repolarization is considerably slower in the NU case compared to the U case. However, we generally observed slower repolarization when a wave is able to propagate across a point of increased resistance, and this also holds when the sodium channels are uniformly distributed.

3.5 Effect of cell length on the conduction velocity

In this section, we investigate how the conduction velocity depends on the cell length if the number of sodium channels per cell remains constant. Assuming that the number of sodium channels per cell remains constant, the density of sodium channels on the cell membrane will decrease as the cell length is increased. In this respect, it seems reasonable to expect that the conduction velocity would decrease if we increase the length of the cells, because the sodium channels are important for maintaining the membrane excitability necessary for cardiac conduction [57]. On the other hand, as the cell length is increased, the distance between the cell boundaries in the x-direction will increase, and, for a given propagation length, the propagating wave will have to cross less cell boundaries. This contrarily suggests that the conduction velocity would increase as the cell length is increased. As a result of these opposing effects, we might expect that there could be some optimal cell length which maximizes the conduction velocity.

In Figure 12, we investigate this property and report the conduction velocity computed for a number of simulations with different cell lengths. We consider both a uniform and a non-uniform distribution of the sodium channels. The length of Ω_{O} is varied and the cell width and the sizes of Ω_{W} and Ω_{E} are kept constant in each simulation (see the left panel of Figure 2). In order to keep the total number of sodium channels constant for each cell length, we replace the actual cell membrane area, A_c, by the membrane area A_c^* of the default cell size in Table 1 when computing the sodium channel conductance density by (22) in the NU case. In the U case, we similarly let the sodium channel conductance be scaled by a factor A_c^*/A_c.

In Figure 12, we observe that the conduction velocity indeed reaches a maximum for a given cell length and that the conduction velocity decreases as the cell length is increased or decreased from this value. In particular, for the parameters chosen here (see Table 1), a cell length of approximately 100 μm and 150 μm appears to lead to the maximal conduction velocity in the uniform and non-uniform cases, respectively.

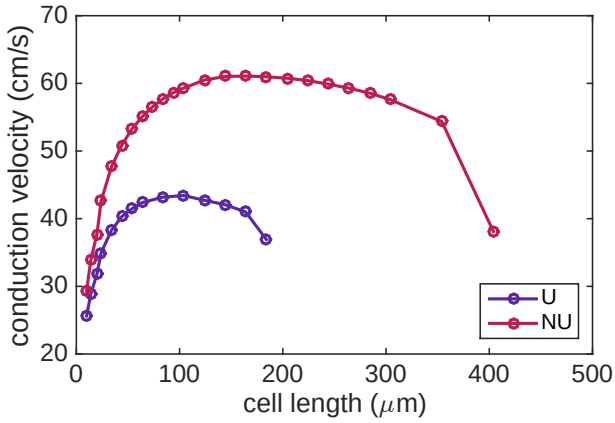

Figure 12: **Conduction velocity as a function of cell length when the number of sodium channels per cell remains constant.** The cell length here refers to the total length of Ω_O, Ω_W and Ω_E (see Figure 2), but only the length of Ω_O is varied in the simulations. The remaining parameter values are given in Table 1, except that for cell lengths shorter than 20 μm, the length of Ω_N and Ω_S in the x-direction is reduced to the cell length minus 6 μm so that they fit on Ω_O. For the simulations of cell lengths of up to 104 μm, the simulation includes 20 cells, the first four cells are stimulated and the conduction velocity is calculated between cells number seven and thirteen. For the remaining cell lengths, the simulation includes ten cells, the first two cells are stimulated and the conduction velocity is computed between cells number three and seven.

3.6 Ephaptic coupling of cardiomyocytes

Action potential propagation from cardiomyocyte to cardiomyocyte is primarily believed to be enabled by current through the gap junctions connecting individual cells [59]. However, ephaptic coupling has been proposed as an alternative or supporting mechanism for conduction between cells [19]. The EMI model is well-suited for studying this mechanism because the extracellular space is explicitly represented in the model as a geometrical subdomain.

3.6.1 Ephaptic coupling for closed gap junctions

In order to investigate the possibility of extracellular potentials alone being an alternative pathway of conduction between neighboring cells, we consider two cells with a gap junction conductance, $G_g = \frac{1}{R_g}$, set to zero on the intercalated disc between the cells. We stimulate the first half of the first cell and investigate whether the resulting propagating wave is able to pass to the second cell despite the fact that there is no current through the gap junctions between the cells.

In the upper panel of Figure 13, we report the intracellular potential, the extracellular potential and the membrane potential in a grid point located on the membrane of the second cell, just after the gap junctions with zero conductance. This point is illustrated by a red circle in the domain description in the panel above the plots. We consider a number of different distances d between the cells, and observe that as d is decreased, the magnitude of the minimum extracellular potential increases considerably for the non-uniform case. Indeed, for a cell distance of $d = 5$ nm, the extracellular potential reaches a value of approximately -30 mV. For the uniform case, however, the magnitude of the extracellular potential does not increase considerably, even for a cell distance of $d = 5$ nm

In the lower panel of Figure 13, we report the maximum intracellular potential, the minimal extracellular potential and the maximum value of the membrane potential for the same grid point as a function of $1/d$. We observe that the minimum value of u_e seems to be almost proportional to $1/d$ for the NU case. In the plot, we illustrate this proportionality by comparing the computed minimal extracellular potentials for the NU case to the linear approximation $\min(e_e) \approx a/d$, where $a = -0.15$ mVμm.

The size of the intracellular potential does not change much for the considered values of d, and the increased membrane potential observed in the rightmost panel of Figure 13 is therefore entirely caused by the decrease in the extracellular potential (recall that $v = u_i - u_e$). We observe that for a cell distance of $d = 5$ nm, the membrane potential just after the blocked gap junction increases to about -52 mV. This is, however, not enough to initiate an action potential in the second cell, so we do not achieve successful propagation through ephaptic coupling in this case.

3.6.2 Ephaptic coupling for a decreased extracellular conductivity

As observed in Figure 13, the extracellular potential reaches a value of almost

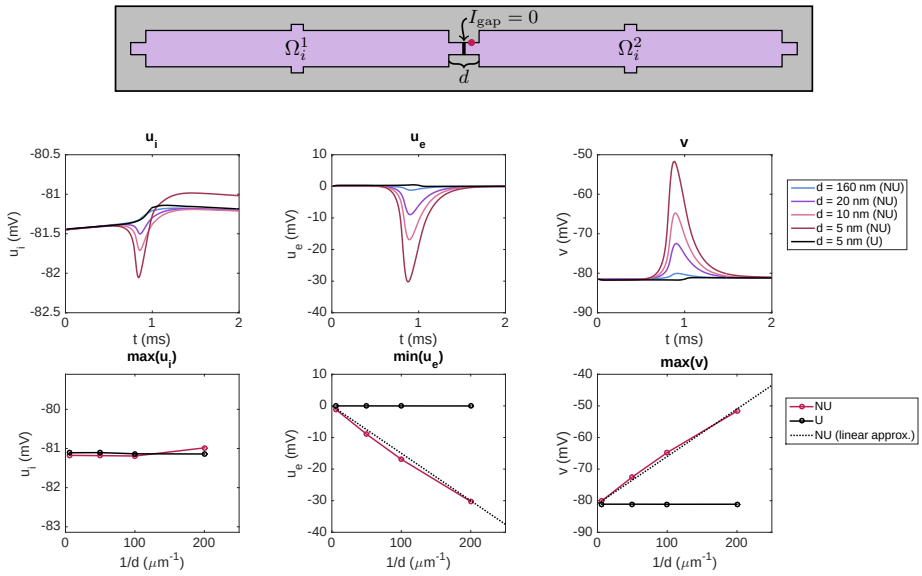

Figure 13: **The extracellular potential between cells is highly affected by the cell distance for the NU case.** The figure shows the intracellular potential, the extracellular potential and the membrane potential observed after blocked gap junctions for different values of the cell distance, d. The distance d is the combined length of Ω_{W} and Ω_{E} (see Figure 2 and the upper panel of this figure). In the NU case, we distribute all sodium channels on the vertical part of the cell ends (see Figure 3C). We consider two cells with gap junction conductance $G_g = \frac{1}{R_g} = 0$ and stimulate the first half of the first cell. The potentials are recorded in a grid point located just after the blocked gap junctions, on the membrane of the second cell, illustrated by a red circle in the upper panel. The parameter values used in the simulations are given in Table 1, except that we use $\Delta t = 0.01$ ms, $\Delta z = 1$ μm and a slightly reduced cell size. We let Ω_{O} be of size 100 μm $\times$ 12 μm $\times$ 12 μm, Ω_{W} and Ω_{E} be of size $d/2 \times 4$ μm $\times 4$ μm and Ω_{S} and Ω_{N} be of size 4 μm $\times 2$ μm $\times 4$ μm. Furthermore, we use $\Delta x = d/4$. The center panel shows the intracellular potential, the extracellular potential and the membrane potential as functions of time. The lower panel shows the maximum intracellular potential, the minimum extracellular potential and the maximum membrane potential as functions of $1/d$.

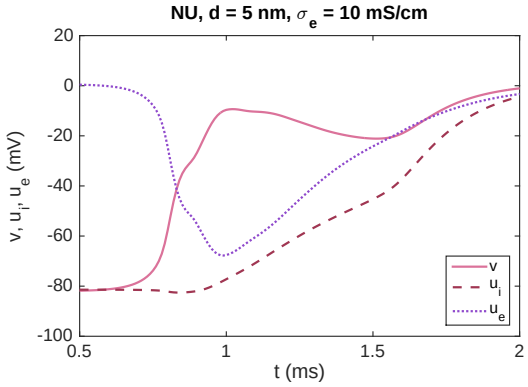

Figure 14: **Propagation of an action potential through ephaptic coupling is achieved for a decreased extracellular conductivity.** The figure shows the intracellular potential, the extracellular potential and the membrane potential observed after an intercalated disc with blocked gap junctions for a simulation with the same setup as in Figure 13, except that the value of σ_e is reduced from 20 mS/cm to 10 mS/cm. We consider a cell distance of $d = 5$ nm and a non-uniform distribution of sodium channels.

-30 mV for a cell distance of 5 nm, but this is not enough to support propagation of the action potential for the case of closed gap junctions. However, this conclusion is expected to depend on the choice of parameter values used in the simulation. For example, if we assume that the extracellular conductivity is 10 mS/cm instead of the default value of 20 mS/cm, the magnitude of the extracellular potential is large enough to enable propagation though ephaptic coupling alone, as illustrated in Figure 14. Here, we show the intracellular potential, the extracellular potential and the membrane potential in the point of the membrane of the second cell illustrated by a red circle in the upper panel of Figure 13. In this case, the magnitude of the extracellular potential seems to be large enough to bring the membrane potential up to a value that triggers the activation of the sodium channels on the membrane of the second cell, and thereby to a significantly increased intracellular potential in the second cell.

3.6.3 Ephaptic effects on the I_{Na} dynamics

In Figure 15, we investigate how ephaptic coupling affects the conduction properties when there is intracellular current through the gap junctions. We consider a case with two cells like in Figure 13, but where the gap junction resistance between the two cells is set to the default value given in Table 1. In particular, we investigate how the distribution of sodium channels and the cell distance affect the dynamics of the sodium channels. The figure shows that, both at the end of the first cell (A) and the start of the second cell (B), NU channel localization accelerates the rate of I_{Na} activation with respect to time, v, and both u_i and u_e.

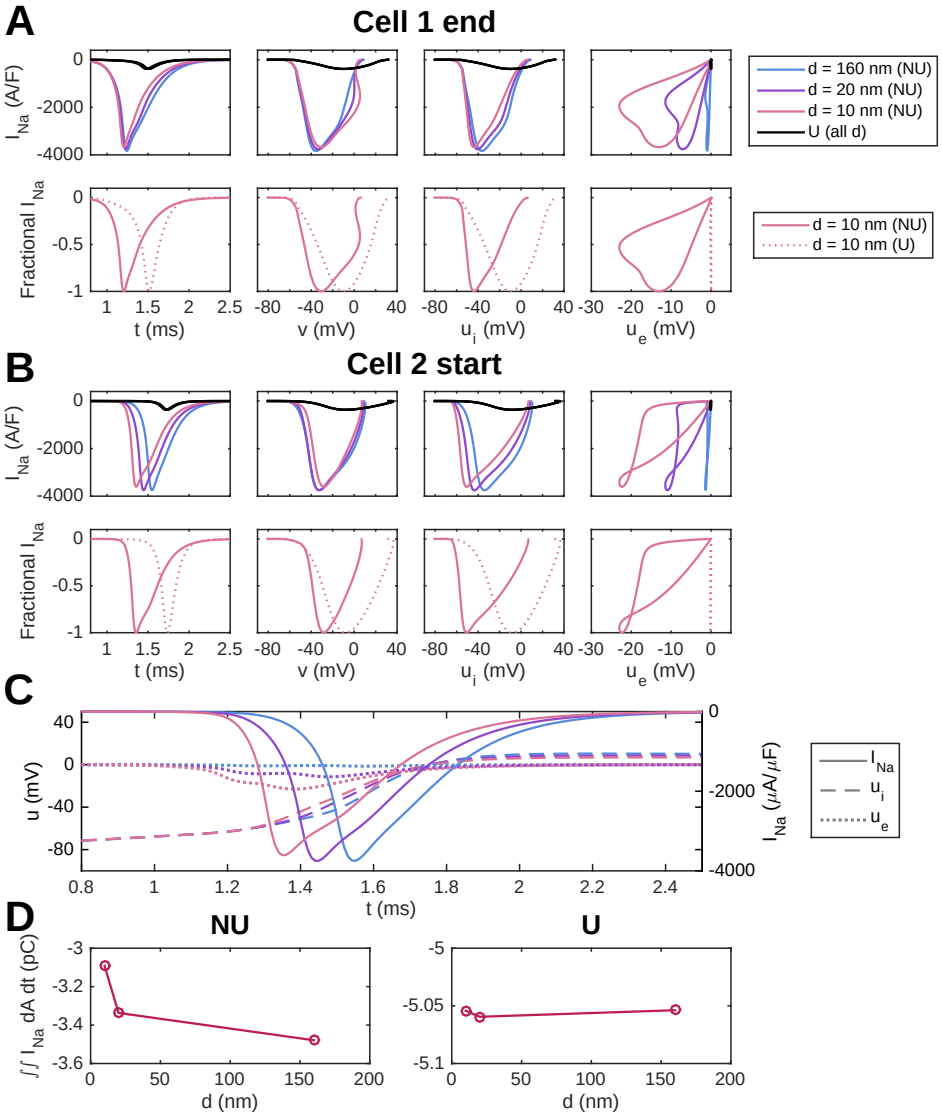

Figure 15: **The activation dynamics of I_{Na} are affected by the sodium channel distribution and cell distance.** (A) Raw (top panels) and normalized (fraction of peak, bottom panels) I_{Na} currents for the distal cell-end membrane in the first cell of a two-cell strand. I_{Na} in this membrane region is shown at each of three different cell distances (d = 5 nm, 10 nm, 160 nm) for the U and NU cases. (B) Similar results for the membrane at the beginning of the second cell. (C) Time development of I_{Na}, u_i and u_e for the beginning of the second cell. (D) Integrated whole-cell I_{Na} influx in the second cell over the entire upstroke for the NU and U cases. The simulation set up and parameters are the same as in Figure 13, except that the gap junction resistance is set to the default value of Table 1.

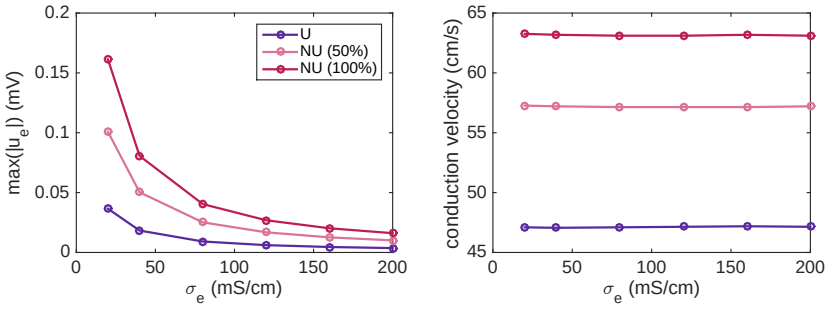

Figure 16: **The conduction velocity for a cell distance of 4 μm is nearly constant as the magnitude of the extracellular potential decreases.** The left panel shows the maximum absolute value of the extracellular potential as the value of σ_e is increased in simulations using the same setup as in Figure 4, with 0% (U), 50% and 100% of the sodium channels moved to the cell ends. The right panel shows the conduction velocity computed in each of the simulations.

These effects are exaggerated at short cell distances, particularly in the second cell (B), to which the AP is being transmitted. In panel C, the ephaptic effects on the sodium channels in the NU case are illustrated further, by considering I_{Na}, u_i and u_e at the beginning of the second cell as functions of time. We observe that as the cell distance is decreased, there is a significant increase in the magnitude of the extracellular potential, activating the sodium channels at an earlier point in time and for a lower intracellular potential. Moreover, in panel D, we integrate the total I_{Na} influx over the entire membrane of the second cell. We observe that the charge movement required for the AP upstroke is reduced substantially for the NU case, especially at short cell distances. Together, these results suggest that NU localization and short cells distances may interact to potentiate sodium channel activation during the AP upstroke, thus reducing both gap junctional delay and the net charge movement required for AP propagation.

3.6.4 Ephaptic effects for large cell distances

In Figures 13–15, we observed that for small cell distances, the magnitude of the extracellular potential increases considerably in the small extracellular junctions between the cells for a non-uniform distribution of sodium channels, enabling ephaptic effects between the cells. In the remaining simulations of this paper, however, the cell distance is much larger than in Figures 13–15, and we therefore expect that the results in Figures 4–12 are not caused by ephaptic effects between the cells.

For example, Figure 16 shows the conduction velocity for 0%, 50% and 100% of the sodium channels moved to the cell ends for an increasing value of σ_e. The left panel shows the maximum absolute value of u_e during the simulation for each of these values of σ_e, and the right panel shows the corresponding conduction

velocities. We observe that as the value of σ_e increases, the magnitude of the extracellular potential decreases, but the conduction velocity seems to remain constant. In other words, the effect that the conduction velocity is increased for a non-uniform distribution of sodium channels seems to be unaffected by a decreased magnitude of the extracellular potential, and the results of Figure 4 therefore do not seem to be caused by ephaptic effects.

4 Discussion

In this paper, we have illustrated how the so-called EMI model may be used to study properties of cardiac conduction. In this model, the cardiac tissue is separated into individual cells connected to each other by gap junctions and to the surrounding extracellular space by a cell membrane, all represented as geometrical parts of the domain. As described above, this explicit representation of the membrane, the intercalated discs and the intracellular and extracellular spaces makes the EMI model suitable for studying properties that are not conveniently studied using the classical homogenized models commonly used to study cardiac conduction (see e.g., [34]). On the other hand, the increased detail of the EMI model is associated with increased computational demands, which impose limitations on the simulations currently achievable [39]. In this section, we discuss the results obtained in this study and the choice of models and parameters used in our investigations.

4.1 Alternative discontinuous tissue models

In addition to the EMI model, several other modelling frameworks have been introduced as alternatives to the homogenized models of cardiac tissue (e.g., [22, 23, 25, 26, 27, 40, 41]). These models all represent the discrete nature of cardiac tissue with different levels of complexity, and most of the models rely on simplifying assumptions that may lead to significantly lower computational demands than the full EMI model.

4.1.1 1D models of a single strand of cells

Some of the simplest models used to study the discontinuous nature of cardiac propagation are based on circuit diagrams of the currents along a 1D strand of cells (see e.g., [20, 21, 22, 57, 60]). In these models, each cell is discretized into a number of nodes in the x-direction and the cell is assumed to be isopotential in the y- and z-directions. In addition, the extracellular potential is usually assumed to be constant outside the main part of the cell, but allowed to vary in the small junctional clefts between the cells for models investigating ephaptic coupling. The gap junctions are usually represented as resistive pathways between the cells, and the 1D model is derived by applying Kirchhoff's current law in each of the computational nodes along the cell strand.

Simulations of these models have found that a non-uniform distribution of sodium channels affects the conduction velocity and that conduction of electrical signals from one cell to the next is possible without gap junctional coupling [20, 22]. Because of the simplicity of the model, mathematical considerations regarding the parameters necessary for successful ephaptic coupling have also been conducted [21].

4.1.2 2D sheet models

The discontinuous nature of cardiac tissue has also been represented using 2D tissue models consisting of a single sheet of cells with explicit representations of the cell boundaries and discrete representations of the gap junctions (see e.g., [13, 40, 41, 61, 62, 63, 64, 65, 66]). Some of these studies assume a negligible effect of the extracellular potential [13, 40, 61, 62, 63], while others introduce a 2D layer of extracellular space above the intracellular 2D sheet [41]. In addition, a monodomain reduction has been applied to the modeling framework, incorporating the extracellular resistivity in the equation for the membrane potential [64, 65, 66].

The 2D sheet models have been extensively used to study the effect of the distribution of gap junctions, the cell geometry and the tissue structure. For example, simulations have shown that local changes in the conduction properties may change the propagating wave front over large tissue areas [61] and that reentrant activity in the heart may be initiated by the formation of isolated sites of wavefront breakthrough caused by microstructural variations in the cardiac tissue [65, 66]. In addition, it has been found that both the cell size, the distribution of gap junctions and the tissue structure affect the longitudinal and transverse conduction velocities [13, 62, 63].

4.1.3 3D microdomain models

Furthermore, a 3D microdomain model has been used in studies of ephaptic coupling of cardiomyocytes [25, 26, 27]. In this model, the extracellular potential is assumed to be uniform across the shortest width between the cells. In addition, the intracellular space of each cell is either assumed to be isopotential or discretized with a much coarser resolution than what has been used in our simulations. Studies using this microdomain model have found that ephaptic effects may have a significant effect on the properties of conduction [25, 26, 27]. Moreover, it was found that the ephaptic effects are not restricted to the junctional clefts between cells, but occur in all areas of the tissue with small extracellular spaces.

Because of the simplified representation of the intracellular and extracellular domains, the microdomain model is clearly more computationally efficient than the full EMI model. Thus, the model allows for simulations of, for example, smaller cell distances and larger collections of cells than what we have currently been able to handle computationally using the EMI model.

4.1.4 Models including diffusion of ions

From another point of view, the EMI model formulated in (1)–(10) is also a simplified representation of the electrophysiological properties of cardiac tissue, and more details could have been included at the cost of even larger computational demands. For example, the model ignores the effect of diffusion of ions, which could have an effect on the properties of conduction. The intracellular diffusion of calcium, for instance, may influence the conduction properties (see e.g., [2]). In our computations, we use a very simplified representation of the intracellular ion dynamics and represent the ionic concentrations only as a part of the action potential model governing the membrane dynamics. In other words, we only define ionic concentrations in the nodes located on the membrane.

Furthermore, local changes in the extracellular potassium and sodium concentrations in the narrow junctional clefts separating the cells have been proposed to have significant effects on the conduction from cell to cell (see e.g., [2, 19, 22, 23, 67]). For example, accumulation of potassium in the junctional cleft has been included in a 1D strand model and it was found that including accumulation of potassium increased the conduction velocity and allowed propagation in cases where conduction was blocked in a model without potassium accumulation [67]. Moreover, a detailed 3D model including diffusion of ions has been used to study properties of conduction under reduced gap-junction coupling [23]. In this study, it was observed that ionic concentrations varied siginficantly in the narrow clefts between cells during propagation. The study also achieved cell coupling through ephaptic coupling for a non-uniform sodium channel distribution if the distance between the cells was small enough. However, the distance needed to achieve cell coupling through ephaptic coupling was smaller than what was needed in [22] using a 1D single strand model.

4.2 Membrane dynamics

To model the membrane dynamics, I_{ion}, we have used the Grandi et al. action potential model [55]. This model is constructed to represent the action potential of human ventricular cardiomyocytes, and a large number of alternative models of varying complexity exists (e.g., [68, 69, 70, 71]). It would be straightforward to replace our choice of membrane model by any of these models, but we expect that the qualitative behavior observed in our simulations would be quite similar for other choices of models.

4.3 Gap junctions

We have used a simple, passive model for the ionic currents through the gap junctions between cells, I_{gap}, in our computations. However, experimental studies have indicated that the function of the gap junctions is in fact regulated by the voltage difference between the neighboring cells, w. Particularly, the gap junction resistance has been shown to increase as w increases [72, 73, 74, 75, 76]. Several models of voltage gated gap junctions have been proposed (e.g., [72, 73, 77, 78,

79, 80]), and such a model could easily be incorporated into the EMI model by, for example, considering a gap junction model of the form

$$I_{\text{gap}} = \frac{1}{R_g} g w, \tag{25}$$

where $g \in [0, 1]$ is a dynamic gating variable for the gap junctions (see e.g., [29]).

4.4 Cell and tissue geometry

In our simulations, we have used a very simplified representation of the geometry of cardiac tissue with cells shaped as rectangular cuboids with smaller rectangular cuboids at the sites of cell connections (see Figure 2). This geometry is chosen for its simplicity, and a more brick like structure (e.g. like in [27, 48, 50]) would be a more realistic representation of cardiac tissue. In addition, we have considered only very small collections of cardiac cells, organized in a single strand, and the distance between the cells has been quite large (4 μm) in most of the simulations. Because of computational limitations, we have not been able to represent more densely packed three-dimensional cardiac fibers, which would have been a more realistic representation of the structure of cardiac tissue (see e.g., [48]).

Furthermore, in the majority of the simulations of a non-uniform distribution of sodium channels, the sodium channels are placed at the horizontal membrane surfaces close to the cell connections (see Figure 3B). This was done in order to place to sodium channels as close as possible to the cell transitions for the cases when the cell distance was quite large (4 μm). A more realistic representation would be to place the sodium channels on the vertical intercalated discs between cells with small cell distances. However, that would have resulted in intractable computational problems.

4.5 Computational costs

As mentioned above, the representation of the intracellular and extracellular spaces as separate geometrical domains makes the computational costs of the EMI model larger than those of the classical bidomain or monodomain models, which represents the tissue in a homogenized manner, thus permitting much coarser spatial resolutions. This has limited the number of cells we have been able to include in our simulations. Note, however, that in the simulations, a large portion of the CPU time is typically spent solving the equations for the membrane dynamics [39], and for 3D simulations of the bidomain or monodomain models, the membrane is assumed to exist everywhere in the 3D volume, whereas in the EMI model, the membrane is represented only on a 2D surface. Therefore, as the number of computational nodes increases (either because of a refined discretization or because of a larger domain), the number of membrane nodes will grow faster for the bidomain or monodomain models than for the EMI model. The EMI model could therefore theoretically be more computationally effective than the bidomain and monodomain models for a very large number of computational nodes.

Note also that the computational costs of the EMI model may be reduced by for example using different spatial resolutions in different parts of the mesh (e.g. using a finer resolution in the extracellular space between cells than in the main intracellular domain) or by reducing the domain size by exploiting the geometrical symmetry of the domain (e.g. in the z-direction).

4.6 Non-uniform distribution of sodium channels

It has been demonstrated experimentally in a number of studies that the sodium channels on the membrane of cardiomyocytes are highly localized at the intercalated discs between neighboring cells (see e.g., [17, 22, 28, 30, 31, 32]), but precisely how such a non-uniform distribution of sodium channels affects the properties of cardiac conduction is still considered an open question [33].

A non-uniform distribution of ion channels on the cell membrane is, as described above, hard to represent using the classical bidomain and monodomain models because in these models, the intracellular space, the extracellular space and the cell membrane are all assumed to exist everywhere in the tissue. In the EMI model, on the other hand, the membrane of each individual cell is represented as a geometrical part of the domain, and it is therefore straightforward to represent different spatial distributions of ion channels on the cell membrane.

In this paper, we have therefore used the EMI model to investigate how different properties of cardiac conduction are affected by a non-uniform distribution of sodium channels, and we found that a number of properties were highly affected by this distribution.

4.6.1 Conduction velocity increases for a non-uniform distribution of sodium channels

First, we investigated the effect of a non-uniform sodium channel distribution on the conduction velocity and found that as a larger percentage of sodium channels were moved to the cell ends, the conduction velocity increased (see Figure 4). This is the opposite effect of what was found in earlier computational studies [22, 23, 25], which found that the conduction velocity was higher for a uniform distribution of sodium channels than for a non-uniform distribution for normal values of R_g. The different effects observed in the different studies could be due to different choices of models and parameters. In addition, the effect could be influenced by the small, more realistic, cell distances used in the previous studies (in the range 5 nm–1 μm) compared to the large cell distance used in our simulations (4 μm). In fact, in the microdomain study [25], the conduction velocity was slightly higher for a non-uniform distribution than for a uniform distribution if the cell distance was large. As observed in Figures 13 and 16, a large cell distance results in very limited effects on the extracellular potential in the junctional cleft between cells. This means that potential ephaptic effects on the conduction velocity might not be adequately represented in our simulations. Specifically, the ephaptic effects are believed to potentially lead to a decreased conduction velocity due to a decreased

driving force on I_{Na} [22]. This process is termed self-attenuation of I_{Na}. Because of the extreme resolution needed to represent cells located realistically close, we have not been able to study how such effects impact conduction velocity in our computations.

4.6.2 Discontinuous conduction

In Figures 5 and 6, we illustrated the discontinuous nature of conduction by plotting the activation times along a strand of cells and along a single cell. We observed that as the gap junction resistance was increased, and the time delays across the gap junctions were increased, the propagating wave crossed the intracellular domain faster. Related results have been found previously, showing that the maximal upstroke velocity of the membrane potential, $(dv/dt)_{\max}$ increases for moderately reduced gap junction coupling [5, 11, 57].

Moreover, we observed differences for the uniform and non-uniform distributions of sodium channels. As also observed in Figure 9, we found that the time delays across the gap junctions were increased for the uniform case compared to the non-uniform case. In Figure 6, we also observed a clear difference in the local variations of the activation curves over a single cell. Specifically, for a uniform distribution of sodium channels, the activation curve seemed to steepen towards the end of the cell, corresponding to a decrease of the local conduction velocity along the length of the cell. For a non-uniform distribution, on the other hand, the curve seemed to flatten out toward the end of the cell, corresponding to an increased local conduction velocity along the length of the cell.

4.6.3 Conduction velocity increases for non-uniform sodium channel distribution due to increased upstroke velocity

We have seen that the conduction velocity increases when the sodium channels are concentrated at cell ends (see Figure 4). This may be because of reduced delay over the gap junctions or because of improved speed along each cell. By comparing the results of Figure 5 (time delay) and Figure 6 (speed along individual cells) we observe that both components contribute to increased conduction velocity for NU compared to U. However, for the parameters considered here, the effect of gap junction time delay on the conduction velocity is significantly larger than the effect of the speed within each cell.

The reduced time delay seems to be caused by significantly increased upstroke velocity in the NU case (see Figure 7). The relation between time delay and upstroke velocity is elaborated in Figure 8 and clearly shows that increased upstroke velocity strongly reduce the time delay between two consecutive cells.

4.6.4 Time delays across gap junctions of reduced coupling

Next, in Figure 9, we observed how the time delays across gap junctions increased as the gap junction resistance was increased. As observed earlier, there may be

significant time delays across gap junctions between regions of structural inhomogeneities [60], and in our simulations, we obtained conduction delays of up to about 25 ms as the gap junction coupling was severely reduced. Moreover, we found that the time delays were consistently larger for a uniform distribution of sodium channels than for a non-uniform distribution. This is in agreement with previous computational studies [22, 23, 25, 26], which reported that the conduction velocity was larger in the non-uniform case than in the uniform case for weakly coupled cells.

4.7 Effect of cell length on the conduction velocity

The exact effect of the cell shape and size on the conduction velocity still remains an open question (see e.g., [4]). Since the shape and size of the individual cells are explicitly represented in the EMI model, the model could be a suitable framework for studying these questions. In this study, we illustrated this capability by investigating how the conduction velocity is affected by the cell length for a constant number of sodium channels per cell, and we observed that a cell length of approximately 100 μm and 150 μm seemed to give an optimal conduction velocity for a uniform and non-uniform distribution of sodium channels, respectively (see Figure 12). The existence of such an optimal cell length might be due to two conflicting effects as the cell length is increased. On the one hand, an increased cell length reduces the frequency of cell boundaries, potentially leading to an increased conduction velocity. On the other hand, an increased cell length reduces the cell's sodium channel density, potentially decreasing the conduction velocity.

4.8 Ephaptic coupling

Ephaptic coupling between cells has long been hypothesized to have significant effects on the properties of conduction (see e.g., [81]). In particular, ephaptic coupling has been proposed as an alternative to gap junction coupling between cells [19]. However, whether ephaptic coupling contributes significantly to cardiac propagation and the potential nature of this contribution still remain open questions (see e.g., [2, 82]).

Experimental studies supporting the hypothesis of cell coupling through ephaptic coupling includes studies of mice and guinea pigs with down-regulated expression of Cx43, which is the most abundant gap junction protein found in mammalian ventricular cardiomyocytes. The results of these studies are contradictory, with some studies showing a $17-44\%$ reduction of ventricular conduction velocity for approximately 50% reduction of Cx43 [83, 84, 85, 86], while others found no decrease in conduction velocity [87, 88, 89, 90, 91]. It has been proposed that the difference in these studies might be explained by different extracellular conditions (see e.g., [26]), thus supporting the significance of ephaptic effects. In addition, successful propagation was observed for cell strands with no Cx43 present, although this propagation was very slow and highly discontinuous [90]. Moreover, it has been shown experimentally that the conduction velocity (especially in the

transverse direction) decreased as the intercellular distance was increased [17]. This is the opposite of what is expected by classical cable theory, ignoring ephaptic effects, and the result therefore supports the significance of ephaptic effects on conduction. On the other hand, as reported in [2], the mannitol used to increase the extracellular volume, simultaneously reduces the cell width, and it is hard to differentiate between the effects of these individual geometrical changes.

4.8.1 Ephaptic coupling as an alternative to gap junction coupling

A large number of computational studies have been conducted, investigating the effect of ephaptic coupling using mathematical models of varying detail and complexity (e.g., [21, 22, 23, 24, 25, 26, 27]). These studies have indicated that ephaptic coupling could potentially serve as an alternative to gap junction coupling, but most studies found that this effect relies on a non-uniform distribution of sodium channels and a small distance between the cells. Moreover, the exact cell distance needed to obtain propagation through ephaptic coupling alone varies for the different models used in the studies. For example, Kucera et al. [22] used a 1D strand model and modelled the ionic currents by a version of the Luo-Rudy ventricular action potential model [92]. In their study, propagation by ephaptic coupling was achieved for a cell distance of 35 nm. Mori et al. [23], on the other hand, needed a cell distance of 5 nm to achieve propagation through ephaptic coupling. Their study used a model more similar to the EMI model, but with the effects of ionic diffusion included. The ionic currents over the membrane were modelled by a modified version of the Bondarenko et al. model [93] for the action potential of mouse ventricular cardiomyocytes.

In our simulations, we investigated the possibility of conduction through ephaptic coupling by considering two cardiac cells with no conductance through the gap junctions between them. In Figure 13, we observed that as the distance between the cells was decreased, the extracellular potential in the cleft between the cells decreased significantly for a non-uniform sodium channel distribution, and the minimal extracellular potential appeared to be close to inversely proportional to the cell distance. For the smallest cell distance considered in our computations ($d = 5$ nm), the extracellular potential in the cleft reached a value of approximately -30 mV, leading to a corresponding increase in the membrane potential just after the closed gap junctions. This effect seems to support the concept of cell coupling through ephaptic coupling. However, the increased membrane potential was not enough to trigger an action potential in the second cell, so we did not obtain successful propagation through ephaptic coupling in this case. On the other hand, this result is expected to depend on the choice of parameters used in the simulations. Indeed, in Figure 14 we observed that when the value of the extracellular conductivity was decreased from 20 mS/cm to 10 mS/cm, the propagating wave was able to travel from one cell to the next despite the fact that the gap junction conductance was zero.

4.8.2 Ephaptic effects of the I_{Na} dynamics

In addition, we investigated the effect of ephaptic coupling on the sodium channel dynamics in the case of an open gap junction. These effects have recently been systematically explored in a detailed 2D model of the intercalated disc in a voltage clamp configuration [94]. In the simulations of [94], two types of ephaptic effects were observed — self-activation and self-attenuation. At intracellular potentials far above the I_{Na} activation threshold, the development of large extracellular potentials rapidly brought the membrane potential close to the sodium equilibrium potential, thereby reducing the driving force for I_{Na} and resulting in self-attenuation of the current (and a lower peak I_{Na}). At potentials near the threshold, on the other hand, the large extracellular potentials were capable of accelerating the channel activation, leading to a higher peak I_{Na}.

In our computations, we investigated the effects during an action potential upstroke using the EMI model with two connected cells. We observed that, for a non-uniform distribution of sodium channels, the sodium channels were activated faster and at a lower intracellular potential as the distance between the cells was reduced. This suggests that ephaptic effects between cells might contribute to potentiate sodium channel activation during the upstroke of the action potential. On the other hand, the peak I_{Na} was slightly reduced for a decreasing cell distance. In addition, we observed that the integral of I_{Na} was markedly smaller for the NU distribution than for the U distribution of sodium channels, indicating that the net charge movement required for action potential propagation might be reduced for the NU distribution.

4.8.3 Ephaptic effects for large cell distances

In Figures 13–15, we observed that the magnitude of the extracellular potential increased considerably in the small extracellular junctions between the cells as the cell distance was decreased for a non-uniform distribution of sodium channels. This effect was shown both to impact the dynamics of the sodium channels when the gap junctions were open (see Figure 15) and to potentially enable propagation of an action potential from one cell to the next when the gap junction conductance was zero (see Figure 14).

However, in the remaining simulations of this paper the cell distance was much larger than in Figures 13–15, and the magnitude of the extracellular potential and the resulting ephaptic effects are therefore expected to be much smaller in these cases. Indeed, in Figure 16, we observed that the magnitude of the extracellular potential in the simulations measuring the conduction velocity (Figure 4) was much smaller than for the small cell distances of Figures 13–15. Moreover, the observation that a non-uniform distribution of sodium channels resulted in an increased conduction velocity seemed to be unaffected as the extracellular conductivity, σ_e, was increased, leading to a smaller magnitude of the extracellular potential. We therefore conclude that the increased conduction velocity observed for a non-uniform distribution of sodium channels in Figure 4 is not caused by ephaptic effects, but rather by an increased upstroke velocity caused by the relo-

cation of the sodium channels to a location close to the gap junctions (see Figure 7) and that this increased upstroke velocity makes the intracellular currents over the gap junctions faster and thereby the conduction delays over the gap junctions shorter (see Figure 8).

On the other hand, this result might have been influenced by ephaptic effects if the cell distance in the simulations had been smaller. For example, the fact that the sodium channels were activated faster as the cells distance was decreased in Figure 15 suggests that the conduction velocity might be even higher for a non-uniform distribution of sodium channels in simulations with smaller cell distances. Conversely, the fact that the peak sodium current was slightly reduced as the cell distance was decreased could potentially lead to a lower conduction velocity for cells placed close enough to exhibit ephaptic effects. In addition, ephaptic effects could be expected to lead to even shorter time delays over gap junctions of reduced coupling for a non-uniform sodium channel distribution than that observed in Figure 9. Because of computational challenges, we have not been able to study the potential ephaptic effects on the results of Figures 4–12, but these effects may be investigated in future studies using more efficient numerical strategies for the EMI model, enabling larger cell collections with small cell distances.

5 Conclusion

In this paper we have used a detailed mathematical model to investigate the properties of electrical conduction in small collections of cardiomyocytes. We have compared uniform (U) and non-uniform (NU) distributions of sodium channels and found significant differences. In particular, the conduction velocity is higher and the conduction delays over gap junctions are shorter when the NU case is compared to the U case. In addition, we have illustrated differences between the optimal cell lengths with respect to conduction velocity for the two cases and seen that for the NU case, the magnitude of the extracellular potential between cells increases considerably as the cell distance is decreased.

References

[1] Gary Tse and Jie Ming Yeo. Conduction abnormalities and ventricular arrhythmogenesis: the roles of sodium channels and gap junctions. *IJC Heart & Vasculature*, 9:75–82, 2015.

[2] Stefan Dhein, Thomas Seidel, Aida Salameh, Joanna Jozwiak, Anja Hagen, Martin Kostelka, Gerd Hindricks, and Friedrich-Wilhelm Mohr. Remodeling of cardiac passive electrical properties and susceptibility to ventricular and atrial arrhythmias. *Frontiers in Physiology*, 5:424, 2014.

[3] Maurice P Pye and Stuart M Cobbe. Mechanisms of ventricular arrhythmias in cardiac failure and hypertrophy. *Cardiovascular Research*, 26(8):740–750, 1992.

[4] Rengasayee Veeraraghavan, Robert G Gourdie, and Steven Poelzing. Mechanisms of cardiac conduction: a history of revisions. *American Journal of Physiology-Heart and Circulatory Physiology*, 306(5):H619–H627, 2014.

[5] Madison S Spach, Walter T Miller, David B Geselowitz, Roger C Barr, J Mailen Kootsey, and Edward A Johnson. The discontinuous nature of propagation in normal canine cardiac muscle. Evidence for recurrent discontinuities of intracellular resistance that affect the membrane currents. *Circulation Research*, 48(1):39–54, 1981.

[6] Madison S Spach, Walter T Miller, Paul C Dolber, J Mailen Kootsey, Joachim R Sommer, and Charles E Mosher. The functional role of structural complexities in the propagation of depolarization in the atrium of the dog. Cardiac conduction disturbances due to discontinuities of effective axial resistivity. *Circulation Research*, 50(2):175–191, 1982.

[7] Madison S Spach. Transition from a continuous to discontinuous understanding of cardiac conduction. *Circulation Research*, 92:125–126, 2003.

[8] Roy L White, David C Spray, Antonio C Campos De Carvalho, Beatrice A Wittenberg, and Michael V Bennett. Some electrical and pharmacological properties of gap junctions between adult ventricular myocytes. *American Journal of Physiology-Cell Physiology*, 249(5):C447–C455, 1985.

[9] Robert Weingart. Electrical properties of the nexal membrane studied in rat ventricular cell pairs. *The Journal of Physiology*, 370(1):267–284, 1986.

[10] H Tritthart, H Luedcke, R Bayer, H Stierle, and R Kaufmann. Right ventricular hypertrophy in the cat–an electrophysiological and anatomical study. *Journal of Molecular and Cellular Cardiology*, 7(3):163–174, 1975.

[11] Ronald W Joyner. Effects of the discrete pattern of electrical coupling on propagation through an electrical syncytium. *Circulation Research*, 50(2):192–200, 1982.

[12] Hugh McIntyre and Christopher H Fry. Abnormal action potential conduction in isolated human hypertrophied left ventricular myocardium. *Journal of Cardiovascular Electrophysiology*, 8(8):887–894, 1997.

[13] Madison S Spach, J Francis Heidlage, Paul C Dolber, and Roger C Barr. Electrophysiological effects of remodeling cardiac gap junctions and cell size. *Circulation Research*, 86(3):302–311, 2000.

[14] Madison S Spach, J Francis Heidlage, Roger C Barr, and Paul C Dolber. Cell size and communication: role in structural and electrical development and remodeling of the heart. *Heart Rhythm*, 1(4):500–515, 2004.

[15] Haisam A Ghaly, Patrick M Boyle, Edward J Vigmond, Yakhin Shimoni, and Anders Nygren. Simulations of reduced conduction reserve in the diabetic rat heart: response to uncoupling and reduced excitability. *Annals of Biomedical Engineering*, 38(4):1415–1425, 2010.

[16] Thomas Seidel, Aida Salameh, and Stefan Dhein. A simulation study of cellular hypertrophy and connexin lateralization in cardiac tissue. *Biophysical Journal*, 99(9):2821–2830, 2010.

[17] Rengasayee Veeraraghavan, Mohamed E Salama, and Steven Poelzing. Interstitial volume modulates the conduction velocity-gap junction relationship. *American Journal of Physiology-Heart and Circulatory Physiology*, 302(1):H278–H286, 2012.

[18] Robert Plonsey and Roger C Barr. *Bioelectricity: a quantitative approach*. Springer Science & Business Media, 2007.

[19] Nicholas Sperelakis and Keith McConnell. Electric field interactions between closely abutting excitable cells. *IEEE Engineering in Medicine and Biology Magazine*, 21(1):77–89, 2002.

[20] Kunichika Tsumoto, Takashi Ashihara, Ryo Haraguchi, Kazuo Nakazawa, and Yoshihisa Kurachi. Roles of subcellular Na^+ channel distributions in the mechanism of cardiac conduction. *Biophysical Journal*, 100(3):554–563, 2011.

[21] Elizabeth D Copene and James P Keener. Ephaptic coupling of cardiac cells through the junctional electric potential. *Journal of Mathematical Biology*, 57(2):265–284, 2008.

[22] Jan P Kucera, Stephan Rohr, and Yoram Rudy. Localization of sodium channels in intercalated disks modulates cardiac conduction. *Circulation Research*, 91(12):1176–1182, 2002.

[23] Yoichiro Mori, Glenn I Fishman, and Charles S Peskin. Ephaptic conduction in a cardiac strand model with 3D electrodiffusion. *Proceedings of the National Academy of Sciences*, 105(17):6463–6468, 2008.

[24] Nicholas Sperelakis. An electric field mechanism for transmission of excitation between myocardial cells. *Circulation Research*, 91(11):985–987, 2002.

[25] Joyce Lin and James P Keener. Modeling electrical activity of myocardial cells incorporating the effects of ephaptic coupling. *Proceedings of the National Academy of Sciences*, 107(49):20935–20940, 2010.

[26] Joyce Lin and James P Keener. Ephaptic coupling in cardiac myocytes. *IEEE Transactions on Biomedical Engineering*, 60(2):576–582, 2013.

[27] Joyce Lin and James P Keener. Microdomain effects on transverse cardiac propagation. *Biophysical Journal*, 106(4):925–931, 2014.

[28] Rengasayee Veeraraghavan, Joyce Lin, Gregory S Hoeker, James P Keener, Robert G Gourdie, and Steven Poelzing. Sodium channels in the Cx43 gap junction perinexus may constitute a cardiac ephapse: an experimental and modeling study. *Pflügers Archiv-European Journal of Physiology*, 467(10):2093–2105, 2015.

[29] Seth H Weinberg. Ephaptic coupling rescues conduction failure in weakly coupled cardiac tissue with voltage-gated gap junctions. *Chaos: An Interdisciplinary Journal of Nonlinear Science*, 27(9):093908, 2017.

[30] Esperanza Agullo-Pascual, Xianming Lin, Alejandra Leo-Macias, Mingliang Zhang, Feng-Xia Liang, Zhen Li, Anna Pfenniger, Indra Lübkemeier, Sarah Keegan, David Fenyö, Klaus Willecke, Eli Rothenberg, and Mario Delmar. Super-resolution imaging reveals that loss of the C-terminus of connexin43 limits microtubule plus-end capture and Na_V1. 5 localization at the intercalated disc. *Cardiovascular Research*, 104(2):371–381, 2014.

[31] Ruth E Westenbroek, Sebastian Bischoff, Ying Fu, Sebastian KG Maier, William A Catterall, and Todd Scheuer. Localization of sodium channel subtypes in mouse ventricular myocytes using quantitative immunocytochemistry. *Journal of Molecular and Cellular Cardiology*, 64:69–78, 2013.

[32] Rengasayee Veeraraghavan and Robert G Gourdie. Stochastic optical reconstruction microscopy–based relative localization analysis (STORM-RLA) for quantitative nanoscale assessment of spatial protein organization. *Molecular Biology of the Cell*, 27(22):3583–3590, 2016.

[33] Jan P Kucera, Stephan Rohr, and Andre G Kleber. Microstructure, cell-to-cell coupling, and ion currents as determinants of electrical propagation and arrhythmogenesis. *Circulation: Arrhythmia and Electrophysiology*, 10(9):e004665, 2017.

[34] James Keener and James Sneyd. *Mathematical physiology*. Springer Science & Business Media, 2010.

[35] Jonathan Cooper, Raymond J Spiteri, and Gary R Mirams. Cellular cardiac electrophysiology modeling with Chaste and CellML. *Frontiers in Physiology*, 5:511, 2015.

[36] Edward J Vigmond, Matt Hughes, G Plank, and L Joshua Leon. Computational tools for modeling electrical activity in cardiac tissue. *Journal of Electrocardiology*, 36:69–74, 2003.

[37] Jazmin Aguado-Sierra, Roy CP Kerckhoffs, Fred Lionetti, Darlene Hunt, Chris Villongco, Matt Gonzales, Stuart G Campbell, and Andrew D McCulloch. A computational framework for patient-specific multi-scale cardiac modeling. In *Patient-Specific Modeling of the Cardiovascular System*, pages 203–223. Springer, 2010.

[38] Anders Logg, Kent-Andre Mardal, and Garth Wells. *Automated solution of differential equations by the finite element method: The FEniCS book*, volume 84. Springer Science & Business Media, 2012.

[39] Aslak Tveito, Karoline H Jæger, Miroslav Kuchta, Kent-Andre Mardal, and Marie E Rognes. A cell-based framework for numerical modeling of electrical conduction in cardiac tissue. *Frontiers in Physics*, 5:48, 2017.

[40] Madison S Spach and J Francis Heidlage. The stochastic nature of cardiac propagation at a microscopic level: electrical description of myocardial architecture and its application to conduction. *Circulation Research*, 76(3):366–380, 1995.

[41] Madison S Spach, J Francis Heidlage, Paul C Dolber, and Roger C Barr. Extracellular discontinuities in cardiac muscle: evidence for capillary effects on the action potential foot. *Circulation Research*, 83(11):1144–1164, 1998.

[42] Hervé Hogues, L Joshua Leon, and Fernand A Roberge. A model study of electric field interactions between cardiac myocytes. *IEEE Transactions on Biomedical Engineering*, 39(12):1232–1243, 1992.

[43] Wanda Krassowska and John C Neu. Response of a single cell to an external electric field. *Biophysical Journal*, 66(6):1768–1776, 1994.

[44] Wenjun Ying and Craig S Henriquez. Hybrid finite element method for describing the electrical response of biological cells to applied fields. *IEEE Transactions on Biomedical Engineering*, 54(4):611–620, 2007.

[45] Andres Agudelo-Toro and Andreas Neef. Computationally efficient simulation of electrical activity at cell membranes interacting with self-generated and externally imposed electric fields. *Journal of Neural Engineering*, 10(2):026019, 2013.

[46] Sarah F Roberts, Jeroen G Stinstra, and Craig S Henriquez. Effect of nonuniform interstitial space properties on impulse propagation: a discrete multidomain model. *Biophysical Journal*, 95(8):3724–3737, 2008.

[47] Jeroen G Stinstra, Craig S Henriquez, and Rob S MacLeod. Comparison of microscopic and bidomain models of anisotropic conduction. In *Computers in Cardiology*, pages 657–660. IEEE, 2009.

[48] Jeroen Stinstra, Rob MacLeod, and Craig Henriquez. Incorporating histology into a 3D microscopic computer model of myocardium to study propagation at a cellular level. *Annals of Biomedical Engineering*, 38(4):1399–1414, 2010.

[49] Jeroen G Stinstra, Sarah F Roberts, John B Pormann, Rob S MacLeod, and Craig S Henriquez. A model of 3D propagation in discrete cardiac tissue. In *Computers in Cardiology, 2006*, pages 41–44. IEEE, 2006.

[50] Jeroen G Stinstra, Bruce Hopenfeld, and Rob S MacLeod. On the passive cardiac conductivity. *Annals of Biomedical Engineering*, 33(12):1743–1751, 2005.

[51] Aslak Tveito, Karoline H Jæger, Glenn T Lines, Łukasz Paszkowski, Joakim Sundnes, Andrew G Edwards, Tuomo Mäki-Marttunen, Geir Halnes, and Gaute T Einevoll. An evaluation of the accuracy of classical models for computing the membrane potential and extracellular potential for neurons. *Frontiers in Computational Neuroscience*, 11:27, 2017.

[52] Silvio Weidmann. Electrical constants of trabecular muscle from mammalian heart. *The Journal of Physiology*, 210(4):1041, 1970.

[53] Wayne E Cascio, Gan-Xin Yan, and Andre G Kleber. Passive electrical properties, mechanical activity, and extracellular potassium in arterially perfused and ischemic rabbit ventricular muscle. Effects of calcium entry blockade or hypocalcemia. *Circulation Research*, 66(6):1461–1473, 1990.

[54] RA Chapman and CH Fry. An analysis of the cable properties of frog ventricular myocardium. *The Journal of Physiology*, 283:263, 1978.

[55] Eleonora Grandi, Francesco S Pasqualini, and Donald M Bers. A novel computational model of the human ventricular action potential and Ca transient. *Journal of Molecular and Cellular Cardiology*, 48:112–121, 2010.

[56] Bertil Hille. *Ion channels of excitable membranes*, volume 507. Sinauer Sunderland, MA, 2001.

[57] Robin M Shaw and Yoram Rudy. Ionic mechanisms of propagation in cardiac tissue. Roles of the sodium and L-type calcium currents during reduced excitability and decreased gap junction coupling. *Circulation Research*, 81(5):727–741, 1997.

[58] Aslak Tveito, Glenn Lines, Andrew G Edwards, Mary M Maleckar, Anushka Michailova, Johan Hake, and Andrew D McCulloch. Slow calcium-depolarization-calcium waves may initiate fast local depolarization waves in ventricular tissue. *Progress in Biophysics and Molecular Biology*, 110(2–3):295–304, July 2012.

[59] Stephan Rohr. Role of gap junctions in the propagation of the cardiac action potential. *Cardiovascular Research*, 62(2):309–322, 2004.

[60] Yan Wang and Yoram Rudy. Action potential propagation in inhomogeneous cardiac tissue: safety factor considerations and ionic mechanism. *American Journal of Physiology-Heart and Circulatory Physiology*, 278(4):H1019–H1029, 2000.

[61] Ronald W Joyner, Fidel Ramón, and JW Morre. Simulation of action potential propagation in an inhomogeneous sheet of coupled excitable cells. *Circulation Research*, 36(5):654–661, 1975.

[62] Madison S Spach, J Francis Heidlage, Paul C Dolber, and C Roger. Changes in anisotropic conduction caused by remodeling cell size and the cellular distribution of gap junctions and Na^+ channels. *Journal of Electrocardiology*, 34(4):69–76, 2001.

[63] Marjorie Letitia Hubbard, Wenjun Ying, and Craig S Henriquez. Effect of gap junction distribution on impulse propagation in a monolayer of myocytes: a model study. *Europace*, 9(suppl 6):vi20–vi28, 2007.

[64] Marjorie L Hubbard and Craig S Henriquez. Increased interstitial loading reduces the effect of microstructural variations in cardiac tissue. *American Journal of Physiology-Heart and Circulatory Physiology*, 298(4):H1209–H1218, 2010.

[65] Marjorie L Hubbard and Craig S Henriquez. Microscopic variations in interstitial and intracellular structure modulate the distribution of conduction delays and block in cardiac tissue with source–load mismatch. *Europace*, 14(suppl 5):v3–v9, 2012.

[66] Marjorie L Hubbard and Craig S Henriquez. A microstructural model of reentry arising from focal breakthrough at sites of source-load mismatch in a central region of slow conduction. *American Journal of Physiology-Heart and Circulatory Physiology*, 306(9):H1341–H1352, 2014.

[67] John B Picone, Nicholas Sperelakis, and James E Mann. Expanded model of the electric field hypothesis for propagation in cardiac muscle. *Mathematical and Computer Modelling*, 15(8):17–35, 1991.

[68] George W Beeler and Harald Reuter. Reconstruction of the action potential of ventricular myocardial fibres. *The Journal of Physiology*, 268(1):177–210, 1977.

[69] Flavio Fenton and Alain Karma. Vortex dynamics in three-dimensional continuous myocardium with fiber rotation: Filament instability and fibrillation. *Chaos: An Interdisciplinary Journal of Nonlinear Science*, 8(1):20–47, 1998.

[70] Kirsten HWJ ten Tusscher, Denis Noble, Peter-John Noble, and Alexander V Panfilov. A model for human ventricular tissue. *American Journal of Physiology-Heart and Circulatory Physiology*, 286(4):H1573–H1589, 2004.

[71] Kirsten HWJ ten Tusscher and Alexander V Panfilov. Alternans and spiral breakup in a human ventricular tissue model. *American Journal of Physiology-Heart and Circulatory Physiology*, 291(3):H1088–H1100, 2006.

[72] Nerijus Paulauskas, Henrikas Pranevicius, Jonas Mockus, and Feliksas F Bukauskas. Stochastic 16-state model of voltage gating of gap-junction channels enclosing fast and slow gates. *Biophysical Journal*, 102(11):2471–2480, 2012.

[73] Xianming Lin, Joanna Gemel, Eric C Beyer, and Richard D Veenstra. Dynamic model for ventricular junctional conductance during the cardiac action potential. *American Journal of Physiology-Heart and Circulatory Physiology*, 288(3):H1113–H1123, 2005.

[74] Rolf Vogel and Robert Weingart. The electrophysiology of gap junctions and gap junction channels and their mathematical modelling. *Biology of the Cell*, 94(7-8):501–510, 2002.

[75] Feliksas F Bukauskas, Angele Bukauskiene, Michael VL Bennett, and Vytas K Verselis. Gating properties of gap junction channels assembled from connexin43 and connexin43 fused with green fluorescent protein. *Biophysical Journal*, 81(1):137–152, 2001.

[76] Feliksas F Bukauskas and Vytas K Verselis. Gap junction channel gating. *Biochimica et Biophysica Acta (BBA)-Biomembranes*, 1662(1):42–60, 2004.

[77] Mindaugas Snipas, Tadas Kraujalis, Nerijus Paulauskas, Kestutis Maciunas, and Feliksas F Bukauskas. Stochastic model of gap junctions exhibiting rectification and multiple closed states of slow gates. *Biophysical Journal*, 110(6):1322–1333, 2016.

[78] Mindaugas Snipas, Henrikas Pranevicius, Mindaugas Pranevicius, Osvaldas Pranevicius, Nerijus Paulauskas, and Feliksas F Bukauskas. Application of stochastic automata networks for creation of continuous time markov chain models of voltage gating of gap junction channels. *BioMed Research International*, 2015:936295, 2015.

[79] Alexandra P Henriquez, Rolf Vogel, Barbara J Muller-Borer, Craig S Henriquez, Robert Weingart, and Wayne E Cascio. Influence of dynamic gap junction resistance on impulse propagation in ventricular myocardium: a computer simulation study. *Biophysical Journal*, 81(4):2112–2121, 2001.

[80] Rolf Vogel and Robert Weingart. Mathematical model of vertebrate gap junctions derived from electrical measurements on homotypic and heterotypic channels. *The Journal of Physiology*, 510(1):177–189, 1998.

[81] Nicholas Sperelakis and James E Mann. Evaluation of electric field changes in the cleft between excitable cells. *Journal of Theoretical Biology*, 64(1):71–96, 1977.

[82] Bradley J Roth. Does ephaptic coupling contribute to propagation in cardiac tissue? *Biophysical Journal*, 106(4):774–775, 2014.

[83] Patricia A Guerrero, Richard B Schuessler, Lloyd M Davis, Eric C Beyer, Carolyn M Johnson, Kathryn A Yamada, and Jeffrey E Saffitz. Slow ventricular conduction in mice heterozygous for a connexin43 null mutation. *Journal of Clinical Investigation*, 99(8):1991–1998, 1997.

[84] Suma A Thomas, Richard B Schuessler, Charles I Berul, Michael A Beardslee, Eric C Beyer, Michael E Mendelsohn, and Jeffrey E Saffitz. Disparate effects of deficient expression of connexin43 on atrial and ventricular conduction. *Circulation*, 97(7):686–691, 1998.

[85] Benjamin C Eloff, Deborah L Lerner, Kathryn A Yamada, Richard B Schuessler, Jeffrey E Saffitz, and David S Rosenbaum. High resolution optical mapping reveals conduction slowing in connexin43 deficient mice. *Cardiovascular Research*, 51(4):681–690, 2001.

[86] Paramdeep S Dhillon, Rosaire Gray, Pipin Kojodjojo, Rita Jabr, Rasheda Chowdhury, Christopher H Fry, and Nicholas S Peters. The relationship between gap junction conductance and conduction velocity in mammalian myocardium. *Circulation: Arrhythmia and Electrophysiology*, 6(6):1208–1214, 2013.

[87] Gregory E Morley, Dhananjay Vaidya, Faramarz H Samie, Cecilia Lo, Mario Delmar, and Jose Jalife. Characterization of conduction in the ventricles of normal and heterozygous Cx43 knockout mice using optical mapping. *Journal of Cardiovascular Electrophysiology*, 10(10):1361–1375, 1999.

[88] Dhananjay Vaidya, Houman S Tamaddon, Cecilia W Lo, Steven M Taffet, Mario Delmar, Gregory E Morley, and José Jalife. Null mutation of connexin43 causes slow propagation of ventricular activation in the late stages of mouse embryonic development. *Circulation Research*, 88(11):1196–1202, 2001.

[89] Stuart P Thomas, Jan P Kucera, Lilly Bircher-Lehmann, Yoram Rudy, Jeffrey E Saffitz, and André G Kléber. Impulse propagation in synthetic strands of neonatal cardiac myocytes with genetically reduced levels of connexin43. *Circulation Research*, 92(11):1209–1216, 2003.

[90] Philippe Beauchamp, Cécile Choby, Thomas Desplantez, Karin de Peyer, Karen Green, Kathryn A Yamada, Robert Weingart, Jeffrey E Saffitz, and André G Kléber. Electrical propagation in synthetic ventricular myocyte strands from germline connexin43 knockout mice. *Circulation Research*, 95(2):170–178, 2004.

[91] Harold VM van Rijen, Dominik Eckardt, Joachim Degen, Martin Theis, Thomas Ott, Klaus Willecke, Habo J Jongsma, Tobias Opthof, and Jacques MT de Bakker. Slow conduction and enhanced anisotropy increase the propensity for ventricular tachyarrhythmias in adult mice with induced deletion of connexin43. *Circulation*, 109(8):1048–1055, 2004.

[92] Ching-hsing Luo and Yoram Rudy. A dynamic model of the cardiac ventricular action potential. I. simulations of ionic currents and concentration changes. *Circulation Research*, 74(6):1071–1096, 1994.

[93] Vladimir E Bondarenko, Gyula P Szigeti, Glenna CL Bett, Song-Jung Kim, and Randall L Rasmusson. Computer model of action potential of mouse ventricular myocytes. *American Journal of Physiology-Heart and Circulatory Physiology*, 287(3):H1378–H1403, 2004.

[94] Echrak Hichri, Hugues Abriel, and Jan P Kucera. Distribution of cardiac sodium channels in clusters potentiates ephaptic interactions in the intercalated disc. *The Journal of Physiology*, 596(4):563–589, 2018.

Paper IV

Inversion and Computational Maturation of Drug Response Using Human Stem Cell Derived Cardiomyocytes in Microphysiological Systems

IV

Aslak Tveito, Karoline H. Jæger, Nathaniel Huebsch, Bérénice Charrez, Andrew G. Edwards, Samuel Wall, and Kevin E. Healy

Scientific Reports 8:17626 (2018).

Inversion and Computational Maturation of Drug Response Using Human Stem Cell Derived Cardiomyocytes in Microphysiological Systems

Aslak Tveito[1], Karoline H. Jæger[1], Nathaniel Huebsch[2], Berenice Charrez[2], Andrew G. Edwards[1,3], Samuel Wall[1], and Kevin E. Healy[2]

[1]Simula Research Laboratory, Norway
[2]Departments of Bioengineering, Material Science and Engineering, University of California, Berkeley, California, USA
[3]Department of Biosciences, University of Oslo, Norway

Abstract

While cardiomyocytes differentiated from human induced pluripotent stems cells (hiPSCs) hold great promise for drug screening, the electrophysiological properties of these cells can be variable and immature, producing results that are significantly different from their human adult counterparts. Here, we describe a computational framework to address this limitation, and show how *in silico* methods, applied to measurements on immature cardiomyocytes, can be used to both identify drug action and to predict its effect in mature cells. Our synthetic and experimental results indicate that optically obtained waveforms of voltage and calcium from microphysiological systems can be inverted into information on drug ion channel blockage, and then, through assuming functional invariance of proteins during maturation, this data can be used to predict drug induced changes in mature ventricular cells. Together, this pipeline of measurements and computational analysis could significantly improve the ability of hiPSC derived cardiomycocytes to predict dangerous drug side effects.

1 Introduction

The discovery of human induced pluripotent stem cells (hiPSCs) has started a new era in biological science and medicine. These reprogrammed somatic cells can be differentiated into a wide variety of cell lineages, and allow *in vitro* examination of cellular properties at the level of the human individual. In particular, this technology has large implications in drug development, moving us away from well studied

but often unrepresentative animal models towards direct testing of compounds in specific human phenotypes and genotypes. This new access offers the potential for creating more cost effective, better, safer drug treatments; both from the ability to target precision, patient specific approaches, and to reveal possible side effects of drugs in the broader human population. However, despite its promise, the technology needed to fully utilize hiPSCs for drug testing is still under development and currently faces many difficulties limiting practical applicability.

In particular, the problem of *maturation* is a major challenge to the successful use of hiPSCs in drug discovery and development. Although hiPSCs can be used to create specialized human cells and tissues, these rapidly grown cells and tissues may have significant proteomic and structural differences to, and are often more fetal-like than, their adult *in vivo* counterparts. This is especially true in hiPSC derived cardiomyocytes (hiPSC-CMs), where the adult cells they are intended to represent have undergone decades of growth and development under cyclical physiological loading and stimulation. However, despite this limitation, hiPSC-CMs have already been successfully used to assess unwanted side effects of drugs (see e.g., [1, 2]), and new technologies such as microphysiological systems (MPS) [3], are emerging to improve maturation and better capture drug effects. Still, the overall applicability of hiPSC-CMs to find unwanted side effects of drugs for adult cardiomyocytes remains limited by the fact that only relatively immature cells are available for analysis (see e.g., [4, 5, 6, 7]). And, as pointed out in numerous papers (e.g., [8, 9, 10, 11, 12]), the electrophysiological characteristics of hiPSC-CMs and adult cardiomyocytes differ significantly and, for determining potential dangerous drug side-effects, these differences may lead to both false positives and false negatives (see e.g., [13, 3]).

Meanwhile, *in silico* methods for investigating the properties of the action potential (AP) of excitable cells is a well-developed field (see e.g. [14, 15, 16]) and includes models of human cardiomyocytes (see e.g., [17, 18, 19, 20]), and models where the effect of drugs are taken into account (see e.g., [21, 22, 23]). Also, mathematical models of the action potential of hiPSC-CMs have been developed (see e.g., [9, 24]) based on measurements reported in [8, 25, 26, 27]. This field has progressed to the point where computational models are now an active part of cardiotoxicity research [28], and are being integrated into guidelines for comprehensive drug arrhythmia analysis.

In this work, we discuss how computational models of immature (IM) and mature (M) cardiomycytes can contribute to the improvement of the applicability of exploiting hiPSCs in the drug development pipeline. Despite remarkable progress in handling hiPSC-CMs under lab conditions (see, e.g [29]), the ability to create fully mature hiPSC-CMs for drug screening is likely to remain a significant challenge. In the present report, we therefore address how *in silico* computational modeling can be used to deduce properties of mature (adult) cardiomyocytes based on two real time measurements of their immature counterpart.

A key idea in our approach is that individual proteins are functionally invariant under maturation. Therefore, maturation is multiplication in the sense that, for every type of protein, the number of proteins multiply during maturation, but the

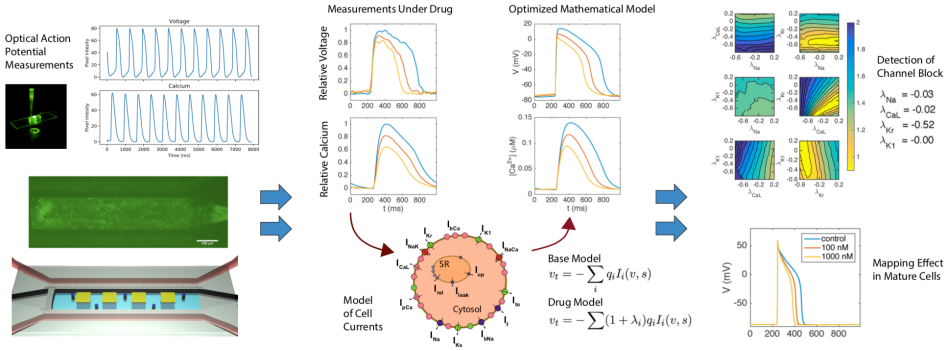

Figure 1: Depiction of in silico modeling and analysis of an MPS system. Optical measurements of calcium and voltage are taken at baseline and in the presence of drug. These waveforms are inverted using a mathematical model of cell dynamics, into a set of parameters that define key ion channel conductances. Changes in this parameter set give information about specific changes in conductances under drug, and this parameter set can then mapped to a model of mature cell behavior using the assumption of functional invariance of individual channels.

function of every protein remains unaltered. In addition, the surface area of the cell and the cell volume also increase significantly during maturation, leading to large changes in current densities between the IM and M cells. The invariance of the functional properties of the IM and M versions of every protein suggests a proportionality between the associated individual currents of the IM and M cells which may explain the results obtained in [12]. We use the proportionality between the individual currents to define a maturation matrix that maps the parameterization of a model of the IM cell to a parameterization of a model of the M cell.

Our approach to estimate effects of drugs on M cells based on measurements of IM cells can be summarized as follows and is shown in Figure 1:

1. A MPS system is used to collect time averaged voltage and intracellular (cystolic) calcium waveforms, both under control conditions and in the presence of drug.

2. These voltage and calcium traces are inverted in order to define a mathematical model of the membrane and calcium dynamics of the tested IM cells. The effect of the drug is reflected in terms of changes in the maximum conducances of ion channels in the model.

3. The IM models are multiplied by a maturation matrix in order to obtain models for the M cells. The effect of the drug for adult cells is estimated by comparing the AP models of the M cells.

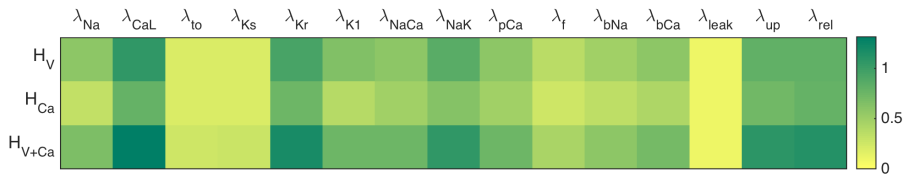

Figure 2: Sensitivity of maximum conductances of the immature base model assessed by the three cost functions defined in (3)–(4) with $\varepsilon = 0.2$. The color intensities correspond to the sum of the cost function upon perturbing the maximum conductance of the given current (or flux) by $\pm 10\%$.

To demonstrate this process, we start by showing that a cost function, measuring the difference between data and model, is sensitive with respect to changes in the maximum conductance of major currents. Next, we show that this sensitivity is sufficient to invert simulated data and obtain a mathematical model of a drug effect. This model can be mapped from the IM case to the M case simply by multiplying a parameter vector by a diagonal maturation matrix. Finally, we apply the method of inversion to obtain an IM model based on experimental data obtained using voltage- and calcium sensitive dyes in an MPS. Again, the IM model is mapped to an M model. The effects of drugs are identified by inverting MPS data (voltage and cytosolic calcium concentration) and then mapping the resulting model from IM to M giving a mathematical model of the mature cardiomyocytes under the influence of a drug.

2 Results

2.1 Model inversion is sensitive to perturbations in major ion channel currents

The inversion of data through the minimization of a cost function requires that this cost function is sensitive to changes in model parameters. In Figure 2, we illustrate the sensitivity of three cost functions utilizing voltage, calcium, or both, to perturbations in the conductances of major cellular currents or fluxes. Here the base model (see Methods) is defined by a modified version of the Paci et al. model [9] (the details of the modification are given in the supplementary information).

The results indicate that the cost function using voltage alone, H_V, is sensitive to only some of the currents and fluxes, and in particular, it is largely insensitive to changes in I_{to} and I_{Ks}. Similar trends are seen in the calcium mismatch, H_{Ca}, and this cost function is, in general, less sensitive than the H_V version. Finally, we consider the cost function combining both the voltage and calcium data, $H_{V+\text{Ca}}$, and observe that it is more sensitive to perturbations than both H_V and H_{Ca} alone, although some currents are still largely invisible.

Of note the maximum upstroke velocity of the action potential is not added as a part of the H_V cost function. Adding this component would likely improve sensitivity, especially for the sodium current, but our measurements (see Methods) do not at present provide sufficient accuracy of the upstroke velocity. However, the upstroke velocity of the calcium transient can be accurately estimated from the MPS measurements and is therefore a part of the cost function describing the calcium mismatch.

2.2 Simulated channel block identification

Although Figure 2 shows the sensitivity of the computed cost functions with respect to individual currents, we need to establish that the cost functions are adequately sensitive when multiple currents are allowed to vary. In Figure 3, we show the values of $H_{V+\mathrm{Ca}}$ as a function of pairwise perturbations in the maximum conductances of four major channels. The traces are theoretically computed using known effects of two chosen drugs; Verapamil which blocks I_{CaL} and I_{Kr}, and Cisapride which blocks I_{Kr}, see [28].

Our results indicate that the cost functional using both voltage and calcium can theoretically identify the simulated channel block of the chosen drugs. The left panels show the value of $H_{V+\mathrm{Ca}}$ as a function of the perturbation of the maximum conductances when the drug data are computed using the specified blocking due to the application of Verapamil. Six different configurations of pairwise blocking perturbations were tested and a minimum is clearly obtained close to the correct blocking of I_{CaL} and I_{Kr}. Meanwhile, in the right panel, we show the values of $H_{V+\mathrm{Ca}}$ when I_{Kr} is blocked by 50%, simulating the effect of Cisapride. The pairwise perturbations clearly identify that I_{Kr} is blocked by around 50%. These results indicate that an optimization algorithm of the cost function could find unique minima corresponding to specific channel blocks.

2.3 Simulated drug effect identification using the inversion procedure

Our methodology for inversion and mapping from the IM to the M state is first illustrated in Figure 4 using simulated data. This process is used to identify the theoretical effect of the two drugs of Verapamil and Cisapride on mature cells from waveforms that would be obtained from known channel blocking. From the left panel, we observe that the inversion algorithm is able to identify the specified effect of both Verapamil and Cisapride very accurately, reproducing chosen blocks nearly exactly. This is consistent with the results of Figure 3. The figure also shows the IM (middle panel) and M (right panel) action potentials and calcium transients. The M models are computed using the maturation map introduced in the Methods section showing how these detected blocks would appear in mature cells.

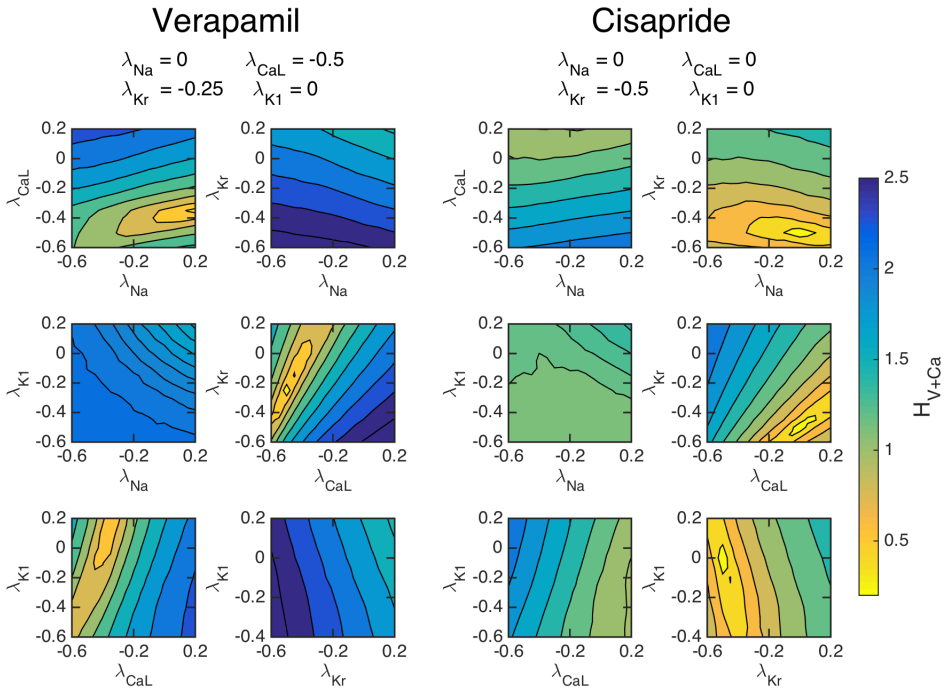

Figure 3: The cost function (4) with $\varepsilon = 0.2$ for simulated drug data, evaluated with pairwise perturbations of maximum conductances to examine if a unique minimum can be found corresponding to chosen drug effects. Left panels: The effect of Verapamil is simulated by blocking the I_{CaL} and I_{Kr} by 50% and 25%, respectively. Right panels: The effect of Cisapride is simulated by blocking the I_{Kr} by 50%. For both drugs, clear minimums are observed at the specified channel blockages.

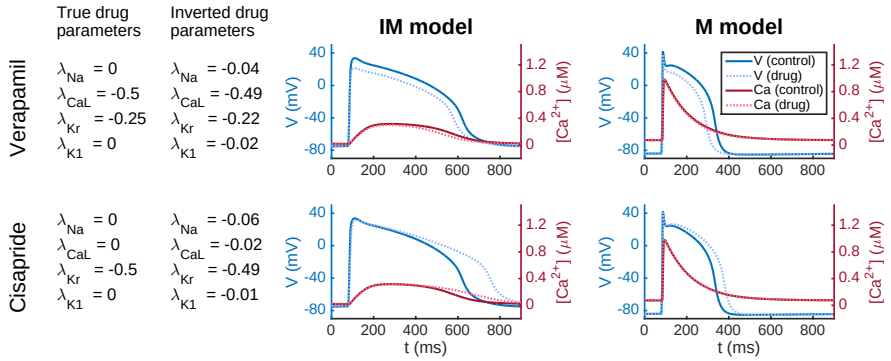

Figure 4: Identification of drug effects on M cells based on simulated data of IM cells. Left panel: Results of inversion by minimizing the cost function (4) with $\varepsilon = 0.2$. Middle panel: Action potential (blue) and calcium transient (red) before and after (dotted) the drug is applied. Right panel: Model results after application of the maturation matrix.

2.4 Identification of simulated channel block of major and minor currents

Figure 3 demonstrates using simulated data that the cost function $H_{V+\mathrm{Ca}}$ is able to theoretically identify induced changes to the I_{Kr} and I_{CaL} currents. In Figure 5, we extend this analysis to consider 50% single channel block of each of the major currents I_{Na}, I_{CaL}, I_{Kr} and I_{K1}. Again, we show the values of $H_{V+\mathrm{Ca}}$ for pairwise perturbations of the maximum conductance of these four currents. In the supplementary information, similar plots are given for the cost functions H_V and H_{Ca}.

Figure 5 indicates that the cost function $H_{V+\mathrm{Ca}}$ is theoretically able to identify each of the simulated single channel blocks. On the other hand, we expect that the cost function might fail to identify channel block of some of the minor, less sensitive membrane currents, for example I_{to} and I_{Ks}, which both have low sensitivity values in Figure 2. In Table 1, we rank the currents by their total inward and outward contributions to the action potential, and report how well the inversion algorithm is able to identify simulated 10%, 30%, 50%, and 70% single-channel block of these currents. We observe that the inversion algorithm is not able to correctly identify the block of the smaller contributing currents I_{to} and I_{Ks}, but identifies the block of I_{K1}, I_{CaL}, I_{Kr}, and I_{Na} quite accurately for the investigated channel blockings.

2.5 Channel block identification using a combined *in vitro / in silico system*

After demonstrating the theoretical sensitivity of inversion and drug effect prediction, we turn to the application of inverting actual cardiac MPS data. Average

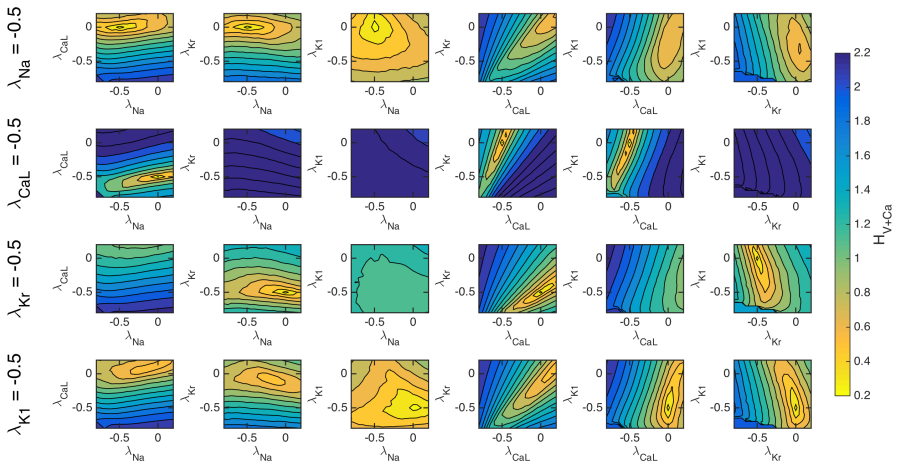

Figure 5: The cost function (4) with $\varepsilon = 0.2$ evaluated for pairwise perturbations of the maximum conductances of four major currents for simulated single-channel block of each of the currents. In the upper panel, I_{Na} is blocked by 50%, and in the next panels, I_{CaL}, I_{Kr} and I_{K1} are similarly blocked by 50%. Like in Figure 3, clear minimums are observed at the correct blockages in all four cases.

	$\int \lvert I \rvert dt$ (nC/μF)	$\lambda = -0.1$	$\lambda = -0.3$	$\lambda = -0.5$	$\lambda = -0.7$
I_{K1}	388.3	-0.08	-0.30	-0.47	-0.69
I_{CaL}	225.1	-0.13	-0.32	-0.58	-0.71
I_{Kr}	187.0	-0.11	-0.28	-0.50	-0.70
I_{Na}	119.4	-0.11	-0.32	-0.47	-0.68
I_{to}	12.6	0.00	0.00	-0.15	-0.27
I_{Ks}	3.6	0.00	0.00	-0.05	-0.10

Table 1: Identification of simulated single-channel block of six currents and four levels of block. We used the cost function $H_{V+\mathrm{Ca}}$ defined in (4) with $\varepsilon = 0.2$. The second column of the table reports the integral of the absolute value of each of the currents in the unperturbed case, and the last four columns report the estimated channel blocks returned by the inversion algorithm for each single-channel block. In all cases, the conductance of all six currents was allowed to vary in the inversion procedure.

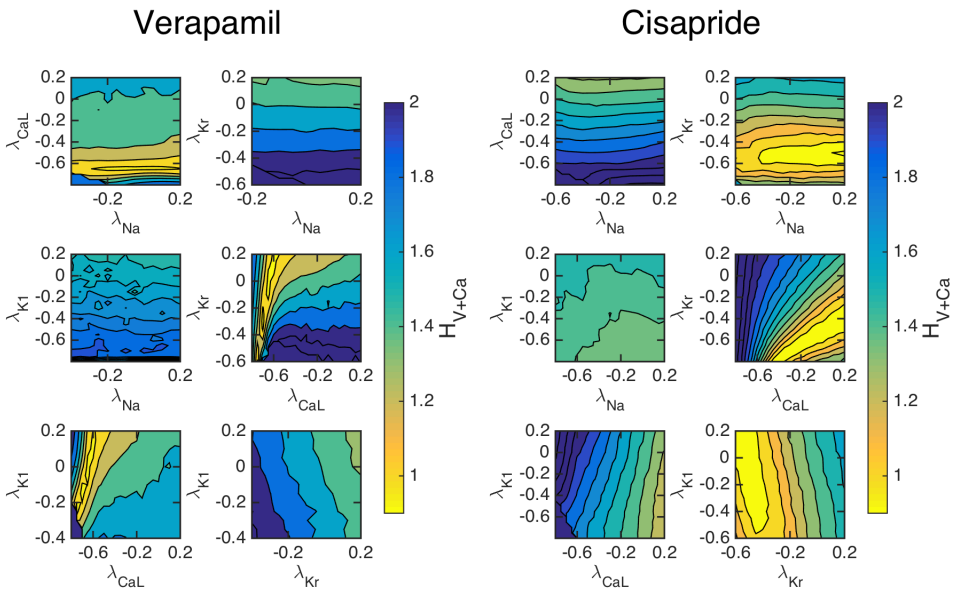

Figure 6: The cost function (4) with $\varepsilon = 0.2$ evaluated for pairwise perturbations of maximum conductances using measured data from the MPS. Left panels: The effect of a dose of 100 nM of Verapamil is shown; it clearly blocks I_{CaL} and it also blocks I_{Kr}. Right panels: The effect of a dose of 10 nM of Cisapride is shown; it clearly blocks I_{Kr}. The results of the inversion is given in Figure 7.

voltage and calcium traces $(v, Ca) = (v(t), Ca(t))$ from an MPS [3] were inverted to yield parameterized mathematical models of the IM cells. This was done first for control data, denoted by (v^C, Ca^C) to yield a control model. We then show the sensitivity of the cost function $H_{V+\mathrm{Ca}}$ comparing this model with obtained voltage and calcium waveforms under the effect of actual doses of Verapamil and Cisparide, (v^D, Ca^D). In Figure 6, we present pairwise perturbations of maximum conductances and we observe again that the cost function $H_{V+\mathrm{Ca}}$ is sensitive to these perturbations. For Verapamil, we see that the cost function clearly indicates that I_{CaL} is blocked by around 50%. Furthermore, I_{Kr} seems to be blocked significantly, but it is not clear from the figure the extent of the block. In the right panel, we also consider the effect of Cisapride. Here, the cost function indicates that I_{Kr} is blocked to a large extent.

The full inversion procedure (see the Methods section) is then applied, and it finds that I_{CaL} is blocked by 71% and I_{Kr} is blocked by 19% (see Figure 7) for Verpamil, in rough agreement with known properties of Verapamil at this dose. For Cisapride, the inversion predicts that I_{Kr} is blocked by 52%, and it predicts that the other currents are nearly unaffected by the drug.

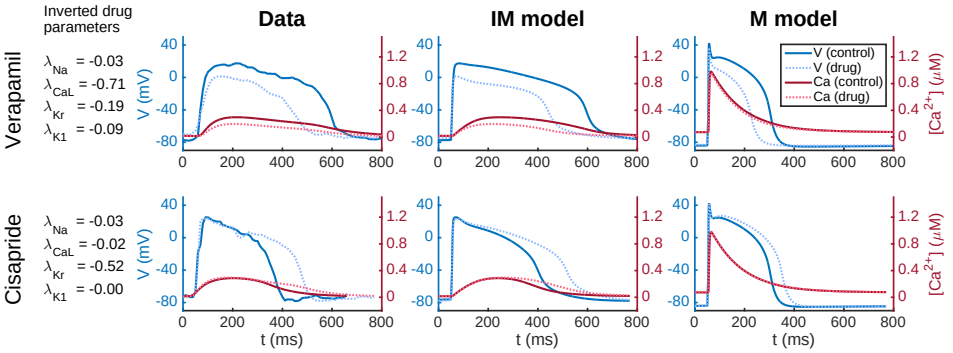

Figure 7: Results obtained by applying the inversion procedure to measured MPS data. First column: Results of inversion by minimizing the cost function (4) with $\varepsilon = 0.2$. Second column: Average voltage and calcium traces from MPS measurements. Third column: The AP model of the IM cells. Fourth column: The AP model of the M cells.

2.6 Mature AP change prediction using MPS data

In Panel 1 (leftmost) of Figure 7, we show the numeric results of inversion using measured data. The next three panels show action potentials and calcium transients for measured data (Panel 2), simulation of IM cells (Panel 3) and simulation of M cells (Panel 4). The simulations presented in Panel 3 are based on inversion of the MPS data giving the block values shown in Panel 1. The parameter vector (see the Methods section) representing the IM cells is multiplied by the maturation matrix in order to define the parameter vector representing the M cells. The figure illustrates how MPS measurements of IM cells can be used to estimate the effect of an unknown compound for M cells.

3 Discussion

In this paper, we present a mathematical analysis framework to define the electrophysiologic mechanisms of drug action in mature human cardiomyocytes using only optical recordings of membrane potential and calcium in hiPSC-CMs. This procedure overcome a number of major existing challenges in hiPSC-CM-based screening: (1) data inversion of measured drug effects can be successfully applied to all-optical experimental data, thus allowing detailed pharmacologic characterization without the need for intracellular electrodes, (2) the mathematical approach to mapping between hiPSC-CM and adult myocyte electrophysiology is straightforward and generalizable, and (3) the MPS-based optical recordings are averaged over relatively large populations of hiPSC-CMs, thus reducing errors associated with the well-known phenotypic heterogeneity of hiPSC-CM preparations.

3.1 Inversion of voltage and calcium traces into action potential models

Modern cardiac AP models have been developed more or less continually since the celebrated sinoatrial node model of Noble [30]. As a result, a range of cardiac cellular models have evolved to represent the accumulated knowledge of nearly six decades of multidisciplinary research, and the models are detailed and complex. Conventional approaches to developing these models have relied heavily upon voltage-clamp microelectrode data. These techniques provide exquisite resolution of single-channel [31, 32, 33, 34], through to whole-cell currents [35, 36, 37], and has thereby allowed the models to provide remarkably accurate reconstructions of cardiac cellular APs and calcium dynamics. However, while generalized cell models built using such data are widely used, especially to mechanistically understand how drug compounds alter electrophysiology, the experimental methods used to build them are technically challenging, have intrinsically low-throughput and cannot be used on tissue models like MPS.

In the present paper, we have developed an alternative approach that attempts to exploit the decades of information stored in modern cardiac AP models to rapidly parameterize *base models* for hiPSC-CMs. Rather than the data traditionally used to develop AP models, we used metrics that can readily be measured in a MPS, namely the optically assessed transmembrane potential and cytosolic calcium concentration. However, these data are fundamentally different from the detailed measurements of single currents traditionally used to invert measurements into biophysical models, and new methodology is needed. The approach taken in this report is based on minimization of a cost function comparing the predicted and measured waveforms, which seems to provide reasonable accuracy in analysis, but it is clear that some currents are still largely invisible even theoretically, and alternative approaches may lead to broader or more focused results.

For example, it was observed in Figure 2 that the cost function $H_{V+\mathrm{Ca}}$ is more sensitive than both H_V and H_{Ca} (see (3)–(4)). This indicates that both voltage and calcium traces must be measured in order to get optimal inversion of the measurements. However, this depends on the application. For instance, if the main purpose is to study side effects on the I_{Kr} current, it may be sufficient to only consider voltage traces. In addition, cost functions which take into account measured extracellular potential or contractile force generated by the IM cells may also be used to better invert specific drug induced changes.

3.2 Uniqueness of conductance defined action potential models

One significant question is the uniqueness of the parameters obtained in inversion of the optical waveforms, as mathematical models of excitable tissue often exhibit non unique behavior. For example, in models of neurons it is well known that different cell models can provide similar neuronal activity, see e.g. [38, 39, 40]. Similar observations have been made for a variety of models of cardiac cells, in [41]

using the ten Tusscher et al. model [19], and in [42] using the O'Hara et al. model [17]. The implication of these observations is that it is generally very challenging to uniquely determine conductances from AP observations, and indeed, it has clearly been demonstrated that single action potential waveforms can have multiple conductance parameterizations that a give low fit error when many parameters are allowed to vary [37]. Several methods have been tried to solve this problem; see e.g. [43, 44], and promising approaches have been suggested by a number of groups. For example, in [41] it was shown that using several physical properties of the dynamics improve the invertibility of the conductances. More recently, optmized voltage-clamping protocols [37] have been introduced to give better resolution of smaller currents and more uniquely determine conductances. We see in our results the same lack of uniqueness, especially when we try to invert smaller currents such I_{to} and I_{Ks}. However, we are able to observe that four major currents appear largely visible and invertible with a combined measure of voltage and calcium from a single paced waveform and a CPU-intensive method that avoids the differentiation of a rough cost-function.

3.3 Using correlations for parametrization and mapping

Others have also approached the question of how to map changes in cardiac dynamics between populations using model results. In a series of papers (see [45, 41, 46, 47, 12]) by Sobie and co-authors, a comprehensive theory has been developed for using correlations between simulation results to parameterize models and for mapping between species, and between immature and mature cells. Starting in [45], it is observed that input parameters such as maximum conductances of ion currents are correlated with output parameters such as the APD and the net amplitude of the calcium transient. Such correlations are useful because they can be used to understand how natural variability of input parameters affects output characteristics in populations of cell models. The correlations can also, in principle, be used for parameterization by measuring output characteristics and use the inverse correlation matrix to parameterize input parameters.

In [12], the correlation is taken one step further by observing that output parameters from simulations of one species are correlated to the output parameters of simulations based on a model of another species. Similarly, the authors observe that simulation outputs from a model of immature cells are correlated with output results of simulations based on a model of mature cells. Therefore, it is, in principle, possible to perform measurements of immature data and map the results to the mature case.

The correlation approach to mapping between species and between immature and mature cells is highly promising. However, the theory is based on observed correlations between simulated data and provide no mechanistic insight into the relations. In our approach, it follows directly from the assumptions that the proteins are the same for immature and mature cells, that there *must* be a mapping between models of immature and mature cells.

3.4 The maturation map

While the inversion of data from hiPSC-derived cells will be essential for understanding the electrophysiology of immature cells, understanding how such electrophysiolgical changes translate into mature cells could provide powerful means to screen drugs for side effects. We introduce the idea of a maturation map, which assumes that the essential difference between an immature (IM) cell and a mature (M) cell can be described by the number of proteins, the membrane area and the volume of the cell and the intracellular storage structures. Based on these assumptions, we have argued that we can map any IM parameter vector, p_{IM}, to an associated M parameter vector, p_M, simply by multiplying by a diagonal matrix Q: $p_M = Qp_{IM}$. We have illustrated this mapping and noted that reasonable models of an IM AP are mapped over to a reasonable M AP. In addition, we have seen that measured IM data can be inverted to yield p_{IM}, and then the maturation mapping gives the adult AP parameterized by $p_M = Qp_{IM}$.

In the present report, we have simply addressed the mapping directly from an IM state to the M cells. However, maturation is clearly a dynamic process with rapid changes, and it may therefore be of interest to use this mapping to investigate the time dependent behaviour of the cells. Measurements of several time instances of IM cells may give insight into the developmental trajectories of hiPSC-CMs and how different maturation protocols alter the electrophysiological properties of generated test cells. Such studies may be useful for both choosing maturation protocols to optimize data inversion sensitivity, and for quality control measures of batch to batch cells.

In addition, taking into account more aspects of cellular electrophysiology could refine our approach. For example, one could take into account that proteins exist in various forms; for instance, the sodium channel has nine different forms with different associated possible channelopathies. These variants may proliferate at different rates and thus potentially lead to significant changes in the properties of the M cells.

3.5 hiPSC data sources

While our results show the promise of this methodology, considerable current limitations exist that need to be addressed. First, variability in hiPSC-CMs remains a challenge ([48, 49]). In the preparation of the data, we have dealt with variability by discarding individual voltage and calcium traces that are significantly different from the average behaviour of the cells. This seems to give sufficient accuracy for inversion, and the effects of the drugs we have considered have shown significant cellular changes. However, even if the average results clearly respond to the doses of the drugs applied in this study, work on reducing the variability of generated hiPSC-CMs in MPSs is clearly needed for batch to batch consistency.

In addition, improvements in data acquisition from the cell systems may also improve the methodology, in particular it may increase the sensitivity of cost functions to currents that are presently less visible. For instance, the voltage

waveform can not currently be imaged at the time resolution needed to obtain accurate measurements of the upstroke, due to a combination of hardware and optical light collection limitations. In the same manner, the signal to noise ratio in this waveform, due to background dye absorption, prevents adequate resolution of the plateau phase and in particular of the notch in the action potential, preventing inversion of the I_{to} current. Improvements in the methodology for collection of high resolution optical voltage data will therefore lead to substantial improvements in mapping resolution.

It should also be noted that it is possible to measure the extracellular field potential in the microphysiological systems using a multi-electrode array (MEA) system, see e.g., [50, 1]. Such data can be incorporated in our method by using the EMI model (see e.g., [51]) instead of the common AP models. In this case, the function H given by (4) would have to be extended to include the EFPs. This would be considerably more computationally demanding than the present method, but it may also increase the accuracy of the inversion.

3.6 Extension to species - species mapping

The basic idea underpinning the maturation mapping is that the proteins populating the cell membrane are the same for the IM cells and the M cells; the reason for the significant difference in AP between these cell types is the difference in densities of membrane proteins. Similarly, the proteins of the cell membranes are also quite similar from one specie to another, but again the densities of these proteins vary considerably. Therefore, the procedure for detecting side effects of drugs developed in this report *may* be generalized to be used between species. More specifically; it may be possible to measure the effect of drugs for mouse cells and deduce the effect for human cells following the steps detailed in the Method section below. This may be of significance because of the abundance of mouse data.

4 Methods

Our aim is to enable automatic characterization of side-effects of drugs for mature cardiomyocytes based on measurements of voltage and calcium traces of immature cells in an MPS. Here, we describe the methods applied above; we briefly explain how appropriate optical measurements of voltage and calcium are obtained, how a model of the AP of a mature cardiomyocyte can be obtained from a model of an immature cardiomyocyte, and how data is inverted to define a mathematical model of the AP of immature cells. Furthermore, we describe how the effects of drugs on M cardiomyocytes can be estimated using measurements of the effect on IM cardiomyocytes.

4.1 Measuring voltage and calcium traces using an MPS

Using previously developed techniques [3], cardiac MPS systems were loaded and matured prior to drug exposure. On the day upon which studies were performed, freshly measured drug was dissolved into DMSO (Cisapride) or media (Verapamil) and serially diluted. Each concentration of the drug to be tested was preheated for 15-20 min in a water bath at 37°C and subsequently sequentially injected in the device. At each dose, after 5 min of exposure, the drug's response on the microtissue was recorded using a Nikon Eclipse TE300 microscope fitted with a QImaging camera. Fluorescent images were acquired at 100 frames per second using filters to capture GCaMP and BeRST-1 fluorescence as previously described. Images were obtained across the entire chip for 6-8 seconds, with cell excitation paced at 1 Hz, to capture multiple beats for processing.

Fluorescence videos were analyzed using custom Python software utilizing the open source Bio-Formats tool to produce characteristic voltage and calcium waveforms for each chip and tested drug dose. Briefly, for each analysis, the fluorescent signal for the entire visual field was averaged, excluding pixels which did not change significantly in intensity over the acquisition. The signal was then smoothed using a 3 point median filter, and 5-7 individual action potentials or calcium transients overlayed by aligning the maximum dF/dt and then averaged into a single transient.

4.2 Inversion of voltage and cytosolic calcium traces

In order to complete the description of the steps presented in Table 2 (below), we need to explain how the inversion used in steps 4 and 5 is performed, and the key question is how to do the inversion. To this end, we assume that we have a base model of the form

$$v_t = -\sum_i q_i I_i(v, s), \tag{1}$$

where I_i represents the dynamics of the individual membrane proteins and q_i represents the maximum conductance of the ion channels (or the maximum rate of an exchanger or a pump). Furthermore, v is the transmembrane potential and s represents the remaining state variables of the model. In order to adjust this model to a set of measured data given by (v^*, c^*), we seek parameters λ_i such the solution of

$$v_t = -\sum (1 + \lambda_i) q_i I_i(v, s) \tag{2}$$

is as close as possible to the measured data, (v^*, c^*). The distance from the computed solution $(v, c) = (v(\lambda), c(\lambda))$ to the measured data (v^*, c^*) is given by a cost function $H = H(\lambda)$.

We consider the following cost functions

$$H_V(\lambda) = \left(\sum_{j=1}^{4} H_j(\lambda) + \varepsilon \sum_i \lambda_i^2 \right)^{1/2}, H_{\mathrm{Ca}}(\lambda) = \left(\sum_{j=5}^{8} H_j(\lambda) + \varepsilon \sum_i \lambda_i^2 \right)^{1/2}, \tag{3}$$

$$H_{V+\mathrm{Ca}}(\lambda) = \left(\sum_{j=1}^{8} H_j(\lambda) + \varepsilon \sum_i \lambda_i^2 \right)^{1/2}, \tag{4}$$

where

$$H_1 = \frac{|\int_{t_0(\lambda)}^{t_1(\lambda)} v(\lambda)dt - \int_{t_0^*}^{t_1^*} v^* dt|}{|\int_{t_0^*}^{t_1^*} v^* dt|}, \qquad H_2 = \frac{|\mathrm{APD}_{V,30}(\lambda) - \mathrm{APD}^*_{V,30}|}{|\mathrm{APD}^*_{V,30}|},$$

$$H_3 = \frac{|\mathrm{APD}_{V,50}(\lambda) - \mathrm{APD}^*_{V,50}|}{|\mathrm{APD}^*_{V,50}|}, \qquad H_4 = \frac{|\mathrm{APD}_{V,80}(\lambda) - \mathrm{APD}^*_{V,80}|}{|\mathrm{APD}^*_{V,80}|},$$

$$H_5 = \frac{|(\frac{dc}{dt})_{\max}(\lambda) - (\frac{dc}{dt})^*_{\max}|}{|(\frac{dc}{dt})^*_{\max}|}, \qquad H_6 = \frac{|\mathrm{APD}_{\mathrm{Ca},30}(\lambda) - \mathrm{APD}^*_{\mathrm{Ca},30}|}{|\mathrm{APD}^*_{\mathrm{Ca},30}|},$$

$$H_7 = \frac{|\mathrm{APD}_{\mathrm{Ca},50}(\lambda) - \mathrm{APD}^*_{\mathrm{Ca},50}|}{|\mathrm{APD}^*_{\mathrm{Ca},50}|}, \qquad H_8 = \frac{|\mathrm{APD}_{\mathrm{Ca},80}(\lambda) - \mathrm{APD}^*_{\mathrm{Ca},80}|}{|\mathrm{APD}^*_{\mathrm{Ca},80}|}.$$

Here, the star $*$ is used to denote observed data, either generated by simulations or gathered from the MPS. Also, $(\frac{dc}{dt})_{\max}$ is the maximal upstroke velocity of the calcium concentration. Furthermore, $\mathrm{APD}_{V,30}$ is defined as the length (in ms) of the time from the value of the transmembrane potential, in the upstroke, is 30% below its maximum value (t_0) until it again is repolarized to 30% of its maximum value (t_1). The values $\mathrm{APD}_{V,50}$ and $\mathrm{APD}_{V,80}$ are defined similarly. Likewise, the terms $\mathrm{APD}_{\mathrm{Ca},30}$, $\mathrm{APD}_{\mathrm{Ca},50}$ and $\mathrm{APD}_{\mathrm{Ca},80}$ represent the corresponding transient durations for the calcium concentration. In H_1, we compute the integral of the transmembrane potential from $t = t_0$ to $t = t_1$. Note that H_V only depends on characteristics of the voltage trace, whereas H_{Ca} only depends on characteristics of the calcium trace; finally, $H_{V+\mathrm{Ca}}$ includes the terms of both the two former cost functions and therefore depends on the characteristics of both the voltage trace and the calcium trace.

4.2.1 The minimization procedure

The inversion procedure aims to minimize the cost function measuring the difference between the target and model voltage and calcium waveforms. In every minimization, we have an existing parameter vector $\bar{p}$, and we seek an optimal perturbation of this vector where each component is given by $(1 + \lambda_i)\bar{p}_i$. Here, i runs over the components of the parameter vector and λ_i denotes the perturbation.

The cost function introduced above is irregular and hard to minimize. Therefore, we introduce a brute force search algorithm that avoids any attempt to take the gradient into account. To start searching for suitable values of $\lambda = \{\lambda_i\}$, we first set up a bounding box of allowed values of λ. This is initially set up so that each λ_i is in some interval, for instance [-0.5, 0.5]. Next, we draw N choices of λ randomly from the bounding box and compute $H(\lambda)$ for each of these N choices. We then pick out the five choices of λ that give the smallest values of $H(\lambda)$ and set up a new bounding box of reduced size around each of these five

choices of λ. More specifically, these bounding boxes are set up by centering the boxes around the chosen λ and letting the length of the interval for each λ_i be reduced to 90% of the length of the previous intervals. Note that this means that the new bounding boxes are not necessarily contained in the initial bounding box, but may extend beyond the initial intervals. We do, however, set up a restriction so that no bounding box is allowed to contain values of λ smaller than or equal to -1. In addition, when searching for the effect of drugs, we assume that the drug is a channel blocker and therefore only consider $\lambda \in (-1, 0]$.

After setting up the five new bounding boxes, we draw $N/5$ choices of λ randomly from each box and compute $H(\lambda)$ for each of these N choices of λ. We then select the five choices of λ that give the smallest values of $H(\lambda)$ and repeat the steps above for a given number of iterations. For the applications of the minimization method reported in the Results section, we generally use 10 iterations and $N = 5000$.

4.3 Maturation through multiplication

Our model of the maturation process rely on the assumption that the individual membrane proteins are functionally invariant under maturation, whereas the number of proteins, the membrane area and the cell volume change significantly (see e.g., [52, 53, 54, 11]). Also, different membrane proteins proliferate at different rates leading to large differences in the expression levels between IM and M cells. This, in turn, leads to characteristic differences between the IM and M voltage and calcium traces. The maturation process is illustrated in Figure 8.

4.4 A drug effects a singel protein in the same manner for IM and M cells

Since we assume that exactly the same proteins are present in the IM and M cells, it follows that the effect of a given drug on a protein in the IM case is identical to the effect on the same protein type in a M cell. This observation is essential in order to understand side effects on M cells based on measurements of the IM cells.

4.5 The membrane potential for IM and M cells in the presence of a single current

In order to illustrate the modeling process going from IM to M, we consider the following simplest possible case where the transmembrane potential v (in mV) is governed by a single current

$$Cv'(t) = -I, \tag{5}$$

with $I = go(v - v_0)$. Here, C is the membrane capacitance (in μF/cm^2), g is the maximum conductance of the channels (in mS/cm^2), o is the open probability of the channels (unitless), and v_0 is the resting potential of the channels (in mV).

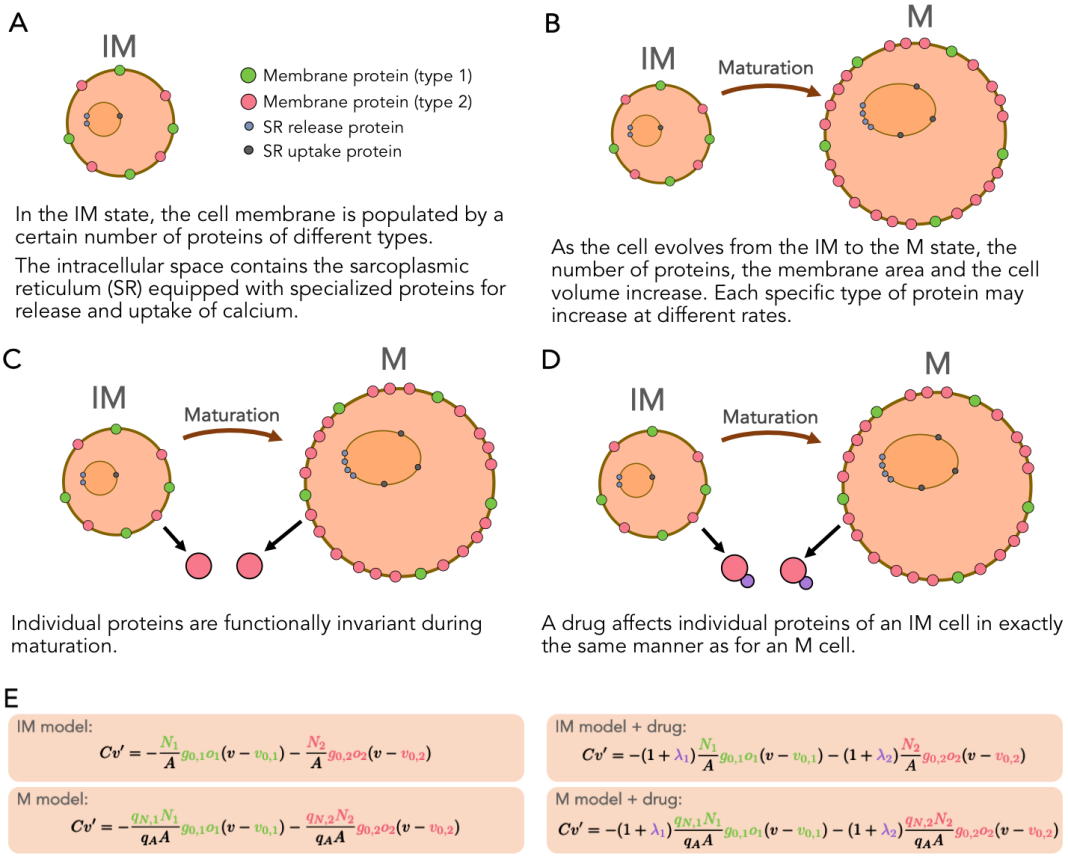

Figure 8: Illustration of the assumptions underlying our model of maturation. **A**: The immature cell with two types of membrane proteins, with a cytosolic space containing the sarcoplasmic reticulum with associated release and uptake proteins. **B**: Maturation is multiplication in the sense that the number of proteins increases at a protein specific rate. **C**: A specific protein in the IM cell is the same as in the M cell. **D**: A drug affects every single protein in the IM cell in exactly the same manner as for the M cell. **E**: Model of the transmembrane potential for IM and M cells, and the relation between these models; and how these models are affected when a drug is applied.

In this formulation, the current I is given in units of μA/cm^2. The maximum conductance can be written on the form

$$g = \frac{Ng_0}{A}, \tag{6}$$

where g_0 is the conductance (in mS) of a single channel, N is the number of channels and A is the membrane area of the cell (in cm^2).

Let N_{IM} and A_{IM} denote the number of ion channels and the surface area of the IM cell, respectively. Then there are constants q_N and q_A such that the number of channels in the M cell is given by $N_M = q_N N_{IM}$, and the membrane area of the M cell is given by $A_M = q_A A_{IM}$. Therefore, the maximum conductance of the M cell can be expressed in terms of the maximum conductance of the IM cell as follows,

$$g_M = \frac{N_M g_0}{A_M} = \frac{q_N N_{IM} g_0}{q_A A_{IM}} = \frac{q_N}{q_A} g_{IM} = q g_{IM}, \tag{7}$$

with $q = \frac{q_N}{q_A}$.

Here, we have explained that the representation of a single current can be mapped from IM to M simply by multiplying the maximum conductance by a factor. This derivation relies heavily on the assumption that the dynamics of the single channel, represented by the open probability o in (6), remains the same during maturation (see Figure 8). As a consequence, the Markov model (see e.g., [23]) representing the open probability of the single channel should be the same for the IM and the M version of the channel protein. Similar arguments can be presented for other membrane proteins such as exchangers and pumps. Furthermore, the intracellular Calcium machinery can be treated in exactly the same manner, leaving the IM and M models of a single protein to be distinguished only by a factor. Details of the mapping of calcium concentration fluxes are provided in the supplementary information.

The factors for the individual components of an AP model can be gathered in a parameter vector p, and a diagonal matrix Q can be used to store the maturation mapping from the IM parameter vector to the M parameter vector such that $p_M = Qp_{IM}$.

In Figure 9, we illustrate the use of the maturation mapping for well established AP models of hiPSC-CMs using the Paci et al. model [9], and of the adult human cardiomyocyte using the ten Tusscher et al. model [19]. For the Paci et al. model, we define the maturation map $Q_P = \text{diag}(\frac{q_A}{q_V}, q_{\text{Na}}, q_{\text{CaL}}, q_{\text{to}}, q_{\text{Ks}}, q_{\text{Kr}}, q_{\text{K1}}, q_{\text{NaCa}}, q_{\text{NaK}}, q_{\text{pCa}}, q_{\text{f}}, q_{\text{bNa}}, q_{\text{bCa}}, q_{\text{leak}}, q_{\text{up}}, q_{\text{rel}}) = (1.7, 0.4, 3, 5, 20, 0.7, 1.3, 0.05, 0.3, 0.6, 0.1, 0.5, 0.4, 200, 1, 36)$. Since p_{IM} is given by the paper [9], we can compute $p_M = Q_P p_{IM}$. Similarly, for the ten Tusscher et al. model we use $Q_T = \text{diag}(\frac{q_A}{q_V}, q_{\text{Na}}, q_{\text{CaL}}, q_{\text{to}}, q_{\text{Ks}}, q_{\text{Kr}}, q_{\text{K1}}, q_{\text{NaCa}}, q_{\text{NaK}}, q_{\text{pCa}}, q_{\text{f}}, q_{\text{pK}}, q_{\text{bNa}}, q_{\text{bCa}}, q_{\text{leak}}, q_{\text{up}}, q_{\text{rel}}) = (1.7, 4, 4.2, 17, 40, 1, 2.2, 0.4, 0.7, 1.7, 0.05, 19, 0.1, 0.6, 500, 1.3, 34)$, and since p_M is given by the paper [19], we can compute the IM version by $p_{IM} = Q_T^{-1} p_M$. The maturation maps are set up using an extended version of the standard inversion

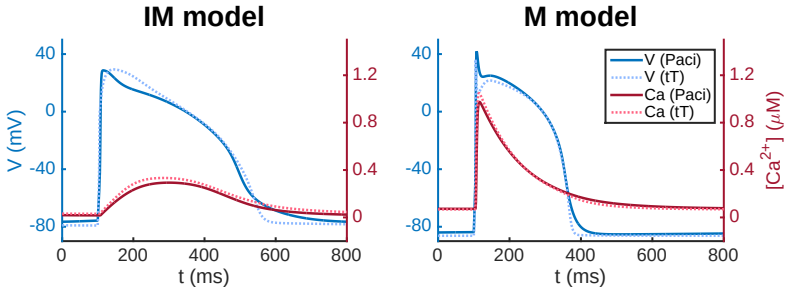

Figure 9: Immature and mature versions of the Paci et al. model [9] and the ten Tusscher et al. (tT) model [19]. The APs of the M cells are shorter and the upstroke velocity of the calcium transient is faster than for the IM case; compare left and right panels.

procedure described in Section 4.2 with characteristics of the currents I_{Na}, I_{CaL}, I_{Kr}, and I_{K1} included in the cost function (see the supplementary information for details).

We observe that these AP models display characteristic differences between IM and M cells; the upstroke of calcium transient of the IM cells is considerably slower than for the M cells, and the action potential duration is longer for the IM cells than for the M cells.

4.6 Estimating side-effects drugs

The method for identifying side effects of drugs is summarized in Table 2. The method involves eight steps:

Step 1: Base model Assume that there exists an *AP base model*, characterized by a parameter vector $p^{IM,B}$, representing a prototypical IM cell, and an associated *base maturation map* Q^B. The associated M cells are characterized by $p^M = Q^B p^{IM,B}$. The M model, parameterized by p^M, provides a normal mature AP. No drug is involved in parameterizing the base model. Note also that the base model is used for numerous (independent) measurements. The base model in our computations is a modified version of the model of hiPSC-CMs suggested by Paci et al. [9]; see the supplementary information for details concerning the base model.

Step 2 and 3: MPS-measurements For the IM cells, we measure the transmembrane potential and the cytosolic calcium concentration, stored as (v^C, c^C), and make similar measurements for the case when a drug has been applied, stored as (v^D, c^D). Here C is for control (no drug) and D is for drug.

Step 4 and 5: Inversion Generally, the notation

$$(v, c) \xrightarrow{\text{inversion}(q)} p \tag{8}$$

1	Base model	$p^{M,B} = Q^B p^{IM,B}$
2	Measure control (C) data, no drug	(v^C, c^C)
3	Measure data with drug (D) applied	(v^D, c^D)
4	Invert C-data	$(v^C, c^C) \xrightarrow{\text{inversion}(p^{IM,B})} p^{IM,C}$
5	Invert D-data	$(v^D, c^D) \xrightarrow{\text{inversion}(p^{IM,C})} p^{IM,D}$
6	Update maturation map	$Qp^{IM,C} = p^M$
7	Parameterize M version of D cells	$p^{M,D} = Qp^{IM,D}$
8	Compare M version of C and D cells	Simulate M cells with $p^{M,D}$ and p^M

Table 2: The table shows a summary of the method for computing possible side effects of drugs for mature cells based on measurements conducted on immature hiPSC-derived cells.

means that the data (v, c) are inverted to yield a model parameterized by the vector p, using the model parameterized by the vector q as a starting point for the inversion. The control data (no drug) given by (v^C, c^C) are inverted to yield the model parameterized by $p^{IM,C}$, using the parameter vector p^B as a starting point for the inversion. Likewise, the D-data are inverted to give the model $p^{IM,D}$, where the parameter vector $p^{IM,C}$ is used as starting point.

Step 6: Update maturation map The maturation map can now be updated to secure that if Q is applied to the IM parameter vector, $p^{IM,C}$, the resulting parameter vector is the base model of the M cell parameterized by the vector p^M.

Step 7: Map from IM to M The updated maturation map Q is used to compute the parameterization of the M version of the drugged cells.

Step 8: Drug affected M cell The effect of the drug on the M cells is analyzed by comparing the vectors p^M and $p^{M,D}$. The components of $p^{M,D}$ that are significantly different from its p^M counterpart, has been significantly affected by the drug. The effect of the drug on the mature AP is estimated by comparing the result of simulations of the models characterized by p^M and $p^{M,D}$.

References

[1] Hiroyuki Ando, Takashi Yoshinaga, Wataru Yamamoto, Keiichi Asakura, Takaaki Uda, Tomohiko Taniguchi, Atsuko Ojima, Raku Shinkyo, Kiyomi Kikuchi, Tomoharu Osada, Seiji Hayashi, Chieko Kasai, Norimasa Miyamoto, Hiroyuki Tashibu, Daiju Yamazaki, Atsushi Sugiyama, Yasunari Kanda, Kohei Sawada, and Yuko Sekino. A new paradigm for drug-induced torsadogenic risk assessment using human iPS cell-derived cardiomyocytes. *Journal of Pharmacological and Toxicological Methods*, 84:111 – 127, 2017.

[2] Luca Sala, Milena Bellin, and Christine L Mummery. Integrating cardiomyocytes from human pluripotent stem cells in safety pharmacology: has the time come? *British Journal of Pharmacology*, 2016.

[3] Anurag Mathur, Peter Loskill, Kaifeng Shao, Nathaniel Huebsch, SoonGweon Hong, Sivan G Marcus, Natalie Marks, Mohammad Mandegar, Bruce R Conklin, Luke P Lee, and Kevin E Healy. Human iPSC-based cardiac microphysiological system for drug screening applications. *Scientific Reports*, 5:8883, 2015.

[4] John P Wikswo. The relevance and potential roles of microphysiological systems in biology and medicine. *Experimental Biology and Medicine*, 239(9):1061–1072, 2014.

[5] Eric W Esch, Anthony Bahinski, and Dongeun Huh. Organs-on-chips at the frontiers of drug discovery. *Nature Reviews. Drug Discovery*, 14(4):248, 2015.

[6] Yosuke K Kurokawa and Steven C George. Tissue engineering the cardiac microenvironment: Multicellular microphysiological systems for drug screening. *Advanced Drug Delivery Reviews*, 96:225–233, 2016.

[7] Renjun Zhu, Adriana Blazeski, Ellen Poon, Kevin D. Costa, Leslie Tung, and Kenneth R. Boheler. Physical developmental cues for the maturation of human pluripotent stem cell-derived cardiomyocytes. *Stem Cell Research & Therapy*, 5(5):117, Oct 2014.

[8] Junyi Ma, Liang Guo, Steve J Fiene, Blake D Anson, James A Thomson, Timothy J Kamp, Kyle L Kolaja, Bradley J Swanson, and Craig T January. High purity human-induced pluripotent stem cell-derived cardiomyocytes: electrophysiological properties of action potentials and ionic currents. *American Journal of Physiology-Heart and Circulatory Physiology*, 301(5):H2006–H2017, 2011.

[9] Michelangelo Paci, Jari Hyttinen, Katriina Aalto-Setälä, and Stefano Severi. Computational models of ventricular-and atrial-like human induced pluripotent stem cell derived cardiomyocytes. *Annals of Biomedical Engineering*, 41(11):2334–2348, 2013.

[10] Jie Liu, Zachary Laksman, and Peter H Backx. The electrophysiological development of cardiomyocytes. *Advanced Drug Delivery Reviews*, 96:253–273, 2016.

[11] Fikru B Bedada, Matthew Wheelwright, and Joseph M Metzger. Maturation status of sarcomere structure and function in human ipsc-derived cardiac myocytes. *Biochimica et Biophysica Acta (BBA)-Molecular Cell Research*, 1863(7):1829–1838, 2016.

[12] Jingqi QX Gong and Eric A Sobie. Population-based mechanistic modeling allows for quantitative predictions of drug responses across cell types. *NPJ systems biology and applications*, 4(1):11, 2018.

[13] Ping Liang, Feng Lan, Andrew S Lee, Tingyu Gong, Veronica Sanchez-Freire, Yongming Wang, Sebastian Diecke, Karim Sallam, Joshua W Knowles, Patricia K Nguyen, et al. Drug screening using a library of human induced pluripotent stem cell-derived cardiomyocytes reveals disease specific patterns of cardiotoxicity. *Circulation*, 127:1677–1691, 2013.

[14] Yoram Rudy and Jonathan R Silva. Computational biology in the study of cardiac ion channels and cell electrophysiology. *Quarterly Reviews of Biophysics*, 39(01):57–116, 2006.

[15] Yoram Rudy. From genes and molecules to organs and organisms: Heart. *Comprehensive Biophysics*, pages 268–327, 2012.

[16] Zhilin Qu, Gang Hu, Alan Garfinkel, and James N Weiss. Nonlinear and stochastic dynamics in the heart. *Physics Reports*, 543(2), 2014.

[17] Thomas O'Hara, László Virág, András Varró, and Yoram Rudy. Simulation of the undiseased human cardiac ventricular action potential: Model formulation and experimental validation. *PLoS Computational Biology*, 7(5):e1002061, 2011.

[18] Eleonora Grandi, Francesco S. Pasqualini, and Donald M. Bers. A novel computational model of the human ventricular action potential and Ca transient. *Journal of Molecular and Cellular Cardiology*, 48(1):112–121, 2010.

[19] Kirsten HWJ ten Tusscher, Denis Noble, Penelope J Noble, and Alexander V Panfilov. A model for human ventricular tissue. *American Journal of Physiology-Heart and Circulatory Physiology*, 286(4):H1573–H1589, 2004.

[20] Kirsten HWJ ten Tusscher and Alexander V Panfilov. Cell model for efficient simulation of wave propagation in human ventricular tissue under normal and pathological conditions. *Physics in Medicine and Biology*, 51(23):6141, 2006.

[21] Colleen E Clancy, Zheng I Zhu, and Yoram Rudy. Pharmacogenetics and anti-arrhythmic drug therapy: A theoretical investigation. *AJP: Heart and Circulatory Physiology*, 292(1):H66–H75, 2007.

[22] Jonathan D Moreno and Colleen E Clancy. Using computational modeling to predict arrhythmogenesis and antiarrhythmic therapy. *Drug Discovery Today: Disease Models*, 6(3):71–84, 2009.

[23] Aslak Tveito and Glenn T Lines. *Computing Characterizations of Drugs for Ion Channels and Receptors Using Markov Models*. Springer-Verlag, Lecture Notes, vol. 111, 2016.

[24] Michelangelo Paci, Elisa Passini, Stefano Severi, Jari Hyttinen, and Blanca Rodriguez. Phenotypic variability in LQT3 human induced pluripotent stem cell-derived cardiomyocytes and their response to anti-arrhythmic pharmacological therapy: an in silico approach. *Heart Rhythm*, 2017.

[25] Dongrui Ma, Heming Wei, Yongxing Zhao, Jun Lu, Guang Li, Norliza Binte Esmail Sahib, Teng Hong Tan, Keng Yean Wong, Winston Shim, Philip Wong, et al. Modeling type 3 long QT syndrome with cardiomyocytes derived from patient-specific induced pluripotent stem cells. *International Journal of Cardiology*, 168(6):5277–5286, 2013.

[26] Azra Fatima, Shao Kaifeng, Sven Dittmann, Guoxing Xu, Manoj K Gupta, Matthias Linke, Ulrich Zechner, Filomain Nguemo, Hendrik Milting, Martin Farr, et al. The disease-specific phenotype in cardiomyocytes derived from induced pluripotent stem cells of two long QT syndrome type 3 patients. *PloS one*, 8(12):e83005, 2013.

[27] Kirsi Kujala, Jere Paavola, Anna Lahti, Kim Larsson, Mari Pekkanen-Mattila, Matti Viitasalo, Annukka M Lahtinen, Lauri Toivonen, Kimmo Kontula, Heikki Swan, et al. Cell model of catecholaminergic polymorphic ventricular tachycardia reveals early and delayed afterdepolarizations. *PloS one*, 7(9):e44660, 2012.

[28] William J. Crumb, Jose Vicente, Lars Johannesen, and David G. Strauss. An evaluation of 30 clinical drugs against the comprehensive in vitro proarrhythmia assay (CiPA) proposed ion channel panel. *Journal of Pharmacological and Toxicological Methods*, 81:251 – 262, 2016. Focused Issue on Safety Pharmacology.

[29] Anurag Mathur, Zhen Ma, Peter Loskill, Shaheen Jeeawoody, and Kevin E Healy. In vitro cardiac tissue models: Current status and future prospects. *Advanced Drug Delivery Reviews*, 96:203–213, 2016.

[30] Denis Noble. A modification of the Hodgkin–Huxley equations applicable to Purkinje fibre action and pacemaker potentials. *The Journal of Physiology*, 160(2):317–352, 1962.

[31] Bert Sakmann and Erwin Neher, editors. *Single-Channel Recording*. Springer, 2nd edition, 1995.

[32] David Colquhoun, AG Hawkes, and Bernard Katz. On the stochastic properties of bursts of single ion channel openings and of clusters of bursts. *Philosophical Transactions of the Royal Society London B*, 300:1–59, 1982.

[33] Ivo Siekmann, James Sneyd, and Edmund J. Crampin. MCMC Can Detect Nonidentifiable Models. *Biophysical Journal*, 103(11):2275–2286, December 2012.

[34] Aslak Tveito, Glenn Lines, Andrew G Edwards, and Andrew D McCulloch. Computing rates of Markov models of voltage-gated ion channels by inverting partial differential equations governing the probability density functions of the conducting and non-conducting states. *Mathematical Biosciences*, 277:126–135, 2016.

[35] Alan L Hodgkin and Andrew F Huxley. The components of membrane conductance in the giant axon of loligo. *The Journal of Physiology*, 116(4):473–496, 1952.

[36] Meron Gurkiewicz and Alon Korngreen. A numerical approach to ion channel modelling using whole-cell voltage-clamp recordings and a genetic algorithm. *PLoS Computational Biology*, 3(8):1633–1647, August 2007.

[37] Willemijn Groenendaal, Francis A Ortega, Armen R Kherlopian, Andrew C Zygmunt, Trine Krogh-Madsen, and David J Christini. Cell-specific cardiac electrophysiology models. *PLoS computational biology*, 11(4):e1004242, 2015.

[38] Astrid A Prinz, Dirk Bucher, and Eve Marder. Similar network activity from disparate circuit parameters. *Nature neuroscience*, 7(12):1345, 2004.

[39] Pablo Achard and Erik De Schutter. Complex parameter landscape for a complex neuron model. *PLoS Computational Biology*, 2(7):e94, 2006.

[40] Eve Marder and Adam L Taylor. Multiple models to capture the variability in biological neurons and networks. *Nature Neuroscience*, 14(2):133, 2011.

[41] Amrita X Sarkar and Eric A Sobie. Regression analysis for constraining free parameters in electrophysiological models of cardiac cells. *PLoS Computational Biology*, 6(9):e1000914, 2010.

[42] Stefan A Mann, Mohammad Imtiaz, Annika Winbo, Annika Rydberg, Matthew D Perry, Jean-Philippe Couderc, Bronislava Polonsky, Scott McNitt, Wojciech Zareba, Adam P Hill, et al. Convergence of models of human ventricular myocyte electrophysiology after global optimization to recapitulate clinical long qt phenotypes. *Journal of Molecular and Cellular Cardiology*, 100:25–34, 2016.

[43] Socrates Dokos and Nigel H Lovell. Parameter estimation in cardiac ionic models. *Progress in Biophysics and Molecular Biology*, 85(2-3):407–431, 2004.

[44] Jaspreet Kaur, Anders Nygren, and Edward J Vigmond. Fitting membrane resistance along with action potential shape in cardiac myocytes improves convergence: application of a multi-objective parallel genetic algorithm. *PLoS one*, 9(9):e107984, 2014.

[45] Eric A Sobie. Parameter sensitivity analysis in electrophysiological models using multivariable regression. *Biophysical Journal*, 96(4):1264–1274, 2009.

[46] Amrita X Sarkar and Eric A Sobie. Quantification of repolarization reserve to understand interpatient variability in the response to proarrhythmic drugs: a computational analysis. *Heart Rhythm*, 8(11):1749–1755, 2011.

[47] Amrita X Sarkar, David J Christini, and Eric A Sobie. Exploiting mathematical models to illuminate electrophysiological variability between individuals. *The Journal of Physiology*, 590(11):2555–2567, 2012.

[48] Renjun Zhu, Michal A Millrod, Elias T Zambidis, and Leslie Tung. Variability of action potentials within and among cardiac cell clusters derived from human embryonic stem cells. *Scientific Reports*, 6, 2016.

[49] Daniel Ortmann and Ludovic Vallier. Variability of human pluripotent stem cell lines. *Current Opinion in Genetics & Development*, 46:179–185, 2017.

[50] Keiichi Asakura, Seiji Hayashi, Atsuko Ojima, Tomohiko Taniguchi, Norimasa Miyamoto, Chiaki Nakamori, Chiho Nagasawa, Tetsuo Kitamura, Tomoharu Osada, Yayoi Honda, et al. Improvement of acquisition and analysis methods in multi-electrode array experiments with iPS cell-derived cardiomyocytes. *Journal of Pharmacological and Toxicological Methods*, 75:17–26, 2015.

[51] Aslak Tveito, Karoline H Jæger, Miroslav Kuchta, Kent-Andre Mardal, and Marie E. Rognes. A cell-based framework for numerical modeling of electrical conduction in cardiac tissue. *Frontiers in Physics*, 5:48, 2017.

[52] Bertil Hille. *Ion channels of excitable membranes*, volume 507. Sinauer Sunderland, MA, 2001.

[53] Harald Sontheimer, Bruce R Ransom, and Stephen G Waxman. Different Na^+ currents in P0- and P7-derived hippocampal astrocytes in vitro: evidence for a switch in Na^+ channel expression in vivo. *Brain Research*, 597(1):24–29, 1992.

[54] William J Moody and Martha M Bosma. Ion channel development, spontaneous activity, and activity-dependent development in nerve and muscle cells. *Physiological Reviews*, 85(3):883–941, 2005.

Supplementary information

1 Modification of the action potential model

In the process of adjusting the Paci et al. [1] model to the data obtained from an MPS (microphysiological system, [2]), we have to run the model many thousand times with varying choices of parameters. One difficulty encountered in this process is drift of ion concentrations. This is a well-known problem of mathematical models of electrophysiology; see e.g. [3, 4, 5]. In Figure S1, we illustrate this problem for the original Paci et al. model. One approach to solve this problem is to decompose stimulus currents into ion concentrations and thereby retain conservation of the ion concentrations, see e.g. [3]. A problem with this approach is that drift is observed also when no stimulus is applied (see Figure S1). Another approach relies on the fact that some ion concentrations vary little and can therefore be kept constant. Here, we follow this latter approach and freeze the intracellular sodium concentration and the SR calcium concentration at their initial value. In Figure S2, we show the properties of this approximation. In the right panel, we note that the cytosolic calcium concentration no longer drifts even for very long simulations. In the left panel, we show that the effect of this approximation on the transmembrane potential and the cytosolic calcium concentration is very small. With this approximation, convergence towards the steady state solution (a steady periodic solution) is rapid and the solutions appears to be stable. This is demonstrated in Figure S3 where convergence to steady state is illustrated. First, we compute the steady state solution of the modified model using the original parameters of the Paci et al. model. Then, we reduce I_{Kr} by 50% and note that the solution rapidly reaches equilibrium.

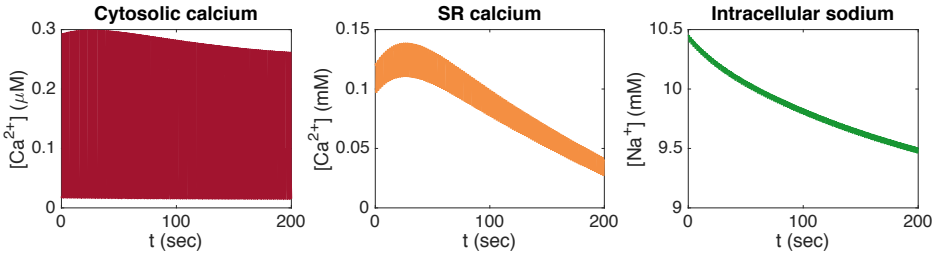

Figure S1: Example of drift of ionic concentrations in the Paci et al. model [1] with no stimulus current applied. First, we compute the steady state solution of the original Paci et al. model. Then, we reduce the I_{Kr} current by 50% and run a simulation of this adjusted model for 200 seconds (corresponding to approximately 120 AP cycles). The plots show how the cytosolic calcium concentration (left panel), the SR calcium concentration (center panel), and the intracellular sodium concentration (right panel) change with time during this long simulation.

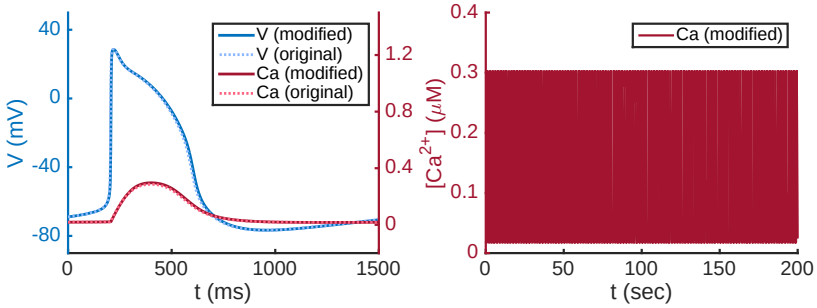

Figure S2: Effect of freezing the intracellular sodium concentration and the SR calcium concentration in the Paci et al. model [1]. Left panel: Comparison of the transmembrane potential and the cytosolic calcium concentration in the original Paci et al. model and the modified model with constant intracellular sodium and SR calcium concentrations. Right panel: Long-term effect on the cytosolic calcium concentration of reducing the I_{Kr} current by 50%. The corresponding effect in the original Paci et al. model is given in the left panel of Figure S1.

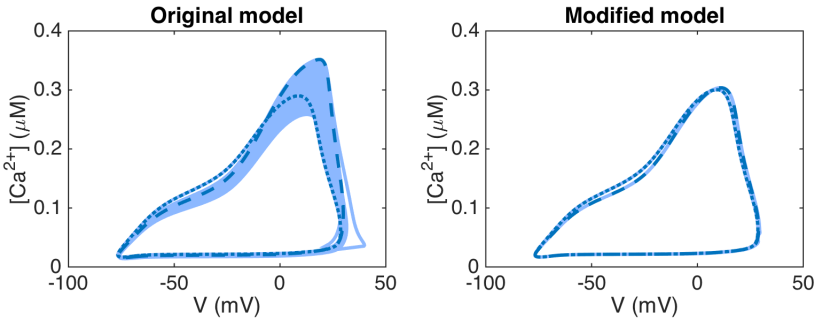

Figure S3: Convergence to steady state after scaling the I_{Kr} current down by 50%. We first run a single cycle of the original Paci et al. model, before running a simulation of the model with a reduced I_{Kr} for 5000 seconds (corresponding to approximately 3000 AP cycles). The cytosolic calcium concentration is plotted against the transmembrane potential of each cycle in light blue. The dotted line shows the cycle with the parameter values of the original Paci et al. model and the dashed line shows the new steady state solution obtained for a reduced I_{Kr}. Left panel: For the original Paci et al. model [1], a new steady state solution is not reached until after approximately 1000 AP cycles. Right panel: In the modified model with constant intracellular sodium and SR calcium concentrations, the solution does not change much after the first cycle with a reduced I_{Kr} current.

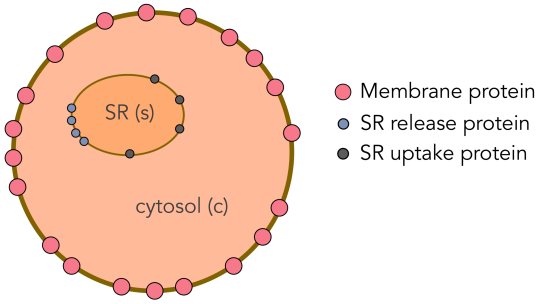

Figure S4: Illustration of the intracellular volume consisting of the cytosolic space (c) and the SR (s). The SR is equipped with specialized proteins for uptake and release of calcium.

2 The maturation map of the Calcium dynamics

We consider how the Ca-dynamics change under maturation. As for the membrane ion channel case, we do this by illustrating the maturation process for a very simple model.

We consider an intracellular volume consisting of the cytosol (c) surrounding the sarcoplasmic reticulum (SR (s)); see Figure S4.

We let N_c denote the number of Ca^{2+}-ions in the cytosol and N_s denote the number of Ca^{2+}-ions in the sarcoplasmic reticulum; both given in mmol. The associated volumes are given by V_c and V_s, both given in L. Let $J_{c,s}$ and $J_{s,c}$ denote the flux (in mmol/ms) of Ca^{2+}-ions from the cytosol to the SR, and from the SR to the cytosol, - respectively. Conservation of Ca^{2+}-ions yields the model

$$\frac{dN_c}{dt} = J_{s,c} - J_{c,s}, \tag{1}$$

$$\frac{dN_s}{dt} = J_{c,s} - J_{s,c}. \tag{2}$$

The fluxes are models of proteins carrying ions from one volume to the other. Let $g^0_{c,s}$ (in mmol/ms) be the flux representing one single protein transporting Ca^{2+}-ions from the cytosol to the SR. Similarly, $g^0_{s,c}$ (in mmol/ms) is the flux representing one single protein releasing Ca^{2+}-ions from the SR to the cytosol. The number of such proteins are given by $N_{c,s}$ and $N_{s,c}$. Then, the system (1) and (2) takes the form

$$\frac{dN_c}{dt} = N_{s,c}g^0_{s,c} - N_{c,s}g^0_{c,s}, \tag{3}$$

$$\frac{dN_s}{dt} = N_{c,s}g^0_{c,s} - N_{s,c}g^0_{s,c}. \tag{4}$$

By defining the fluxes (in mM/ms)

$$j_{c,s} = \frac{N_{c,s} g^0_{c,s}}{V_c}, \quad j_{s,c} = \frac{N_{s,c} g^0_{s,c}}{V_c}, \tag{5}$$

the system takes the form

$$\frac{dC_c}{dt} = j_{s,c} - j_{c,s}, \tag{6}$$

$$\frac{dC_s}{dt} = \frac{V_c}{V_s}(j_{c,s} - j_{s,c}), \tag{7}$$

where C_c and C_s are the concentrations (in mM) of Ca^{2+}-ions in the cytosol and SR, respectively;

$$C_c = \frac{N_c}{V_c}, \; C_s = \frac{N_s}{V_s}. \tag{8}$$

For maturation, we can now follow the same steps as for the membrane proteins. During maturation, the properties of the single proteins will remain constant, but the number of proteins and the volumes will increase. Therefore, we introduce constants $q_{V_c}, q_{V_s}, q_{N_{c,s}}$ and $q_{N_{s,c}}$ such that

$$V_c^M = q_{V_c} V_c^{IM}, \quad V_s^M = q_{V_s} V_s^{IM}, \tag{9}$$

$$N_{c,s}^M = q_{N_{c,s}} N_{c,s}^{IM}, \quad N_{s,c}^M = q_{N_{s,c}} N_{s,c}^{IM}. \tag{10}$$

With

$$j_{c,s}^{IM} = \frac{N_{c,s}^{IM} g^0_{c,s}}{V_c^{IM}}, \quad j_{s,c}^{IM} = \frac{N_{s,c}^{IM} g^0_{s,c}}{V_c^{IM}}, \tag{11}$$

we get

$$j_{c,s}^M = \frac{N_{c,s}^M g^0_{c,s}}{V_c^M} = \frac{q_{N_{c,s}} N_{c,s}^{IM} g^0_{c,s}}{q_{V_c} V_c^{IM}} = \frac{q_{N_{c,s}}}{q_{V_c}} j_{c,s}^{IM}, \tag{12}$$

$$j_{s,c}^M = \frac{N_{s,c}^M g^0_{s,c}}{V_c^M} = \frac{q_{N_{c,s}} N_{s,c}^{IM} g^0_{s,c}}{q_{V_c} V_c^{IM}} = \frac{q_{N_{s,c}}}{q_{V_c}} j_{s,c}^{IM}. \tag{13}$$

Consequently, we have the IM model

$$\frac{dC_c}{dt} = j_{s,c}^{IM} - j_{c,s}^{IM}, \tag{14}$$

$$\frac{dC_s}{dt} = \frac{V_c^{IM}}{V_s^{IM}}(j_{c,s}^{IM} - j_{s,c}^{IM}), \tag{15}$$

and the associated M model

$$\frac{dC_c}{dt} = \frac{q_{N_{s,c}}}{q_{V_c}} j_{s,c}^{IM} - \frac{q_{N_{c,s}}}{q_{V_c}} j_{c,s}^{IM}, \tag{16}$$

$$\frac{dC_s}{dt} = \frac{q_{V_c} V_c^{IM}}{q_{V_s} V_s^{IM}} \left(\frac{q_{N_{c,s}}}{q_{V_c}} j_{c,s}^{IM} - \frac{q_{N_{s,c}}}{q_{V_c}} j_{s,c}^{IM}\right). \tag{17}$$

Again, we observe that the M model is obtained simply by multiplication by a set of maturation factors.

	$[Na^+]_i$ (mM)	$[K^+]_i$ (mM)	$[Ca^{2+}]_{SR}$ (mM)
Paci IM	10.45	150.00	0.12
Paci M	10.45	150.00	0.55
ten Tusscher IM	11.37	138.20	0.12
ten Tusscher M	11.37	138.20	0.53

Table S1: Intracellular concentrations used in the IM and M versions of the modified Paci et al. [1] and ten Tusscher et al. [6] models with fixed intracellular sodium, intracellular potassium and SR calcium concentrations.

3 Technical specifications of the model formulation and inversion procedure

In this section, technical specifications regarding the model formulation used in the simulations and the inversion procedure will be provided.

3.1 Intracellular concentrations

In almost all of our computations, we use the modified version of the Paci et al. model described above with fixed intracellular sodium and SR calcium concentrations. The only exception is that we also run some simulations of ten Tusscher et al. model [6] in Figure 9 of the paper. In these simulations, the intracellular potassium, sodium and SR calcium concentrations are also fixed at constant values. The intracellular concentrations used in the IM and M formulations of the modified Paci et al. model and the similarly modified ten Tusscher et al. model are given in Table S1.

3.2 Numerical stimulation protocol

In all simulations, the cells are stimulated every 1000 ms by a 5 ms long stimulus current of 8 μA/μF. The simulations are run for five AP cycles before recording the action potential and calcium transient for each new parameter combination.

3.3 Technical specifications for the drug inversions

When the inversion procedure is used to fit simulated or measured drug and control data, we only consider adjustments of the q_{Na}, q_{CaL}, q_{Kr} and q_{K1} factors, unless otherwise specified. Note, however, that for the inversion of the Verapamil data in Figures 6 and 7 of the paper, the I_{Na} current was reduced by 50%, the I_{NaK} current was reduced by 60%, the I_{CaL} current was increased by 60%, and the I_{up} and I_{rel} fluxes were increased by 30% before running the inversion of the q_{Na}, q_{CaL}, q_{Kr} and q_{K1} factors, in order to make the base model used in the inversion more similar to the control data.

3.4 Technical specifications for the construction of the maturation map

In the construction of the maturation maps demonstrated in Figure 9 of the paper, we use the inversion procedure to fit an immature model (Paci et al. [1]) to a mature model (ten Tusscher et al. [6]) and to fit the mature model to the immature model. In these inversions, we consider adjustments of the q_{Na}, q_{CaL}, q_{to}, q_{Ks}, q_{Kr}, q_{K1}, q_{NaCa}, q_{NaK}, q_{pCa}, q_{f}, q_{bNa}, q_{bCa}, q_{leak}, q_{up}, and q_{rel} factors (in addition to the q_{pK}-factor for the ten Tusscher et al. model). Note that the I_{f} current is added to the ten Tusscher et al. model in these simulations using the same formulation as in the default Paci et al. model, but with a conductance reduced by a factor of 10 for the mature ten Tusscher model, i.e. $g_{\mathrm{f}} = 0.003$ mS/μF.

Because of the large number of free parameters, we conducted a more detailed inversion procedure in this case with twelve iterations and 15000 randomly chosen adjustment factors in each iteration. In addition, we included some additional terms in the cost function containing information that is not available from the optical measurements, but may be obtained from the mathematical models. More specifically, we used a cost function of the form

$$H(\lambda) = \left(\sum_{j=1}^{20} H_j(\lambda) \right)^{1/2}, \tag{18}$$

where $H_1 - H_8$ are the same as in the remaining applications of the inversion procedure, that is

$$H_1 = \frac{|\int_{t_0(\lambda)}^{t_1(\lambda)} v(\lambda)dt - \int_{t_0^*}^{t_1^*} v^* dt|}{|\int_{t_0^*}^{t_1^*} v^* dt|}, \qquad H_2 = \frac{|\mathrm{APD}_{V,30}(\lambda) - \mathrm{APD}^*_{V,30}|}{|\mathrm{APD}^*_{V,30}|},$$

$$H_3 = \frac{|\mathrm{APD}_{V,50}(\lambda) - \mathrm{APD}^*_{V,50}|}{|\mathrm{APD}^*_{V,50}|}, \qquad H_4 = \frac{|\mathrm{APD}_{V,80}(\lambda) - \mathrm{APD}^*_{V,80}|}{|\mathrm{APD}^*_{V,80}|},$$

$$H_5 = \frac{|(\frac{dc}{dt})_{\max}(\lambda) - (\frac{dc}{dt})^*_{\max}|}{|(\frac{dc}{dt})^*_{\max}|}, \qquad H_6 = \frac{|\mathrm{APD}_{\mathrm{Ca},30}(\lambda) - \mathrm{APD}^*_{\mathrm{Ca},30}|}{|\mathrm{APD}^*_{\mathrm{Ca},30}|},$$

$$H_7 = \frac{|\mathrm{APD}_{\mathrm{Ca},50}(\lambda) - \mathrm{APD}^*_{\mathrm{Ca},50}|}{|\mathrm{APD}^*_{\mathrm{Ca},50}|}, \qquad H_8 = \frac{|\mathrm{APD}_{\mathrm{Ca},80}(\lambda) - \mathrm{APD}^*_{\mathrm{Ca},80}|}{|\mathrm{APD}^*_{\mathrm{Ca},80}|},$$

where the star $*$ is used to denote the simulated data to which we are trying to adjust the model. Furthermore, $\mathrm{APD}_{V,30}$ is defined as the length (in ms) of the time from the value of the membrane potential, in the upstroke, is 30% below its maximum value (t_0) until it again is repolarized to 30% of its maximum value (t_1). In H_1, we compute the integral of the membrane potential with respect to time t from $t = t_0$ to $t = t_1$. The values $\mathrm{APD}_{V,50}$ and $\mathrm{APD}_{V,80}$ are defined similarly to $\mathrm{APD}_{V,30}$, and the terms $\mathrm{APD}_{\mathrm{Ca},30}$, $\mathrm{APD}_{\mathrm{Ca},50}$ and $\mathrm{APD}_{\mathrm{Ca},80}$ represent the corresponding transient durations for the calcium concentration. Moreover, in H_5, $(\frac{dc}{dt})_{\max}$ is the maximal upstroke velocity of the calcium concentration.

The additional terms for the construction of the maturation map are given by

$$H_9 = \frac{|v(\lambda)_{\max} - v^*_{\max}|}{|v^*_{\max}|}, \qquad H_{10} = \frac{|v(\lambda)_{\text{rest}} - v^*_{\text{rest}}|}{|v^*_{\text{rest}}|},$$
$$H_{11} = \frac{|c(\lambda)_{\max} - c^*_{\max}|}{|c^*_{\max}|}, \qquad H_{12} = \frac{|c(\lambda)_{\text{rest}} - c^*_{\text{rest}}|}{|c^*_{\text{rest}}|},$$
$$H_{13} = \frac{\|I_{\text{Na}}(\lambda) - I^*_{\text{Na}}\|_2}{\|I^*_{\text{Na}}\|_2}, \qquad H_{14} = \frac{\|I_{\text{Na}}(\lambda) - I^*_{\text{Na}}\|_\infty}{\|I^*_{\text{Na}}\|_\infty},$$
$$H_{15} = \frac{\|I_{\text{CaL}}(\lambda) - I^*_{\text{CaL}}\|_2}{\|I^*_{\text{CaL}}\|_2}, \qquad H_{16} = \frac{\|I_{\text{CaL}}(\lambda) - I^*_{\text{CaL}}\|_\infty}{\|I^*_{\text{CaL}}\|_\infty},$$
$$H_{17} = \frac{\|I_{\text{Kr}}(\lambda) - I^*_{\text{Kr}}\|_2}{\|I^*_{\text{Kr}}\|_2}, \qquad H_{18} = \frac{\|I_{\text{Kr}}(\lambda) - I^*_{\text{Kr}}\|_\infty}{\|I^*_{\text{Kr}}\|_\infty},$$
$$H_{19} = \frac{\|I_{\text{K1}}(\lambda) - I^*_{\text{K1}}\|_2}{\|I^*_{\text{K1}}\|_2}, \qquad H_{20} = \frac{\|I_{\text{K1}}(\lambda) - I^*_{\text{K1}}\|_\infty}{\|I^*_{\text{K1}}\|_\infty}.$$

Here, $v_{\max}$ and $c_{\max}$ denote the maximum value of the membrane potential and the calcium concentration, respectively. Similarly, v_{rest} and c_{rest} denote the resting membrane potential and calcium concentration, respectively, defined as the values obtained 10 ms before stimulation. Moreover, $\|I\|_2$ and $\|I\|_\infty$ are defined as

$$\|I\|_2 = \sqrt{\sum_n I(t_n)^2},$$
$$\|I\|_\infty = \max_n |I(t_n)|,$$

where n runs over all the time steps of an action potential. The currents I_{Na}, I_{CaL}, I_{Kr}, and I_{K1} are chosen to be included in the cost function because we are especially interested in obtaining realistic behaviors for these currents since these are the currents considered in the drug inversions.

4 Identification of simulated single-channel block using H_{V} and H_{Ca}

In Figure 5 of the paper we showed the value of $H_{V+\text{Ca}}$ for pairwise perturbations of the maximum conductance of four major currents for simulated single channel block of each of the currents. Figures S5 and S6 show corresponding plots for the cost functions H_V and H_{Ca}, respectively. In these figures, we observe that the terms of H_V seem to contain the main part of $H_{V+\text{Ca}}$ observed in Figure 5 of the paper.

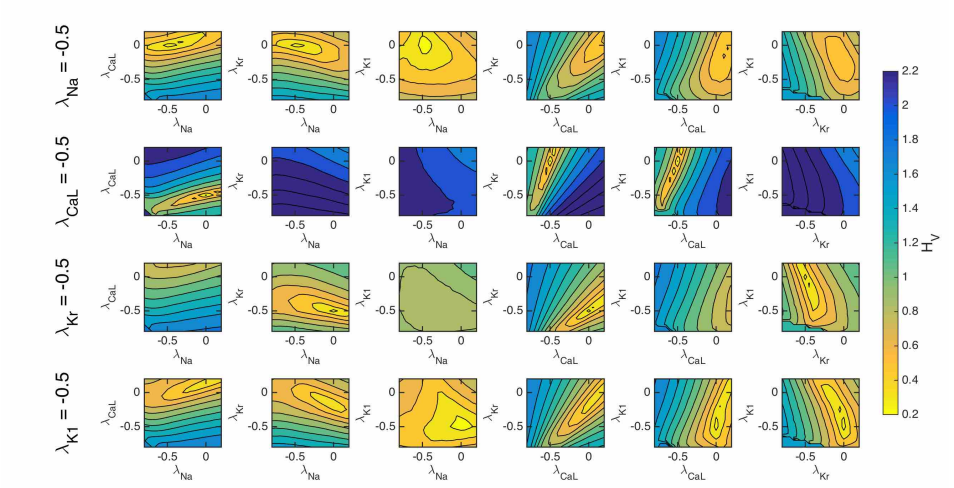

Figure S5: The cost function H_V with $\varepsilon = 0.2$ evaluated for pairwise perturbations of the maximum conductances of four major currents for simulated single-channel block of each of the currents. In the upper panel, I_{Na} is blocked by 50%, and in the next panels, I_{CaL}, I_{Kr} and I_{K1} are similarly blocked by 50%.

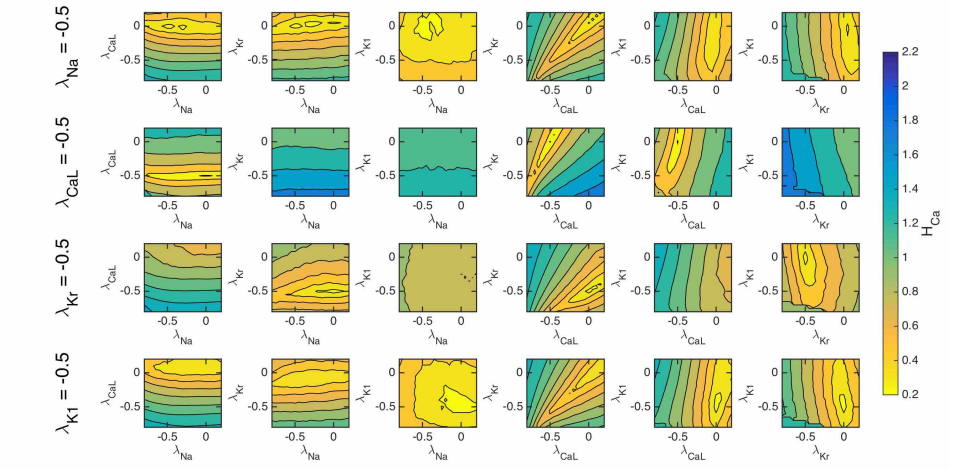

Figure S6: Like Figure S5, except that we cosnider the cost function H_{Ca} instead of H_V.

References

[1] Michelangelo Paci, Jari Hyttinen, Katriina Aalto-Setälä, and Stefano Severi. Computational models of ventricular-and atrial-like human induced pluripotent stem cell derived cardiomyocytes. *Annals of Biomedical Engineering*, 41(11):2334–2348, 2013.

[2] Anurag Mathur, Peter Loskill, Kaifeng Shao, Nathaniel Huebsch, SoonGweon Hong, Sivan G. Marcus, Natalie Marks, Mohammad Mandegar, Bruce R. Conklin, Luke P. Lee, and Kevin E. Healy. Human iPSC-based cardiac microphysiological system for drug screening applications. *Scientific Reports*, 5:8883, 2015.

[3] Thomas J Hund, Jan P Kucera, Niels F Otani, and Yoram Rudy. Ionic charge conservation and long-term steady state in the Luo-Rudy dynamic cell model. *Biophysical Journal*, 81(6):3324–3331, 2001.

[4] Ronald Wilders. Computer modelling of the sinoatrial node. *Medical and Biological Engineering and Computing*, 45(2):189–207, 2007.

[5] Victor A Maltsev, Yael Yaniv, Anna V Maltsev, Michael D Stern, and Edward G Lakatta. Modern perspectives on numerical modeling of cardiac pacemaker cell. *Journal of Pharmacological Sciences*, 125(1):6–38, 2014.

[6] Kirsten HWJ ten Tusscher, Denis Noble, Penelope J Noble, and Alexander V Panfilov. A model for human ventricular tissue. *American Journal of Physiology-Heart and Circulatory Physiology*, 286(4):H1573–H1589, 2004.

Paper V

Improved Computational Identification of Drug Response Using Optical Measurements of Human Stem Cell Derived Cardiomyocytes in Microphysiological Systems

Karoline H. Jæger, Verena Charwat, Bérénice Charrez,
Henrik Finsberg, Samuel Wall, Kevin E. Healy, and Aslak Tveito

Preliminary draft, not ready for publication

Improved Computational Identification of Drug Response Using Optical Measurements of Human Stem Cell Derived Cardiomyocytes in Microphysiological Systems

Karoline H. Jæger[1], Verena Charwat[2], Bérénice Charrez[2], Henrik Finsberg[1], Samuel Wall[1], Kevin E. Healy[2], and Aslak Tveito[1]

[1]Simula Research Laboratory, Norway
[2]Departments of Bioengineering, Material Science and Engineering, University of California, Berkeley, California, USA

Abstract

Cardiomyocytes derived from human induced pluripotent stem cells hold a great potential for drug screening applications. However, their usefulness is limited by the immaturity of the cells' electrophysiological properties compared to the native cardiomyocytes in the adult human heart. In this paper, we apply a previously introduced computational procedure aimed at predicting drug effects for mature cells based on drug effects observed for immature cells. In the procedure, drug effects on individual ion channels are estimated from optical measurements of the action potential and calcium transient of immature cells and the identified drug effects are mapped to the mature case using an assumption of functional invariance of the intracellular and membrane proteins during maturation.

In the current paper, we improve and extend the previously applied methodology by extending the action potential model used to represent the immature and mature cells, applying an IC50-based modeling of dose-dependent drug effects, and introducing a continuation-based optimization algorithm for inverting the optical measurements. The improved methodology is shown to give reasonable results for measurements of human induced pluripotent stem cell-derived cardiomyocytes exposed to five drugs with known effects. Consequently, the updated methodology could be a step in the right direction towards applying the computational procedure to estimate mature drug effects for new drugs based on optical measurements of immature cells.

1 Introduction

The development of human induced pluripotent stems cells (hiPSCs) opens promising perspectives for a wide variety of fundamental questions regarding cell physiology (for recent reviews, see e.g., [1, 2, 3]). One important application of hiPSCs is to improve drug development which traditionally has relied on animal models. The usefulness of animal testing is limited by the fact that the electrophysiology of animal cells and human cells differs significantly. For instance, the heart rate is much faster for mouse compared to human ($\sim$600 bpm vs. $\sim$60 bpm), and therefore, drug effects cannot be directly translated from one specie to another (see e.g., [1, 3, 4, 5]). Using hiPSCs, it is possible to measure drug effects directly on human cells, and the effects can therefore, at least in principle, be adjusted to the needs of individual patients. This opens up great possibilities for treatment of a whole range of illnesses, including disorders caused by rare mutations. In addition, it opens up for new ways of identifying side effects of drugs for human cells. On the other hand, the technology is also associated with a variety of scientific challenges that must be resolved in order to realize the full potential of hiPSCs (see e.g., [4, 6, 7, 8, 9, 10]). One particularly important challenge is maturation of hiPSC-derived cardiomyocytes (hiPSC-CMs). Human cardiomyocytes develop over many years (see [11], ch. 21) and during this period the density of specific ion channels changes significantly, both due to an increased area of the cell membrane, and due to proliferation of membrane proteins (see e.g., [12, 13, 14]). Therefore, immature cells cannot be directly applied to infer properties of adult human cells. Even if we know exactly how a drug affects an immature hiPSC-CM, it is difficult to deduce the effect on adult cells; direct interpretation may in fact lead to both false positives and false negatives (see [10, 15]).

In [16], we addressed two particular challenges associated with the application of hiPSC-CMs to discover side effects of novel drugs. First, we presented an algorithm for inverting measurements of the membrane potential and the cytosolic calcium concentration in order to obtain parameters in a mathematical model representing the action potential (AP) of the hiPSC-CMs. Second, we showed how the model of immature cells can be mapped to a model representing mature cells. We were able to estimate the effect of a drug on essential ion currents for hiPSC-CMs based on measurements from a microphysiological system [10], and then map the effect onto the adult model. The combination of these two methods allowed us, at least in principle, to deduce drug effects on mature cells based on measurements of immature cells. Albeit promising, the results of [16] clearly called for refinements in order to improve the accuracy of the methodology.

The overall framework for detecting unknown side effects of novel drugs developed in [16] is illustrated in Figure 1. For the control case, optical measurements are used to define traces of the membrane potential and the cytosolic calcium concentration. Based on these traces, a mathematical model is defined by identifying parameters denoted by $p^{\mathrm{IM,c}}$ (IM is for immature, c is for control) in an AP model. Using the model of the immature cells, we define a maturation matrix Q such that $Qp^{\mathrm{IM,c}} = p^{\mathrm{M,B}}$ where $p^{\mathrm{M,B}}$ (M is for mature, B is for base) are *known* parameters

representing a generic adult AP model. Note that the matrix Q represents the change in protein density and geometry from IM to M and is therefore independent of the drug. This is important because it means that if we can map the non-drugged case from IM to M, we can similarly map the models representing the data when a drug has been applied. The procedure is repeated when the cells are subject to an unknown drug. Again, traces of the membrane potential and the cytosolic calcium concentration are used to define a mathematical AP model represented by a parameter-vector $p^{\mathrm{IM,D}}$ (Immature, Drug). By assuming that the drug affects *every individual ion channel protein* in the same manner for the IM and M cells, the parameter vector for the mature case is given by $p^{\mathrm{M,D}} = Qp^{\mathrm{IM,D}}$. *Hence, we can find an AP model for mature cells under the influence of the drug even though only the immature case has been measured.*

Note that we assume that a drug has the same effect on one single channel for the IM and M cases. This is a reasonable assumption, but we also assume that the effect a drug can be expressed by multiplying the non-drugged current by a factor. Clearly, the effect of drugs can be more complex and depend on both the membrane potential and ion concentrations (see e.g., [17, 18, 19, 20, 21]). Markov model representation of the effect of drugs on single channels (see e.g., [20]) can improve the IM model, but the maturation process remains the same since, again, the effect of the drug on every individual ion channel is the same provided that the drug concentration is the same. At present, we surmise that the accuracy of the available data does not merit more sophisticated modeling of the drug effect than can be achieved by simply multiplying individual currents by individual constants. This modeling assumption should be revisited as more accurate data become available.

It was demonstrated in [16] that the procedure depicted in Figure 1 works, but that improvements of accuracy are needed. The purpose of the present report is therefore to present a number of improvements of the methodology introduced in [16]. First, a new AP model is derived in order to improve representation of the data. The new model is designed to be numerically stable and thus enable more reliable simulations. In particular, the model of the intracellular Ca^{2+}-dynamics has been improved in order to avoid instabilities in the balance between the influx and out-flux of Ca^{2+} to the sarcoplasmic reticulum (SR). The development of mathematical models of the action potential of excitable cells is a very active field of research and a series of sophisticated models have been developed in order to simulate both single cells and cardiac tissue dynamics (see e.g., [22, 23, 24, 25, 26, 27, 28, 29, 30, 31]). Since we consider human cells, the AP models of O'Hara et al. [22], Grandi et al. [23], and Paci et al. [32, 33, 34, 35] have formed the basis of our work. As explained above, our aim has been to have models that can be mapped back and forth between immature and mature cases. A vital modeling assumption has been that the individual proteins are the same in the immature and mature cases, and therefore only the protein density should change between these cases. A consequence of this is that there exists a maturation matrix that maps a model from IM to M, and the inverse of the matrix maps the model from M to IM. This observation is the key for allowing IM data to be used for estimating drug effect on

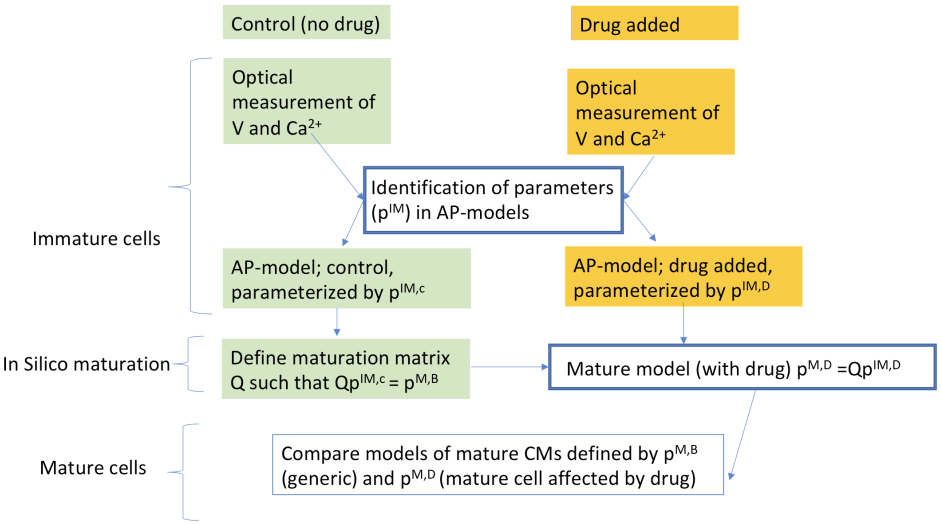

Figure 1: The effect of a drug on mature cardiomyocytes (CMs), can be identified by the process illustrated in the figure. Cytosolic calcium concentration (Ca^{2+}) and the membrane potential (V) are measured in a microphysiological system ([4, 10]) using immature cells (hiPSC-CMs). Data are collected when no drug have been applied (control, c) and when a drug has been applied (D). The data are used to identify the parameterization of a model for both cases represented by the parameter vectors $p^{IM,c}$ and $p^{IM,D}$ for the control and the drugged cases, respectively. The control parameter vector $p^{IM,c}$ is used to define the maturation matrix Q such that $Qp^{IM,c} = p^{M,B}$, where $p^{M,B}$ is the parameter vector of a generic base model of mature cardiomyocytes. By comparing the mature parameter vector for control and drug, the effect of the drug is identified.

M cells. However, existing models are not derived with this mapping in mind, and consequently, the models of identical single protein dynamics vary significantly between models. Therefore, we derive a new AP model where we strictly adhere to the principle that every current (and flux) should be written as a product of the protein density and the dynamics of a single protein; identical proteins are represented by identical mathematical models. Consequently, the mathematical model of a single protein is the same for the IM and M cases.

In addition, we have developed a new method for inverting the data into parameters for the AP model by introducing a continuation-based approach, searching for optimal parameters gradually moving from known parameters to the parameters we want to identify. Continuation methods are well developed in scientific computing (see e.g., [36, 37]).

In the present report, the accuracy of the inversion procedure is first tested using simulated data. Afterwards, the new methods are used to identify the effect of five known drugs based on optical measurements of hiPSC-CMs. In all the considered cases, the predicted effects seem to be consistent with known drug effects. However, variability in experimental results naturally limits the degree of accuracy that can be obtained. In this report, we focus on characterization of drugs that are already known. The purpose of this is to learn how accurate this methodology is before it is applied to novel drugs where the effect of the drug is unknown; we aim at proving the principle that drug effect on adult cells can reliably be estimated using measurements of hiPSC-CMs.

2 Methods

The purpose of this section is to give a detailed presentation of all the steps illustrated in Figure 1. The derivation of a new AP model represents the bulk part of this section and the main goal is to derive a stable model that allows for mapping between IM and M parameterizations. In addition, we describe the inversion method used in our computations. The inversion algorithm is updated from the version used in [16] and is based on continuation. Furthermore, the cost function used in the inversion is updated and described below. Finally, we discuss how to characterize the identifiability of the parameters involved in the inversion. The method used for that purpose is based on singular value decomposition (SVD) of the model currents.

2.1 The base model

As mentioned above, we want to define an AP model that can be scaled from very early stages (days) to fully developed adult cells. If we consider one specific membrane current, we assume that the only difference between the immature (IM) case and the mature (M) case is that the number of channel proteins and the membrane area has changed; thus, the density of the specific membrane protein carrying the current has changed, but the properties of every individual protein remains the

same. The same principle holds for the intracellular calcium machinery; the individual channels and buffers remain the same, but both the intracellular volumes and the number of proteins change from IM to M. Our model will therefore be based on models of single protein dynamics and only the density of these single proteins will change from IM to M. When a drug is involved, we assume that the effect of the drug on a single protein is the same in the IM and M cases, and therefore we can use the effect in the IM case to estimate the effect for the M case.

The membrane currents and intracellular compartments of the base model are illustrated in Figure 2. In the formulation of the base model, the membrane potential (v) is given in units of mV, and the calcium concentrations are given in units of mM. All currents are expressed in units of A/F, and the calcium fluxes are expressed as mmol/ms per total cell volume (i.e., in units of mM/ms). Time is given in ms.

2.2 Modeling the membrane currents

The standard model (see e.g., [38, 39, 40, 41]) of the membrane potential of an excitable cell is given by the equation

$$\frac{dv}{dt} = -\sum_x I_x, \tag{1}$$

where v is the membrane potential (in mV), and I_x are the transmembrane currents through different types of ion channels, pumps and exchangers located on the cell membrane. These currents are all given in units of A/F, and may be written on the form

$$I_x = \frac{N_x}{AC_m} i_x, \tag{2}$$

where N_x is the number of channels of type x on the cell membrane, A is the area of the cell membrane (in μm^2) and C_m is the specific membrane capacitance of the cell membrane (in $\text{pF}/\mu\text{m}^2$). Furthermore, i_x represents the average current through a single channel of type x (in pA). For voltage-gated ion channels, this average single-channel current is given on the form

$$i_x = g_0^x o_x (v - E_x), \tag{3}$$

where g_0^x is the conductance of a single open channel (in nS), E_x is the equilibrium potential of the channel (in mV), and o_x is the unitless open probability of the channel. Note that in models given on this form, it is common to consider a lumped parameter g_x, given by

$$g_x = \frac{N_x}{AC_m} g_0^x,$$

and parameters of this type is given for each of the ion channels in the Supplementary information. For membrane pumps and exchangers, the single-channel current is given on a similar form. The specific currents included in the model will be described below.

2.2.1 Scaling of the membrane currents

As mentioned above, we assume that the specific membrane capacitance and the proteins responsible for each of the membrane currents are the same in different stages of development for the cell, but that the number of proteins, N_x, and the membrane area, A, may differ. Therefore, currents can be mapped from one stage of development, S_1, to another stage of development, S_2, simply by adjusting the channel density of the currents.

More specifically, for the formulation (1)–(2), this means that we assume that the parameter C_m and the expressions for the single-channel currents, i_x, are the same for S_1 and S_2, but that the protein density $\frac{N_x}{A}$ can be different. Let $A_x^{\mathrm{S}_1}, A_x^{\mathrm{S}_2}$ and $N_x^{\mathrm{S}_1}, N_x^{\mathrm{S}_2}$ denote the membrane area and number of proteins of type x for the S_1 and S_2 cases, respectively. Furthermore, we let λ_x represent the change of proteins density in the sense that

$$\frac{N_x^{\mathrm{S}_1}}{A_x^{\mathrm{S}_1}} = (1+\lambda_x)\frac{N_x^{\mathrm{S}_2}}{A_x^{\mathrm{S}_2}}. \tag{4}$$

Now, the S_1 and S_2 currents are related according to

$$I_x^{\mathrm{S}_1} = \frac{N_x^{\mathrm{S}_1}}{A_x^{\mathrm{S}_1} C_m} i_x = (1+\lambda_x)\frac{N_x^{\mathrm{S}_2}}{A_x^{\mathrm{S}_2} C_m} i_x = (1+\lambda_x) I_x^{\mathrm{S}_2}, \tag{5}$$

for each of the currents x. The individual currents will be specified below.

2.2.2 The base model is the generic mature model

It will be useful to have *one* base model, and then derive other models by mapping from that model. Intuitively, it seems natural to define the base model to represent IM cells, since the M cells develops from these IM cells. However, in the scheme illustrated in Figure 1, there is only one fixed model – the generic M model – and all other models change depending on the measurements. We therefore define the generic M model to be the *default base model*, and scale all other models relative to that model.

2.2.3 Main currents present in human cardiomyocytes

In the formulation of the model (1), our aim has been to include the main currents present in human cardiomyocytes, but keep the number of currents as low as possible in order to keep the model relatively simple. Modern models of human cardiomyocytes are complex and the individual currents are based on years of experience using patch-clamp measurements. Data based on sensitive dyes are not expected to be able to uncover equally fine details of the dynamics and it is therefore reasonable to represent the data using simpler models. Our choice of currents is based on the O'Hara-Rudy et al. model [22] and the Grandi et al. model [23] for human mature ventricular cardiomyocytes, in addition to the Paci et al. model [32] for hiPSC-CMs. Furthermore, we have focused on including the

currents considered to be important for the depolarization and repolarization of the action potential and therefore typically investigated for drug responses (see e.g., [42]).

In [42], the fast sodium current, I_{Na}, the late sodium current, I_{NaL}, the L-type calcium current, I_{CaL}, the transient outward potassium current, I_{to}, the rapid and slow delayed rectifier potassium currents, I_{Kr} and I_{Ks}, and the inward rectifier potassium current, I_{K1}, were investigated for their drug response, and we have included each of these currents in our model. In addition, we have included the sodium-potassium pump, I_{NaK}, the sodium-calcium exchanger, I_{NaCa}, the calcium pump, I_{pCa}, the background calcium current, I_{bCa}, and the background chloride current, I_{bCl}, because they all appeared to have a significant effect on the computed action potential and calcium transient of the Grandi et al. model [23]. Furthermore, we have included the hyperpolarization-activated cyclic nucleotide-gated funny current, I_{f}. This current is very small for mature ventricular cardiomyocytes, but is substantial for hiPSC-CMs [43]. The formulation used for each of the currents is given in the Supplementary information and the formulations are based on the formulation of the currents in the Paci et al. model [32], the Grandi et al. model [23], and the O'Hara-Rudy et al. model [22].

2.3 Modeling the intracellular Ca^{2+} dynamics

In addition to the membrane potential, we also want the base model to represent changes to the intracellular calcium concentration. We consider the following five intracellular compartments:

1. The dyad, representing the small cytosolic subspace between the L-type calcium channels and the ryanodine receptors (RyRs),

2. The subsarcolemmal space, representing the remaining part of the cytosolic space that is located close to the membrane,

3. The bulk cytosolic space,

4. The junctional sarcoplasmic reticulum (jSR), representing the part of the SR that is close to the RyR-channels,

5. The network sarcoplasmic reticulum (nSR), representing the remaining part of the SR.

The calcium concentrations and volume fractions defined for each of these compartments are given in Table 1. In all compartments, except in the nSR, we consider both the concentration of free calcium and the concentration of calcium bound to a buffer. The calcium concentration in the extracellular space is assumed to remain constant. The intracellular calcium fluxes between the compartments are illustrated in Figure 2, and the membrane currents involving exchange of Ca^{2+}-ions between the intracellular and extracellular spaces are marked with pink circles. All the calcium fluxes considered in the base model are summarized in Table 2.

Compartment	Volume fraction	Free Ca^{2+} concentration	Buffered Ca^{2+} concentration
Dyad	$V_d = 0.001$	c_d	b_d
Subsarcolemmal space	$V_{sl} = 0.028$	c_{sl}	b_{sl}
Bulk cytosol	$V_c = 0.917$	c_c	b_c
jSR	$V_s = 0.004$	c_s	b_s
nSR	$V_n = 0.05$	c_n	

Table 1: Intracellular compartments of the base model with the associated volume fractions and concentrations of free calcium and calcium bound to a buffer.

2.3.1 Modeling release from the SR

In our model of the calcium dynamics, we deviate from previous modeling approaches in two specific ways:

1. Calcium is released from the SR to the subsarcolemmal space (SL) and not to the dyad.

2. The release model from the SR is a product of two factors; one factor models the open probability of the RyR-channels, whereas the other models the availability of channels that can be opened. We assume that each channel can only process a certain amount of Ca^{2+} before it deactivates.

We will see below that these two modeling assumptions lead to a model that exhibits two important features of calcium release from the SR of cardiomyocytes, so-called *high gain* and *graded release* (see Section 4.1.2 for explanations of these terms).

2.3.2 Definition of calcium fluxes

As mentioned above, all calcium fluxes, J, are defined in terms of the number of ions flowing per time per total cell volume, in units of mM/ms. Accordingly, the size of a flux in mmol/ms is given by $\bar{J} = V_{\text{cell}} J$, where V_{cell} is the cell volume (in L).

Similarly, for a single compartment with volume $\bar{V}_x$ (in L), volume fraction (dimensionless) $V_x = \frac{\bar{V}_x}{V_{\text{cell}}}$ and Ca^{2+} concentration c_x (in mM), the total number of Ca^{2+}-ions in the compartment (in mmol) is given by $n_x = c_x \bar{V}_x$. The change in the number of Ca^{2+}-ions in the compartment is given by

$$\frac{dn_x}{dt} = \bar{J}_x, \tag{6}$$

where $\bar{J}_x$ is the flux of ions into the compartment given in mmol/ms. It is also useful to define an associated concentration flux per total cell volume, $J_x = \bar{J}_x / V_{\text{cell}}$

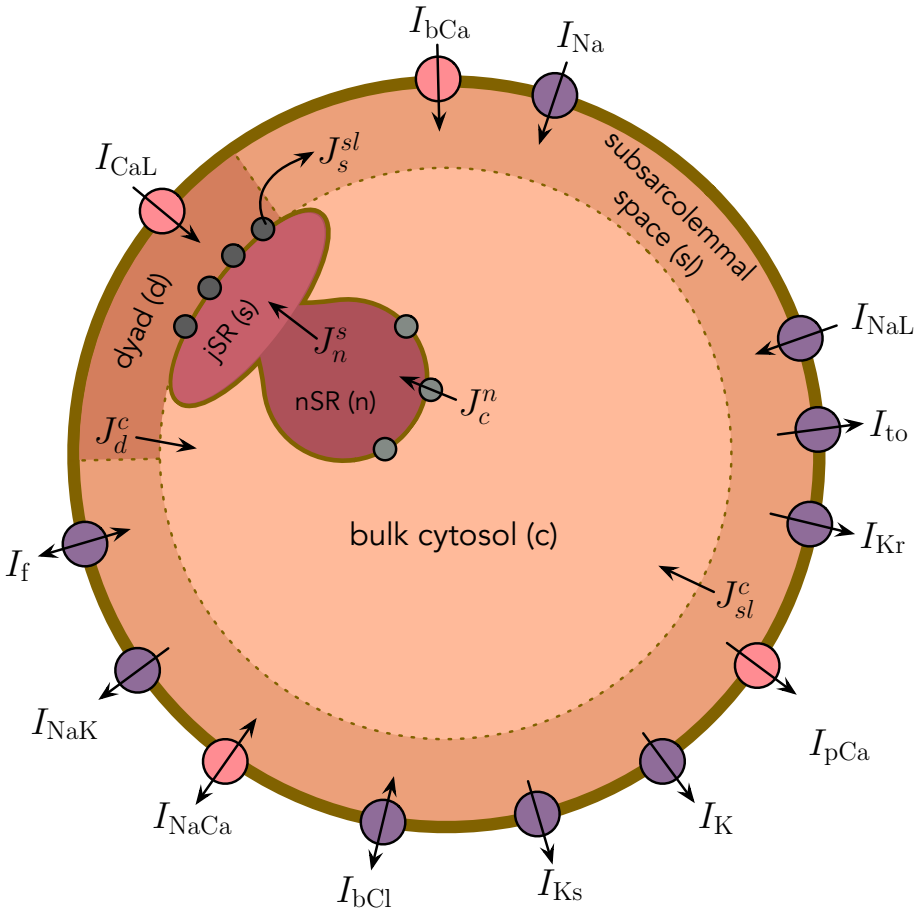

Figure 2: Membrane currents, calcium fluxes and intracellular compartments of the base model. Spaces and fluxes are described in the text.

Flux	Description
J_s^{sl}	Flux through the RyRs from the jSR to the SL
J_c^n	Flux through the SERCA pumps from the bulk cytosol to the nSR
J_d^c	Passive diffusion flux between the dyad and the bulk cytosol
J_{sl}^c	Passive diffusion flux between the SL and the bulk cytosol
J_n^s	Passive diffusion flux between the nSR and the jSR
J_d^b	Free Ca^{2+} binding to a buffer in the dyad
J_{sl}^b	Free Ca^{2+} binding to a buffer in the SL
J_c^b	Free Ca^{2+} binding to a buffer in the bulk cytosol
J_s^b	Free Ca^{2+} binding to a buffer in the jSR
J_{CaL}	Ca^{2+}-flux through the L-type calcium channels from the extracellular space to the dyad
J_{bCa}	Background Ca^{2+}-flux from the extracellular space to the SL
J_{pCa}	Ca^{2+}-flux through the calcium pump between the extracellular space and the SL
J_{NaCa}	Ca^{2+}-flux through the sodium-calcium exchanger between the extracellular space and the SL
J_e^{sl}	Total Ca^{2+}-flux from the extracellular space to the SL, defined as $J_e^{sl} = J_{\mathrm{bCa}} + J_{\mathrm{pCa}} + J_{\mathrm{NaCa}}$.

Table 2: Ca^{2+}-fluxes of the base model. The direction of all membrane fluxes are defined such that a positive flux corresponds to Ca^{2+}-ions flowing into the cell.

(in mM/ms). Dividing both sides of (6) by the compartment volume $\bar{V}_x$, we obtain the following equation for the change in calcium concentration:

$$\frac{dc_x}{dt} = \frac{1}{\bar{V}_x}\bar{J}_x = \frac{1}{\bar{V}_x}V_{\text{cell}}J_x = \frac{1}{V_x}J_x. \tag{7}$$

Expanding this approach to all the compartments and fluxes of the model, we obtain the following system of equations for the intracellular calcium dynamics:

$$\frac{dc_d}{dt} = \frac{1}{V_d}(J_{\text{CaL}} - J_d^b - J_d^c), \qquad \frac{db_d}{dt} = \frac{1}{V_d}J_d^b, \tag{8}$$

$$\frac{dc_{sl}}{dt} = \frac{1}{V_{sl}}(J_e^{sl} - J_{sl}^c - J_{sl}^b + J_s^{sl}), \qquad \frac{db_{sl}}{dt} = \frac{1}{V_{sl}}J_{sl}^b, \tag{9}$$

$$\frac{dc_c}{dt} = \frac{1}{V_c}(J_{sl}^c + J_d^c - J_c^n - J_c^b), \qquad \frac{db_c}{dt} = \frac{1}{V_c}J_c^b, \tag{10}$$

$$\frac{dc_s}{dt} = \frac{1}{V_s}(J_n^s - J_s^{sl} - J_s^b), \qquad \frac{db_s}{dt} = \frac{1}{V_s}J_s^b, \tag{11}$$

$$\frac{dc_n}{dt} = \frac{1}{V_n}(J_c^n - J_n^s). \tag{12}$$

The expressions for each of the calcium fluxes are defined below.

Expressions for fluxes through proteins Every flux $J = J_x$ in the model representing fluxes through a type of protein will be written on the form

$$J_x = \frac{N_x}{V_{\text{cell}}}j_x$$

where N_x is the number of proteins of type x, and j_x is the average flux through a single protein of type x.

Flux through the SERCA pumps (J_c^n) The flux from the bulk cytosol to the nSR through the SERCA pumps is given on the form

$$J_c^n = \frac{N_{\text{SERCA}}}{V_{\text{cell}}}j_{\text{SERCA}}, \tag{13}$$

where N_{SERCA} is the number of SERCA pumps on the membrane of the nSR, V_{cell} is the total cell volume (in L) and j_{SERCA} is the flux through a single SERCA pump (in mmol/ms). The flux through a single pump is given by an expression based on the formulation in the Grandi et al. model [23]:

$$j_{\text{SERCA}} = J_{\text{SERCA}}^{\max,0}\frac{\left(\frac{c_c}{K_c}\right)^2 - \left(\frac{c_n}{K_n}\right)^2}{1 + \left(\frac{c_c}{K_c}\right)^2 + \left(\frac{c_n}{K_n}\right)^2}, \tag{14}$$

where $J_{\text{SERCA}}^{\max,0}$ has unit mmol/ms and K_c and K_n have unit mM. Defining the parameter

$$\bar{J}_{\text{SERCA}} = \frac{N_{\text{SERCA}}}{V_{\text{cell}}} J_{\text{SERCA}}^{\max,0}, \tag{15}$$

with unit mM/ms, the SERCA flux may be written as

$$J_c^n = \bar{J}_{\text{SERCA}} \frac{\left(\frac{c_c}{K_c}\right)^2 - \left(\frac{c_n}{K_n}\right)^2}{1 + \left(\frac{c_c}{K_c}\right)^2 + \left(\frac{c_n}{K_n}\right)^2}. \tag{16}$$

Scaling of the SERCA flux Like for the proteins on the membrane between the extracellular space and the intracellular space, we assume that cells of different levels of maturity may have different geometries and different densities of SERCA pumps, but that the function of the individual SERCA pumps are the same. This means that we assume that the expression for the single-protein flux, j_{SERCA}, remains the same, but that the factor $\frac{N_{\text{SERCA}}}{V_{\text{cell}}}$ may differ between immature and mature cells. In the same manner as above, we represent the change in the SERCA pump density by introducing a scaling factor λ_{SERCA} between one stage of maturity, S_1, to another stage, S_2, such that

$$\frac{N_{\text{SERCA}}^{S_1}}{V_{\text{cell}}^{S_1}} = (1 + \lambda_{\text{SERCA}}) \frac{N_{\text{SERCA}}^{S_2}}{V_{\text{cell}}^{S_2}}, \tag{17}$$

where $\frac{N_{\text{SERCA}}^{S_1}}{V_{\text{cell}}^{S_1}}$ is the SERCA pump density in the model for the maturity stage S_1 and $\frac{N_{\text{SERCA}}^{S_2}}{V_{\text{cell}}^{S_2}}$ is the density in the model for the maturity stage S_2. In the model formulation, this may be represented on the form

$$J_c^{n,S_1} = (1 + \lambda_{\text{SERCA}}) J_c^{n,S_2}, \tag{18}$$

where J_c^{n,S_1} is the expression for the SERCA pump flux in the S_1 state and J_c^{n,S_2} is the expression in the S_2 state.

Flux through the RyRs (J_s^{sl}) Because we want to be able to use the base model for many different parameter combinations, we have to construct a model for the RyR-flux that is stable, in the sense that careful tuning of the model is not necessary to ensure reasonable activation and deactivation of the RyRs. As mentioned above, our attempt to construct a stable RyR model relies on two main modeling assumptions. Note, however, that these assumptions are introduced in order to construct a stable model, and not necessarily to represent the details of the underlying physiological mechanisms accurately.

First, we let the calcium released from the SR enter the SL space instead of the dyad. This is done in order to achieve graded release (see Section 4.1.2), in the sense that the amount of calcium leaving the SR through the RyRs should depend

directly upon the amount of calcium entering the cell through the L-type calcium channels. If the calcium released from the jSR had entered the dyad, it would be difficult to distinguish the increase in dyadic calcium concentration resulting from the L-type calcium channels from that resulting from the release through the RyRs. By directing the RyR-flux into the SL, the concentration change in the dyad is almost exclusively due to the influx through the L-type calcium channels, and by letting the flux through the RyRs depend on the calcium concentration in the dyad, we achieve graded release.

Second, a common modeling approach for the RyR-flux is to let the channels be inactivated by a decreased jSR concentration (see e.g., [44]). However, for large variations in the parameter values, this might lead to instabilities because the jSR concentration depends upon the balance between the flux through the SERCA pumps and the RyRs, which again depends upon the balance between the calcium fluxes into and out of the cell. In order to avoid an RyR model whose inactivation mechanism depends on the jSR concentration, we instead introduce the assumption that each RyR protein is only able to carry a given amount of Ca^{2+}-ions in each action potential.

We assume that a small portion of the RyR channels are always open (type 0), while the remaining channels (type 1) are activated by an increased dyadic calcium concentration and are inactivated after they have transported a given amount of Ca^{2+}-ions. Therefore, the total flux through the RyRs may be expressed as

$$J_s^{sl} = J_{\text{RyR}} + J_{\text{leak}}, \tag{19}$$

where J_{RyR} represents the flux through the RyR channels of type 1 and J_{leak} represents the flux through the RyR channels of type 0. We assume that the flux through the two types of RyR channels are given by expressions of the form

$$J_{\text{RyR}} = \frac{Mp}{V_{\text{cell}}} j_{\text{RyR}}, \tag{20}$$

$$J_{\text{leak}} = \frac{M_0}{V_{\text{cell}}} j_{\text{RyR}}, \tag{21}$$

where j_{RyR} denotes the flux through a single open RyR protein (in mmol/ms) and V_{cell} denotes the total cell volume (in L). In addition, M_0 denotes the number of RyR proteins that are always open (type 0), M denotes the number of available RyR proteins of type 1, and p is the open probability of the proteins of type 1. The single channel flux through the RyRs is given by

$$j_{\text{RyR}} = \alpha_{\text{RyR},0}(c_s - c_{sl}), \tag{22}$$

where $\alpha_{\text{RyR},0}$ (in L/ms) represents the rate of release. Furthermore, the open probability of the RyR proteins of type 1 is modelled by a simple function that increases sigmoidally with the dyadic calcium concentration, c_d, based on the model in [45]:

$$p = \frac{c_d^3}{c_d^3 + \kappa_{\text{RyR}}^3}. \tag{23}$$

We let the total number of RyR-proteins of type 1 be given by N_{RyR} and the total number of RyR-proteins of type 0 be given by

$$M_0 = \gamma_{\mathrm{RyR}} N_{\mathrm{RyR}}. \tag{24}$$

In other words, the total number of RyR proteins (of both types) is given by $(1 + \gamma_{\mathrm{RyR}})N_{\mathrm{RyR}}$.

We assume that every RyR-channel of type 1 is able to transport a fixed amount of Z calcium ions during an action potential. After Z ions have been transported, the protein becomes inactivated. However, we assume that as the dyadic calcium concentration, c_d, returns to rest and the open probability, p, consequently decreases, the inactivated channels gradually recover from inactivation. We let the number of available proteins of type 1 be governed by

$$\frac{dM}{dt} = -\frac{V_{\mathrm{cell}}}{Z} J_{\mathrm{RyR}} + \frac{\eta_{\mathrm{RyR}}}{p}(N_{\mathrm{RyR}} - M). \tag{25}$$

Here, the first term dominates for large values of p, driving M towards zero as more Ca^{2+} is transported through the RyR channels of type 1. Furthermore, for small values of p (i.e., at rest), the second term dominates and drives M towards the maximum value N_{RyR}.

In order to reduce the number of free parameters in the model, we may define a scaled variable r, defined as $r = \frac{M}{N_{\mathrm{RyR}}}$, and divide both sides of equation (25) by N_{RyR}. The equation then reads

$$\frac{dr}{dt} = -\frac{J_{\mathrm{RyR}}}{\beta_{\mathrm{RyR}}} + \frac{\eta_{\mathrm{RyR}}}{p}(1 - r), \tag{26}$$

where

$$\beta_{\mathrm{RyR}} = \frac{N_{\mathrm{RyR}}}{V_{\mathrm{cell}}} Z. \tag{27}$$

Inserting $M = rN_{\mathrm{RyR}}$ into (20) and defining

$$\alpha_{\mathrm{RyR}} = \frac{N_{\mathrm{RyR}}}{V_{\mathrm{cell}}} \alpha_{\mathrm{RyR},0}, \tag{28}$$

we get the following expression for the active RyR-flux

$$J_{\mathrm{RyR}} = p \cdot r \cdot \alpha_{\mathrm{RyR}}(c_s - c_{sl}), \tag{29}$$

where we recall that

$$p = \frac{c_d^3}{c_d^3 + \kappa_{\mathrm{RyR}}^3}. \tag{30}$$

Moreover, inserting (24) and (28) into (21), we obtain

$$J_{\mathrm{leak}} = \gamma_{\mathrm{RyR}} \cdot \alpha_{\mathrm{RyR}}(c_s - c_{sl}). \tag{31}$$

Scaling of the RyR flux When considering cells of different levels of maturity, we again assume that the number of RyR proteins and the cell volume may be different, but that the function of a single RyR protein is the same for different levels of maturity. We also assume that the ratio between RyR proteins of type 0 and 1, γ_{RyR}, and the number of Ca^{2+}-ions that each RyR protein of type 1 can transport, Z, is the same for the different maturity levels. Considering the model (26)–(31), this means that the only adjustment necessary between two maturity levels S_1 and S_2 is an adjustment of the density $\frac{N_{\mathrm{RyR}}}{V_{\mathrm{cell}}}$ in the definition of α_{RyR} and β_{RyR}. We therefore introduce a scaling factor λ_{RyR} such that

$$\frac{N_{\mathrm{RyR}}^{S_1}}{V_{\mathrm{cell}}^{S_1}} = (1+\lambda_{\mathrm{RyR}})\frac{N_{\mathrm{RyR}}^{S_2}}{V_{\mathrm{cell}}^{S_2}}, \tag{32}$$

and represent this adjustment of the RyR protein density in the model by scaling α_{RyR} and β_{RyR} by

$$\alpha_{\mathrm{RyR}}^{S_1} = (1+\lambda_{\mathrm{RyR}})\alpha_{\mathrm{RyR}}^{S_2}, \tag{33}$$

$$\beta_{\mathrm{RyR}}^{S_1} = (1+\lambda_{\mathrm{RyR}})\beta_{\mathrm{RyR}}^{S_2}, \tag{34}$$

where superscript S_1 and S_2 denote the S_1 and S_2 versions of the parameters, respectively.

Passive diffusion fluxes between compartments (J_d^c, J_{sl}^c, and J_n^s) Following the approach in e.g. [46], diffusion between compartments are considered to take place, on average, between the center of adjacent compartments. Fick's law of diffusion may then be approximated as

$$J_a^b = \frac{D_a^b A_a^b}{V_{\mathrm{cell}}}\frac{c_a - c_b}{l_a^b}, \tag{35}$$

where D_a^b is the diffusion coefficient (in $\mathrm{dm}^2/\mathrm{ms}$) representing the ease with which Ca^{2+}-ions flow between the compartments, A_a^b is the area (in dm^2) of the interface between the compartments, c_a and c_b are the calcium concentrations of the compartments (in mM), and l_a^b is the distance between the centers of the two compartments (in dm). Again, V_{cell} is the total cell volume (in L), and the flux J_a^b is defined as the number of ions flowing between the compartments per ms per total cell volume. In order to reduce the number of parameters, we may define the lumped parameter

$$\alpha_a^b = \frac{D_a^b A_a^b}{V_{\mathrm{cell}} l_a^b}, \tag{36}$$

and write the flux as

$$J_a^b = \alpha_a^b(c_a - c_b). \tag{37}$$

We consider passive diffusion fluxes of this form between the dyad and the bulk cytosol, between the SL and the bulk cytosol, and between the nSR and jSR, and

define the fluxes as:

$$J_d^c = \alpha_d^c(c_d - c_c), \tag{38}$$
$$J_{sl}^c = \alpha_{sl}^c(c_{sl} - c_c), \tag{39}$$
$$J_n^s = \alpha_n^s(c_n - c_s). \tag{40}$$

Scaling of the diffusion fluxes In the same manner as above, we define adjustment factors λ_a^b for the diffusion fluxes on the form

$$\frac{D_a^{b,S_1} A_a^{b,S_1}}{V_{\text{cell}}^{S_1} l_a^{b,S_1}} = (1 + \lambda_a^b) \frac{D_a^{b,S_2} A_a^{b,S_2}}{V_{\text{cell}}^{S_2} l_a^{b,S_2}}. \tag{41}$$

Here, λ_a^b may represent a change in any of the geometrical properties A_a^b, V_{cell} or l_a^b, a change in the diffusion coefficient D_a^b, or a combination of these changes. The adjustment is represented in the model for each of the diffusion fluxes by

$$J_d^{c,S_1} = (1 + \lambda_d^c) J_d^{c,S_2}, \tag{42}$$
$$J_{sl}^{c,S_1} = (1 + \lambda_{sl}^c) J_{sl}^{c,S_2}, \tag{43}$$
$$J_n^{s,S_1} = (1 + \lambda_n^s) J_n^{s,S_2}, \tag{44}$$

where J_d^{c,S_1}, J_{sl}^{c,S_1}, and J_n^{s,S_1} denote the S_1 fluxes and J_d^{c,S_2}, J_{sl}^{c,S_2}, and J_n^{s,S_2} denote the S_2 fluxes.

Buffer fluxes (J_d^b, J_{sl}^b, J_c^b, and J_s^b) The chemical reaction between calcium and a buffer may be written as

$$\mathrm{P} + \mathrm{Ca}^{2+} \underset{k_{\text{off}}}{\overset{k_{\text{on}}}{\rightleftarrows}} \mathrm{B}, \tag{45}$$

where P represents the buffering protein and B represents calcium bound to the buffer. Here, k_{on} and k_{off} are the rates of the reaction and are given in units of $\text{ms}^{-1}\text{mM}^{-1}$ and ms^{-1}, respectively. If we let B_{tot} denote the total buffer concentration in some compartment, c denote the concentration of free calcium and b denote the concentration of calcium bound to the buffer, the law of mass action (see e.g., [47]) gives that the rate of decrease in the free calcium concentration in the compartment and the rate of increase in the concentration of calcium bound to a buffer due to calcium-buffer reactions is given by

$$R = k_{\text{on}} c(B_{\text{tot}} - b) - k_{\text{off}} b, \tag{46}$$

in units of mmol/ms per compartment volume, $\bar{V}_x$. The corresponding flux in terms of mmol/ms per total cell volume, V_{cell}, may be defined as

$$J = \frac{\bar{V}_x}{V_{\text{cell}}} R = V_x(k_{\text{on}} c(B_{\text{tot}} - b) - k_{\text{off}} b). \tag{47}$$

Consequently, the flux of free calcium binding to a buffer in the dyad, the SL, the bulk cytosol and the jSR are given by

$$J_d^b = V_d(k_{\text{on}}^d c_d(B_{\text{tot}}^d - b_d) - k_{\text{off}}^d b_d), \tag{48}$$
$$J_{sl}^b = V_{sl}(k_{\text{on}}^{sl} c_{sl}(B_{\text{tot}}^{sl} - b_{sl}) - k_{\text{off}}^{sl} b_{sl}), \tag{49}$$
$$J_c^b = V_c(k_{\text{on}}^c c_c(B_{\text{tot}}^c - b_c) - k_{\text{off}}^c b_c), \tag{50}$$
$$J_s^b = V_s(k_{\text{on}}^s c_s(B_{\text{tot}}^s - b_s) - k_{\text{off}}^s b_s), \tag{51}$$

respectively.

Scaling of the calcium buffers Like for the membrane proteins and the proteins on the membrane of the SR, we assume that cells of different levels of maturity contain the same types of calcium buffers, with the same rates k_{on} and k_{off}, but that the concentration of the calcium buffers, B_{tot}, may differ for different types of cells. Therefore, we define scaling parameters for the buffer concentrations on the form

$$B_{\text{tot}}^{d,S_1} = (1 + \lambda_B^d) B_{\text{tot}}^{d,S_2}, \tag{52}$$
$$B_{\text{tot}}^{sl,S_1} = (1 + \lambda_B^{sl}) B_{\text{tot}}^{sl,S_2}, \tag{53}$$
$$B_{\text{tot}}^{c,S_1} = (1 + \lambda_B^c) B_{\text{tot}}^{c,S_2}, \tag{54}$$
$$B_{\text{tot}}^{s,S_1} = (1 + \lambda_B^s) B_{\text{tot}}^{s,S_2}, \tag{55}$$

where B_{tot}^{d,S_1}, B_{tot}^{sl,S_1}, B_{tot}^{c,S_1}, and B_{tot}^{s,S_1} are the buffer concentrations in the S_1 model, and B_{tot}^{d,S_2}, B_{tot}^{sl,S_2}, B_{tot}^{c,S_2}, and B_{tot}^{s,S_2} are the buffer concentrations in the S_2 model.

Membrane fluxes (J_{CaL}, J_{bCa}, J_{pCa}, and J_{NaCa}) The membrane fluxes J_{CaL}, J_{bCa}, J_{pCa}, and J_{NaCa} may be defined from the expressions for the corresponding membrane currents, I_{CaL}, I_{bCa}, I_{pCa}, and I_{NaCa}. Recall from Section 2.2 that the membrane currents are expressed on the form

$$I_x = \frac{N_x}{AC_m} i_x, \qquad \text{for } x = \text{CaL, bCa, pCa, and NaCa,} \tag{56}$$

where N_x is the total number of proteins of type x on the cell membrane, A is the total membrane area (in μm^2), C_m is the specific membrane capacitance (in $\text{pF}/\mu\text{m}^2$) and i_x is the average single-channel current through a protein of type x (in pA). The corresponding membrane fluxes per total cell volume may similarly be defined as

$$J_x = \frac{N_x}{V_{\text{cell}}} j_x, \qquad \text{for } x = \text{CaL, bCa, pCa, and NaCa,} \tag{57}$$

where V_{cell} is the total cell volume (in L), and j_x is the average calcium flux through a single protein of type x (in mmol/ms). The average flux of calcium through a

single calcium channel may be written as

$$j_x = -\frac{10^{-15}}{2F} i_x, \tag{58}$$

where F is Faraday's constant (in C/mmol), representing the electric charge per mmol of ions with elementary charge. Note that the reason for the factor two in the denominator is that the valence of a Ca^{2+}-ion is two, and the factor 10^{-15} is included in the numerator to convert the flux from unit amol/ms to unit mmol/ms. Moreover, the reason for the negative sign in (58) is that the positive direction of the single channel current by convention is from the inside to the outside of the cell, whereas the positive direction of the calcium flux is defined to be from the outside to the inside of the cell. Note also that since the sodium-calcium exchanger exchanges three Na^+-ions for one Ca^{2+}-ion, the flux of one Ca^{2+}-ion through the exchanger represents the exchange of one charge instead of two, and a positive current out of the cell is associated with a flux of Ca^{2+} into the cell. Therefore (58) is replaced by

$$j_{\mathrm{NaCa}} = \frac{10^{-15}}{F} i_{\mathrm{NaCa}} \tag{59}$$

in this case.

Combining (56)–(59), we see that the total membrane fluxes may be written as

$$J_{\mathrm{CaL}} = -\frac{\chi C_m}{2F} I_{\mathrm{CaL}}, \qquad J_{\mathrm{pCa}} = -\frac{\chi C_m}{2F} I_{\mathrm{pCa}}, \tag{60}$$

$$J_{\mathrm{bCa}} = -\frac{\chi C_m}{2F} I_{\mathrm{bCa}}, \qquad J_{\mathrm{NaCa}} = \frac{\chi C_m}{F} I_{\mathrm{NaCa}}, \tag{61}$$

where

$$\chi = \frac{A}{10^{15} V_{\mathrm{cell}}} \tag{62}$$

is the surface-to-volume ratio of the cell (in $\mu\mathrm{m}^{-1}$). The expressions for the currents I_{CaL}, I_{bCa}, I_{pCa}, and I_{NaCa} are defined in the Supplementary information.

Scaling of the surface-to-volume ratio As explained above, we assume that the density of the membrane proteins responsible for the calcium fluxes may be different for IM and M cells. This change in protein density is represented in the model by scaling the currents (see (4)–(5)), which will also affect the corresponding calcium fluxes (60)–(61).

In addition, we assume that the geometry of the cells (i.e., the membrane area, A, and the cell volume, V_{cell}) may be different for different levels of maturity. From (60)–(63), we see that this change in geometry may be represented by scaling the surface-to-volume ratio χ by

$$\chi^{S_1} = (1 + \lambda_\chi)\chi^{S_2}, \tag{63}$$

where χ^{S_1} is the surface-to-volume ratio for maturity stage S_1, and χ^{S_2} is the value for the stage S_2.

2.4 Inversion of optical measurements

In this section, we describe the inversion procedure used to make base model representations of data obtained from optical measurements of the action potential and calcium transient of hiPSC-CMs. First, in Section 2.4.1, we describe how adjustment factors λ are set up to represent control cells from different data sets. Next, in Section 2.4.2, we describe how the effect of a drug is modeled using IC50-values and corresponding factors denoted by ε. The aim of the inversion procedure is to find optimal parameter vectors λ and ε so that the model parameterized by λ and ε fits the measured data as good as possible. This is explained in more detail in Section 2.4.3. In Section 2.4.4, we describe the cost function set up to measure the difference between the model and the data. Finally, in Section 2.4.5, we describe the continuation-based minimization method used to minimize the cost function in our computations.

2.4.1 Definition of the adjustment factors

In order to make base model representations of control cells from different data sets, we seek adjustment factors λ for a set of parameters of the base model. These adjustment factors represent adjustments of the protein densities and geometry of the cells under consideration, as explained above. For example, for each membrane protein type x, the adjustment factor λ_x is defined as

$$\frac{N_x}{A} = (1 + \lambda_x)\frac{N_x^b}{A^b}, \tag{64}$$

where $\frac{N_x}{A}$ is the protein density on the cell membrane for the fitted model and $\frac{N_x^b}{A^b}$ is the protein density in the default base model. We generally consider adjustment factors for the membrane protein densities for all the currents of the model, i.e. λ_{Na}, λ_{NaL}, λ_{CaL}, λ_{to}, λ_{Kr}, λ_{Ks}, λ_{K1}, λ_{NaCa}, λ_{NaK}, λ_{pCa}, λ_{bCl}, λ_{bCa}, and λ_{f}, although some of the factors are fixed in some cases (see Section 3.1.4).

For the protein density of an intracellular protein type x, the adjustment factor λ_x is similarly defined as

$$\frac{N_x}{V_{\mathrm{cell}}} = (1 + \lambda_x)\frac{N_x^b}{V_{\mathrm{cell}}^b}, \tag{65}$$

where $\frac{N_x}{V_{\mathrm{cell}}}$ and $\frac{N_x^b}{V_{\mathrm{cell}}^b}$ are the protein densities for the fitted model and the default base model, respectively. We consider the following adjustment factors for the intracellular protein densities: λ_{RyR}, λ_{SERCA}, λ_B^d, λ_B^{sl}, λ_B^c, and λ_B^s. In addition, we consider adjustments of the intracellular diffusion coefficients, λ_d^c, λ_{sl}^c, and λ_n^s (see (41)). In order to reduced the number of free parameters to determine in the inversion procedure, we assume that the buffer concentrations change with the same rate in all intracellular compartments, so that we only consider a single adjustment factor

$$\lambda_B^d = \lambda_B^{sl} = \lambda_B^c = \lambda_B^s := \lambda_B. \tag{66}$$

Similarly, we assume that the intracellular diffusion coefficients change with the same rate, so that

$$\lambda_d^c = \lambda_{sl}^c = \lambda_n^s := \lambda_\alpha. \tag{67}$$

Furthermore, because we wish to avoid ending up with unrealistic values of the surface-to-volume ratio, χ, we assume that the scaling factor for the cell surface-to-volume ratio varies little between data sets and only use two different values of χ in the computations. We use the value $\chi = 0.6\ \mu\text{m}^{-1}$ for mature cells and the value $\chi = 0.9\ \mu\text{m}^{-1}$ for immature cells, based on the values used in the Grandi et al. AP model for mature cells [23] and the Paci et al. AP model for hiPSC-CMs [32].

2.4.2 IC50 modeling of drug effects

In our applications of the inversion procedure presented below, we will assume that the effect of the drug is to block ion channels to a certain degree. Following previous modeling of channel blockers (see e.g., [33, 48, 49, 50]), we model the dose-dependent effect of a drug by scaling the channel conductances according to

$$g_i^D = \frac{1}{1 + \frac{D}{\text{IC50}_i}} g_i^c, \tag{68}$$

where g_i^D is the conductance of channel i in the presence of a drug with concentration D, IC50_i is the drug concentration that leads to 50% block of channel i, and g_i^c is the channel conductance in the control case (i.e., in the absence of drugs). Specifically, this means that if the drug concentration D equals the IC50-value, we have $g_i^D = \frac{1}{2} g_i^c$.

It should be mentioned that a drug may certainly affect a channel in a more complex manner than is assumed here. The effect of drugs can realistically be represented by introducing new states in Markov models representing the ion channel. In such models, the transition rates between different model states represent the properties of the drugs (see e.g., [17, 51, 20, 52]). Although Markov model representations of drug effects are more versatile and realistic than the simple blocking assumption (68), it would greatly increase the complexity of the inversion process, because much more parameters would have to be computed. We therefore prefer the simplest possible blocking assumption here.

From (68), we see that for a given drug dose $D > 0$, the effect of the drug would increase if the IC50-value was decreased, and the effect of the drug would be very small if the IC50-value was much larger than the considered dose. In the continuation-based minimization method applied in our computations (see Section 2.4.5 below), it is most practical to deal with parameters that are small when no change occurs and large when large changes occur. Therefore, we introduce the parameters

$$\varepsilon_i = \frac{1}{\text{IC50}_i}. \tag{69}$$

Here, a small value of ε_i represents small drug effects and a large value of ε_i represents large drug effects, and the channel blocking is given by

$$g_i^D = \frac{1}{1 + D\varepsilon_i} g_i^c. \tag{70}$$

In our computations, we assume that the considered drugs block either I_{CaL}, I_{NaL}, I_{Kr}, or a combination of these currents, and we therefore only consider the ε-parameters $\varepsilon_{\mathrm{CaL}}$, $\varepsilon_{\mathrm{NaL}}$, $\varepsilon_{\mathrm{Kr}}$.

2.4.3 Coupled inversion of data from several doses

The control data obtained from different experiments tend to vary significantly, and in order to be able to accurately estimate the drug effect from the measurements, the λ-parameters need to be tuned so that the control model fits the control data as good as possible. In addition, we want the λ-parameters to be set up in such a way that the scaling (70) for $\varepsilon_{\mathrm{CaL}}$, $\varepsilon_{\mathrm{NaL}}$, and $\varepsilon_{\mathrm{Kr}}$ is enough to fit the model to the considered drug doses. In order to increase the chance of obtaining such a control model, we fit the control parameters, λ, and the drug parameters, ε, simultaneously, instead of first finding the optimal control parameters, λ, by fitting the base model to the control data, and then finding appropriate drug parameters, ε, for each dose. In addition, all doses are included in the inversion, so that the estimated values of ε are based on all the drug doses included in the data set.

In order to illustrate the role of the λ- and ε-parameters more clearly, consider a very simplified model consisting of just two currents, and assume that the base model is given by (see Section 2.2)

$$\frac{dv}{dt} = -g_1 o_1 (v - E_1) - g_2 o_2 (v - E_2). \tag{71}$$

Assume further that we have data from cells with no drug present and with different doses of a drug (e.g., one low dose and one high dose). We assume that the drug may block any of the two model currents. In the inversion procedure, we try to find optimal values of the four parameters λ_1, λ_2, ε_1 and ε_2 so that the adjusted model of the form

$$\frac{dv}{dt} = -\frac{1 + \lambda_1}{1 + D\varepsilon_1} g_1 o_1 (v - E_1) - \frac{1 + \lambda_2}{1 + D\varepsilon_2} g_2 o_1 (v - E_2) \tag{72}$$

fits the data as good as possible both for the control case ($D = 0$) and for the considered drug doses. In other words, for a given parameter set λ_1, λ_2, ε_1 and ε_2, we need to compute the solution of the model (72) both for the control case ($D = 0$) and for the considered drug doses and compare the obtained solutions to the corresponding data.

In the more general case considered in our computations, the idea is the same, but since we also consider scaling of parameters that are not assumed to possibly be affected by the drug, we also have some parameters simply scaled by a factor $(1+\lambda_i)$ instead of by $\frac{1+\lambda_i}{1+D\varepsilon_i}$.

2.4.4 Properties of the cost function

In order to find the optimal parameters that make the difference between the model and the data as small as possible as explained in the previous section, we need to define a cost function that measures the difference between a given model solution and the data. This cost function is defined as

$$H(\lambda, \varepsilon) = \sum_d \sum_j w_{d,j} (H_j(\lambda, \varepsilon, D_d))^2. \tag{73}$$

Here, d runs over each of the considered drug doses, D_d, including the control case, $D_0 = 0$, and j runs over each cost function term, H_j, representing various differences between the data and the model solution. The parameters $w_{d,j}$ represent weights for each of the cost function terms for each of the doses. The weights are generally set to 1, unless otherwise specified.

The data from the microphysiological systems are traces representing the membrane potential and the cytosolic calcium transient. Since these data are obtained using voltage- and calcium-sensitive dyes, we do not get the values in proper units (mV and mM). Rather, we get images representing relative strengths of the measured quantities. Therefore, some characteristics of the action potential and calcium transient cannot be sampled directly from the data. For instance, we do not know the maximum and minimum values of the voltage and the calcium concentration. On the other hand, the action potential duration and similar characteristics of the calcium transient is readily obtained from the data. This observation is important for the definition of the cost function. The cost function must be based on characteristics obtainable from the data or other known characteristics of the cells. When necessary for comparing simulation results (with units) and experimental data (unitless), the experimental data values are mapped so that the maximum and minimum values of the membrane potential and the calcium transient match the maximum and minimum values of the model solution.

Each of the cost function terms, H_j, are defined below, and the definition of some of the quantities involved in the cost function terms are illustrated in Figure 3.

Action potential and calcium transient durations The terms in the cost function includes terms for the differences in the action potential and calcium transient durations of the form

$$H_{\mathrm{APD}p}(\lambda, \varepsilon, D_d) = \frac{|\mathrm{APD}p(\lambda, \varepsilon, D_d) - \mathrm{APD}p^*(D_d)|}{|\mathrm{APD}p^*(D_d)|}, \tag{74}$$

$$H_{\mathrm{CaD}p}(\lambda, \varepsilon, D_d) = \frac{|\mathrm{CaD}p(\lambda, \varepsilon, D_d) - \mathrm{CaD}p^*(D_d)|}{|\mathrm{CaD}p^*(D_d)|}, \tag{75}$$

for $p = 20, 25, ...75, 80$. Here, as an example, APD30 represents the time from the membrane potential is 30% below its maximum value during the upstroke of the action potential, t_1, to the membrane potential again reaches a value 30% below

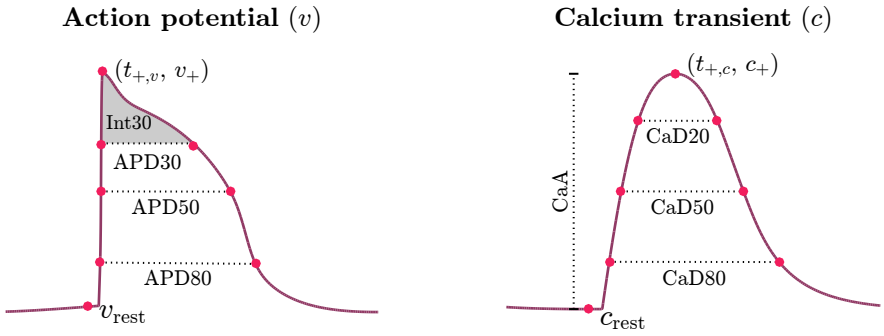

Figure 3: Illustration of some of the quantities used to define the terms of the cost function (73) from the action potential and calcium transient.

its maximum value during the repolarization phase, t_2. $\text{APD30}(\lambda, \varepsilon, D_d)$ is the value obtained from the solution of the model given by the parameter vectors λ and ε for the drug dose D_d, while $\text{APD30}^*(D_d)$ is the value obtained from the measured data for the drug dose D_d. The same notation with a '$*$' marking the measured data values is used for all the terms in the cost function. The calcium transient durations, CaDp, are defined in the same manner as the action potential durations.

Integral of voltage Because the APDp values for low values of p may be difficult to obtain from the optical measurements due to noise, we also include a term that considers the integral of the membrane potential from t_1 to t_2 as illustrated in Figure 3. This term is defined as

$$H_{\text{Int30}}(\lambda, \varepsilon, D_d) = \frac{|\text{Int30}(\lambda, \varepsilon, D_d) - \text{Int30}^*(D_d)|}{|\text{Int30}^*(D_d)|}, \tag{76}$$

where Int30 is defined as

$$\text{Int30} = \int_{t_1}^{t_2} [v - v(t_1)]\, dt, \tag{77}$$

and v is the membrane potential. Note that the values of t_1 and t_2 are here the ones defined in the computation of APD30.

Norm of the calcium transient difference There is typically less noise in the data obtained from the optical measurements of the calcium transient than for the measurements of the membrane potential. Therefore, we also include a term for the discrete l^2-norm of the difference between the calcium transient of the data

and the model,

$$H_{\mathrm{Ca}}(\lambda, \varepsilon, D_d) = \frac{\|c(\lambda, \varepsilon, D_d) - c^*(D_d)\|_2}{\|c^*(D_d)\|_2}, \tag{78}$$

where c is the cytosolic calcium concentration. When the data c^* is obtained from optical measurements, the timing of the calcium transient relative to the stimulation time is not known. Therefore, the value of H_{Ca} is taken as the smallest value obtained when the timing of $c^*(D_d)$ may be adjusted to fit the timing of $c(\lambda, \varepsilon, D_d)$.

Upstroke velocity In order to capture information about the upstroke of the action potential and the calcium transient, we also consider the terms

$$H_{\mathrm{dvdt}}(\lambda, \varepsilon, D_d) = \frac{\left| \left(\frac{dv(\lambda,\varepsilon,D_d)}{dt} \right)_{-20\mathrm{mV}} - \left(\frac{dv^*(D_d)}{dt} \right)_{-20\mathrm{mV}} \right|}{\left| \left(\frac{dv^*(D_d)}{dt} \right)_{-20\mathrm{mV}} \right|}, \tag{79}$$

$$H_{\mathrm{dcdt}}(\lambda, \varepsilon, D_d) = \frac{\left| \left(\frac{dc(\lambda,\varepsilon,D_d)}{dt} \right)_{\max} - \left(\frac{dc^*(D_d)}{dt} \right)_{\max} \right|}{\left| \left(\frac{dc^*(D_d)}{dt} \right)_{\max} \right|}, \tag{80}$$

where $\left(\frac{dv}{dt}\right)_{-20\mathrm{mV}}$ is the upstroke velocity of the membrane potential obtained at $v = -20$ mV, and $\left(\frac{dc}{dt}\right)_{\max}$ is the maximal upstroke velocity of the calcium transient. We use the upstroke velocity obtained at $v = -20$ mV instead of the maximal upstroke velocity to ensure that the value obtained in the model is not determined by the stimulus current. Note, however, that because of the noise in the optical measurements of the membrane potential, the H_{dvdt}-term is currently only included in the inversions used to determine a mature base model. In that case, the "experimental" data are generated by simulations and therefore, the dv/dt can accurately be computed.

Calcium transient amplitude Because one of the main characteristics able to distinguish between blocking of I_{CaL} and I_{NaL} is the calcium transient amplitude, we also include the term

$$H_{\mathrm{CaA}}(\lambda, \varepsilon, D_d) = \frac{|\mathrm{CaA}(\lambda, \varepsilon, D_d) - \mathrm{CaA}^*(D_d)|}{|\mathrm{CaA}^*(D_d)|}, \tag{81}$$

where CaA denotes the calcium transient amplitude (see Figure 3).

Note, however, that the actual values of the calcium transient amplitude are not known from the optical measurements, and only the relative differences of the amplitude between the control case and the different drug doses are known. Therefore, we do not include the H_{CaA}-term for the control case. For the non-zero drug doses, we define the data values $\mathrm{CaA}^*(D_d)$ so that the relative difference

between $\mathrm{CaA}^*(D_d)$ and the amplitude in the control model is the same as the relative difference between the amplitude in the data for drug dose D_d and the control data. In other words, $\mathrm{CaA}^*(D_d)$ is defined as

$$\mathrm{CaA}^*(D_d) = \frac{\tilde{\mathrm{CaA}}(D_d)}{\tilde{\mathrm{CaA}}(D_0)}\mathrm{CaA}(\lambda, \varepsilon, D_0), \tag{82}$$

where $\tilde{\mathrm{CaA}}(D_d)$ and $\tilde{\mathrm{CaA}}(D_0)$ are the unitless measured calcium transient amplitudes for the drug dose D_d and the control case ($D_0 = 0$), respectively. Furthermore, $\mathrm{CaA}(\lambda, \varepsilon, D_0)$ is the amplitude of the calcium transient in the current control model given by the adjustment parameters λ.

Maximum and resting values of the membrane potential and calcium concentration In cases where we wish to include information about the resting and maximum values of the membrane potential and/or the cytosolic calcium concentration, we include terms of the form

$$H_{v,\mathrm{rest}}(\lambda) = \frac{|v_{\mathrm{rest}}(\lambda) - v^*_{\mathrm{rest}}|}{|v^*_{\mathrm{rest}}|}, \qquad H_{c,\mathrm{rest}}(\lambda) = \frac{|c_{\mathrm{rest}}(\lambda) - c^*_{\mathrm{rest}}|}{|c^*_{\mathrm{rest}}|}, \tag{83}$$

$$H_{v_+}(\lambda) = \frac{|v_+(\lambda) - v^*_+|}{|v^*_+|}, \qquad H_{c_+}(\lambda) = \frac{|c_+(\lambda) - c^*_+|}{|c^*_+|}, \tag{84}$$

$$H_{t_{+,v}}(\lambda) = \frac{|t_{+,v}(\lambda) - t^*_{+,v}|}{|t^*_{+,v}|}, \qquad H_{t_{+,c}}(\lambda) = \frac{|t_{+,c}(\lambda) - t^*_{+,c}|}{|t^*_{+,c}|}, \tag{85}$$

where v_{rest} and c_{rest} are the resting membrane potential and calcium concentration, respectively, defined as the values obtained 10 ms before stimulation in the applied stimulation protocol. Similarly, v_+ and c_+ are the maximum values of the membrane potential and calcium concentration, respectively, and $t_{+,v}$ and $t_{+,c}$ are the points in time when these values are reached. Note that these terms are only included when the base model is fitted to the Grandi et al. model to define a mature base model.

Information about individual currents When the inversion procedure is used to define a default base model for mature and immature cells, we also include information about the individual currents and fluxes. These data are obtained from mathematical models of mature [23] and immature [32] cells, and are represented by cost function terms of the form

$$H_{I_x}(\lambda) = \frac{\|I_x(\lambda) - I^*_x\|_2}{\|I^*_x\|_2}, \qquad H_{I^{\max}_x}(\lambda) = \frac{|I^{\max}_x(\lambda) - I^{*,\max}_x|}{|I^{*,\max}_x|}, \tag{86}$$

for each of the considered currents or fluxes, x. Here, $\|\cdot\|_2$ is the discrete l^2-norm, and $I^{\max}_x$ is defined as $I^{\max}_x = \max(|I_x|)$.

Calcium balance We wish to select values of λ so that the resulting control model does not exhibit large degrees of drift of the intracellular calcium concentrations. Therefore, we include a calcium balance term of the form

$$H_{\mathrm{Ca},b}(\lambda) = \frac{1}{b}\left|\int_0^T (J_{\mathrm{CaL}}(\lambda) + J_e^{sl}(\lambda))dt\right|, \tag{87}$$

which is zero if the amount of calcium entering the cell through the proteins on the cell membrane equals the amount of calcium leaving the cell. The main term is here the absolute value of the integral of the sum of the J_{CaL} and J_e^{sl} fluxes of the model over the simulated time interval, and b is a scaling factor set equal to 0.1 mM in our simulations.

Regularization of adjustment factors In cases where several choices of parameters λ and ε fit the data equally well, we wish to choose values of λ and ε close to zero. We therefore include the regularization terms

$$H_\varepsilon(\varepsilon) = \sum_{i\in S_\varepsilon}\left(\frac{\varepsilon_i}{\bar{\varepsilon}}\right)^2, \qquad H_\lambda(\lambda) = \sum_{i\in S_{\lambda^\star}} \lambda^2. \tag{88}$$

Here, $\bar{\varepsilon} = \frac{1}{\bar{D}}$, where $\bar{D}$ is the median of the non-zero drug doses included in the data set. Furthermore, S_ε is the set of indices for all the individual ε-factors, and $S_{\lambda^\star}$ is the set of indices for the λ-values we wish to remain as close as possible to the default base model in the inversion. In the inversions reported below, this set consists of the indices for λ_{CaL} and λ_{Kr} because the size of these currents is based on measurements of hiPSC-CMs (see below) and because we are especially interested in obtaining reasonable values for these currents since we are investigating the drug effects on these currents.

Specification of the cost function weights The choice of terms included in the cost function depends on the specific application of the inversion procedure. In particular, for inversions of data from optical measurements (and for inversions of simulated drugs), we include the terms H_{APD30}, H_{APD50}, H_{APD80}, $H_{\mathrm{CaD20}} - H_{\mathrm{CaD80}}$, H_{int30}, H_{dcdt}, H_{Ca}, H_ε and H_λ. The reason why we only include three APD-values, but 13 CaD-values is that the quality of the calcium data is generally better than the voltage data. To make up for the large number of CaD-terms compared to APD-terms, the weight of the CaD-terms are set to 0.5, while the APD-terms are given the weight 1, except that the weight of the APD80 and CaD80-terms are set to 5. The upstroke velocity of the action potential is not included because of the level of noise in the voltage data.

Furthermore, for the control case, the term $H_{\mathrm{Ca},b}$ with weight 1 is included, and for the drug doses, H_{CaA} is included with weight 10. The large weight is in this case due to the fact that this is one of the most important characteristics for distinguishing between block of I_{CaL} and I_{NaL}. We also include the regularization terms H_ε and H_λ with weights, 0.01 and 10, respectively. All the ε-parameters

are included in the ε-regularization, but only λ_{CaL} and λ_{Kr} are included in the λ-regularization as explained above.

In addition, the weight of all the cost function terms (except $H_{\text{Ca},b}$) are for the control case multiplied by the number of non-zero doses included in the data set. This is done because a good fit for the control model is essential for being able to use the model to estimate drug effects.

In the inversions aiming to define default values for the immature and mature base models, additional terms, for example terms for the individual currents, are also included in the cost function. This is specified in more detail in Sections 3.1.1 and 3.1.2.

2.4.5 A continuation-based minimization method

As explained in the previous sections, we wish to adjust the base model to data by finding λ- and ε-parameters that minimize a cost function of the form (73), measuring the difference between the data and the model solution. In order to search for the optimal values of λ and ε, we apply a continuation-based optimization method. The idea behind the method is to find the final optimal parameter vectors λ and ε by, in a number of iterations, finding the optimal λ and ε for data that is gradually changing from the default model solution ($\lambda = 0$, $\varepsilon = 0$) to the data we are trying to invert.

Cost function in the continuation case More specifically, we assume that for each drug dose, D_d, (including the control case) the data we are trying to invert is given by some vector pair $(v^1(D_d), c^1(D_d))$, where $v^1(D_d)$ is the membrane potential of the data and $c^1(D_d)$ is the calcium transient of the data. In addition, from the default base model specified by $\lambda = \varepsilon = 0$, we can compute a vector pair (v^0, c^0) for the membrane potential and calcium transient in the starting point of the inversion.

The goal of the continuation method is to compute a path for λ and ε from $\lambda = \varepsilon = 0$, which fit (v^0, c^0) perfectly, to some λ and ε that fit the final data $(v^1(D_d), c^1(D_d))$ for each of the drug doses, D_d, as good as possible. This is done by defining a cost function of the form

$$\bar{H}(\theta, \lambda, \varepsilon) = \sum_d \sum_j w_{d,j} \left(\bar{H}_j(\theta, \lambda, \varepsilon, D_d) \right)^2, \tag{89}$$

for the intermediate steps in the algorithm. Here, θ is a parameter that is gradually increased from zero to one. In the definition (89), the terms $\bar{H}_j(\theta, \lambda, \varepsilon, D_d)$ correspond to each of the terms $H_j(\lambda, \varepsilon, D_d)$ defined above. Specifically, the terms take the form

$$\bar{H}_j(\theta, \lambda, \varepsilon, D_d) = \frac{|R_j(v(\lambda, \varepsilon, D_d), c(\lambda, \varepsilon, D_d)) - R_j^\theta(D_d)|}{|R_j^\theta(D_d)|}, \tag{90}$$

$$R_j^\theta(D_d) = (1 - \theta) R_j(v^0, c^0) + \theta R_j(v^1(D_d), c^1(D_d)), \tag{91}$$

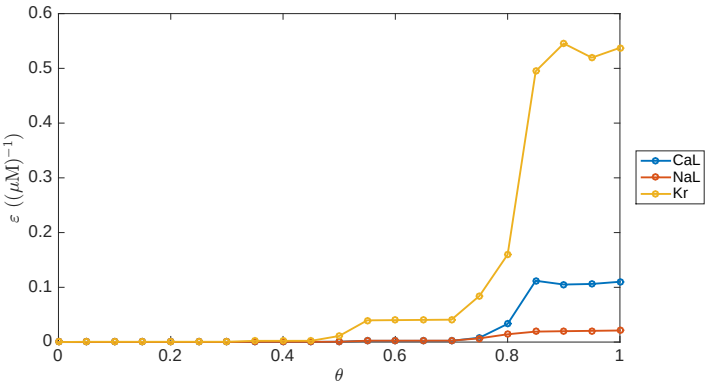

Figure 4: Example of how the optimal ε-values gradually move from zero to the optimal values for the data as θ is increased from zero to one in the continuation-based inversion procedure. The shown development of ε comes from an inversion aiming to identify the effect of the drug Flecainide based on optical measurements of the membrane potential and calcium transient in Section 3.3.4 below.

where $R_j(v, c)$ represent different characteristics of the action potential or calcium transient, e.g., the action potential duration at some percentage or the upstroke velocity (see (75)–(86)[1]). In the case $\theta = 0$, $R_j^\theta(D_d)$ is equal to the terms defined by the default model ($\lambda = \varepsilon = 0$) for all the doses D_d. Therefore, $\bar{H}(0, 0, 0, D_d) = 0$,[2] so the optimal solution for $\theta = 0$ is $\lambda = \varepsilon = 0$. In the case $\theta = 1$, the terms $R_j^\theta(D_d)$ are equal to the characteristics computed for the data we wish to invert. In other words, $\bar{H}(1, \lambda, \varepsilon) = H(\lambda, \varepsilon)$, where $H(\lambda, \varepsilon)$ is defined in (73). For the intermediate values of θ, the characteristics $R_j^\theta(D_d)$ represent weighted averages of the characteristics for the model used as a staring point of the inversion and the data we are trying to invert. Therefore, we expect the optimal values of λ and ε to gradually move from zero to the optimal values for the data as θ is increased from zero to one.

The minimization algorithm In the minimization algorithm, we find the optimal solution in M iterations. We define $\theta_m = \Delta\theta \times m$ for $m = 0, \ldots, M$ where $\Delta\theta = 1/M$. For $m = 1, ..., M$, we assume that the optimal values $\lambda(\theta_{m-1})$ and $\varepsilon(\theta_{m-1})$ have been computed, and we want to find $\lambda(\theta_m)$ and $\varepsilon(\theta_m)$ by finding the minimum of $\bar{H}(\theta_m, \lambda, \varepsilon)$. Since the step in θ is small, we assume that the changes in λ and ε are also relatively small. We use the Nelder-Mead algorithm [53] to minimize $\bar{H}(\theta_m, \lambda, \varepsilon)$, and we use $\lambda(\theta_{m-1})$ and $\varepsilon(\theta_{m-1})$ as suggestions for the starting vectors to find $\lambda(\theta_m)$ and $\varepsilon(\theta_m)$. However, in order to increase the

[1]Note that this does not apply to the regularization terms (87)–(88). These terms are assumed to be the same for all values of θ.

[2]Note that this relies on either the flux balance term $H_{\mathrm{Ca},b}$ being zero for the default base model or on the weight for this term being zero.

chance of finding the true optimal value in every iteration, we start the Nelder-Mead algorithm from several randomly chosen starting vectors in the vicinity of $\lambda(\theta_{m-1})$ and $\varepsilon(\theta_{m-1})$. Figure 4 illustrates the development of the ε-values in one of the inversions aiming to identify drugs in the next section.

Technical specifications In the applications of the inversion procedure presented below, we use $M = 20$, and in each iteration m, we draw 63 guesses (since the specific computer used for these simulations has 64 cores) for the starting vectors for the Nelder-Mead algorithm from $[\lambda(\theta_{m-1}) - 0.2,\ \lambda(\theta_{m-1}) + 0.2]$ and $\left[\frac{\varepsilon(\theta_{m-1})}{5},\ 5 \cdot \varepsilon(\theta_{m-1})\right]$ for λ and ε, respectively. In the first 15 iterations, we use five iterations of the Nelder-Mead algorithm for each guess, and for the last five iterations we use 25 iterations of the Nelder-Mead algorithm. For each new parameter set, we generally run the simulation for 15 AP cycles before measuring the action potential and calcium transient, unless otherwise specified.

2.5 Identifiability of the base model based on singular value decomposition of the currents

In the inversion procedure outlined above, we try to find the optimal adjustment factors λ and ε for the model so that the membrane potential and the cytosolic calcium transient in the model solution match some measurements of the membrane potential and calcium transient as good as possible. An important element to consider in this process is whether the identified adjustment factors found by the inversion procedure are the only combination of adjustment factors that fit the data, or whether other adjustment factors might exists, fitting the data equally well.

In order to investigate the identifiability of the adjustment factors for the currents in the base model, we apply a method based on a singular value decomposition (see e.g., [54, 55]) of the currents. This approach is described in detail in [56]. In short, the identifiability of the currents is investigated by collecting the model currents at time points $t_n = n\Delta t$, for $n = 1, ..., N_t$ into a matrix $A \in R^{N_t, N_c}$, where N_c is the number of model currents. Then, the singular value decomposition of the matrix

$$A = USV^T$$

is computed. Here, the matrices $U \in R^{N_t, N_t}$ and $V \in R^{N_c, N_c}$ are unitary matrices, and the matrix $S \in R^{N_t, N_c}$ is a diagonal matrix with singular values σ_i along the diagonal. The columns u_i and v_i of U and V, respectively, are the associated singular vectors.

From the properties of the singular value decomposition it can be shown that perturbations of the adjustment factors along singular vectors v_i associated with large singular values σ_i are expected to result in significant changes in the action potential, whereas perturbations of the adjustment factors along singular vectors v_i associated with small singular values are expected to result in small changes in the action potential.

In [56] it was shown that this expected result seemed to hold for three well-known AP models of mature, ventricular cardiomyocytes. In addition, it was demonstrated how this analysis could be used to define an *identifiability index* for the individual model currents. This index was defined for each current $j = 1, ..., N_c$ as

$$k(e_j) = \|e_j - P_N e_j\|_2, \tag{92}$$

where $e_j \in R^{N_c}$ is the vector that is one in element number j and zero elsewhere. Moreover, $P_N e_j \in R^{N_c}$ is the projection of e_i onto the unidentifiable space spanned by the singular vectors v_i associated with small singular values (or small perturbation effects). In other words, if $k(e_j)$ is close to zero, almost the entire current I_j is in the unidentifiable space, and we cannot be sure that the value of the associated adjustment factors λ_j or ε_j are the only values that fits the data (i.e., result in the same AP). On the other hand, if $k(e_j)$ is close to one, we expect that other values of λ_j or ε_j would not fit the data as good as the the current values because perturbations of the adjustment factors would result in large changes in the AP that perturbations of other adjustment factors could not cancel out.

Note that this approach only aims to identify the identifiability of the adjustment factors for the model currents. The analysis could be extended to include other state variables than the membrane potential (e.g., the calcium concentrations). In that case, the identifiability of the remaining adjustment factors might also be suggested. However, since we at this stage is primarily interested in identifying the drug effects on membrane ion channels, we are particularly interested in ensuring that the adjustment factors for the currents are unique. Therefore, we are currently satisfied with investigating the identifiability of the model currents based on the effects on the action potential.

3 Results

In this section, we demonstrate a few applications of the inversion procedure outlined above. First, in Section 3.1, we define the default immature and mature versions of the general base model formulation. We also demonstrate that these models exhibit high gain and graded release of the calcium fluxes. In addition, we illustrate the identifiability of the model currents using the SVD analysis described above. This analysis is used to determine which model currents should be fixed in the applications of the inversion procedure. Next, in Section 3.2, we use the inversion procedure to identify the drug effects for data generated by simulations. Finally, in Section 3.3, we apply the inversion procedure to the identification of drug effects from data obtained from optical measurements of hiPSC-CMs.

3.1 The base model

In this section, we set up the default mature and immature base model formulations used in the inversion procedure in the following sections.

3.1.1 Base model approximation of the Grandi model

The right panel of Figure 5 shows the action potential and calcium transient of the Grandi et al. model [23] for healthy mature ventricular cardiomyocytes and the action potential and calcium transient of the mature version of the base model. The base model is fitted to approximate the Grandi et al. model using the inversion procedure described above. More specifically, the cost function of the inversion procedure includes all the terms defined in Section 2.4.4, except for the regularization terms (88). The currents I_{Na}, I_{CaL}, I_{to}, I_{Kr}, I_{Ks}, I_{K1}, I_{NaCa}, I_{pCa}, and I_{bCa}, as well as the fluxes J_{RyR} and J_{SERCA} are included in (86). All terms measuring the difference in membrane potential or calcium concentration are given the weight $w_j = 1$ and the terms measuring differences in the currents are given the weight $w_j = 0.5$.

As mentioned above, we let the default base model be given by the mature base model because this model will be fixed, whereas the immature models will change depending on the measurements. The parameter values obtained in the inversion procedure therefore define the default base model and are specified in the Supplementary information.

3.1.2 Immature base model

The left panel of Figure 5 shows the solution of the immature base model fitted to optical measurements of the action potential and calcium transient of immature cells. In this case, the cost function consists of the terms H_{APD30}, H_{APD50}, H_{APD80}, $H_{\mathrm{CaD20}} - H_{\mathrm{CaD80}}$, H_{int30}, H_{dvdt}, H_{dcdt}, H_{Ca}, $H_{\mathrm{Ca},b}$, $H_{I_{\mathrm{Na}}^{\mathrm{max}}}$, $H_{I_{\mathrm{CaL}}^{\mathrm{max}}}$, $H_{I_{\mathrm{Kr}}^{\mathrm{max}}}$, $H_{I_{\mathrm{Ks}}^{\mathrm{max}}}$, $H_{I_{\mathrm{K1}}^{\mathrm{max}}}$, $H_{I_{\mathrm{to}}^{\mathrm{max}}}$, $H_{I_{\mathrm{f}}^{\mathrm{max}}}$, where the information about the currents is obtained from the Paci et al. model [32] which is based on patch-clamp recordings of the ionic currents of hiPSC-CMs from [57]. The terms $H_{\mathrm{CaD20}} - H_{\mathrm{CaD75}}$ are given the weight 0.5, and H_{APD80} and H_{CaD80} are given the weight 5. Furthermore, $H_{I_{\mathrm{Na}}^{\mathrm{max}}}$, $H_{I_{\mathrm{Ks}}^{\mathrm{max}}}$, $H_{I_{\mathrm{K1}}^{\mathrm{max}}}$, $H_{I_{\mathrm{to}}^{\mathrm{max}}}$, and $H_{I_{\mathrm{f}}^{\mathrm{max}}}$ are given the weight 0.5 and $H_{I_{\mathrm{CaL}}^{\mathrm{max}}}$ and $H_{I_{\mathrm{Kr}}^{\mathrm{max}}}$ are given the weight 5. The remaining terms are given the weight 1.

The adjustment between immature and mature cells returned by the inversion procedure are reported in Table 3. Note that these adjustment factors represent the default immature base model used as a starting point for the inversion of the remaining control data sets. In other words, the specific adjustment factors between the immature and mature models will differ for each new data set.

3.1.3 High gain and graded release of the base model

As mentioned above, the base model formulation of Ca^{2+}-release is designed to exhibit both high gain and graded release. This has proved impossible to achieve using common pool models (see e.g., [58, 59]), and is discussed in more detail in Section 4.1 below.

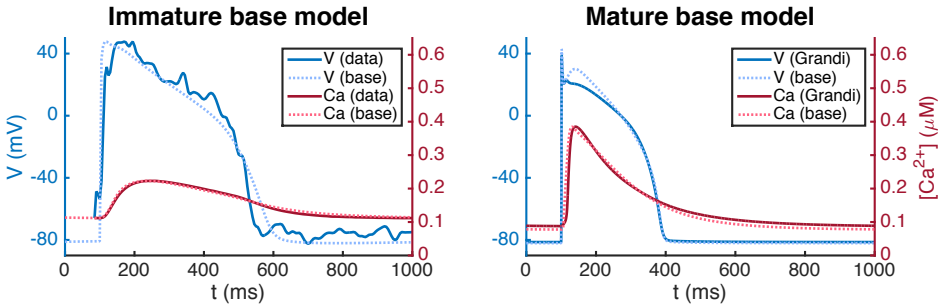

Figure 5: Action potential (blue) and cytosolic calcium transient (red) for the immature and mature versions of the base model. In the left panel, the base model is adjusted to fit data obtained from optical measurements of the action potential and calcium transient of hiPSC-CMs. In the right panel, the base model is adjusted to approximate the Grandi et al. model [23] of mature cardiomyocytes.

λ_{Na}	2.00	λ_{CaL}	-0.53
λ_{NaL}	-0.08	λ_{bCa}	0.97
λ_{Kr}	-0.57	λ_{pCa}	-0.94
λ_{Ks}	0.68	λ_{NaCa}	-0.87
λ_{K1}	2.23	λ_{RyR}	-0.21
λ_{to}	8.45	λ_{SERCA}	-0.58
λ_{f}	-0.99	λ_{sl}^{c}, λ_{n}^{s}, λ_{d}^{c}	-0.12
λ_{bCl}	42.4	λ_{B}^{c}, λ_{B}^{d}, λ_{B}^{sl}, λ_{B}^{s}	-0.55
λ_{NaK}	-0.16	λ_{χ}	-0.33

Table 3: Values defining the maturation map between the default immature and mature base models illustrated in Figure 5. The mature parameters, p^M, are related to the immature parameters, p^{IM}, by the relation $p^M = (1 + \lambda)p^{IM}$. See Sections 2.2–2.3 for more detailed definitions of each of the λ-values.

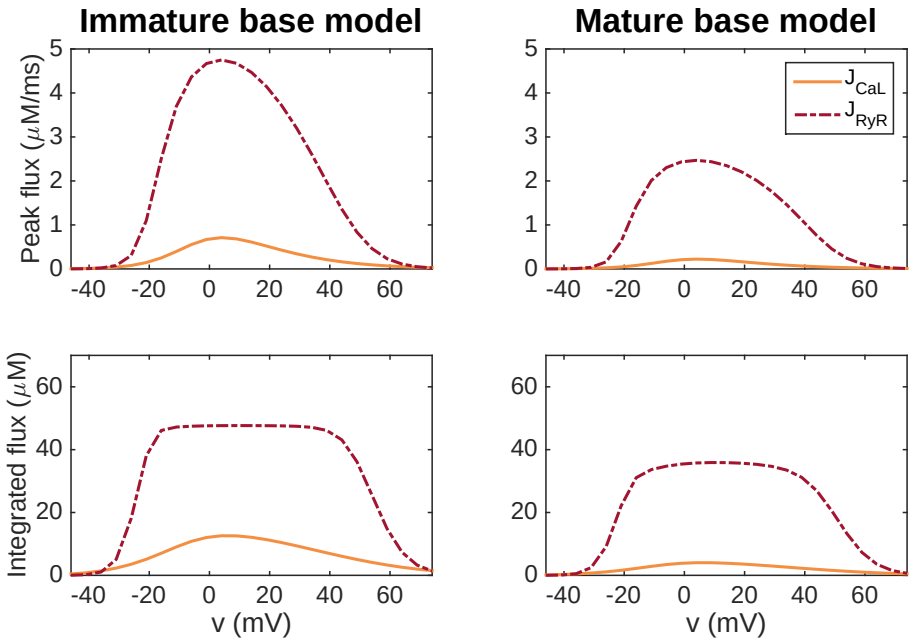

Figure 6: Graded release for the immature (left) and mature (right) versions of the base model. In the upper panel, we report the peak of the J_{CaL} and J_{RyR} fluxes for simulations in which the membrane potential is fixed at specific values between - 50 mV and 80 mV. In the lower panel, we show the fluxes integrated with respect to time from $t = 0$ ms to $t = 100$ ms. After 100 ms, both J_{CaL} and J_{RyR} have roughly returned to their resting levels.

The Ca^{2+}-release model we have designed (see (8)–(12) and (26)–(31) above) differs from the classical common pool models in two ways: First, release of Ca^{2+} from the SR is not directed into the dyad (d), but rather directly to the subsarcolemmal (SL) space (see Figure 2), and second; the release mechanism is formulated in terms of an availability rate and open probability (see (29)).

In Figure 6, we show that this model exhibits high gain and graded release both when the IM and M parameters are applied. In the figure, we report the peak of the J_{CaL} and J_{RyR} fluxes as well as the integrated fluxes for simulations in which the membrane potential is fixed at specific values. The remaining state variables of the models start at the default initial conditions corresponding to the default resting membrane potential of the model, and the simulations record the J_{CaL} and J_{RyR} fluxes resulting from the clamped membrane potential.

We observe that for most values of v, the J_{RyR} flux is considerably larger than the J_{CaL} flux, indicating high gain. Furthermore, a small J_{CaL} flux seems to be associated with a small J_{RyR} flux, whereas a large J_{CaL} flux is associated with a large J_{RyR} flux, indicating graded release.

3.1.4 Identifiability of the currents in the immature base model

In order to investigate the identifiability of the individual model currents, we apply the singular value decomposition analysis from [56] described in Section 2.5. The result of the analysis is displayed in Figure 7. The titles above each plot indicate the value of each of the singular values of the current matrix, A. The upper plots below the singular values show the singular vectors corresponding to each of the singular values. Here, each letter corresponds to a single current specified in the table on the right-hand side. The below left plots show the values of the cost function (73) evaluated using the default immature base model as data and a perturbed model as the model solution. In the perturbed model, the maximum conductances are perturbed with λ-values (see (5)) equal to $\omega \cdot v_i$, where v_i is the considered singular vector and ω is varied between zero and one. The cost function includes the terms H_{APD30}, H_{APD50}, H_{APD80}, and H_{Int30} with weight 1 for all terms except H_{APD80}, which is given the weight 5. The maximum values of H are given in the top of the plots. The right plots show the solutions resulting from the perturbations for a few selection of ω.

In [56] it was shown that perturbations along singular vectors corresponding to large singular values generally resulted in large perturbation effects, whereas perturbations along singular vectors corresponding to small singular values generally resulted in small perturbation effects for the ten Tusscher et al. [60], the Grandi et al. [23] and the O'Hara et al. [22] AP models. Figure 7 shows that this result also seem to hold quite well for the immature base model. The main discrepancy is observed for σ_2, corresponding to a singular vector consisting almost exclusively of the fast sodium current, I_{Na}. The reason why the perturbation effects in this case is very small for this singular value is probably that the upstroke velocity is not included in the cost function (cf. [56]).

In order to quantify the identifiability of the individual currents, we compute the identifiability index, k, defined in (92). The unidentifiable space is defined as the space spanned by the singular vectors v_i whose maximum value of $H(\omega \cdot v_i)$ for $0 \leq \omega \leq 1$ is smaller than 0.05. The computed values of the identifiability index for each of the model currents are given in the orange box on the right-hand side of Figure 7. A value of k close to 1 indicates a high degree of identifiability, while a value of k close to 0 indicates an unidentifiable current.

From the indices in Figure 7, we see that I_{CaL}, I_{Kr}, and I_{NaCa} are highly identifiable in the immature base model, but that the currents I_{NaL}, I_{Na}, I_{bCa}, I_{Ks}, and I_{bCl} are less than 50% identifiable. As a consequence, we fix the conductance of I_{Na}, I_{bCa}, I_{Ks}, and I_{bCl} in the applications of the inversion procedure presented below. In addition, we are aware that the I_{NaL} current might be hard to identify, and that estimated drug effects for this current are associated with a level of uncertainty.

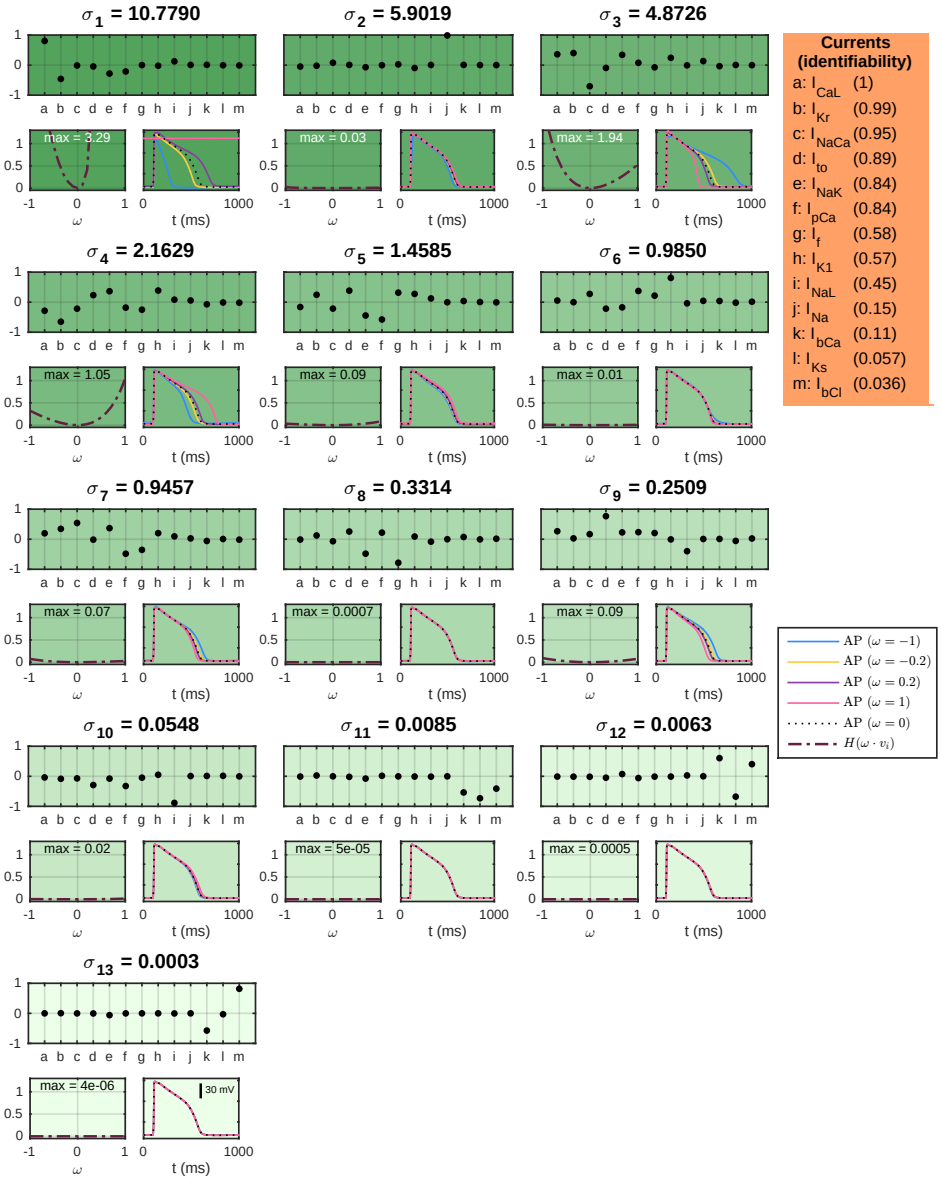

Figure 7: SVD analysis of the currents in the immature base model. The titles above each plot give the singular values of the current matrix A, and the upper plots show the corresponding singular vectors. The below plots show how a perturbation of the currents corresponding to the singular vector affects the computed AP for a few examples (right) and measured by a cost function (left). The identifiability index (92) of each current is given in the orange panel.

3.2 Identification of drug effects on hiPSC-CMs based on simulated data

Our first application on the inversion procedure for identifying drug effects will be to use the method to identify drug effects based on simulated data. To generate the data, we set $\lambda_{\mathrm{CaL}} = \lambda_{\mathrm{NaL}} = \lambda_{\mathrm{Kr}} = 0.1$ in the immature version of the base model. In addition, we apply a set of ε-values to represent five specific drugs – Nifedipine, Lidocaine, Cisapride, Flecainide, and Verapamil. We assume that Nifedipine is a pure I_{CaL}-blocker with an IC50-value of 10 nM, that Lidocaine is a pure I_{NaL}-blocker with an IC50-value of 10 μM, and that Cisapride is a pure I_{Kr}-blocker with an IC50-value of 10 nM. Furthermore, Flecainide is assume to block a combination of all the three currents with IC50-values of 25 μM, 20 μM and 10 μM for I_{CaL}, I_{NaL}, and I_{Kr}, respectively. Verapamil is assumed to block I_{CaL} with an IC50-value of 200 nM and I_{Kr} with an IC50-value of 500 nM. Both when the data is generated and in the inversion procedure, we record the sixth generated AP after each parameter change.

Figure 8 shows the result of the inversion procedure using the λ-values λ_{CaL}, λ_{NaL}, and λ_{Kr} and the ε-values $\varepsilon_{\mathrm{CaL}}$, $\varepsilon_{\mathrm{NaL}}$, and $\varepsilon_{\mathrm{Kr}}$ as free parameters in the inversion procedure. The left panel shows the ε-values used to generate the data (yellow) and the corresponding ε-values returned by the inversion procedure (pink). The center and right panels show the action potential and calcium transient, respectively, for the control case and for each of the drug doses included in the data sets. The solid lines show the simulated data and the dotted lines show the solutions generated by the model using the λ- and ε-values returned by the inversion procedure. Note that to clearly see differences in the calcium transient amplitude, the calcium transients are adjusted so that the calcium transient amplitude is preserved, but the minimum calcium concentration is set to zero. We observe that the inversion procedure is able to identify the correct ε-values quite accurately, except that the ε-value for Lidocaine is predicted to be considerably lower than the value used to generate the data. This suggests that it might be difficult to obtain correct values of $\varepsilon_{\mathrm{NaL}}$, as also supported by the low identifiability index for I_{NaL} reported in Figure 7. In addition, we observe that the inversion procedure predicts some block of I_{NaL} for the drug Cisapride, even though only I_{Kr} was blocked when the data was generated.

3.3 Identification of drug effects on hiPSC-CMs based on optical measurements

In this section, we use the inversion procedure outlined above to identify the effect of drugs from optical measurements of the action potential and calcium transient of hiPSC-CMs.

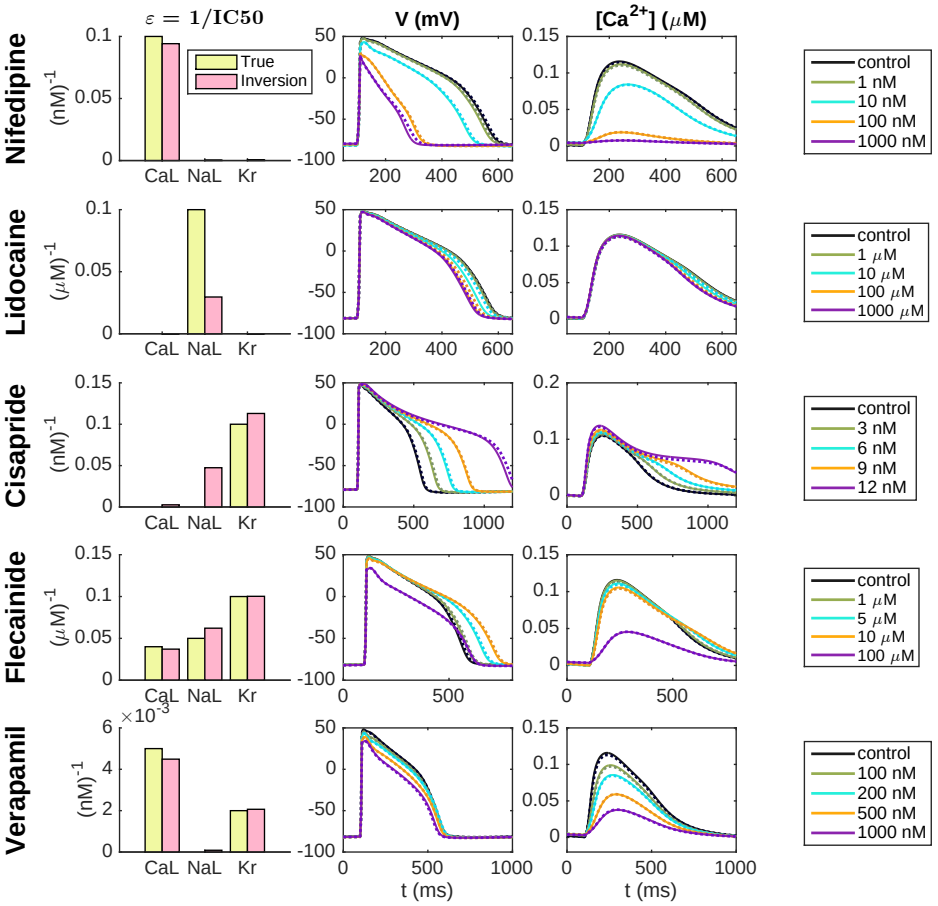

Figure 8: Identification of drug effects for five drugs based on simulated data. The λ-values λ_{CaL}, λ_{NaL}, and λ_{Kr} and the ε-values $\varepsilon_{\mathrm{CaL}}$, $\varepsilon_{\mathrm{NaL}}$, and $\varepsilon_{\mathrm{Kr}}$ are allowed to vary in the inversion. The left panel shows the ε-values used to generate the simulated drug data (yellow) and the corresponding ε-values estimated by the inversion procedure (pink). The center and right panels show the membrane potential and calcium transients, respectively, for each of the drug doses included in the data sets. The solid lines represent the simulated data and the dotted lines show the fitted model solutions returned by the inversion procedure. Note that to clearly see changes in the calcium transient amplitude, the calcium transients are adjusted so that the calcium transient amplitude is preserved, but the minimum value is set to zero in all cases.

3.3.1 Nifedipine

Figure 9 shows the result of the inversion procedure applied to data from optical measurements of hiPSC-CMs exposed to the drug Nifedipine. The data includes the control case with no drug present and four different drug doses (3 nM, 30 nM, 300 nM, and 3000 nM). The left panel of Figure 9A shows the voltage and calcium traces obtained from optical measurements, and the center panel shows the corresponding solutions of the immature version of the base model fitted to the optical measurements. Note that the values of the data are mapped so that the maximum and minimum values of the membrane potential and calcium concentration match those of the fitted immature model. Panel C of Figure 9 shows a comparison between the data and the fitted model for each of the doses. We observe that the model seems to fit both the voltage and the calcium data quite well for most of the doses, but that the calcium transient appears to last a bit longer in the model than in the data for the highest considered drug doses.

The dose-dependent effect of the drug on the I_{CaL}, I_{NaL} and I_{Kr} currents are modeled using IC50-values like explained in Section 2.4.2. The values of $\varepsilon_i = \frac{1}{\text{IC50}_i}$ for $i = \text{CaL}$, NaL, and Kr are given in Figure 9B. A large value of ε_i corresponds to a large drug effect on the current i, and a small value of ε_i corresponds to a small drug effect on the current i. From Figure 9B, we observe that the inversion procedure predicts that Nifedipine primarily blocks I_{CaL}. The IC50-values corresponding to the estimated ε-values are given in Table 4. Here, we observe that the IC50-value for I_{CaL} is estimated to be 38 nM, in agreement with values found in literature (12 nM–60 nM [61, 62]). The IC50-value for I_{NaL} and I_{Kr} are estimated to be 23 600 nM and 40 200 nM, respectively — considerably larger than the doses considered in the data set. We have not found an IC50-values for I_{NaL} for comparison in literature, but the IC50-values found for I_{Kr} support the claim that the IC50-value is much larger than the drug doses included in the data set, although the literature values (275 000–440 000 nM [63, 61]) are even higher than the value predicted by the inversion procedure.

3.3.2 Lidocaine

Figure 10 shows similar results for inversion of measurements of hiPSC-CMs exposed to the drug Lidocaine. In panel A, we observe that the action potential duration is reduced by the drug, and in panel B, we observe that the inversion procedure predicts that the drug primarily blocks the I_{NaL} current. In Table 4, we see that the IC50-value for I_{NaL} is estimated to be 4.3 μM, in rough agreement with the value 11 μM found in literature [42]. Panel C of Figure 10 shows comparisons of the data and the fitted model for each of the doses included in the data set. We observe that the model fits the data quite well, but that the action potential duration for a drug dose of 10 μM seem to be longer in the model than in the data.

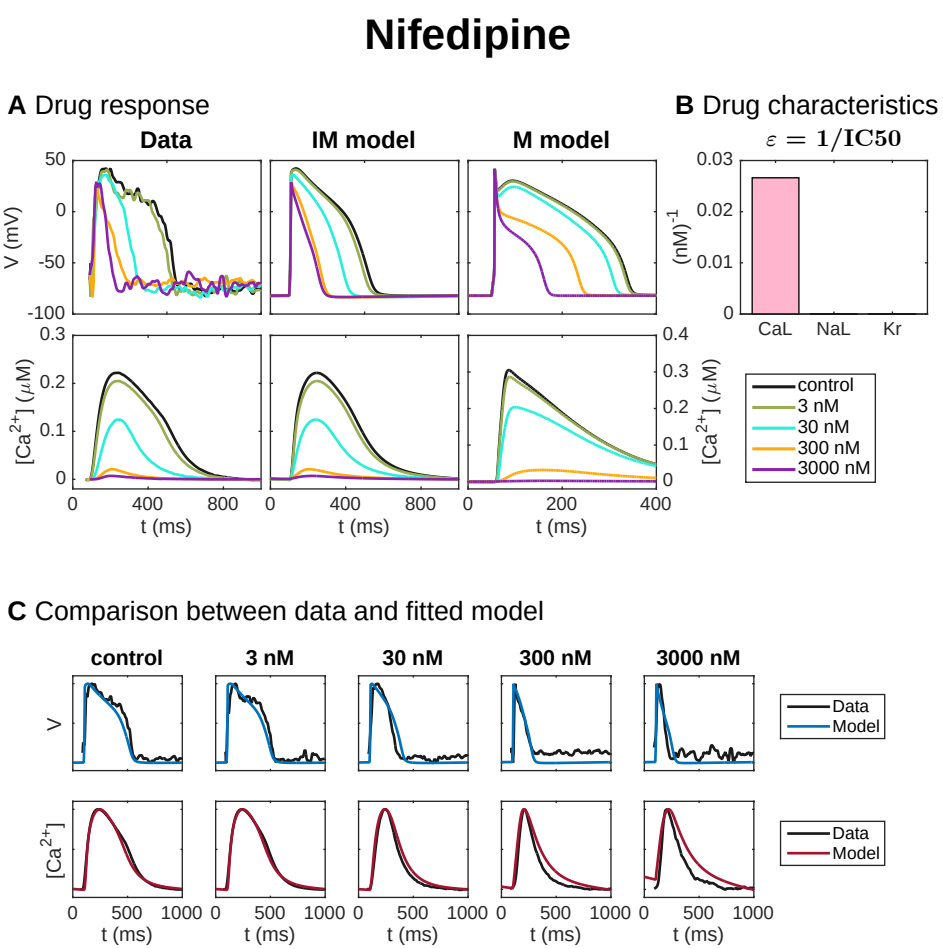

Figure 9: Identification and mapping of drug effects for the drug Nifedipine based on optical measurements of the action potential and calcium transient of hiPSC-CMs. A: Action potential and calcium transient in the control case and for four drug doses for the data (left) and the fitted immature (IM) model (center). The predicted drug effects for mature (M) cells are given in the right panel (note that the scaling of the axes is adjusted for the M case). Note also that to clearly see differences in the calcium transient amplitude, the displayed calcium concentrations are adjusted so that the calcium transient amplitude is preserved, but the resting concentration is set to zero in each case. B: Drug effect on I_{CaL}, I_{NaL} and I_{Kr} in the form of ε-values estimated by the inversion procedure. C: Comparison between the voltage and calcium traces and the fitted immature model solutions for each of the doses in the data set.

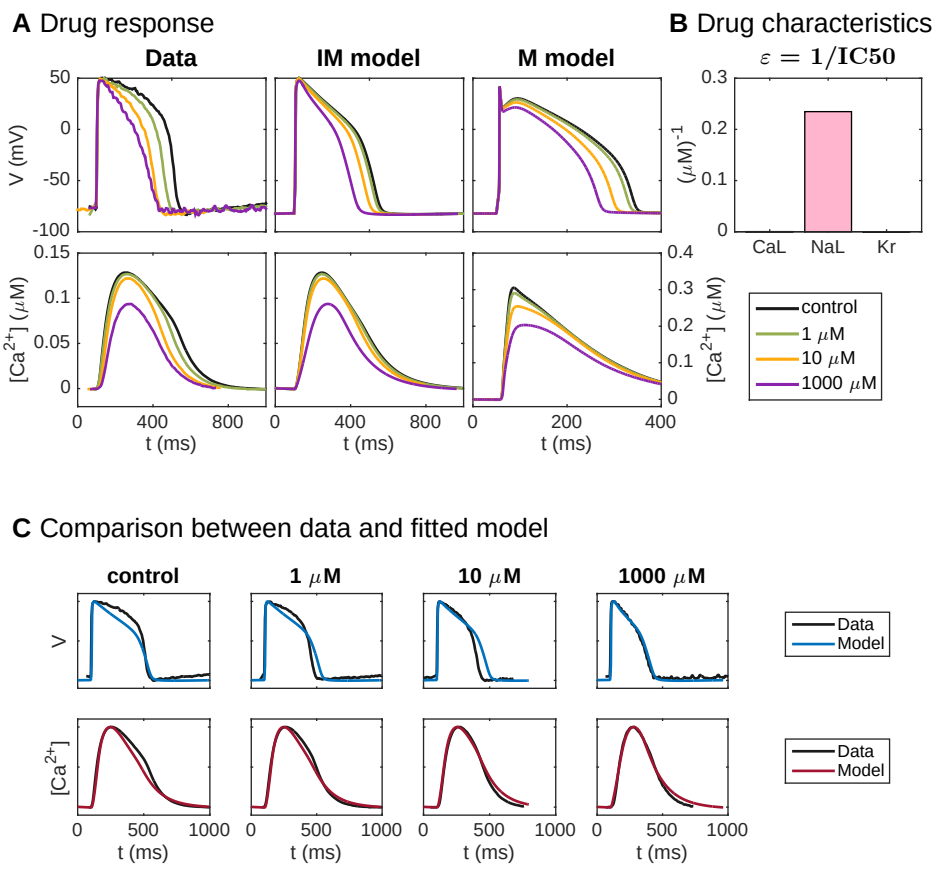

Figure 10: Identification and mapping of drug effects for the drug Lidocaine based on optical measurements of the action potential and calcium transient of hiPSC-CMs following the same structure as Figure 9.

3.3.3 Cisapride

Figure 11 shows the result of the inversion procedure applied to a data set for hiPSC-CMs exposed to the drug Cisapride. In panel A, we observe that the drug increases the action potential duration. However, for the drug dose of 1 nM, we observe that the prolongation of the action potential duration is much more prominent in the data than in the fitted immature model. This is also confirmed in panel C, where we observe that the model does not fit the voltage data for the control case and the 1 nM dose case very well. The fit for the largest dose, on the other hand, seems to be quite good. In panel B, we observe that the inversion procedure predicts that Cisapride primarily blocks the I_{Kr} current. Furthermore, in Table 4, we observe that the IC50-value is estimated to be 13 nM, in good agreement with values found in literature (6.5 nM–20 nM [64, 61, 42]).

3.3.4 Flecainide

Figure 12 shows the result for the inversion procedure applied to optical measurements of hiPSC-CMs exposed to the drug Flecainide. In panel A, we observe that the drug appears to lead to an increased action potential duration. In panel C, we observe that the fitted model seems to fit the data quite well, except that the action potential duration at high percentages of repolarization is longer for the data than for the model for the highest considered dose. In addition, the shape of the calcium transient for the low doses does not seem to be entirely captured in the model.

In panel B, we observe that the inversion procedure estimates that the drug primarily blocks I_{Kr} and to some degree I_{CaL}. In Table 4, we observe that the IC50-value for I_{Kr} predicted by the inversion procedure (1.9 μM) is in quite good agreement with literature values (0.7-1.5 μM [42, 61]), but that the predicted IC50-value for I_{CaL} (9 μM) is too low compared to the reported literature values (26-27 μM [42, 61]). In addition, the estimated IC50-value for I_{NaL} (47 μM) is larger than the literature value of 19 μM [42].

3.3.5 Verapamil

Figure 13 shows the result of the inversion procedure applied to measurements of hiPSC-CMs exposed to the drug Verapamil. In panel A, we observe that the drug appears to lead to a decreased action potential duration. However, the effect on the action potential duration for the smallest considered dose (100 nM) appears to be more prominent in the data than in the fitted model. This is also confirmed in panel C, where we observe that the fitted model seems to fit the calcium data considerably better than the voltage data. In particular, the action potential duration seem to be too short in the control case and too long for the dose of 100 nM.

Panel B shows that the inversion procedure predicts that Verapamil primarily blocks I_{CaL} and to some extent I_{Kr}. In Table 4, we observe that the IC50-values of I_{CaL} and I_{Kr} are estimated to be 495 nM and 2150 nM, respectively. These

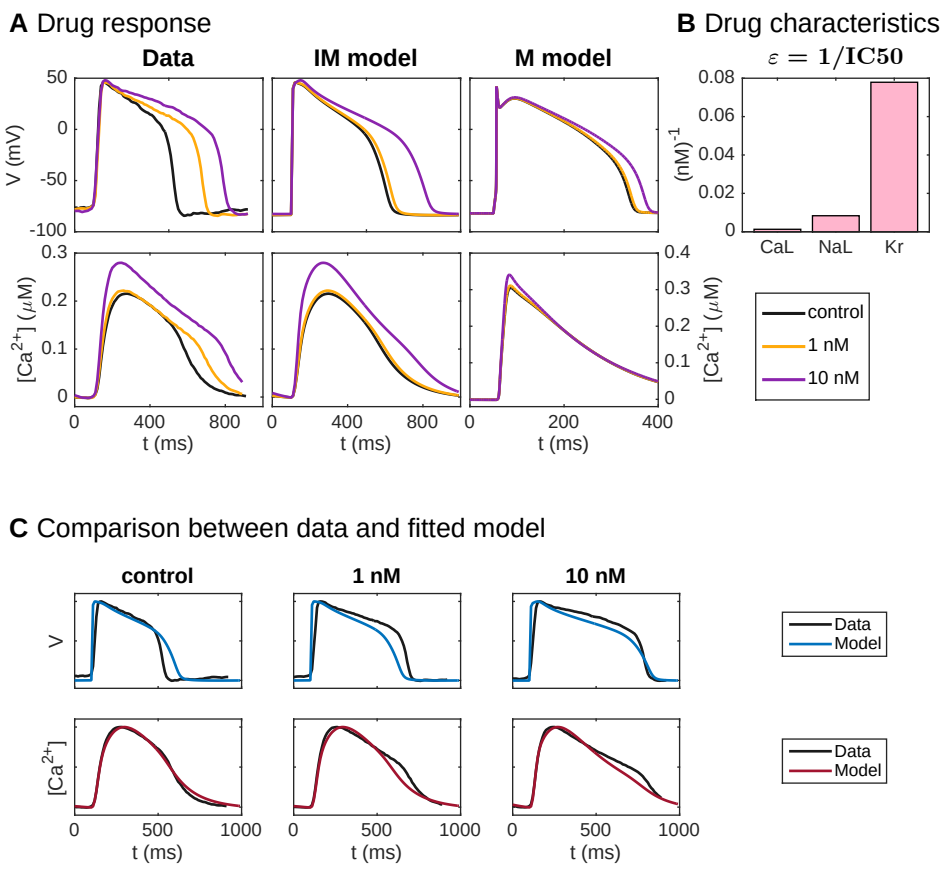

Figure 11: Identification and mapping of drug effects for the drug Cisapride based on optical measurements of the action potential and calcium transient of hiPSC-CMs following the same structure as Figure 9.

		Nifedipine	Lidocaine	Cisapride	Flecainide	Verapamil
CaL	**Inversion**	**38 nM**	**3400 μM**	**775 nM**	**9 μM**	**495 nM**
	Literature	12 nM [61]		11 800 nM	26 μM [42]	202 nM [42]
		60 nM [62]		[61]	27 μM [61]	200 nM [61]
						100 nM [65]
NaL	**Inversion**	**23 600 nM**	**4.3 μM**	**120 nM**	**47 μM**	**23 000 nM**
	Literature		11 μM [42]		19 μM [42]	
Kr	**Inversion**	**40 200 nM**	**50 000 μM**	**13 nM**	**1.9 μM**	**2150 nM**
	Literature	440 000 nM [61]		12 nM [42]	0.7 μM [42]	499 nM [42]
		275 000 nM [63]		20 nM [61]	1.5 μM [61]	250 nM [61]
				6.5 nM [64]		143 nM [66]

Table 4: Comparison between the IC50-values obtained from the inversion procedure and values found in literature.

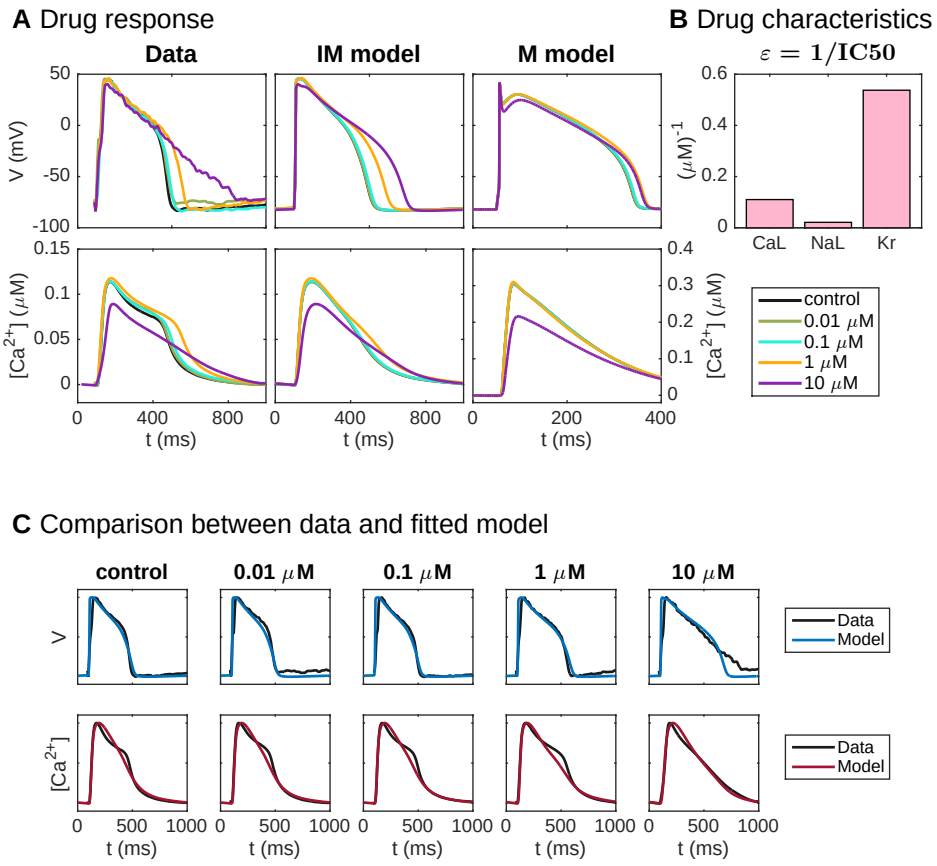

Figure 12: Identification and mapping of drug effects for the drug Flecainide based on optical measurements of the action potential and calcium transient of hiPSC-CMs following the same structure as Figure 9.

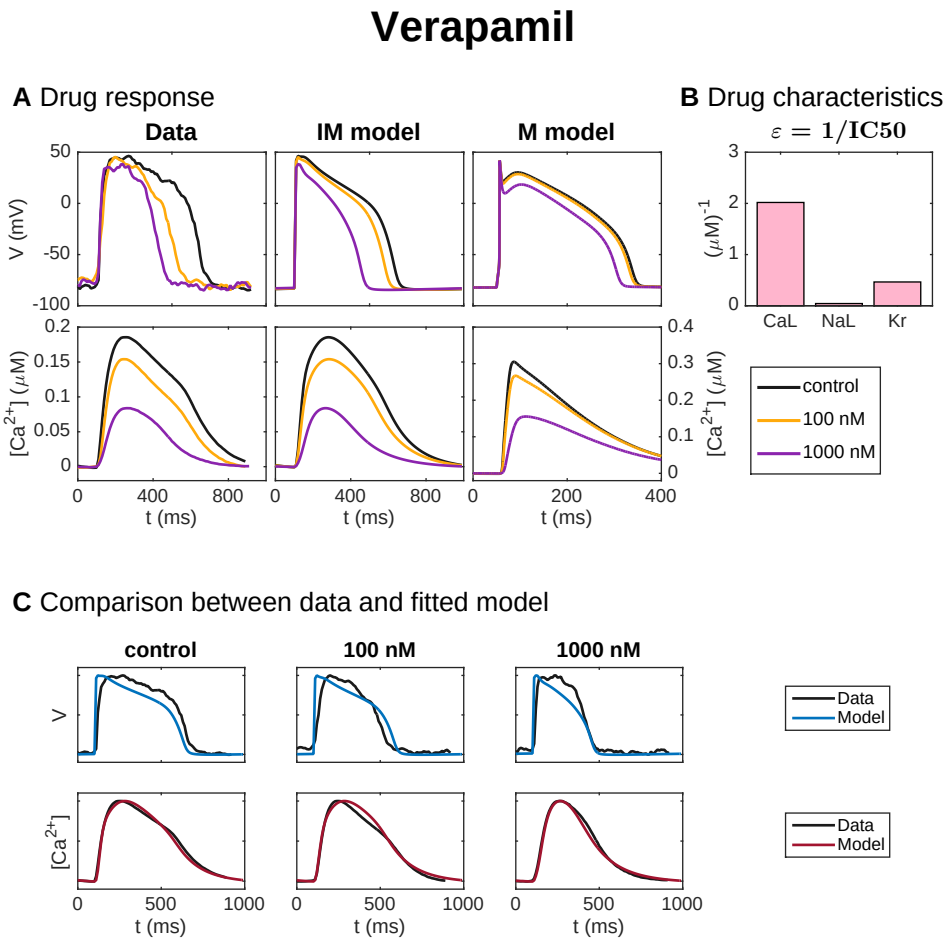

Figure 13: Identification and mapping of drug effects for the drug Verapamil based on optical measurements of the action potential and calcium transient of hiPSC-CMs following the same structure as Figure 9.

values are both higher than the corresponding literature values (100–202 nM for I_{CaL} [65, 61, 42] and 143–499 nM for I_{Kr} [66, 61, 42]).

3.4 Mapping of drug effects from hiPSC-CMs to mature cells

The rightmost plots of panel A of Figures 9–13 show the predicted drug effects for mature cells for each of the considered drugs. More specifically, the plots show the solution of the mature base model exposed to the drug effects (ε-values) estimated by the inversion procedure for each of the drug doses included in the data set. In other words, this represents the predicted drug response for a mature action potential and calcium transient exposed to each of the drugs, based on the optical measurements of the membrane potential and calcium transient conducted for hiPSC-CMs. The predictions are made by first using the inversion procedure to estimate the effect of the drug on the I_{CaL}, I_{NaL}, and I_{Kr} currents in the immature case and then mapping the corresponding drug effects up to a mature cell using the maturation map based on the assumptions of differences in the protein densities and geometry of immature and mature cells (see Section 2).

4 Discussion

In this paper, we have presented a procedure for estimating drug effects for mature cells based on optical measurements of the action potential and calcium transient of hiPSC-CMs. The procedure is based on the method introduced in [16], and the aim of the current paper is to improve several aspects of the methodology from [16]. First, we introduce a new base model formulation for representing mature and immature cells. In particular, the model of the intracellular calcium dynamics is updated to a formulation constructed to be stable with respect to parameter changes. In addition, we use an IC50-based modeling of dose-dependent drug effects and find the optimal parameters by running a coupled inversion of both the control data and data for several drug doses. We have also updated the definition of the cost function measuring the difference between the data and the model, and we apply a continuation-based minimization method to minimize the cost function.

In the formulation of the base model, one of the main challenges was associated with formulating a model for the release of Ca^{2+} from the SR that was stable with respect to parameter changes. These challenges are discussed in more detail below.

Since we plan to conduct more work improving the base model and inversion procedure before submitting the paper for publication, the results reported in the current version of the paper might not be included in the final version of the paper. Therefore, we have chosen not to include a discussion of the obtained results in this preliminary version of the manuscript.

4.1 Modeling the intracellular Ca^{2+} dynamics

The inversion algorithm (see above) requires many thousand simulations testing different parameters. The parameters of the model represent geometrical properties and protein densities, either in terms of membrane channels, exchangers and pumps or in terms of channels, pumps or buffers involved in the intracellular Ca^{2+} machinery. In order for the inversion to work properly, it is essential that the AP model is stable with respect to variations in the parameters. In particular, it is important that the simulation doesn't break down because of instabilities in the model.

Modeling the intracellular Ca^{2+} dynamics of cardiac cells has been a long-standing challenge and a very active field of research for at least 40 years; for reviews see e.g., [59, 67, 68, 69, 70]. The Ca^{2+} dynamics is a complex time-dependent, 3D and highly non-linear problem. Mathematical models have attempted to represent the dynamics using a system of ordinary differential equations. Essentially, the goal of these models has been to remove the spatial variance and compute solutions that are spatially averaged and therefore merely depend on time. The main motivation for this strategy is to achieve models that are practical to work with in terms of computational complexity. But the strategy has run into serious modeling challenges that have been addressed with ingenuity in numerous models (see e.g., [71, 72, 73, 74, 75, 76, 46, 77, 59]). Also spatial models (see e.g., [78, 79, 80, 81]) and homogenized spatial models (see e.g., [82, 83, 84, 85, 86]) have been applied and these models clearly capture the intricate dynamics more convincingly, but at a computational cost that renders them impracticable for the purpose of this study: Many thousand simulations with spatially resolved 3D models of the Ca^{2+} dynamics of cardiac cells is presently not possible on any computer. In this section, we will discuss some important concepts involved in the intracellular Ca^{2+} dynamics of cardiac cells and some of the previously introduced modeling approaches for these dynamics.

4.1.1 Calcium-induced calcium release (CICR)

In the early phase of the upstroke of the AP, the membrane potential increases sufficiently for the voltage sensitive dihydropyridine receptors (DHPR) to open the L-type calcium channels on the membrane. Because of the huge gradient in the Ca^{2+} concentration between the intracellular and extracellular spaces, Ca^{2+}-ions cross the membrane and flow into the cell. Inside the cell, the Ca^{2+} enters a tiny dyad (see Figure 2) located between the cell membrane and the sarcoplasmic reticulum (SR). Since the dyad is very small, the Ca^{2+} concentration increases rapidly and the increased concentration is sensed by the ryanodine receptors (RyRs) which in turn open and allow large amounts of Ca^{2+} to flow out of the SR. The increased Ca^{2+} concentration spreads by diffusion and recruits other RyRs to open and thus even more Ca^{2+} is poured into the bulk cytosolic space. This process is usually referred to as calcium-induced calcium release (CICR), and it takes place in many thousand local calcium release units (CRUs) close to the cell membrane (see e.g., [87, 88, 58, 78]).

4.1.2 High gain and graded release

The CICR is designed to provide both *high gain* and *graded release* (see e.g., [58, 59]). High gain means that, even when only a small amount of Ca^{2+} enters the cell through the cell membrane, this small amount leads to release of a much larger amount of Ca^{2+} from the SR. However, the release is also graded (see e.g., [89, 90, 87, 58, 59]) in the sense that the release of Ca^{2+} from the SR into the bulk cytosolic space depends continuously on the amount of Ca^{2+} flowing into the cell through the channels on the cell membrane. In other words, the amount of Ca^{2+} flowing into the cytosol during an AP is believed to be controlled by the flow through the membrane calcium channels, even if most of the Ca^{2+} is released from the internal storage structures (the SR).

4.1.3 Restoring the Ca^{2+} concentration

The AP is periodic and at the end of one cycle, all variables are brought back to the repolarized state of the cell. Ca^{2+} is pumped back to SR by the SERCA (sarcoplasmic reticulum Ca^{2+}ATPase) pump, and back to the extracellular space through the membrane calcium pump and the sodium-calcium exchanger.

4.1.4 Common pool models

A standard approach to modeling CICR is illustrated in Figure 14. Here, the dynamics of the many CRUs is modeled by one representative unit, hence all CRUs are assumed to be in the same state. In the model, Ca^{2+} enters the dyad through L-type calcium channels, which leads to an increased dyadic Ca^{2+} concentration, and thus the RyRs open and Ca^{2+} leaves the SR. Models of the form illustrated in Figure 14 is referred to as *common pool models* and are characterized by the fact that Ca^{2+} released through the RyRs (from the SR) enters the same, small, dyadic space that Ca^{2+} enters through the L-type calcium channel. It has been known for a long time (see [71]) that it is impossible to obtain graded release using stable common pool models. The problem is that when the release of Ca^{2+} from the SR has started, the release from the SR will itself cause an increased dyadic Ca^{2+} concentration, and release will continue until some inactivation mechanism of the release (e.g., a sufficiently decreased SR Ca^{2+} concentration [44]) kicks in. Consequently, the release becomes an *all or nothing* process, depending only on whether the amount of Ca^{2+} entering the dyad through L-type calcium channels is enough to trigger release. Therefore, graded release cannot be obtained using a model of the form given in Figure 14.

4.1.5 Local control models

The difficulties associated with the common pool models can be circumvented by allowing many CRUs in the model (see e.g., [78, 79, 58, 80]). By introducing a large number of CRUs that are weakly coupled and where the release mechanisms are governed by stochastic Markov models, it is possible to achieve both high gain

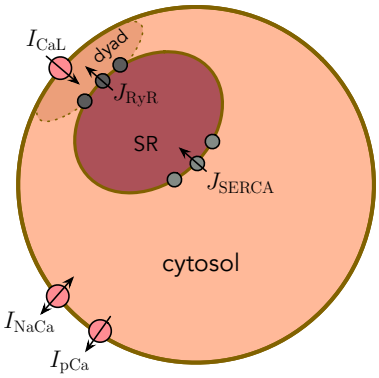

Figure 14: A prototypical sketch of common pool model with Ca^{2+} flowing into the dyad through L-type calcium channels; the RyR-channels are activated when the Ca^{2+} concentration increases, and Ca^{2+} is transported back to the SR from the cytosol via the SERCA pumps and back to the extracellular space through the sodium-calcium exchangers and the calcium pumps on the cell membrane.

and graded release. Suppose there are $\sim$ 20.000 CRUs (as suggested in [80]) and every CRU has the elements illustrated in Figure 14 where the release mechanism of the L-type Calcium channel and the RyR are governed by Markov models. For simplicity we assume that the open probability of the L-type calcium channels and the RyRs increases with increasing membrane potential and increasing dyadic Ca^{2+} concentration, respectively. Then, when the voltage increases slightly, the open probability of the L-type calcium channels increases sufficiently for a few membrane channels to open, and thus calcium will flow into the dyad of the associated CRUs. Locally, in these CRUs, the increased dyadic Ca^{2+} concentration will lead to increased open probability of the RyRs and when these channels open, the local SR of that particular CRU will be emptied. When the membrane potential increases more, the number of active CRUs will increase, and thus, the release will be graded by the voltage. So even if every single CRU is an all or nothing process, the integrated process is controlled by the membrane potential. Unfortunately, since these models requires a large number of CRUs, the computational cost of these models is prohibitive for our purposes.

4.1.6 CICR in the base model

In the base model introduced above, we introduce two main modeling assumptions to obtain a model that exhibits both high gain and graded release without the high computational costs of the local control models. First, the Ca^{2+} released from the SR is not released into the dyad, but is instead directed into a separate subsarcolemmal (SL) space. By directing the Ca^{2+} into this space, the Ca^{2+} entering the dyad though the membrane calcium channels are clearly distinguishable from that released from the SR, and we avoid the graded-release problem associated with the common pool models. In addition, instead of inactivating the release from the SR by a decreased SR Ca^{2+} concentration, we introduce an assumption that each channel can only release a certain amount of Ca^{2+} during an AP cycle. This is done because the SR Ca^{2+} concentration can potentially vary significantly for the large parameter changes considered in the inversion procedure. In Figure 6, we observe that the model constructed from these modeling assumptions exhibits both high gain and graded release for the immature and mature versions of the parameters. Note, however, that the assumptions are introduced to obtain a stable model, and not necessarily to represent the underlying physiological mechanisms accurately.

4.2 Identification of drug effects based on simulated data and optical measurements of hiPSC-CMs

The results obtained from the inversion of simulated data and optical measurements will be discussed in the final version of the manuscript.

References

[1] Yoshinori Yoshida and Shinya Yamanaka. Induced pluripotent stem cells 10 years later. *Circulation Research*, 120(12):1958–1968, 2017.

[2] Angela Di Baldassarre, Elisa Cimetta, Sveva Bollini, Giulia Gaggi, and Barbara Ghinassi. Human-induced pluripotent stem cell technology and cardiomyocyte generation: Progress and clinical applications. *Cells*, 7(6):48, 2018.

[3] Lingqun Ye, Xuan Ni, Zhen-Ao Zhao, Wei Lei, and Shijun Hu. The application of induced pluripotent stem cells in cardiac disease modeling and drug testing. *Journal of Cardiovascular Translational Research*, 11(5):366–374, 2018.

[4] Anurag Mathur, Zhen Ma, Peter Loskill, Shaheen Jeeawoody, and Kevin E Healy. In vitro cardiac tissue models: current status and future prospects. *Advanced Drug Delivery Reviews*, 96:203–213, 2016.

[5] Barry Fine and Gordana Vunjak-Novakovic. Shortcomings of animal models and the rise of engineered human cardiac tissue. *ACS Biomaterials Science & Engineering*, 3(9):1884–1897, 2017.

[6] Klaus Christensen, Filip Roudnicky, Christoph Patsch, and Mark Burcin. Requirements for using ipsc-based cell models for assay development in drug discovery. In Ulrich Martin, Robert Zweigerdt, and Ina Gruh, editors, *Engineering and Application of Pluripotent Stem Cells*, pages 207–220. Springer International Publishing, Cham, 2018.

[7] Cristina Mora, Marialaura Serzanti, Antonella Consiglio, Maurizio Memo, and Patrizia Dell'Era. Clinical potentials of human pluripotent stem cells. *Cell Biology and Toxicology*, 33(4):351–360, 2017.

[8] Kacey Ronaldson-Bouchard, Stephen P Ma, Keith Yeager, Timothy Chen, LouJin Song, Dario Sirabella, Kumi Morikawa, Diogo Teles, Masayuki Yazawa, and Gordana Vunjak-Novakovic. Advanced maturation of human cardiac tissue grown from pluripotent stem cells. *Nature*, 556(7700):239, 2018.

[9] Zhihan Zhao, Huan Lan, Ibrahim El-Battrawy, Xin Li, Fanis Buljubasic, Katherine Sattler, Gökhan Yücel, Siegfried Lang, Malte Tiburcy, Wolfram-Hubertus Zimmermann, et al. Ion channel expression and characterization in human induced pluripotent stem cell-derived cardiomyocytes. *Stem Cells International*, 2018, 2018.

[10] Anurag Mathur, Peter Loskill, Kaifeng Shao, Nathaniel Huebsch, SoonGweon Hong, Sivan G Marcus, Natalie Marks, Mohammad Mandegar, Bruce R Conklin, Luke P Lee, and Kevin E Healy. Human iPSC-based cardiac microphysiological system for drug screening applications. *Scientific Reports*, 5:8883, 2015.

[11] Bertil Hille. *Ion channels of excitable membranes*, volume 507. Sinauer Sunderland, MA, 2001.

[12] Harald Sontheimer, Bruce R Ransom, and Stephen G Waxman. Different Na^+ currents in P0-and P7-derived hippocampal astrocytes in vitro: evidence for a switch in Na^+ channel expression in vivo. *Brain Research*, 597(1):24–29, 1992.

[13] William J Moody and Martha M Bosma. Ion channel development, spontaneous activity, and activity-dependent development in nerve and muscle cells. *Physiological Reviews*, 85(3):883–941, 2005.

[14] Fikru B Bedada, Matthew Wheelwright, and Joseph M Metzger. Maturation status of sarcomere structure and function in human iPSC-derived cardiac myocytes. *Biochimica et Biophysica Acta (BBA)-Molecular Cell Research*, 1863(7):1829–1838, 2016.

[15] Ping Liang, Feng Lan, Andrew S Lee, Tingyu Gong, Veronica Sanchez-Freire, Yongming Wang, Sebastian Diecke, Karim Sallam, Joshua W Knowles, Patricia K Nguyen, et al. Drug screening using a library of human induced pluripotent stem cell-derived cardiomyocytes reveals disease specific patterns of cardiotoxicity. *Circulation*, (127):1677–1691, 2013.

[16] Aslak Tveito, Karoline H Jæger, Nathaniel Huebsch, Berenice Charrez, Andrew G Edwards, Samuel Wall, and Kevin E Healy. Inversion and computational maturation of drug response using human stem cell derived cardiomyocytes in microphysiological systems. *Scientific Reports*, 8(1):17626, 2018.

[17] Colleen E Clancy, Zheng I Zhu, and Yoram Rudy. Pharmacogenetics and anti-arrhythmic drug therapy: A theoretical investigation. *AJP: Heart and Circulatory Physiology*, 292(1):H66–H75, 2007.

[18] Vladimir Yarov-Yarovoy, Toby W Allen, and Colleen E Clancy. Computational models for predictive cardiac ion channel pharmacology. *Drug Discovery Today: Disease Models*, 14:3–10, 2014.

[19] Colleen E Clancy, Gary An, William R Cannon, Yaling Liu, Elebeoba E May, Peter Ortoleva, Aleksander S Popel, James P Sluka, Jing Su, Paolo Vicini, et al. Multiscale modeling in the clinic: drug design and development. *Annals of Biomedical Engineering*, 44(9):2591–2610, 2016.

[20] Aslak Tveito and Glenn T Lines. *Computing Characterizations of Drugs for Ion Channels and Receptors Using Markov Models*. Springer-Verlag, Lecture Notes, vol. 111, 2016.

[21] Aslak Tveito, Glenn T Lines, Andrew G Edwards, and Andrew D McCulloch. Computing rates of Markov models of voltage-gated ion channels by inverting partial differential equations governing the probability density functions of the

conducting and non-conducting states. *Mathematical Biosciences*, (277):126–135, 2016.

[22] Thomas O'Hara, László Virág, András Varró, and Yoram Rudy. Simulation of the undiseased human cardiac ventricular action potential: Model formulation and experimental validation. *PLoS Computational Biology*, 7(5):e1002061, 2011.

[23] Eleonora Grandi, Francesco S Pasqualini, and Donald M Bers. A novel computational model of the human ventricular action potential and Ca transient. *Journal of Molecular and Cellular Cardiology*, 48(1):112–121, 2010.

[24] Yoram Rudy and Jonathan R Silva. Computational biology in the study of cardiac ion channels and cell electrophysiology. *Quarterly Reviews of Biophysics*, 39(01):57–116, 2006.

[25] Zhilin Qu, Gang Hu, Alan Garfinkel, and James N Weiss. Nonlinear and stochastic dynamics in the heart. *Physics Reports*, 543(2), 2014.

[26] Yoram Rudy. From genes and molecules to organs and organisms: Heart. *Comprehensive Biophysics*, pages 268–327, 2012.

[27] Alfio Quarteroni, Toni Lassila, Simone Rossi, and Ricardo Ruiz-Baier. Integrated heart—coupling multiscale and multiphysics models for the simulation of the cardiac function. *Computer Methods in Applied Mechanics and Engineering*, 314:345–407, 2017.

[28] Piero C Franzone, Luca F Pavarino, and Simone Scacchi. *Mathematical cardiac electrophysiology*, volume 13. Springer, 2014.

[29] Andrew G Edwards and William E Louch. Species-dependent mechanisms of cardiac arrhythmia: a cellular focus. *Clinical Medicine Insights: Cardiology*, 11:1179546816686061, 2017.

[30] Aslak Tveito, Karoline H Jæger, Miroslav Kuchta, Kent-Andre Mardal, and Marie E Rognes. A cell-based framework for numerical modeling of electrical conduction in cardiac tissue. *Frontiers in Physics*, 5:48, 2017.

[31] CellML Model Repository. www.cellml.org/models/.

[32] Michelangelo Paci, Jari Hyttinen, Katriina Aalto-Setälä, and Stefano Severi. Computational models of ventricular-and atrial-like human induced pluripotent stem cell derived cardiomyocytes. *Annals of Biomedical Engineering*, 41(11):2334–2348, 2013.

[33] Michelangelo Paci, Jari Hyttinen, Blanca Rodriguez, and Stefano Severi. Human induced pluripotent stem cell-derived versus adult cardiomyocytes: an *in silico* electrophysiological study on effects of ionic current block. *British Journal of Pharmacology*, 172(21):5147–5160, 2015.

[34] Michelangelo Paci, Elisa Passini, Stefano Severi, Jari Hyttinen, and Blanca Rodriguez. Phenotypic variability in lqt3 human induced pluripotent stem cell-derived cardiomyocytes and their response to anti-arrhythmic pharmacological therapy: an in silico approach. *Heart Rhythm*, 2017.

[35] Michelangelo Paci, Risto-Pekka Pölönen, Dario Cori, Kirsi Penttinen, Katriina Aalto-Setälä, Stefano Severi, and Jari Hyttinen. Automatic optimization of an *in silico* model of human iPSC derived cardiomyocytes recapitulating calcium handling abnormalities. *Frontiers in Physiology*, 9, 2018.

[36] Herbert B Keller. Lectures on numerical methods in bifurcation problems. *Applied Mathematics*, 217:50, 1987.

[37] Eugene L Allgower and Kurt Georg. *Numerical continuation methods: an introduction*, volume 13. Springer Science & Business Media, 2012.

[38] Robert Plonsey and Roger C Barr. *Bioelectricity, A Quantitative Approach*. Springer, 2007.

[39] Eugene M Izhikevich. *Dynamical Systems in Neuroscience*. Cambridge, MA: MIT Press, 2007.

[40] G Bard Ermentrout and David H Terman. *Mathematical Foundations of Neuroscience*, volume 35. 2010.

[41] David Sterratt, Bruce Graham, Andrew Gillies, and David Willshaw. *Principles of Computational Modelling in Neuroscience*. Cambridge University Press, 2011.

[42] William J Crumb, Jose Vicente, Lars Johannesen, and David G Strauss. An evaluation of 30 clinical drugs against the comprehensive in vitro proarrhythmia assay (CiPA) proposed ion channel panel. *Journal of Pharmacological and Toxicological Methods*, 81:251 – 262, 2016. Focused Issue on Safety Pharmacology.

[43] Priyanka Garg, Vivek Garg, Rajani Shrestha, Michael C. Sanguinetti, Timothy J. Kamp, and Joseph C. Wu. Human induced pluripotent stem cell–derived cardiomyocytes as models for cardiac channelopathies. *Circulation Research*, 123(2):224–243, 2018.

[44] Eric A Sobie, M Saleet Jafri, and WJ Lederer. Models of cardiac Ca^{2+}-induced Ca^{2+} release and Ca^{2+} sparks. In Martin Falcke and Dieter Malchow, editors, *Understanding Calcium Dynamics. Experiments and Theory*. Springer-Verlag.

[45] David D Friel. $[Ca^{2+}]_i$ oscillations in sympathetic neurons: an experimental test of a theoretical model. *Biophysical Journal*, 68(5):1752–1766, 1995.

[46] Thomas R Shannon, Fei Wang, José Puglisi, Christopher Weber, and Donald M Bers. A mathematical treatment of integrated ca dynamics within the ventricular myocyte. *Biophysical Journal*, 87(5):3351–3371, 2004.

[47] James P Keener and James Sneyd. *Mathematical Physiology*. Springer, 2009.

[48] Thomas Brennan, Martin Fink, and Blanca Rodriguez. Multiscale modelling of drug-induced effects on cardiac electrophysiological activity. *European Journal of Pharmaceutical Sciences*, 36(1):62–77, 2009.

[49] Mark Ri Davies, Hitesh B Mistry, Leyla Hussein, Chris E Pollard, Jean-Pierre Valentin, Jonathan Swinton, and Najah Abi-Gerges. An in silico canine cardiac midmyocardial action potential duration model as a tool for early drug safety assessment. *American Journal of Physiology-Heart and Circulatory Physiology*, 2012.

[50] Nejib Zemzemi, Miguel O Bernabeu, Javier Saiz, Jonathan Cooper, Pras Pathmanathan, Gary R Mirams, Joe Pitt-Francis, and Blanca Rodriguez. Computational assessment of drug-induced effects on the electrocardiogram: from ion channel to body surface potentials. *British Journal of Pharmacology*, 168(3):718–733, 2013.

[51] Aslak Tveito, Glenn T Lines, Pan Li, and Andrew McCulloch. Defining candidate drug characteristics for long-qt (lqt3) syndrome. *Mathematical Biosciences and Engineering*, 8(3):861–73, 2011.

[52] Aslak Tveito, Mary M Maleckar, and Glenn T Lines. Computing optimal properties of drugs using mathematical models of single channel dynamics. *Computational and Mathematical Biophysics*, 6(1):41–64, 2018.

[53] John A Nelder and Roger Mead. A simplex method for function minimization. *The Computer Journal*, 7(4):308–313, 1965.

[54] Jörg Liesen and Volker Mehrmann. *Linear Algebra*. Springer, 2015.

[55] Tom Lyche. *Numerical Linear Algebra and Matrix Factorizations*. University of Oslo, lecture notes, 2017.

[56] Karoline H Jæger, Samuel Wall Wall, and Aslak Tveito. Detecting undetectables: Can conductances of action potential models be changed without appreciable change in the transmembrane potential? Preprint.

[57] Junyi Ma, Liang Guo, Steve J Fiene, Blake D Anson, James A Thomson, Timothy J Kamp, Kyle L Kolaja, Bradley J Swanson, and Craig T January. High purity human-induced pluripotent stem cell-derived cardiomyocytes: electrophysiological properties of action potentials and ionic currents. *American Journal of Physiology-Heart and Circulatory Physiology*, 301(5):H2006–H2017, 2011.

[58] John J Rice, M Saleet Jafri, and Raimond L Winslow. Modeling gain and gradedness of Ca^{2+} release in the functional unit of the cardiac diadic space. *Biophysical Journal*, 77(4):1871–1884, 1999.

[59] Geneviève Dupont, Martin Falcke, Vivien Kirk, and James Sneyd. *Models of calcium signalling*, volume 43. Springer, 2016.

[60] Kirsten HWJ ten Tusscher and Alexander V Panfilov. Cell model for efficient simulation of wave propagation in human ventricular tissue under normal and pathological conditions. *Physics in Medicine and Biology*, 51(23):6141, 2006.

[61] James Kramer, Carlos A Obejero-Paz, Glenn Myatt, Yuri A Kuryshev, Andrew Bruening-Wright, Joseph S Verducci, and Arthur M Brown. MICE models: superior to the HERG model in predicting Torsade de Pointes. *Scientific Reports*, 3:2100, 2013.

[62] Antonella Di Stilo, Sonja Visentin, Clara Cena, Andrea Marcello Gasco, Giuseppe Ermondi, and Alberto Gasco. New 1, 4-dihydropyridines conjugated to furoxanyl moieties, endowed with both nitric oxide-like and calcium channel antagonist vasodilator activities. *Journal of Medicinal Chemistry*, 41(27):5393–5401, 1998.

[63] Pavel Zhabyeyev, Sergiy Missan, Stephen E Jones, and Terence F McDonald. Low-affinity block of cardiac K+ currents by nifedipine. *European Journal of Pharmacology*, 401(2):137–143, 2000.

[64] Saeed Mohammad, Zhengfeng Zhou, Qiuming Gong, and Craig T January. Blockage of the HERG human cardiac K+ channel by the gastrointestinal prokinetic agent cisapride. *American Journal of Physiology-Heart and Circulatory Physiology*, 273(5):H2534–H2538, 1997.

[65] Gary R Mirams, Yi Cui, Anna Sher, Martin Fink, Jonathan Cooper, Bronagh M Heath, Nick C McMahon, David J Gavaghan, and Denis Noble. Simulation of multiple ion channel block provides improved early prediction of compounds? clinical torsadogenic risk. *Cardiovascular Research*, 91(1):53–61, 2011.

[66] Shetuan Zhang, Zhengfeng Zhou, Qiuming Gong, Jonathan C Makielski, and Craig T January. Mechanism of block and identification of the verapamil binding domain to herg potassium channels. *Circulation Research*, 84(9):989–998, 1999.

[67] Eduardo Ríos. Calcium-induced release of calcium in muscle: 50 years of work and the emerging consensus. *The Journal of General Physiology*, 150(4):521–537, 2018.

[68] Eric A Sobie, George SB Williams, and WJ Lederer. Ambiguous interactions between diastolic and SR Ca^{2+} in the regulation of cardiac Ca^{2+} release. *The Journal of General Physiology*, pages jgp–201711814, 2017.

[69] David A Eisner, Jessica L Caldwell, Kornél Kistamás, and Andrew W Trafford. Calcium and excitation-contraction coupling in the heart. *Circulation Research*, 121(2):181–195, 2017.

[70] David A Eisner. Ups and downs of calcium in the heart. *The Journal of Physiology*, 596(1):19–30, 2018.

[71] Michael D Stern. Theory of excitation-contraction coupling in cardiac muscle. *Biophysical Journal*, 63(2):497–517, 1992.

[72] Anders Nygren, Céline Fiset, Ludwik Firek, John W Clark, Douglas S Lindblad, Robert B Clark, and Wayne R Giles. Mathematical model of an adult human atrial cell: the role of K+ currents in repolarization. *Circulation Research*, 82(1):63–81, 1998.

[73] Semahat S Demir, John W Clark, C Richard Murphey, and Wayne R Giles. A mathematical model of a rabbit sinoatrial node cell. *American Journal of Physiology-Cell Physiology*, 266(3):C832–C852, 1994.

[74] Socrates Dokos, Branko Celler, and Nigel Lovell. Ion currents underlying sinoatrial node pacemaker activity: a new single cell mathematical model. *Journal of Theoretical Biology*, 181(3):245–272, 1996.

[75] José L Puglisi and Donald M Bers. LabHEART: an interactive computer model of rabbit ventricular myocyte ion channels and Ca transport. *American Journal of Physiology-Cell Physiology*, 281:2049–2060, 2001.

[76] Eric A Sobie, Keith W Dilly, Jader dos Santos Cruz, W Jonathan Lederer, and M Saleet Jafri. Termination of cardiac Ca^{2+} sparks: an investigative mathematical model of calcium-induced calcium release. *Biophysical Journal*, 83(1):59–78, 2002.

[77] Juan G Restrepo, James N. Weiss, and Alain Karma. Calsequestrin-Mediated Mechanism for Cellular Calcium Transient Alternans. *Biophysical Journal*, 95(8):3767–3789, October 2008.

[78] Michael D Stern, Gonzalo Pizarro, and Eduardo Ríos. Local control model of excitation–contraction coupling in skeletal muscle. *The Journal of General Physiology*, 110(4):415–440, 1997.

[79] Michael D Stern, Long-Sheng Song, Heping Cheng, James SK Sham, Huang Tian Yang, Kenneth R Boheler, and Eduardo Ríos. Local control models of cardiac excitation–contraction coupling: a possible role for allosteric interactions between ryanodine receptors. *The Journal of General Physiology*, 113(3):469–489, 1999.

[80] Michael Nivala, Enno de Lange, Robert Rovetti, and Zhilin Qu. Computational modeling and numerical methods for spatiotemporal calcium cycling in ventricular myocytes. *Frontiers in Physiology*, 3(114), 2012.

[81] Johan Hake, Andrew G Edwards, Zeyun Yu, Peter M Kekenes-Huskey, Anushka P Michailova, J Andrew McCammon, Michael J Holst, Masahiko Hoshijima, and Andrew D McCulloch. Modelling cardiac calcium sparks in a

three-dimensional reconstruction of a calcium release unit. *Journal of Physiology*, 590(18):4403–4422, 2012.

[82] Pranay Goel, James Sneyd, and Avner Friedman. Homogenization of the cell cytoplasm: the calcium bidomain equations. *Multiscale Modeling & Simulation*, 5(4):1045–1062, 2006.

[83] Yuhui Cheng, Zeyun Yu, Masahiko Hoshijima, Michael J Holst, Andrew D McCulloch, J Andrew McCammon, and Anushka P Michailova. Numerical analysis of Ca^{2+} signaling in rat ventricular myocytes with realistic transverse-axial tubular geometry and inhibited sarcoplasmic reticulum. *PLoS Computational Biology*, 6(10):e1000972, 2010.

[84] Pawel Swietach, Kenneth W Spitzer, and Richard D Vaughan-Jones. Modeling calcium waves in cardiac myocytes: importance of calcium diffusion. *Frontiers in Bioscience*, 15:661–680, 2010.

[85] Aslak Tveito, Glenn T Lines, Johan Hake, and Andrew G Edwards. Instabilities of the resting state in a mathematical model of calcium handling in cardiac myocytes. *Mathematical Biosciences*, 236(2):97–107, 2012.

[86] Zhilin Qu, Gang Hu, Alan Garfinkel, and James N Weiss. Nonlinear and stochastic dynamics in the heart. *Physics Reports*, 543(2):61–162, 2014.

[87] Alexandre Fabiato. Calcium-induced release of calcium from the cardiac sarcoplasmic reticulum. *American Journal of Physiology-Cell Physiology*, 245(1):C1–C14, 1983.

[88] Mark B Cannell, Heping Cheng, and William J Lederer. The control of calcium release in heart muscle. *Science*, 268(5213):1045–1049, 1995.

[89] LL Costantin and SR Taylor. Graded activation in frog muscle fibers. *The Journal of General Physiology*, 61(4):424–443, 1973.

[90] Makoto Endo. Calcium release from the sarcoplasmic reticulum. *Physiological Reviews*, 57(1):71–108, 1977.

Supplementary information

1 Base model formulation

In the following formulation of the base model, the membrane potential (v) is given in units of mV, and the calcium concentrations are given in units of mM. All currents are expressed in units of A/F, and the calcium fluxes are expressed as mmol/ms per total cell volume (i.e., in units of mM/ms). Time is given in ms. The parameters of the model are given in Tables 1–6.

1.1 The membrane potential

The membrane potential is governed by the equation

$$\begin{aligned}\frac{dv}{dt} = -(&I_{\mathrm{Na}} + I_{\mathrm{NaL}} + I_{\mathrm{CaL}} + I_{\mathrm{to}} + I_{\mathrm{Kr}} + I_{\mathrm{Ks}} + I_{\mathrm{K1}} \\ &+ I_{\mathrm{NaCa}} + I_{\mathrm{NaK}} + I_{\mathrm{pCa}} + I_{\mathrm{bCl}} + I_{\mathrm{bCa}} + I_{\mathrm{f}} + I_{\mathrm{stim}}),\end{aligned} \tag{1}$$

where I_{stim} is an applied stimulus current, and I_{Na}, I_{NaL}, I_{CaL}, I_{to}, I_{Kr}, I_{Ks}, I_{K1}, I_{NaCa}, I_{NaK}, I_{pCa}, I_{bCl}, I_{bCa}, and I_{f} are membrane currents specified below. In our simulations, I_{stim} is given as a constant current of size -40 A/F for mature cells and -5 A/F for immature cells. The I_{stim} current is applied until the membrane potential reaches a value of -40 mV.

1.2 Membrane currents

The currents through the voltage-gated ion channels on the cell membrane are in general given on the form

$$I = go(v - E),$$

where g is the channel conductance, v is the membrane potential and E is the equilibrium potential of the channel. Furthermore, $o = \prod_i z_i$ is the open probability of the channels, where z_i are gating variables, either given as a function of the membrane potential or governed by equations of the form

$$z_i' = \frac{1}{\tau_{z_i}}(z_{i,\infty} - z_i). \tag{2}$$

The parameters τ_{z_i} and $z_{i,\infty}$ will be specified for each of the gating variables of the model in Table 7.

The fast sodium current The formulation of the fast sodium current is an adjusted version of the model given in [1], supporting slower upstroke velocities more similar to those observed in the optical measurements of hiPSC-CMs. The current is given by

$$I_{\mathrm{Na}} = g_{\mathrm{Na}} o_{\mathrm{Na}} (v - E_{\mathrm{Na}}), \tag{3}$$

where the open probability is given by

$$o_{\mathrm{Na}} = m^3 j, \tag{4}$$

and m and j are gating variables governed by equations of the form (2).

The late sodium current The formulation of the late sodium current, I_{NaL}, is based on [2] and is given by

$$I_{\mathrm{NaL}} = g_{\mathrm{NaL}} o_{\mathrm{NaL}} (v - E_{\mathrm{Na}}), \tag{5}$$

where the open probability is given by

$$o_{\mathrm{NaL}} = m_L h_L, \tag{6}$$

and m_L and h_L are gating variables governed by equations of the form (2).

Transient outward potassium current The formulation of the transient outward potassium current, I_{to}, is based on [3] and is given by

$$I_{\mathrm{to}} = g_{\mathrm{to}} o_{\mathrm{to}} (v - E_{\mathrm{to}}), \tag{7}$$

where the open probability is given by

$$o_{\mathrm{to}} = q_{\mathrm{to}} r_{\mathrm{to}}, \tag{8}$$

and q_{to} and r_{to} are gating variables governed by equations of the form (2).

Rapidly activating potassium current The formulation of the rapidly activating potassium current, I_{Kr}, is based on [3] and is given by

$$I_{\mathrm{Kr}} = g_{\mathrm{Kr}} o_{\mathrm{Kr}} (v - E_{\mathrm{K}}), \tag{9}$$

where

$$o_{\mathrm{Kr}} = x_{\mathrm{Kr1}} x_{\mathrm{Kr2}}, \tag{10}$$

and the dynamics of x_{Kr1} and x_{Kr2} are governed by equations of the form (2).

Slowly activating potassium current The formulation of the slowly activating potassium current, I_{Ks}, is based on [1] and is given by

$$I_{\mathrm{Ks}} = g_{\mathrm{Ks}} o_{\mathrm{Ks}} (v - E_{\mathrm{Ks}}), \tag{11}$$

where

$$o_{\mathrm{Ks}} = x_{\mathrm{Ks}}^2, \tag{12}$$

and the dynamics of x_{Ks} is governed by an equation of the form (2).

Inward rectifier potassium current The formulation of the inward rectifier potassium current, I_{K1}, is based on [1] and is given by

$$I_{\mathrm{K1}} = g_{\mathrm{K1}} o_{\mathrm{K1}} (v - E_{\mathrm{K}}), \tag{13}$$

where

$$o_{\mathrm{K1}} = \frac{a_{\mathrm{K1}}}{a_{\mathrm{K1}} + b_{\mathrm{K1}}}, \tag{14}$$

$$a_{\mathrm{K1}} = \frac{3.9}{1 + e^{0.6(v - E_K - 200)}}, \tag{15}$$

$$b_{\mathrm{K1}} = \frac{-1.5e^{0.0002(v - E_K + 100)} + e^{0.6(v - E_K - 10)}}{1 + e^{0.45(v - E_K)}}. \tag{16}$$

Hyperpolarization activated funny current The formulation for the hyperpolarization activated funny current, I_{f}, is based on [3] and is given by

$$I_{\mathrm{f}} = g_{\mathrm{f}} o_{\mathrm{f}} (v - E_{\mathrm{f}}), \tag{17}$$

where

$$o_{\mathrm{f}} = x_{\mathrm{f}}, \tag{18}$$

and the dynamics of x_{f} is governed by an equation of the form (2).

L-type calcium current The formualtion for the L-type calcium current, I_{CaL}, is based on the formulation in [1] and is given by

$$I_{\mathrm{CaL}} = g_{\mathrm{CaL}} o_{\mathrm{CaL}} \frac{(2F)^2 v}{RT} \frac{0.341 c_d e^{\frac{2Fv}{RT}} - 0.341 c_e}{e^{\frac{2Fv}{RT}} - 1}, \tag{19}$$

where

$$o_{\mathrm{CaL}} = df(1 - f_{\mathrm{Ca}}), \tag{20}$$

and the dynamics of d, f and f_{Ca} are governed by equations of the form (2).

The background currents The formulation of the background currents, I_{bCa} and I_{bCl}, are based on [1] and are given by

$$I_{\mathrm{bCa}} = g_{\mathrm{bCa}} (v - E_{\mathrm{Ca}}), \tag{21}$$

$$I_{\mathrm{bCl}} = g_{\mathrm{bCl}} (v - E_{\mathrm{Cl}}). \tag{22}$$

Sodium-calcium exchanger The formulation of the sodium-calcium exchanger current, I_{NaCa}, is based on [1] and is given by

$$I_{\mathrm{NaCa}} = \bar{I}_{\mathrm{NaCa}} \frac{e^{\frac{\nu Fv}{RT}} [\mathrm{Na}^+]_i^3 c_e - e^{\frac{(\nu - 1)Fv}{RT}} [\mathrm{Na}^+]_e^3 c_{sl}}{s_{\mathrm{NaCa}} \left(1 + \left(\frac{K_{\mathrm{act}}}{c_{sl}}\right)^2\right) \left(1 + k_{\mathrm{sat}} e^{\frac{(\nu - 1)Fv}{RT}}\right)}, \tag{23}$$

where

$$s_{\mathrm{NaCa}} = K_{\mathrm{Ca},i}[\mathrm{Na}^+]_e^3 \left(1 + \left(\frac{[\mathrm{Na}^+]_i}{K_{\mathrm{Na},i}}\right)^3\right) + K_{\mathrm{Na},e}^3 c_{sl} \left(1 + \frac{c_{sl}}{K_{\mathrm{Ca},i}}\right) + K_{\mathrm{Ca},e}[\mathrm{Na}^+]_i^3 + [\mathrm{Na}^+]_i^3 c_e + [\mathrm{Na}^+]_e^3 c_{sl}.$$

Sarcolemmal calcium pump The formulation of the current through the sarcolemmal calcium pump, I_{pCa}, is based on [1] and is given by

$$I_{\mathrm{pCa}} = \bar{I}_{\mathrm{pCa}} \frac{c_{sl}^2}{K_{\mathrm{pCa}}^2 + c_{sl}^2}. \tag{24}$$

Sodium-potassium pump The current through the sodium-potassium pump, I_{NaK}, is based on [1] and is given by

$$I_{\mathrm{NaK}} = \bar{I}_{\mathrm{NaK}} \frac{f_{\mathrm{NaK}}}{1 + \left(\frac{K_{\mathrm{Na,i}}^{\mathrm{NaK}}}{[\mathrm{Na}^+]_{\mathrm{i}}}\right)^4} \frac{[\mathrm{K}^+]_{\mathrm{e}}}{[\mathrm{K}^+]_{\mathrm{e}} + K_{\mathrm{K,e}}}, \tag{25}$$

where

$$f_{\mathrm{NaK}} = \frac{1}{1 + 0.12e^{-0.1\frac{Fv}{RT}}} + \frac{0.037}{7}\left(e^{\frac{[\mathrm{Na}^+]_{\mathrm{e}}}{67}} - 1\right)e^{-\frac{Fv}{RT}}. \tag{26}$$

1.3 Calcium dynamics

The calcium dynamics are governed by

$$\frac{dc_d}{dt} = \frac{1}{V_d}(J_{\mathrm{CaL}} - J_d^b - J_d^c), \qquad \frac{db_d}{dt} = \frac{1}{V_d}J_d^b, \tag{27}$$

$$\frac{dc_{sl}}{dt} = \frac{1}{V_{sl}}(J_e^{sl} - J_{sl}^c - J_{sl}^b + J_s^{sl}), \qquad \frac{db_{sl}}{dt} = \frac{1}{V_{sl}}J_{sl}^b, \tag{28}$$

$$\frac{dc_c}{dt} = \frac{1}{V_c}(J_{sl}^c + J_d^c - J_c^n - J_c^b), \qquad \frac{db_c}{dt} = \frac{1}{V_c}J_c^b, \tag{29}$$

$$\frac{dc_s}{dt} = \frac{1}{V_s}(J_n^s - J_s^{sl} - J_s^b), \qquad \frac{db_s}{dt} = \frac{1}{V_s}J_s^b, \tag{30}$$

$$\frac{dc_n}{dt} = \frac{1}{V_n}(J_c^n - J_n^s), \tag{31}$$

where c_d is the concentration of free calcium in the dyad, b_d is the concentration of calcium bound to a buffer in the dyad, c_{sl} is the concentration of free calcium in the SL compartment, b_{sl} is the concentration of calcium bound to a buffer in the SL compartment, c_c is the concentration of free calcium in the bulk cytosol, b_c is the concentration of calcium bound to a buffer in the bulk cytosol, c_s is the concentration of free calcium in the jSR, b_s is the concentration of calcium bound to a buffer in the jSR, and c_n is the concentration of free calcium in the nSR. The expressions for the fluxes are specified below.

1.4 Calcium fluxes

Flux through the SERCA pumps The flux from the bulk cytosol to the nSR through the SERCA pumps is given by

$$J_c^n = \bar{J}_{\text{SERCA}} \frac{\left(\frac{c_c}{K_c}\right)^2 - \left(\frac{c_n}{K_n}\right)^2}{1 + \left(\frac{c_c}{K_c}\right)^2 + \left(\frac{c_n}{K_n}\right)^2}. \tag{32}$$

Flux through the RyRs The flux from the jSR to the SL compartment is given by

$$J_s^{sl} = J_{\text{RyR}} + J_{\text{leak}}, \tag{33}$$

where J_{RyR} represents the flux through the active RyR channels and J_{leak} represents the flux through the RyR channels that are always open, given by

$$J_{\text{RyR}} = p \cdot r \cdot \alpha_{\text{RyR}}(c_s - c_{sl}), \tag{34}$$

$$J_{\text{leak}} = \gamma_{\text{RyR}} \cdot \alpha_{\text{RyR}}(c_s - c_{sl}), \tag{35}$$

respectively. Here, p is the open probability of the active RyR channels given by

$$p = \frac{c_d^3}{c_d^3 + \kappa_{\text{RyR}}^3}, \tag{36}$$

and r represents the fraction of the total number of RyR channels that are not inactivated and is governed by the equation

$$\frac{dr}{dt} = -\frac{J_{\text{RyR}}}{\beta_{\text{RyR}}} + \frac{\eta_{\text{RyR}}}{p}(1 - r). \tag{37}$$

Passive diffusion fluxes between compartments The passive diffusion fluxes between compartments are given by

$$J_d^c = \alpha_d^c(c_d - c_c), \tag{38}$$

$$J_{sl}^c = \alpha_{sl}^c(c_{sl} - c_c), \tag{39}$$

$$J_n^s = \alpha_n^s(c_n - c_s). \tag{40}$$

Buffer fluxes The fluxes of free calcium binding to a calcium buffer are given by

$$J_d^b = V_d(k_{\text{on}}^d c_d(B_{\text{tot}}^d - b_d) - k_{\text{off}}^d b_d), \tag{41}$$

$$J_{sl}^b = V_{sl}(k_{\text{on}}^{sl} c_{sl}(B_{\text{tot}}^{sl} - b_{sl}) - k_{\text{off}}^{sl} b_{sl}), \tag{42}$$

$$J_c^b = V_c(k_{\text{on}}^c c_c(B_{\text{tot}}^c - b_c) - k_{\text{off}}^c b_c), \tag{43}$$

$$J_s^b = V_s(k_{\text{on}}^s c_s(B_{\text{tot}}^s - b_s) - k_{\text{off}}^s b_s). \tag{44}$$

Parameter	Description	Value
V_d	Volume fraction of the dyadic subspace	0.001
V_{sl}	Volume fraction of the SL compartment	0.028
V_c	Volume fraction of the bulk cytosol	0.917
V_s	Volume fraction of the jSR	0.004
V_n	Volume fraction of the nSR	0.05
χ	Cell surface to volume ratio	0.6 μm^{-1}

Table 1: Default geometry parameters of the base model.

Membrane fluxes The membrane fluxes, J_{CaL}, J_{bCa}, J_{pCa}, and J_{NaCa}, are given by

$$J_{\text{CaL}} = -\frac{\chi C_m}{2F} I_{\text{CaL}}, \qquad J_{\text{pCa}} = -\frac{\chi C_m}{2F} I_{\text{pCa}}, \tag{45}$$

$$J_{\text{bCa}} = -\frac{\chi C_m}{2F} I_{\text{bCa}}, \qquad J_{\text{NaCa}} = \frac{\chi C_m}{F} I_{\text{NaCa}}, \tag{46}$$

where I_{CaL}, I_{bCa}, I_{pCa}, and I_{NaCa} are defined by the expressions given above. Furthermore,

$$J_e^{sl} = J_{\text{NaCa}} + J_{\text{pCa}} + J_{\text{bCa}}. \tag{47}$$

1.5 Nernst equilibrium potentials

The Nernst equilibrium potentials for the ion channels are defined as

$$E_{\text{Na}} = \frac{RT}{F} \log\left(\frac{[\text{Na}^+]_{\text{e}}}{[\text{Na}^+]_{\text{i}}}\right), \tag{48}$$

$$E_{\text{Ca}} = \frac{RT}{2F} \log\left(\frac{[\text{Ca}^{2+}]_{\text{e}}}{c_{sl}}\right), \tag{49}$$

$$E_{\text{K}} = \frac{RT}{F} \log\left(\frac{[\text{K}^+]_{\text{e}}}{[\text{K}^+]_{\text{i}}}\right), \tag{50}$$

$$E_{\text{Ks}} = \frac{RT}{F} \log\left(\frac{[\text{K}^+]_{\text{e}} + 0.018[\text{Na}^+]_{\text{e}}}{[\text{K}^+]_{\text{i}} + 0.018[\text{Na}^+]_{\text{i}}}\right), \tag{51}$$

$$E_{\text{Cl}} = \frac{RT}{F} \log\left(\frac{[\text{Cl}^+]_{\text{e}}}{[\text{Cl}^+]_{\text{i}}}\right), \tag{52}$$

$$E_{\text{f}} = -17 \text{ mV}, \tag{53}$$

for the parameter values given in Table 2.

Parameter	Description	Value
C_m	Specific membrane capacitance	0.01 μF/μm^2
F	Faraday's constant	96.485 C/mmol
R	Universal gas constant	8.314 J/(mol·K)
T	Temperature	310 K
$[Ca^{2+}]_e$	Extracellular calcium concentration	1.8 mM
$[Na^+]_e$	Extracellular sodium concentration	140 mM
$[Na^+]_i$	Intracellular sodium concentration	8 mM
$[K^+]_e$	Extracellular potassium concentration	5.4 mM
$[K^+]_i$	Intracellular potassium concentration	120 mM
$[Cl^-]_e$	Extracellular chloride concentration	150 mM
$[Cl^-]_i$	Intracellular chloride concentration	15 mM

Table 2: Physical constants and ionic concentrations of the base model.

Parameter	Value	Parameter	Value
g_{Na}	12.6 mS/μF	g_{CaL}	0.12 nL/(μF ms)
g_{NaL}	0.025 mS/μF	g_{bCa}	0.00055 mS/μF
g_{to}	0.27 mS/μF	$\bar{I}_{\mathrm{NaCa}}$	4.9 μA/μF
g_{Kr}	0.025 mS/μF	$\bar{I}_{\mathrm{pCa}}$	0.068 μA/μF
g_{Ks}	0.003 mS/μF	$\bar{J}_{\mathrm{SERCA}}$	0.00024 mM/ms
g_{K1}	0.37 mS/μF	α_{RyR}	0.0075 ms^{-1}
g_{f}	0.0001 mS/μF	α_d^c	0.0017 ms^{-1}
g_{bCl}	0.007 mS/μF	α_{sl}^c	0.15 ms^{-1}
$\bar{I}_{\mathrm{NaK}}$	1.8 μA/μF	α_n^s	0.012 ms^{-1}

Table 3: Conductance values and similar parameters for each of the membrane currents and intracellular calcium fluxes of the base model.

Parameter	Flux	Value
K_c	J_c^n	0.00025 mM
K_n	J_c^n	1.7 mM
β_{RyR}	J_s^{sl}	0.038 mM
γ_{RyR}	J_s^{sl}	0.001
κ_{RyR}	J_{RyR}	0.015 mM
η_{RyR}	J_s^{sl}	0.00001 ms^{-1}

Table 4: Parameters for the intracellular calcium fluxes of the base model.

Parameter	Current	Value
k_{sat}	I_{NaCa}	0.3
ν	I_{NaCa}	0.3
K_{act}	I_{NaCa}	0.00015 mM
$K_{\text{Ca},i}$	I_{NaCa}	0.0036 mM
$K_{\text{Ca},e}$	I_{NaCa}	1.3 mM
$K_{\text{Na},i}$	I_{NaCa}	12.3 mM
$K_{\text{Na},e}$	I_{NaCa}	87.5 mM
$K_{\text{Na},i}^{\text{NaK}}$	I_{NaK}	11 mM
$K_{\text{K},e}$	I_{NaK}	1.5 mM
K_{pCa}	I_{pCa}	0.0005 mM

Table 5: Parameters for the membrane currents of the base model.

Parameter	Compartment	Value
B_{tot}^{c}	Bulk cytosol	0.07 mM
k_{on}^{c}	Bulk cytosol	40 $\text{ms}^{-1}\text{mM}^{-1}$
k_{off}^{c}	Bulk cytosol	0.03 ms^{-1}
B_{tot}^{d}	Dyad	1.2 mM
k_{on}^{d}	Dyad	100 $\text{ms}^{-1}\text{mM}^{-1}$
k_{off}^{d}	Dyad	1 ms^{-1}
B_{tot}^{sl}	Subsarcolemmal space	0.9 mM
k_{on}^{sl}	Subsarcolemmal space	100 $\text{ms}^{-1}\text{mM}^{-1}$
k_{off}^{sl}	Subsarcolemmal space	0.15 ms^{-1}
B_{tot}^{s}	Junctional SR	27 mM
k_{on}^{s}	Junctional SR	100 $\text{ms}^{-1}\text{mM}^{-1}$
k_{off}^{s}	Junctional SR	65 ms^{-1}

Table 6: Parameters for the calcium buffers of the base model.

Current	Gate	z_∞	α_z	β_z	τ_z
I_{Na}	m	$\frac{1}{\left(1+e^{(-57-v)/9}\right)^2}$	$0.13e^{-((v+46)/16)^2}$	$0.06e^{-((v-5)/51)^2}$	$\alpha_m+\beta_m$
	j	$\frac{1}{\left(1+e^{(v+72)/7}\right)^2}$	$\begin{cases} 0, \text{ if } v \geq -40 \\ \frac{\left(\begin{matrix}-2.5\cdot 10^4 e^{0.2v} \\ -7\cdot 10^{-6}e^{-0.04v}\end{matrix}\right)(v+38)}{1+e^{0.3(v+79)}}, \text{ otherwise} \end{cases}$	$\begin{cases} \frac{0.6e^{0.06v}}{1+e^{-0.1(v+32)}}, \text{ if } v \geq -40 \\ \frac{0.02e^{-0.01v}}{1+e^{-0.14(v+40)}}, \text{ otherwise} \end{cases}$	$\frac{1}{\alpha_j+\beta_j}$
I_{NaL}	m_L	$\frac{1}{1+e^{(-43-v)/5}}$	$\frac{1}{6.8e^{(v+12)/35}}$	$8.6e^{-(v+77)/6}$	$\alpha_m+\beta_m$
	h_L	$\frac{1}{1+e^{(v+88)/7.5}}$			200 ms
I_{CaL}	d	$\frac{1}{1+e^{-(v+5)/6}}$	$\frac{1-e^{-\frac{v+5}{6}}}{0.035(v+5)}$		α_d
	f	$\frac{1}{1+e^{(v+35)/9}}+\frac{0.6}{1+e^{(50-v)/20}}$	$\frac{1}{0.02e^{-(0.034(v+14.5)^2)}+0.02}$		α_f
	f_{Ca}	$\frac{1.7c_d}{1.7c_d+0.012}$	$\frac{1}{1.7c_d+0.012}$		α_{Ca}
I_{to}	q_{to}	$\frac{1}{1+e^{(v+53)/13}}$	$\frac{39}{0.57e^{-0.08(v+44)}+0.065e^{0.1(v+46)}}$	6	$\alpha_{q_{\text{to}}}+\beta_{q_{\text{to}}}$
	r_{to}	$\frac{1}{1+e^{-(v-22.3)/18.75}}$	$\frac{14.4}{e^{0.09(v+30.61)}+0.37e^{-0.12(v+24)}}$	2.75	$\alpha_{r_{\text{to}}}+\beta_{r_{\text{to}}}$
I_{Kr}	x_{Kr1}	$\frac{1}{1+e^{-(v+20.7)/4.9}}$	$\frac{450}{1+e^{-(v+45)/10}}$	$\frac{6}{1+e^{(v+30)/11.5}}$	$\alpha_{x_{\text{Kr1}}}\cdot\beta_{x_{\text{Kr1}}}$
	x_{Kr2}	$\frac{1}{1+e^{(v+88)/50}}$	$\frac{3}{1+e^{-(v+60)/20}}$	$\frac{1.12}{1+e^{(v-60)/20}}$	$\alpha_{x_{\text{Kr2}}}\cdot\beta_{x_{\text{Kr2}}}$
I_{Ks}	x_{Ks}	$\frac{1}{1+e^{-(v+3.8)/14}}$	$\frac{990}{1+e^{-(v+2.4)/14}}$		$\alpha_{x_{\text{Ks}}}$
I_{f}	x_{f}	$\frac{1}{1+e^{(v+78)/5}}$	$\frac{1900}{1+e^{(v+15)/10}}$		$\alpha_{x_{\text{Ks}}}$

Table 7: Specification of the parameters z_∞ and τ_z, for $z = m$, j, m_L, h_L, d, f, f_{Ca}, q_{to}, r_{to}, x_{Kr1}, x_{Kr2}, x_{Ks} and x_{f} in the equations for the gating variables (2).

References

[1] Eleonora Grandi, Francesco S Pasqualini, and Donald M Bers. A novel computational model of the human ventricular action potential and Ca transient. *Journal of Molecular and Cellular Cardiology*, 48(1):112–121, 2010.

[2] Thomas O'Hara, László Virág, András Varró, and Yoram Rudy. Simulation of the undiseased human cardiac ventricular action potential: Model formulation and experimental validation. *PLoS Computational Biology*, 7(5):e1002061, 2011.

[3] Michelangelo Paci, Jari Hyttinen, Katriina Aalto-Setälä, and Stefano Severi. Computational models of ventricular-and atrial-like human induced pluripotent stem cell derived cardiomyocytes. *Annals of Biomedical Engineering*, 41(11):2334–2348, 2013.

Paper VI

Detecting Undetectables: Can Conductances of Action Potential Models be Changed Without Appreciable Change in the Transmembrane Potential?

Karoline H. Jæger, Samuel Wall, and Aslak Tveito

Submitted for publication

Detecting Undetectables: Can Conductances of Action Potential Models be Changed Without Appreciable Change in the Transmembrane Potential?

Karoline H. Jæger[1], Samuel Wall[1], and Aslak Tveito[1,2]

[1]Simula Research Laboratory, Norway
[2]Department of Informatics, University of Oslo, Norway

Abstract

Mathematical models describing the dynamics of the cardiac action potential are of great value for understanding how changes to the system can disrupt the normal electrical activity of cells and tissue in the heart. However, to represent specific data, these models must be parameterized, and adjustment of the maximum conductances of the individual contributing ionic currents is a commonly used method. Here we present a method for investigating the uniqueness of such resulting parameterizations. Our key question is: Can the maximum conductances of a model be changed without giving any appreciable changes in the action potential? If so, the model parameters are not unique and this poses a major problem in using the models to identify changes in parameters from data, for instance, to evaluate potential drug effects. We propose a method for evaluating this uniqueness, founded on the singular value decomposition of a matrix consisting of the individual ionic currents. Small singular values of this matrix signify lack of parameter uniqueness and we show that the conclusion from linear analysis of the matrix carries over to provide insight in the uniqueness of the parameters in the non-linear case. Using numerical experiments, we quantify the identifiability of the maximum conductances of well known models of the cardiac action potential. Furthermore, we show how the identifiability depends on the time step used in the observation of the currents, how the application of drugs may change identifiability, and finally, how the stimulation protocol can be used to improve identifiability of a model.

Excitable cells are present in the brain, in the heart, in every muscle, and in all critical organs of the body. The dynamics of such cells are surprisingly complex, and are commonly studied using detailed mathematical models based on experimental measurements of underlying biophysical processes. However, such models continue to increase in complexity as more experimental data become available, and it becomes correspondingly more challenging to understand how the parameters of the model affect the solutions. In the present report we investigate this problem in models describing cardiac cell dynamics. In particular, we ask: Can different model parameters give identical output? Answers to this question turn out to be highly important when we want to evaluate the effect of drugs in the cardiac system, or if we want to characterize the effect of genetic mutations on system dynamics. Here, we use the singular value decomposition (SVD) to investigate if it is possible to change model parameters, in our case the maximum conductances of the major ion currents that drive the function of the cell, without seeing any discernible effects on the action potential. We find that commonly used models of the action potential of human cardiac cells have this property; such that significant changes in the parameters can be introduced without any resulting change in commonly measured system outputs.

1 Introduction

In a conversation with Enrico Fermi, John von Neumann famously said, *with four parameters I can fit an elephant, and with five I can make him wiggle his trunk*, [1]. Clearly, both Fermi and von Neumann were cautious in introducing new parameters in mathematical models of physics, because they feared that with large degrees of freedom, the equations could basically be tweaked to fit any observation. Although mathematical models in biology historically have roots in physics, the frugality of classical models in physics has not translated well over to biology. This is particularly the case in recent mathematical models describing the dynamics of electrically active cardiac cells, where it is difficult even to count the number of adjustable parameters, let alone estimate all their values.

Since the seminal papers of Hodgkin and Huxley [2], and Noble [3], mathematical models have been used extensively and successfully to understand the action potential (AP) of excitable cells. Recent years have witnessed a very strong growth in the number of models describing a wide variety of cells and behaviours; see e.g., [4] for a comprehensive collection of models. Introduction to mathematical models of the AP is provided in e.g., [5, 6, 7, 8] and review of recent developments of AP models for cardiac cells is presented in e.g., [9, 10, 11, 12, 13]. Early models of cardiac cells were rather compact, in the sense that they were formulated in terms of relatively few ordinary differential equations, but recent models tend to be quite large. For small models, it is possible to understand the dynamics described by

the model equations, but for large and complex models, it is increasingly hard to understand the dynamics represented by all the terms entering the model, and useful information concerning the output of the model must be based on numerical computations.

It has consequently become increasingly difficult to analyze the mapping between the model parameters and the solution, leading to significant challenges in parameterizing the models to reflect a given data set. Such parametrization is commonly approached using a variety of techniques, from detailed analysis of individual contributing currents, to inheritance from previous work done in completely non relevant experiments [14, 15]. A comprehensive list of challenges associated with the parameterization of AP models is given in [15]; data from numerous sources are combined in a model and the final parametrization is usually done by hand tuning. Promising steps towards improving parametrization is presented in [15], but quality assessment of the final model is still called for.

Here, we will examine this problem assuming that the action potential of a paced cell can be accurately measured and that the problem of parametrization is to adjust a given model to the acquired waveform using a specific stimulation protocol. This is particularly relevant for techniques where the transmembrane potential is measured optically using voltage sensitive fluorescence; see e.g., [16, 17]. Such voltage sensitive reporting is now routinely used to analyze many cells including human induced pluripotent stem cells (hiPSCs); see e.g., [18]. We have recently developed methods for inverting data representing the transmembrane potential and intracellular calcium concentration of hiPSC-derived cardiomyocytes; see [19]. In that project, it turned out to be essential to be able to automatically invert measured data to obtain the maximum conductances of an AP model. Furthermore, it became clear that some currents could be identified using calcium and voltage data, whereas other membrane currents were practically invisible using this data.

The purpose of the present report is to present a method for investigating the identifiability of conductances based on observations of the transmembrane potential. The method is based on the singular value decomposition (SVD; see e.g., [20, 21]) of a matrix representing the individual transmembrane ion currents, I_i. These ion currents contribute to the total transmembrane current

$$I_T = \sum_{i=1}^{N} I_i, \tag{1}$$

and this total transmembrane current governs the dynamics of the cellular transmembrane potential, $v = v(t)$, by

$$\frac{dv(t)}{dt} = -I_T. \tag{2}$$

Here, we have chosen to formulate (2) so that the transmembrane currents are expressed as current per cell capacitance, given in units of Amperes per Farad (A/F),

v is given in millivolts (mV) and time, t, is given in milliseconds (ms). Note, however, that (2) could alternatively be expressed as, for example, $C_m \frac{dv(t)}{dt} = -i_T$, where C_m is the specific cell capacitance (in μF/cm^2), i_T is the total transmembrane current density (in μA/cm^2), and v and t are given in mV and ms, respectively.

We are interested in estimating the effect of replacing an ion current I_i by a perturbed current given by $(1 + \lambda_i)I_i$. If the effect of such a perturbation is small, it will be very difficult to parameterize the current by simply observing changes in the total membrane current I_T given by (1). In order to investigate how changes in the membrane currents, I_i, affect the total current, I_T, we perform an AP simulation using the model (2). At given time steps in the simulation (e.g., every ms) we store the values of every ion current in a matrix A; each row in the matrix represents the individual ion currents at a given time step. Then, we compute the singular values and singular vectors of that matrix. If a singular value of the matrix is zero, it means that if we change the vector of conductances along the corresponding non-zero singular vector, the total current will not change and therefore no changes can be observed in the transmembrane potential.

However, linear analysis of the matrix containing the ion currents cannot directly be used to predict the effect of perturbations on the transmembrane potential. In fact, the original model reads

$$\frac{dv(t)}{dt} = -\sum_{i=1}^{N} I_i(v, s), \tag{3}$$

and the perturbed model reads

$$\frac{dv^\lambda(t)}{dt} = -\sum_{i=1}^{N} (1 + \lambda_i) I_i(v^\lambda, s^\lambda). \tag{4}$$

Here, s is a vector containing other state variables of the model. Therefore, the $(1 + \lambda_i)$ perturbation introduces a non-linear perturbation and we describe below how the linear results translate into non-linear effects.

The common way of investigating the sensitivity of non-linear AP models of the form (1) is to compare the solutions of the model with and without perturbed conductances. When every individual conductance is analyzed, a rough indication of the parameter sensitivity is obtained; see e.g., [22, 23, 24, 25, 19]. This method is well established and clearly provides valuable insight. However, the method can only detect sensitivities for single currents and not combinations of currents. Suppose, for instance, that two currents are very sensitive when they are perturbed individually, but if both are increased, the changes cancel each other out and no discernible changes can be observed in the total membrane current. Such subtle cancellation effects turn out to be surprisingly common and almost (or perhaps entirely) impossible to see if only individual currents are perturbed. It is also very hard to search for such insensitivities by randomly combining various currents because the search space is so large and each simulation is time consuming.

Therefore, the SVD method turns out to be useful and we will demonstrate how it works for well-known models of human ventricular APs.

2 Methods

Our aim is to develop a method for investigating the uniqueness of the maximum conductances in AP models. The question we want to get at is this: For a given AP model and a specific stimulation protocol, can the maximum conductances be changed significantly without appreciable changes in the resulting transmembrane potential?

We will assume that the transmembrane potential is governed by a model of the form

$$\frac{dv(t)}{dt} = -\sum_{i=1}^{N} I_i(v,s), \tag{5}$$

$$\frac{ds(t)}{dt} = F(v,s). \tag{6}$$

Here, as above, v denotes the transmembrane potential, s denotes the other variables of the AP model (concentrations and gating variables), $\{I_i\}_{i=1}^N$ denotes the collection of ion currents and F represents the dynamics of the gating variables and the ion concentrations. We assume that each ion current can, for example, be written on the form

$$I_i = g_i o_i (v - v_i^0), \tag{7}$$

where g_i denotes the maximum conductance, o_i is the open probability, and v_i^0 denotes the resting potential of the $i-$th ion channel.

In addition to the model (5), we will also consider the following perturbed model,

$$\frac{dv^\lambda(t)}{dt} = -\sum_{i=1}^{N}(1+\lambda_i) I_i(v^\lambda, s^\lambda), \tag{8}$$

$$\frac{ds^\lambda(t)}{dt} = F(v^\lambda, s^\lambda; \lambda), \tag{9}$$

which is similar to the original model except that every ion current is perturbed by a term of the form $(1+\lambda_i)$. Clearly $v = v^\lambda$ for $\lambda = 0$, but can we find a vector $\lambda \neq 0$ such that $v \approx v^\lambda$? If such a vector λ exists, then clearly knowing the values of the transmembrane potential for all points in time is not enough to infer the maximum conductances, because different maximum conductances can give the same transmembrane potential.

2.1 Recording currents during an AP simulation

During a simulation based on the model (5)–(6), we store the total membrane current and the individual ion currents at certain time steps. More precisely, we

store the total membrane current I_T^k and the individual currents I_j^k for $j = 1, ..., N$ at time $t_k = k\Delta t$ for $k = 1, .., M$. Here, N denotes the number of ion currents, and M denotes the number of time steps at which the currents are stored. We are interested in the effect of perturbing individual currents and for that purpose we introduce the vector $\mu \in \mathbb{R}^{N,1}$. With $\mu = (1, 1, ..., 1)^T$, we can write the total membrane current as a matrix-vector product,

$$I_T = A\mu, \tag{10}$$

where we have gathered all individual ion currents in the matrix A defined by

$$A = \begin{pmatrix} I_1^1 & \dots & I_N^1 \\ \vdots & & \vdots \\ I_1^M & \dots & I_N^M \end{pmatrix}, \tag{11}$$

and the total current is given by

$$I_T = \begin{pmatrix} I_T^1 \\ I_T^2 \\ \vdots \\ I_T^M \end{pmatrix}.$$

Note that

$$I_T \in \mathbb{R}^{M,1}, \ A \in \mathbb{R}^{M,N}, \text{ and } \mu \in \mathbb{R}^{N,1}.$$

2.2 The singular value decomposition (SVD) of the current matrix

The SVD exists for any matrix A and takes the form

$$A = USV^T, \tag{12}$$

see e.g., [20, 21]. Here, $U \in \mathbb{R}^{M,M}$, $V \in \mathbb{R}^{N,N}$, and $S \in \mathbb{R}^{M,N}$. Note that U and V are unitary matrices, i.e.

$$UU^T = I, \quad U^TU = I, \quad VV^T = I, \quad V^TV = I,$$

where I is the identity matrix. The matrix S is a diagonal matrix with positive singular values σ_i satisfying

$$\sigma_1 \geq \sigma_2 \geq \ldots \geq \sigma_r > 0,$$

where r is the rank of the matrix A. The singular values and singular vectors satisfy the following relations,

$$Av_i = \sigma_i u_i, \qquad i = 1, ..., r \tag{13}$$

$$Av_i = 0, \qquad i = r + 1, ..., N \tag{14}$$

$$A^T u_i = \sigma_i v_i, \qquad i = 1, ..., r \tag{15}$$
$$A^T u_i = 0, \qquad i = r+1, ..., M. \tag{16}$$

Furthermore, the singular vectors define orthonormal bases as follows,

$$\{u_1, ..., u_r\} \text{ is an orthonormal basis for } \mathcal{N}(A^T)^\perp, \tag{17}$$
$$\{u_{r+1}, ..., u_M\} \text{ is an orthonormal basis for } \mathcal{N}(A^T), \tag{18}$$
$$\{v_1, ..., v_r\} \text{ is an orthonormal basis for } \mathcal{N}(A)^\perp, \tag{19}$$
$$\{v_{r+1}, ..., v_N\} \text{ is an orthonormal basis for } \mathcal{N}(A). \tag{20}$$

Here, $\mathcal{N}(A)$ and $\mathcal{N}(A^T)$ are the null spaces of A and A^T, respectively, and $\mathcal{N}(A^T)^\perp$ and $\mathcal{N}(A)^\perp$ are the column and row spaces of A, respectively.

2.3 The effect of perturbing the parameter vector μ; the maximum conductances

We will use the SVD to analyze the effect of perturbing the parameter vector μ. For that purpose, recall that

$$I_T = A\mu,$$

and consider also the total membrane current for a perturbed vector, $\bar{\mu}$,

$$\bar{I}_T = A\bar{\mu}.$$

2.3.1 Perturbation along a singular vector

Let us first consider the special case of

$$\bar{\mu} = \mu + \varepsilon v_i,$$

where v_i is a singular vector of A (see (13)), and ε is a parameter indicating the strength of the perturbation (the Euclidian norm of v_i is one).

Note that

$$I_T - \bar{I}_T = A\mu - A\bar{\mu} = -\varepsilon A v_i = -\varepsilon \sigma_i u_i,$$

and therefore, in the Euclidian norm $\|\cdot\|$ and the associated inner product $(\cdot,\cdot)$, we have

$$\|I_T - \bar{I}_T\|^2 = (I_T - \bar{I}_T, I_T - \bar{I}_T) = \varepsilon^2 \sigma_i^2 (u_i, u_i) = \varepsilon^2 \sigma_i^2,$$

so

$$\|I_T - \bar{I}_T\| = \varepsilon \sigma_i. \tag{21}$$

This means that the effect of a perturbation along a singular vector is proportional to the associated singular value. Therefore, perturbations of the maximum conductances along singular vectors associated with large singular values will be readily observed by significant changes in the total membrane current. Conversely, a perturbation of the maximum conductances along a singular vector for which the associated singular value is zero, or very small, will not result in appreciable changes in the total membrane current and is therefore expected to be impossible to identify by only observing the transmembrane potential.

2.3.2 A general perturbation

Since the collection of singular vectors constitutes an orthonormal collection of vectors, any perturbed vector $\bar{\mu}$ can be written on the form

$$\bar{\mu} = \mu + \sum_{i=1}^{N} \varepsilon_i v_i,$$

for appropriate choices of the constants $\{\varepsilon_i\}$. By using this representation, we find that

$$I_T - \bar{I}_T = A\mu - A\bar{\mu} = -\sum_{i=1}^{N} \varepsilon_i \sigma_i u_i,$$

so

$$\|I_T - \bar{I}_T\|^2 = \sum_{i=1}^{N} \varepsilon_i^2 \sigma_i^2 = \sum_{i=1}^{r} \varepsilon_i^2 \sigma_i^2.$$

In other words, if $\bar{\mu} - \mu$ can be expressed using only the singular vectors $\{v_i\}_{i=r+1}^{N}$, then $\|I_T - \bar{I}_T\|^2 = 0$, and therefore, such a perturbation will not lead to changes in the total membrane current. On the other hand, if $\bar{\mu} - \mu$ can be expressed using the singular vectors $\{v_i\}_{i=1}^{r}$, then $\|I_T - \bar{I}_T\|^2 \neq 0$, and such a perturbation will lead to changes in the total membrane current.

2.4 The identifiability index

We have seen that, according to the SVD analysis, perturbations along vectors that can be spanned by vectors in the space $\mathcal{N}(A) = \text{span}\{v_{r+1}, \ldots, v_N\}$ cannot be identified by observing changes in the total membrane current and, conversely, that perturbations along vectors in the space $\mathcal{N}(A)^{\perp} = \text{span}\{v_1, \ldots, v_r\}$ can be identified. We would like to translate this result to estimate the identifiability of the unit vectors, that is, the conductances of the currents defining the AP model. In other words, we would like to characterize the identifiability of the maximum conductance of the Na-channels, the Kr-channels, and so on. Clearly, if the perturbation of the conductance vector is completely in the space $\mathcal{N}(A)$ or in the space $\mathcal{N}(A)^{\perp}$, the question is simple, but we need to define the identifiability of unit vectors that are partly in both spaces. We will do this by considering the projection of the perturbation to the $\mathcal{N}(A)$ space.

Since $\{v_1, \ldots, v_N\}$ is an orthonormal basis, we can expand any perturbation e using this basis,

$$e = \sum_{i=1}^{N} (e, v_i) v_i. \tag{22}$$

Furthermore, the projection of this vector onto the space $\mathcal{N}(A) = \text{span}\{v_{r+1}, \ldots, v_N\}$ is simply given by

$$P_N e = \sum_{i=r+1}^{N} (e, v_i) v_i. \tag{23}$$

Now, e is the complete vector, $P_N e$ is the part of the vector that cannot be identified, and $e - P_N e$ is the part of the vector that is in the space of identifiable vectors, $\mathcal{N}(A)^\perp$. We now define the *identifiability index* of a vector to be given by

$$k(e) = \|e - P_N e\|. \tag{24}$$

Here it is useful to note that if $e \in \mathcal{N}(A)$, then $e = P_N e$ and $k(e) = 0$. Similarly, if $e \in \mathcal{N}(A)^\perp$, then $P_N e = 0$ and $k(e) = 1$. Hence, a completely unidentifiable vector has identifiability index equal to zero, and a completely identifiable vector has identifiability index equal to one.

2.5 Measuring the perturbation effects

In order to investigate the effect of model perturbations, we define a measure H, measuring the difference between the computed AP in the default version and a perturbed version of the model. This H is set up to detect differences in a selection of action potential characteristics and defined as

$$H(\varepsilon, v_i) = \sum_{q=1}^{5} H_q(\varepsilon, v_i), \tag{25}$$

where

$$H_1(\varepsilon, v_i) = \frac{|\mathrm{APD}_{30}(v^*) - \mathrm{APD}_{30}(\bar{v}(\varepsilon \cdot v_i))|}{|\mathrm{APD}_{30}(v^*)|}, \tag{26}$$

$$H_2(\varepsilon, v_i) = \frac{|\mathrm{APD}_{50}(v^*) - \mathrm{APD}_{50}(\bar{v}(\varepsilon \cdot v_i))|}{|\mathrm{APD}_{50}(v^*)|}, \tag{27}$$

$$H_3(\varepsilon, v_i) = \frac{|\mathrm{APD}_{80}(v^*) - \mathrm{APD}_{80}(\bar{v}(\varepsilon \cdot v_i))|}{|\mathrm{APD}_{80}(v^*)|}, \tag{28}$$

$$H_4(\varepsilon, v_i) = \frac{\left| \left(\frac{dv^*}{dt}\right)_{\max} - \left(\frac{d\bar{v}(\varepsilon \cdot v_i)}{dt}\right)_{\max} \right|}{\left| \left(\frac{dv^*}{dt}\right)_{\max} \right|}, \tag{29}$$

$$H_5(\varepsilon, v_i) = \frac{\|v^* - \bar{v}(\varepsilon \cdot v_i)\|}{\|v^*\|}. \tag{30}$$

Here, v^* is the transmembrane potential of the default model, and $\bar{v}(\varepsilon \cdot v_i)$ is the transmembrane potential of a model for which the currents are perturbed by $\varepsilon \cdot v_i$, where v_i is a singular vector. Furthermore APD_{30}, APD_{50}, and APD_{80} are the action potential durations (in ms) for 30%, 50%, and 80% repolarization, respectively, $(\frac{dv}{dt})_{\max}$ is the maximal upstroke velocity (in mV/ms), and $\|\cdot\|$ is the Euclidian norm.

2.6 Singular values close to zero

The sensitivity index defined in Section 2.4 distinguishes between singular values that are positive and those that are identically equal to zero. There is nothing

wrong in defining the identifiability index in this way, but in actual computations, the main challenge is posed by singular values that are close to zero. From (21), we see that if the singular value is very small, a perturbation in the direction of the associated singular vector changes the total membrane current very little. Therefore, we would also like to include singular vectors associated with small singular values in the space of non-identifiable vectors.

We expect that it would be difficult to select a specific threshold for the size of the singular values so that singular values below the threshold would correspond to undistinguishable perturbation effects for different AP models and simulation conditions. Therefore, we let the identifiability of a singular vector be determined by the observed changes in the APs resulting from perturbations along that singular vector. In other words, we let the null space $\mathcal{N}(A)$ be spanned by the vectors v_i for $i \in S$, where S is defined as

$$S = \left\{ i : \max_{-0.5 \leq \varepsilon \leq 0.5} H(\varepsilon, v_i) < \delta \right\}, \tag{31}$$

for some threshold value δ. Here, H is defined in (25).

2.7 Stimulation protocols and technical specifications

In all simulations presented below, a 1 ms long constant stimulus current of 40 A/F is applied every second for 20 seconds before recording the currents and transmembrane potential. For simulations of cells exposed to drugs (see Section 3.3), the model parameterization is changed to reflect drug effects, then paced in the same manner as above for 1000 seconds to define new initial conditions for the default (unperturbed) versions of the models for cells exposed to drugs. In the simulations exploring a random stimulation protocol (see Section 3.4), we apply the stimulus current at 10 randomly chosen time points during a 5000 ms long simulation (after the 20 second long stimulation protocol used in all simulations). These randomly chosen time points are given by 35.7 ms, 634.9 ms, 1392.5 ms, 2108.8 ms, 2426.9 ms, 2734.4 ms, 3161.8 ms, 3398.7 ms, 4073.6 ms and 4529.0 ms. For these simulations, we record each of the currents every time step of size $\Delta t = 0.1$ ms between $t = 0$ ms and $t = 5000$ ms in the construction of the current matrix, A (see (11)). For the remaining simulations, we record the currents every time step of size $\Delta t = 0.1$ ms between $t = 0$ ms and $t = 500$ ms, unless otherwise specified. All numerical simulations are conducted using the ode15s solver in Matlab.

3 Results

In this section we illustrate a few examples of the SVD analysis outlined above. We consider three AP models for human ventricular cardiomyoctes; the ten Tusscher et al. model [26], the Grandi et al. model [27] and the O'Hara et al. model [28]. We investigate the relationship between the size of the singular values and the effect of perturbing the currents by the corresponding singular vectors for these

three models. In addition, we compute the identifiability index for the currents of the models. We consider both the default versions of the model and versions of the models adjusted to represent cells exposed to drugs. We also investigate how the SVD analysis is affected by the size of the time step, Δt, used to record the currents and transmembrane potential and how the identifiability of the currents is affected when a random stimulation protocol is applied.

Note that the method developed here can be used for any model that can be written on the form (5)–(6), and the choice of models considered here is therefore somewhat arbitrary.

3.1 Singular value decomposition of the currents in the ten Tusscher, Grandi and O'Hara AP models

Figures 1, 2 and 3 show the SVD analysis of the currents in the ten Tusscher model [26], the Grandi model [27] and the O'Hara model [28], respectively. We consider the epicardial version of all the AP models.

In the Grandi model, a number of currents (I_{Na}, I_{bNa}, I_{NaK}, I_{Ks}, I_{pK}, I_{ClCa}, I_{CaL}, I_{NaCa}, I_{pCa}, and I_{bCa}) are divided into two components, one directed into the junctional cleft and one directed into the subsarcolemmal space. In the analysis below, the currents of each type represent the sum of these two components. Furthermore, both in the Grandi model and in the O'Hara model, the L-type calcium current is divided into three ionic components; a calcium component, a sodium component and a potassium component. In the analysis below, the current I_{CaL} is defined as the sum of these three components.

3.1.1 Singular values and vectors

Figure 1 shows the twelve singular values $\sigma_1, ..., \sigma_{12}$, of the SVD of the twelve currents in the ten Tusscher model, ordered from the largest value, $\sigma_1 = 420.26$, to the smallest value, $\sigma_{12} = 0.0063$. The plots located directly below each singular value illustrate the corresponding singular vectors. Each letter between "a" and "l" here corresponds to a specific current in the ten Tusscher model, specified in the orange panel on the right-hand side. The intensity of the green background color of the plots corresponds to the size of the singular value.

We observe that the largest singular value, σ_1, corresponds to a singular vector that is almost equal to the unit vector e_{Na} for the fast sodium current. In addition, the smallest singular value, σ_{12}, corresponds to a singular vector quite close to the unit vector e_{bNa} for the background sodium current, but also with a small contribution from the background calcium current, I_{bCa}.

The Grandi model and the O'Hara model consist of fifteen and thirteen membrane currents, respectively, and Figures 2 and 3 similarly show the singular values and corresponding singular vectors for these two models. We observe that for all the three models, the largest singular value corresponds to a singular vector almost exclusively associated with the fast sodium current, I_{Na}. In addition, we observe that the size of the singular values vary between small values in the range

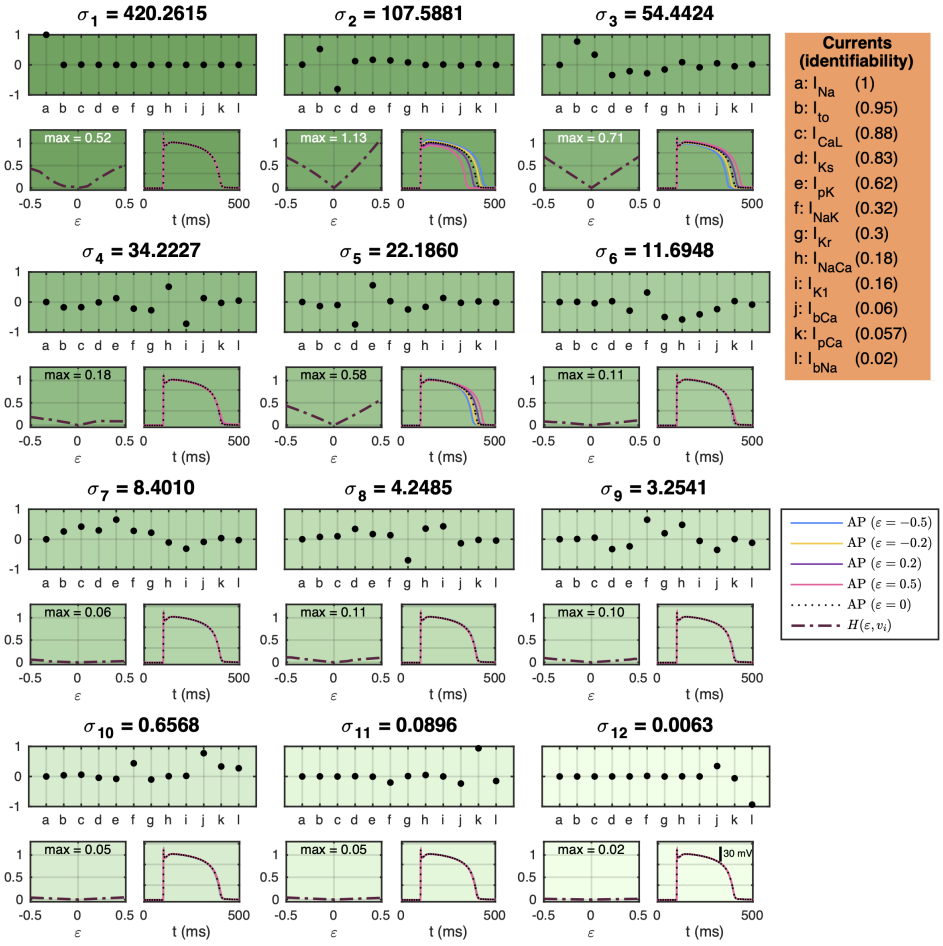

Figure 1: SVD analysis of the currents of the ten Tusscher model [26]. The values σ_1, ..., σ_{12} are the singular values of the current matrix A defined in (11). The plots directly below the singular values are the singular vectors corresponding to each of the singular values. Each letter corresponds to a single current specified in the orange panel to the right. The below plots show how a perturbation of the currents corresponding to the singular vector affects the computed AP of the model. The left plots show the measure $H(\varepsilon, v_i)$, defined by (25). The right plots show the computed action potentials for a selection of perturbations. The numbers given after each current in the orange right panel indicate the identifiability index (24) computed for each of the currents. The null space $\mathcal{N}(A)$ is defined by the singular vectors corresponding to the indices defined in (31) with $\delta = 0.25$.

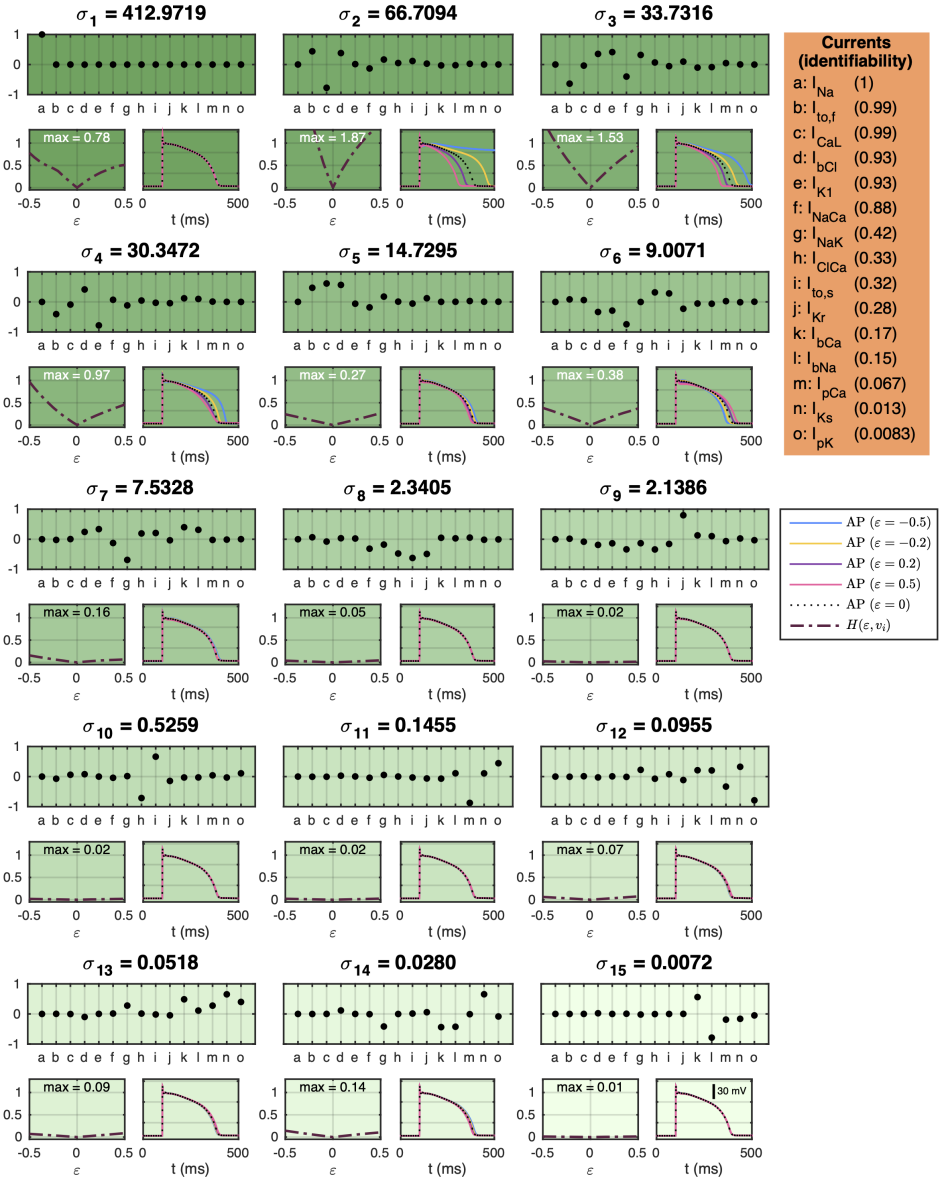

Figure 2: SVD analysis of the currents of the Grandi model [27], following the same structure as Figure 1.

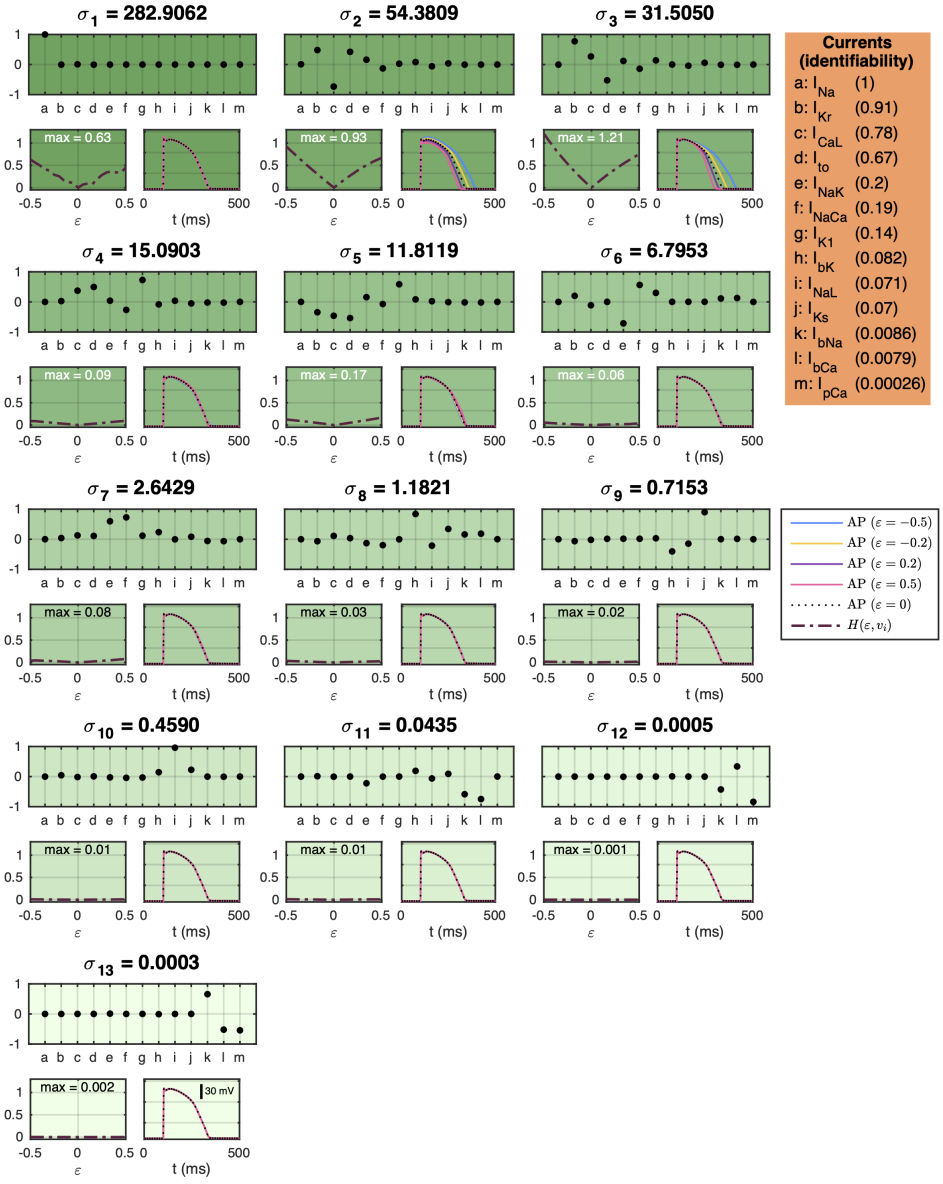

Figure 3: SVD analysis of the currents of the O'Hara model [28], following the same structure as Figure 1.

0.0001-0.01 to large values of about 300-400 for each of the three considered AP models.

3.1.2 Connection between the singular values and the effect of perturbations

According to the SVD analysis outlined above, perturbations of the model currents corresponding to large singular values are expected to result in large effects on the total membrane current, I_T, and thereby, expectedly, to large effects on the resulting action potential. Conversely, perturbations corresponding to small singular values are expected to result in small effects on the total membrane current and the resulting action potential. This theoretical result relies on simplifying assumptions, and, consequently, it might not hold in actual AP model computations. We therefore wish to investigate whether the expected results about the connection between the size of the singular values and the effect of the perturbation hold for the three AP models considered in Figures 1–3.

To investigate this, we run simulations in which each of the model currents are perturbed by the computed singular vectors. More specifically, for each singular vector v_i, each of the currents I_j of the model is multiplied by the factor $(1+\varepsilon \cdot v_{i,j})$, where $v_{i,j}$ denotes the j-th element of the singular vector v_i, and ε is varied between -0.5 and 0.5. For example, in the case of the first singular value, σ_1, of the ten Tusscher model (see Figure 1), the fast sodium current, I_{Na}, is multiplied by a factor close to $(1+\varepsilon)$, while the other currents are almost unperturbed. For the second singular value, σ_2, I_{to} is multiplied by a factor of approximately $(1+0.5 \cdot \varepsilon)$, I_{CaL} is multiplied by approximately $(1-0.8 \cdot \varepsilon)$, and the remaining currents are only perturbed by very small factors.

In each of the figures 1–3, the left plots below the singular vector plots show the measure, H, defined in (25) measuring the difference between the computed AP in the default version of the models and the perturbed models for each of the singular values. The text in the upper part of the plots indicates the maximum value of $H(\varepsilon, v_i)$ computed for the considered values of ε, ignoring cases where any of the action potential features of H_1–H_5 are not possible to compute. Furthermore, the right plots illustrate the computed action potentials for a small selection of ε-values ($\varepsilon = -0.5, -0.2, 0, 0.2, 0.5$).

In the plots we observe that, in general, the expected observation that perturbations corresponding to large singular values will result in large changes in the AP and that perturbations corresponding to small singular values will result in small changes in the AP seems to hold well for each of the three considered AP models. We observe that the effect of a perturbation corresponding to a given singular value is not necessary larger than the effect of a perturbation corresponding to a smaller singular value in all cases, but the largest perturbation effects are observed for the largest singular values, and the small singular values seem to result in quite small perturbation effects in most cases.

For the ten Tusscher model, we observe that perturbations corresponding to the singular values σ_4 and $\sigma_6, ..., \sigma_{12}$ all result in relatively small changes in the

	Δt	0.01 ms	0.1 ms	1 ms	2 ms
	σ_1	1309.9	420.3	138.1	24.7
	σ_{12}	0.02	0.0063	0.0018	0.0012
	σ_{12}/σ_1	1.5e-05	1.5e-05	1.3e-05	4.9e-05
Identifiability index	I_{Na}	1.00	1.00	0.002	0.002
	I_{to}	0.95	0.95	0.95	0.95
	I_{CaL}	0.88	0.88	0.88	0.88
	I_{Ks}	0.83	0.83	0.83	0.83
	I_{pK}	0.62	0.62	0.62	0.61
	I_{NaK}	0.32	0.32	0.32	0.31
	I_{Kr}	0.30	0.30	0.30	0.30
	I_{NaCa}	0.18	0.18	0.19	0.19
	I_{K1}	0.16	0.16	0.15	0.15
	I_{bCa}	0.06	0.06	0.06	0.06
	I_{pCa}	0.06	0.06	0.06	0.06
	I_{bNa}	0.02	0.02	0.02	0.02

Table 1: Results from SVD analysis using the ten Tusscher model and four different time steps Δt for recording the currents and transmembrane potential. The upper rows report the largest and smallest singular values, and the lower rows report the computed identifiability indices defined by (24) and (31).

computed AP, with values of H below 0.25. Similarly, for the Grandi model, perturbations corresponding to $\sigma_7, ..., \sigma_{15}$, result in very small changes of the computed AP. For the O'Hara model, perturbations corresponding to the singular values $\sigma_4, ...\sigma_{13}$ all result in nearly indistinguishable changes in the computed AP.

3.1.3 Identifiability index for individual currents

As observed in Figures 1–3, perturbations corresponding to large singular values seem to result in large effects of the computed AP, whereas perturbations corresponding to small singular values result in relatively small effects on the computed AP. As indicated in the Methods section, we wish to use this knowledge to construct an identifiability index that describes the identifiability of a single current.

The identifiability index defined in (24) computed for each of the currents in Figures 1–3 for $\delta = 0.25$ are shown in the orange panel on the right-hand side of the figures. For the ten Tusscher model, the index suggests that the I_{Na}, I_{to}, and I_{CaL} currents are highly identifiable, but that the currents I_{bNa}, I_{pCa}, I_{bCa}, I_{K1}, I_{NaCa}, I_{Kr}, and I_{NaK} are largely unidentifiable. For the Grandi model, the identifiability index suggests that I_{Na}, $I_{\mathrm{to,f}}$, I_{CaL}, I_{bCl}, I_{K1}, and I_{NaCa} are highly identifiable, but that the remaining currents are largely unidentifiable. Similarly, the index suggest that I_{Na} and I_{Kr} are highly identifiable in the O'Hara model, but I_{NaK}, I_{NaCa}, I_{K1}, I_{bK}, I_{NaL}, I_{Ks}, I_{bNa}, I_{bCa}, and I_{pCa} are largely unidentifiable.

	Δt	0.01 ms	0.1 ms	1 ms	2 ms
	σ_1	1333.8	413.0	330.3	15.0
	σ_{15}	0.023	0.0072	0.0018	0.00021
	σ_{15}/σ_1	1.7e-05	1.7e-05	5.3e-06	1.4e-05
Identifiability index	I_{Na}	1.00	1.00	1.00	0.97
	$I_{\mathrm{to,f}}$	0.99	0.99	0.99	0.99
	I_{CaL}	0.99	0.99	0.99	0.99
	I_{bCl}	0.93	0.93	0.93	0.93
	I_{K1}	0.93	0.93	0.93	0.93
	I_{NaCa}	0.88	0.88	0.88	0.87
	I_{NaK}	0.42	0.42	0.42	0.42
	I_{ClCa}	0.33	0.33	0.34	0.34
	$I_{\mathrm{to,s}}$	0.32	0.32	0.32	0.32
	I_{Kr}	0.28	0.28	0.29	0.29
	I_{bCa}	0.17	0.17	0.17	0.18
	I_{bNa}	0.15	0.15	0.14	0.15
	I_{pCa}	0.07	0.07	0.07	0.07
	I_{Ks}	0.01	0.01	0.01	0.02
	I_{pK}	0.01	0.01	0.01	0.22

Table 2: Results from SVD analysis using the Grandi model and four different values of the time step Δt for recording the currents and transmembrane potential. The upper rows report the largest and smallest singular values, and the lower rows report the computed identifiability indices defined by (24) and (31).

3.2 Effect of the size of the time step Δt

In the SVD analysis reported in Figures 1–3, we record the currents and transmembrane potential in every time step of size $\Delta t = 0.1$ ms. In order to investigate the effect of the time step on the analysis, we report in Tables 1–3 results from similar experiments where the currents and transmembrane potential are recorded for time steps of size $\Delta t = 0.01$ ms, 0.1 ms, 1 ms, and 2 ms. The upper rows of the tables report the maximum and minimum singular values of the current matrix A, as well as the ratio between the smallest and largest singular values. The next rows show the identifiability indices computed in each case for each of the currents.

We observe that as the time step used to record the currents is decreased, the largest and smallest singular values both seem to increase, but the ratio between the smallest and largest singular values remain roughly of the same size. In fact, for small values of Δt, both the smallest and the largest singular values seem to be proportional to $\Delta t^{-1/2}$. Furthermore, we observe that in most cases, the identifiability indices are very similar for the different values of Δt. An exception is observed for the time step of 1 ms or 2 ms for the ten Tusscher model. In that case, the analysis predicts that I_{Na} is largely unidentifiable even though the current is

	Δt	0.01 ms	0.1 ms	1 ms	2 ms
	σ_1	894.5	282.9	88.9	88.7
	σ_{13}	0.00098	0.00031	8.7e-05	1.9e-05
	σ_{13}/σ_1	1.1e-06	1.1e-06	9.8e-07	2.1e-07
Identifiability index	I_{Na}	1.00	1.00	1.00	1.00
	I_{Kr}	0.91	0.91	0.91	0.91
	I_{CaL}	0.78	0.78	0.78	0.77
	I_{to}	0.67	0.67	0.68	0.68
	I_{NaK}	0.20	0.20	0.20	0.20
	I_{NaCa}	0.19	0.19	0.19	0.19
	I_{K1}	0.14	0.14	0.14	0.14
	I_{bK}	0.08	0.08	0.08	0.08
	I_{NaL}	0.07	0.07	0.07	0.07
	I_{Ks}	0.07	0.07	0.07	0.07
	I_{bNa}	0.01	0.01	0.01	0.01
	I_{bCa}	0.01	0.01	0.01	0.01
	I_{pCa}	0.0003	0.0003	0.0003	0.0003

Table 3: Results from SVD analysis using the O'Hara model and four different values of the time step Δt for recording the currents and transmembrane potential. The upper rows report the largest and smallest singular values, and the lower rows report the computed identifiability indices defined by (24) and (31).

		No drug	Verapamil $0.5 \cdot g_{\mathrm{CaL}}$, $0.75 \cdot g_{\mathrm{Kr}}$	Cisapride $0.5 \cdot g_{\mathrm{Kr}}$
Identifiability index	I_{Na}	1.00	1.00	1.00
	I_{to}	0.95	0.98	0.95
	I_{CaL}	0.88	0.92	0.88
	I_{Ks}	0.83	0.85	0.87
	I_{pK}	0.62	0.21	0.64
	I_{NaK}	0.32	0.35	0.32
	I_{Kr}	0.30	0.43	0.14
	I_{NaCa}	0.18	0.16	0.14
	I_{K1}	0.16	0.28	0.15
	I_{bCa}	0.06	0.10	0.05
	I_{pCa}	0.06	0.04	0.06
	I_{bNa}	0.02	0.03	0.02

Table 4: The identifiability index defined by (24) and (31) with $\delta = 0.25$ computed for the default version of the ten Tusscher model (like in Figure 1) and for the ten Tusscher model adjusted to represent cells exposed to two drugs, Verapamil and Cisapride. Verapamil is modeled by reducing the maximum conductance of I_{CaL} and I_{Kr} by 50% and 25%, respectively. Cisapride is modeled by reducing the maximum conductance of I_{Kr} by 50%.

characterized as highly identifiable for smaller values of Δt. This suggest that a Δt of 1 ms might be too large to accurately characterize the identifiability of the currents. Indeed, the fast sodium current, I_{Na}, is almost only active during the upstroke of the action potential, and in Figure 7, we see that the upstroke of the action potential in the ten Tusscher model lasts for less than 2 ms. Therefore, it is not surprising that a time step of less than 1 ms is probably required to capture the relevant information about I_{Na}. However, the time step of $\Delta t = 0.1$ ms appears to be sufficient, and will be used in the remaining computations.

3.3 Identifiability in the presence of drugs

Figures 1–3 show the SVD analysis and identifiability indices computed for the default versions of the ten Tussscher, Grandi, and O'Hara AP models. In order to investigate how the identifiability of the individual model currents changes under different conditions, Tables 4–6 compare the identifiability indices computed for the default models to those computed for models adjusted to represent exposure to two drugs, Verapamil and Cisapride. The presence of the drugs are modeled like in [19], i.e. by reducing the maximum conductance of I_{CaL} by 50% and the maximum conductance of I_{Kr} by 25% for Verapamil and reducing the maximum conductance of I_{Kr} by 50% for Cisapride.

In Tables 4–6, we observe that the identifiability indices vary a bit between

		No drug	Verapamil $0.5 \cdot g_{\mathrm{CaL}}$, $0.75 \cdot g_{\mathrm{Kr}}$	Cisapride $0.5 \cdot g_{\mathrm{Kr}}$
Identifiability index	I_{Na}	1.00	1.00	1.00
	$I_{\mathrm{to,f}}$	0.99	0.99	0.99
	I_{CaL}	0.99	0.99	0.99
	I_{bCl}	0.93	0.90	0.98
	I_{K1}	0.93	0.89	1.00
	I_{NaCa}	0.88	0.43	0.89
	I_{NaK}	0.42	0.39	0.81
	I_{ClCa}	0.33	0.05	0.39
	$I_{\mathrm{to,s}}$	0.32	0.17	0.37
	I_{Kr}	0.28	0.11	0.14
	I_{bCa}	0.17	0.17	0.44
	I_{bNa}	0.15	0.14	0.35
	I_{pCa}	0.07	0.06	0.07
	I_{Ks}	0.01	0.006	0.02
	I_{pK}	0.01	0.005	0.01

Table 5: The identifiability index defined by (24) and (31) with $\delta = 0.25$ computed for the default version of the Grandi model (like in Figure 2) and for the Grandi model adjusted to represent cells exposed to the two drugs, Verapamil and Cisapride.

		No drug	Verapamil $0.5 \cdot g_{\mathrm{CaL}}$, $0.75 \cdot g_{\mathrm{Kr}}$	Cisapride $0.5 \cdot g_{\mathrm{Kr}}$
Identifiability index	I_{Na}	1.00	1.00	1.00
	I_{Kr}	0.91	0.97	0.90
	I_{CaL}	0.78	0.97	0.92
	I_{to}	0.67	1.00	0.90
	I_{NaK}	0.20	0.26	0.32
	I_{NaCa}	0.19	0.22	0.27
	I_{K1}	0.14	0.98	0.54
	I_{bK}	0.08	0.17	0.15
	I_{NaL}	0.07	0.12	0.10
	I_{Ks}	0.07	0.10	0.20
	I_{bNa}	0.01	0.02	0.01
	I_{bCa}	0.01	0.02	0.01
	I_{pCa}	0.0003	0.0003	0.0004

Table 6: The identifiability index defined by (24) and (31) with $\delta = 0.25$ computed for the default version of the O'Hara model (like in Figure 3) and for the O'Hara model adjusted to represent cells exposed to the two drugs, Verapamil and Cisapride.

the three versions of the models for some of the currents, but for each of the models, the currents with identifiability index close to one and the currents with identifiability index close to zero seem to be quite consistent for both the control case and under the simulated effects of the two drugs. Some of the considerable changes in identifiability is observed for the I_{NaCa} and I_{NaK} currents in the Grandi model. For I_{NaCa}, the identifiability drops from 0.88 in the no drug case to 0.43 in the presence of Verapamil. For I_{NaK}, the identifiability increases from 0.42 to 0.81 in the presence of Cisapride. In addition, the identifiability index of I_{K1} increases from 0.14 in the no drug case to 0.98 in the presence of Verapamil in the O'Hara model.

3.4 Identifiability for a random stimulation protocol

In [15] approaches for improving the identifiability of the maximum conductances of AP models were investigated. One of the suggested approaches for increasing the identifiability of currents that were largely unidentifiable from a single paced action potential, was to apply a random stimulation protocol in which the stimulation current was applied at a number of randomly chosen points in time. In [15] it was found that this method improved the parameter identifiability for some of the model conductances.

In Figures 4–6 we apply the above described SVD analysis to investigate a similar approach for the ten Tusscher, Grandi and O'Hara models. We apply a stimulus current at ten randomly chosen points in time during a 5000 ms simulation (see Section 2.7 for the specific stimulation times). The figures follow the same structure as Figures 1–3 except that an extra row of plots is added for each singular value. This row shows the computed transmembrane potential resulting from a selection of perturbations along the singular vectors for the entire 5000 ms simulation. The center right plots show the corresponding solutions for a small time sample. In the computation of H (center left plots), we compute the value of each of the terms H_1–H_5 defined in (26)–(30) for each of the ten computed action potentials (i.e., from the solution between each stimulation). In the computation of the final H defined in (25), we include the maximum value of each $H_j, j = 1, ...5$ over the ten computed action potentials. Furthermore, for reasons of space, we only show the singular vectors and perturbation effects for a selection of six singular values in Figures 4–6.

In the table reporting the identifiability index in Figure 4, we observe that the random pacing protocol greatly increases the identifiability of a number of currents in the ten Tusscher model. For example, the identifiability of I_{pCa}, I_{K1}, I_{NaCa}, I_{Kr}, and I_{NaK} are increased from 0.057, 0.16, 0.18, 0.3, and 0.32, respectively, for the default stimulation protocol in Figure 1 to a value of 1 in the random stimulation protocol in Figure 4. For the random stimulation protocol only a single current, I_{bNa}, obtains an identifiability of less than 0.9. In Figures 5 and 6, we similarly observe that the random stimulation protocol increases the identifiability of a number of currents in the Grandi and O'Hara models.

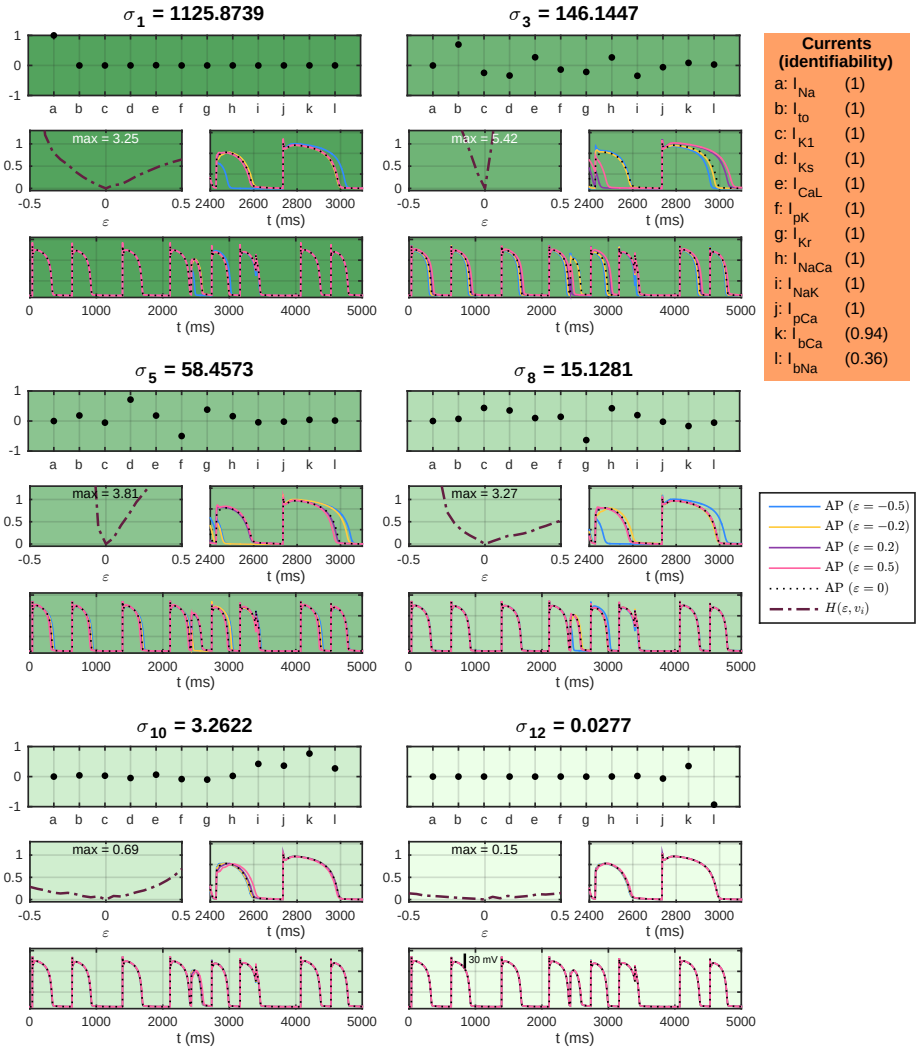

Figure 4: SVD analysis of the currents of the ten Tusscher model [26] using a random stimulation protocol with a stimulation current applied at ten randomly chosen points in time during a 5000 ms period. The values σ_1, σ_3, σ_5, σ_8, σ_{10}, and σ_{12} are a selection of the singular values of the current matrix, A, defined in (11). The plots directly below the singular values show the corresponding singular vectors. The center left plots show the measure $H(\varepsilon, v_i)$, defined by (25). The center right plots show the computed action potentials for a selection of perturbations for a small time interval. The lower plots shows the corresponding solutions for the entire 5000 ms period. The numbers given after each current in the orange right panel indicate the identifiability index defined by (24) and (31) with $\delta = 0.25$.

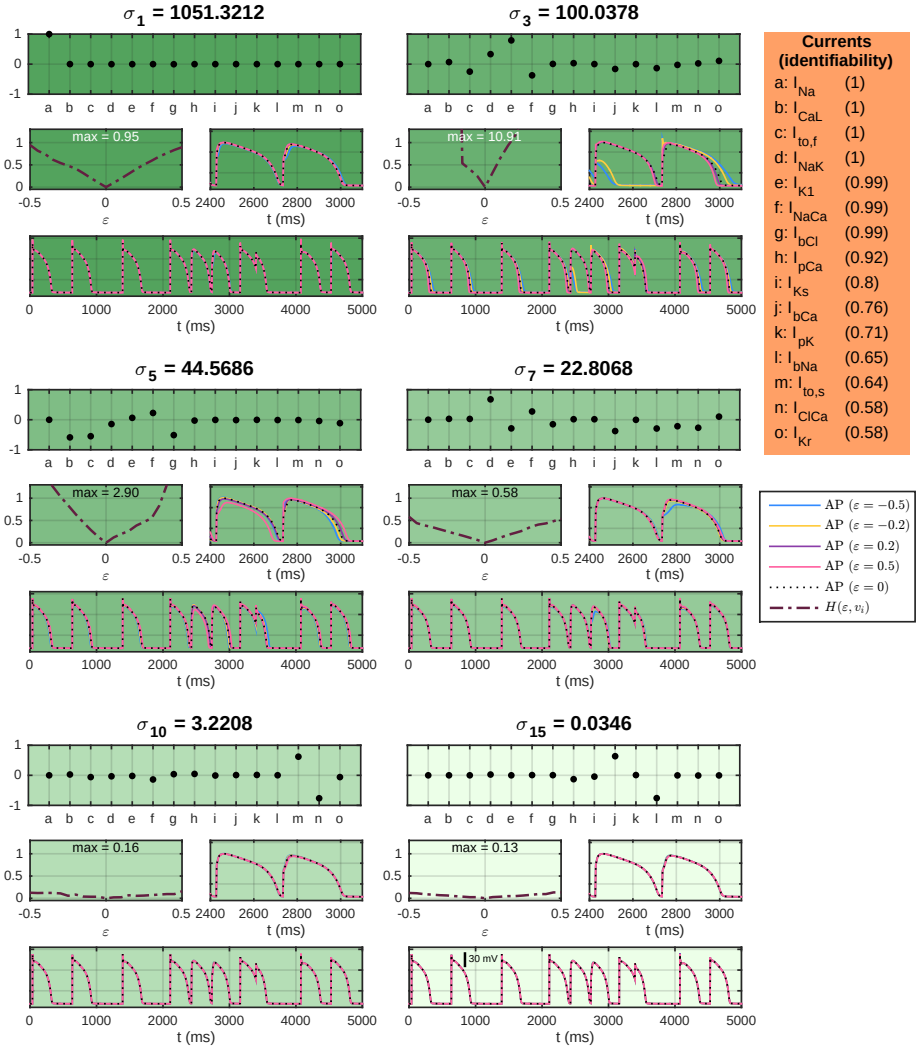

Figure 5: SVD analysis of the currents of the Grandi model [27] using a random stimulation protocol. The figure follows the same structure as Figure 4.

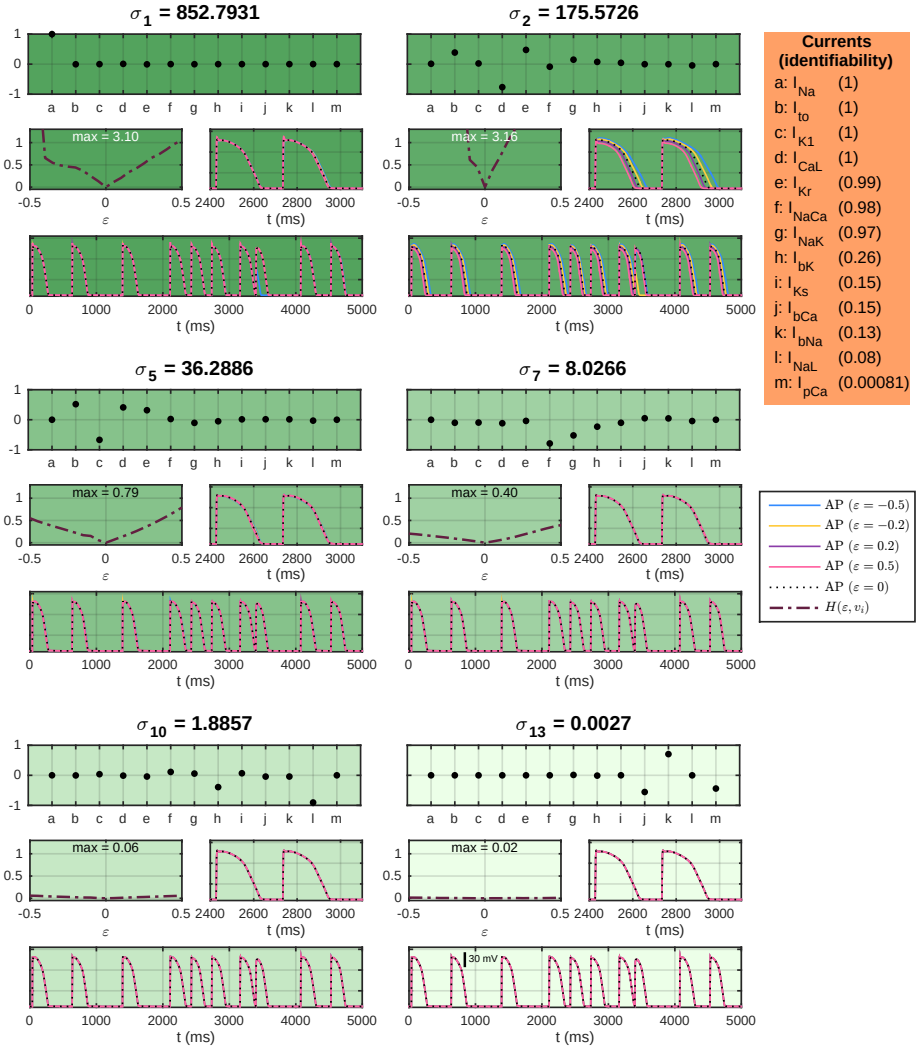

Figure 6: SVD analysis of the currents of the O'Hara model [28] using a random stimulation protocol. The figure follows the same structure as Figure 4.

4 Discussion

It is important to understand the uncertainty of the parameters in AP models. An overview of related problems involved in AP models of cardiac cells is given by Johnstone et al. [29]. One of the problems highlighted in the paper is that there are unidentifiable parameters in the AP model – *multiple parameter sets fit the data equally well and the individual conductances cannot be identified ....* Here, we have developed a method for investigating the identifiability of the maximum conductances of ion channels in a model, when the model is parameterized to fit a single action potential waveform. Simulations of the AP model give the total transmembrane currents and the individual ion currents. Then, by storing the currents in a matrix, the SVD method can be used to analyze what combinations of currents will be largely invisible in the overall waveform. We have developed an identifiability index that uses this information to quantify how identifiable the individual currents are. Although the method is based on linear analysis of a highly non-linear problem, the method gives valuable insight that is difficult to obtain by other methods.

4.1 Perturbation effects

In Figures 1–3, we observed that large singular values were associated with large perturbation effects along their corresponding singular vectors, while small singular values were to a large degree associated with small perturbation effects, as predicted by the linear theoretical considerations outlined in the Methods section. In all three figures, the non-linear perturbation effects were considered by the use of a measure H defined in (25) (lower left plots) to detect differences in the perturbed AP waveform, and in many cases, the trends of H could be readily seen by simply visually inspecting the APs resulting from the perturbations (lower right plots).

In some cases, however, the perturbations produced large values of H even though the perturbed APs seemed to be visually identical. The reason why in these cases H measures large differences is that H includes a term that measures the effect on the maximal upstroke velocity. This effect is hard to observe in the plots of the AP due to the time scale, but the effect is illustrated for two examples from the ten Tusscher model in the lower panel of Figure 7. Here, we show the upstroke of the AP for perturbations along the singular vectors corresponding to the largest singular value (left) and the smallest singular value (right) of the SVD analysis. For the large singular value, σ_1, we observe large changes in the upstroke dynamics, which correspond to the large values of H observed in Figure 1. For the smallest singular value, σ_{12}, on the other hand, the effects of the perturbations on the upstroke are completely indistinguishable, corresponding to the small values of H observed in Figure 1.

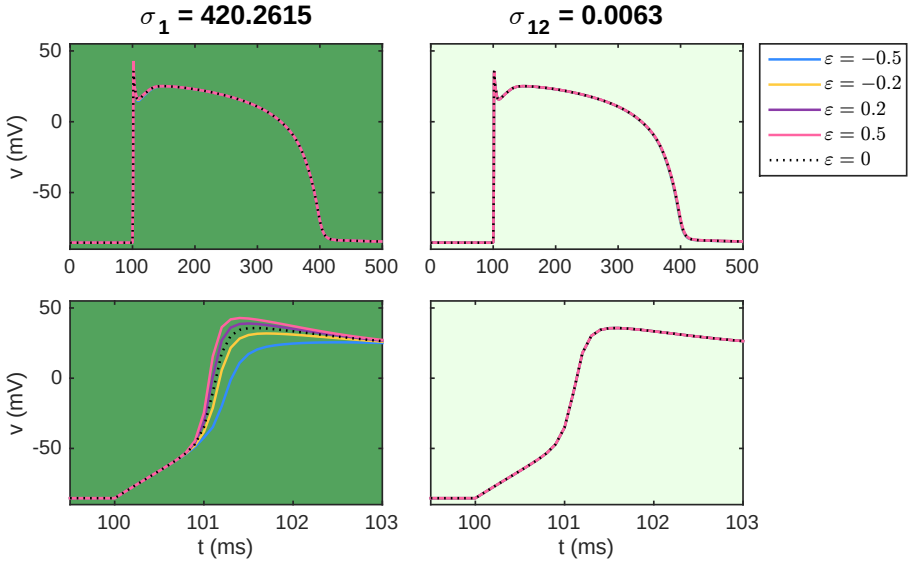

Figure 7: Effect on the transmembrane potential of perturbing the currents corresponding to the largest singular value, σ_1, and the smallest singular value, σ_{12}, of the SVD analysis of the ten Tusscher model (see Figure 1). The upper panel shows the full action potential, and the lower panel focuses only on the upstroke.

4.2 The identifiability index

In order to deduce information about the identifiability of the maximum conductance of the individual model currents from the information gained from the SVD analysis, we defined an identifiability index given by (24), measuring the difference between the unit vector of the current and the projection of the unit vector to the unidentifiable space defined in Section 2.6. If the identifiability index is close to zero, the current lies almost entirely in the unidentifiable space, and is expected to be hard to identify. Similarly, if the identifiability index is close to one, the current lies almost entirely in the identifiable space, and we expect that the maximum conductance of the current is easier to identify. In Figures 1–3, we observed that this index characterized a few model currents in the ten Tusscher, Grandi and O'Hara models as highly identifiable, while other currents were identified as largely unidentifiable. A weakness with this index is that we need to introduce a parameter δ in order to define the subspace of unidentifiable vectors; see (31). In our computations this parameter has been set to 0.25, but in general the parameter needs to be determined using numerical experiments with the model under consideration.

4.2.1 Effect of the time step

In Tables 1–3, we investigated the effect of the time step, Δt, used to record the current matrix, A. We observed that the size of the singular values of A changed when different time steps were used. Moreover, for small values of Δt, the size of the singular values seemed to be proportional to $\Delta t^{-1/2}$. However, the identifiability of the individual model currents remained relatively constant for the different time steps. Yet for ten Tusscher model, the identifiability index of the I_{Na} current dropped from 1 for $\Delta t = 0.01$ ms or $\Delta t = 0.1$ ms to 0.002 for $\Delta t = 1$ ms or $\Delta t = 2$ ms, which suggests that a time step of less than 1 ms is probably needed to accurately capture the relevant information about the currents, and in particular the fast sodium current, I_{Na}. The difficulties related to identifying the sodium current using relatively long time steps is commensurate with the problems encountered in [19], where coarse time resolution rendered the sodium current unidentifiable using voltage sensitive dyes.

4.2.2 Effect of the simulation conditions

In Tables 4–6, we investigated the identifiability of the currents in models adjusted to represent cells exposed to two drugs. We observed that the identifiability of certain currents was clearly affected by the change in conditions, but that the currents characterized as highly identifiable and the ones characterized as largely unidentifiable remained relatively unchanged under the different conditions.

In Figures 4–6, we similarly investigated how the identifiability was affected when a random stimulation protocol was applied. This approach was in [15] shown to increase the identifiability of the maximum conductance of currents in AP models. Consistent with the results in [15], the SVD analysis suggested that

the identifiability of a number of model currents in the ten Tusscher, Grandi and O'Hara AP models would increase using such a random stimulation protocol.

4.3 Uniqueness of model parameters

A key question in deriving and applying AP models is the uniqueness of the parameters. For Markov Models used to represent the open probability of ion channels, this problem was carefully studied by Fink and Noble [30] who found parameter unidentifiability in 9 out of 13 models. Lack of uniqueness has also been observed for models of the AP of neurons; see e.g., [31, 32, 33] and for AP models of cardiomyocytes; see e.g., [34, 35, 36, 37]. The most common way of investigating the sensitivity of AP models is to perturb individual currents and look for the effect. This method is useful in the sense that it indicates how well blocking of individual currents can be identified using the model. Suppose, for instance, that the AP model is very sensitive to changes in the sodium current. Then, if a sodium blocker is applied, such changes will be observed and thus the effect of a sodium blocker can be identified. But this approach will not uncover the identifiability of more subtle effects where a blocker affects many currents simultaneously.

The numerical examples presented above, show that very few ion currents can be completely identified by observing the total membrane currents. According to the identifiability index, less than 50% of the perturbations can be observed for 7 out of 12 ion currents in the ten Tusscher model, 9 out of 15 ion currents in the model of Grandi et al., and 9 out of 13 ion currents in the O'Hara model using the default stimulation protocol in Figures 1–3. This indicates a considerable degree of redundancy in the models in their ability to produce a single paced action potential. However, for the random stimulation protocol in Figures 4–6, the identifiability index was smaller than 0.5 only for 1 of the currents in the ten Tusscher model, 0 of the currents in the Grandi model and 6 of the currents in the O'Hara model.

4.4 Model reduction

Several authors have used redundancy of AP models to derive reduced models. For instance, in both [38] and [39], the authors used redundancy of the AP models to systematically reduce complex models to obtain simpler models. Other authors have developed parsimonious models by only including major currents; see e.g., [40, 41, 42, 43, 44]. A comprehensive overview of models of the cardiac AP is given in [9], where models ranging from 2 to 67 variables are presented. Model reduction can be achieved by identifying insensitive parameters using the SVD method, and more generally this problem is often addressed by the method of proper orthogonal decomposition (POD); see e.g., [45, 46].

4.5 Linear sensitivity analysis

Over the past decade, a series of papers by Sobie and co-authors (see [47, 48, 49, 50]) have developed a theory describing a strong correlation between model parameters like the maximum conductances of the ion channels and output variables like the APD. These relations are surprising given the strong non-linearities involved in the AP models, but the relations are also very useful, in particular in order to understand the behavior of populations of models. We have used the fact that linear models seem to pick up important features of non-linear AP models to devise a method for analyzing how the total transmembrane current changes under perturbations of the individual ion currents using the SVD algorithm.

5 Conclusion

We have presented a method for investigating the uniqueness of parameters of commonly used mathematical models of action potentials. The method is simple to implement and the results are interpreted in a straightforward manner. For three well-known models of human cardiac cells, the method revealed that significant changes in the maximum conductances can be introduced without any appreciable change in the resulting action potential. The method uses the singular value decomposition to find perturbations that give minimal changes in the solution. Such perturbations are impossible to find by simply changing the individual conductances, and the search space is very large if one were to search for combinations of changed conductances that give little effect on the action potential. The method is applicable for any model written on the standard form for action potential models; see equations (5)–(6).

References

[1] Freeman Dyson. A meeting with Enrico Fermi. *Nature*, 427(6972):297, 2004.

[2] Alan L Hodgkin and Andrew F Huxley. The components of membrane conductance in the giant axon of loligo. *The Journal of Physiology*, 116(4):473–496, 1952.

[3] Denis Noble. A modification of the Hodgkin–Huxley equations applicable to Purkinje fibre action and pacemaker potentials. *The Journal of Physiology*, 160(2):317–352, 1962.

[4] CellML Model Repository. www.cellml.org/models/.

[5] G Bard Ermentrout and David H Terman. *Mathematical Foundations of Neuroscience*, volume 35. Springer-Verlag, New York, 2010.

[6] David Sterratt, Bruce Graham, Andrew Gillies, and David Willshaw. *Principles of Computational Modelling in Neuroscience*. Cambridge University Press, 2011.

[7] Robert Plonsey and Roger C Barr. *Bioelectricity, A Quantitative Approach*. Springer, 2007.

[8] James P Keener and James Sneyd. *Mathematical Physiology*. Springer, 2009.

[9] Flavio H Fenton and Elizabeth M Cherry. Models of cardiac cell. *Scholarpedia*, 3(8):1868, 2008. revision #91508.

[10] Zhilin Qu, Gang Hu, Alan Garfinkel, and James N Weiss. Nonlinear and stochastic dynamics in the heart. *Physics Reports*, 543(2), 2014.

[11] Yoram Rudy and Jonathan R Silva. Computational biology in the study of cardiac ion channels and cell electrophysiology. *Quarterly Reviews of Biophysics*, 39(01):57–116, 2006.

[12] Yoram Rudy. From genes and molecules to organs and organisms: Heart. *Comprehensive Biophysics*, pages 268–327, 2012.

[13] Andrew G Edwards and William E Louch. Species-dependent mechanisms of cardiac arrhythmia: a cellular focus. *Clinical Medicine Insights: Cardiology*, 11:1179546816686061, 2017.

[14] Steven A Niederer, Martin Fink, Denis Noble, and Nicolas P Smith. A meta-analysis of cardiac electrophysiology computational models. *Experimental Physiology*, 94(5):486–495, 5 2009.

[15] Willemijn Groenendaal, Francis A Ortega, Armen R Kherlopian, Andrew C Zygmunt, Trine Krogh-Madsen, and David J Christini. Cell-specific cardiac electrophysiology models. *PLoS Computational Biology*, 11(4):e1004242, 2015.

[16] Steven D Girouard, Kenneth R Laurita, and David S Rosenbaum. Unique properties of cardiac action potentials recorded with voltage-sensitive dyes. *Journal of Cardiovascular Electrophysiology*, 7(11):1024–1038, 1996.

[17] Marco Canepari, Dejan Zecevic, Olivier Bernus, et al. *Membrane Potential Imaging in the Nervous System and Heart*. Springer, 2015.

[18] Ksenia Blinova, Jayna Stohlman, Jose Vicente, Dulciana Chan, Lars Johannesen, Maria P Hortigon-Vinagre, Victor Zamora, Godfrey Smith, William J Crumb, Li Pang, Beverly Lyn-Cook, James Ross, Mathew Brock, Stacie Chvatal, Daniel Millard, Loriano Galeotti, Norman Stockbridge, and David G Strauss. Comprehensive translational assessment of human-induced pluripotent stem cell derived cardiomyocytes for evaluating drug-induced arrhythmias. *Toxicological Sciences*, 155(1):234–247, 2017.

[19] Aslak Tveito, Karoline H Jæger, Nathaniel Huebsch, Berenice Charrez, Andrew G Edwards, Samuel Wall, and Kevin E Healy. Inversion and computational maturation of drug response using human stem cell derived cardiomyocytes in microphysiological systems. *Scientific Reports*, 8(1):17626, 2018.

[20] Jörg Liesen and Volker Mehrmann. *Linear Algebra in Every Day Life*. Springer, 2015.

[21] Tom Lyche. *Numerical Linear Algebra and Matrix Factorizations*. University of Oslo, lecture notes, 2017.

[22] Maria T Mora, Jose M Ferrero, Lucia Romero, and Beatriz Trenor. Sensitivity analysis revealing the effect of modulating ionic mechanisms on calcium dynamics in simulated human heart failure. *PloS One*, 12(11):e0187739, 2017.

[23] Michelangelo Paci, Jari Hyttinen, Blanca Rodriguez, and Stefano Severi. Human induced pluripotent stem cell-derived versus adult cardiomyocytes: an in silico electrophysiological study on effects of ionic current block. *British Journal of Pharmacology*, 172(21):5147–5160, 2015.

[24] Michelangelo Paci, Elisa Passini, Stefano Severi, Jari Hyttinen, and Blanca Rodriguez. Phenotypic variability in LQT3 human induced pluripotent stem cell-derived cardiomyocytes and their response to anti-arrhythmic pharmacological therapy: an in silico approach. *Heart Rhythm*, 2017.

[25] Beatriz Carbonell-Pascual, Eduardo Godoy, Ana Ferrer, Lucia Romero, and Jose M Ferrero. Comparison between Hodgkin–Huxley and Markov formulations of cardiac ion channels. *Journal of Theoretical Biology*, 399:92–102, 2016.

[26] Kirsten HWJ Ten Tusscher and Alexander V Panfilov. Alternans and spiral breakup in a human ventricular tissue model. *American Journal of Physiology-Heart and Circulatory Physiology*, 291(3):H1088–H1100, 2006.

[27] Eleonora Grandi, Francesco S Pasqualini, and Donald M Bers. A novel computational model of the human ventricular action potential and Ca transient. *Journal of Molecular and Cellular Cardiology*, 48(1):112–121, 2010.

[28] Thomas O'Hara, László Virág, András Varró, and Yoram Rudy. Simulation of the undiseased human cardiac ventricular action potential: Model formulation and experimental validation. *PLoS Computational Biology*, 7(5):e1002061, 2011.

[29] Ross H Johnstone, Eugene TY Chang, Rémi Bardenet, Teun P De Boer, David J Gavaghan, Pras Pathmanathan, Richard H Clayton, and Gary R Mirams. Uncertainty and variability in models of the cardiac action potential: Can we build trustworthy models? *Journal of Molecular and Cellular Cardiology*, 96:49–62, 2016.

[30] Martin Fink and Denis Noble. Markov models for ion channels: Versatility versus identifiability and speed. *Philosophical Transactions of the Royal Society A: Mathematical, Physical and Engineering Sciences*, 367(1896):2161–2179, 2009.

[31] Eve Marder and Adam L Taylor. Multiple models to capture the variability in biological neurons and networks. *Nature Neuroscience*, 14(2):133, 2011.

[32] Astrid A Prinz, Dirk Bucher, and Eve Marder. Similar network activity from disparate circuit parameters. *Nature Neuroscience*, 7(12):1345, 2004.

[33] Pablo Achard and Erik De Schutter. Complex parameter landscape for a complex neuron model. *PLoS Computational Biology*, 2(7):e94, 2006.

[34] Amrita X Sarkar and Eric A Sobie. Regression analysis for constraining free parameters in electrophysiological models of cardiac cells. *PLoS Computational Biology*, 6(9):e1000914, 2010.

[35] Stefan A Mann, Mohammad Imtiaz, Annika Winbo, Annika Rydberg, Matthew D Perry, Jean-Philippe Couderc, Bronislava Polonsky, Scott McNitt, Wojciech Zareba, Adam P Hill, and Jamie I Vandenberg. Convergence of models of human ventricular myocyte electrophysiology after global optimization to recapitulate clinical long QT phenotypes. *Journal of Molecular and Cellular Cardiology*, 100:25–34, 2016.

[36] Socrates Dokos and Nigel H Lovell. Parameter estimation in cardiac ionic models. *Progress in Biophysics and Molecular Biology*, 85(2-3):407–431, 2004.

[37] Jaspreet Kaur, Anders Nygren, and Edward J Vigmond. Fitting membrane resistance along with action potential shape in cardiac myocytes improves convergence: application of a multi-objective parallel genetic algorithm. *PLoS One*, 9(9):e107984, 2014.

[38] Marco Arieli Herrera-Valdez and Joceline Lega. Reduced models for the pacemaker dynamics of cardiac cells. *Journal of Theoretical Biology*, 270(1):164–176, February 2011.

[39] Daniel M Lombardo and Wouter-Jan Rappel. Systematic reduction of a detailed atrial myocyte model. *Chaos: An Interdisciplinary Journal of Nonlinear Science*, 27(9):093914, 2017.

[40] Rubin R Aliev and Alexander V Panfilov. A simple two-variable model of cardiac excitation. *Chaos, Solitons & Fractals*, 7(3):293–301, 1996.

[41] Flavio Fenton and Alain Karma. Vortex dynamics in three-dimensional continuous myocardium with fiber rotation: Filament instability and fibrillation. *Chaos: An Interdisciplinary Journal of Nonlinear Science*, 8(1):20–47, 1998.

[42] Suran K Galappaththige, Richard A Gray, and Bradley J Roth. Cardiac strength-interval curves calculated using a bidomain tissue with a parsimonious ionic current. *PloS One*, 12(2):e0171144, 2017.

[43] Richard A Gray and Pras Pathmanathan. A parsimonious model of the rabbit action potential elucidates the minimal physiological requirements for alternans and spiral wave breakup. *PLoS Computational Biology*, 12(10):e1005087, 2016.

[44] Philipp Kügler, André H Erhardt, and MAK Bulelzai. Early afterdepolarizations in cardiac action potentials as mixed mode oscillations due to a folded node singularity. *PloS One*, 13(12):e0209498, 2018.

[45] Gaetan Kerschen, Jean-Claude Golinval, Alexander F Vakakis, and Lawrence A Bergman. The method of proper orthogonal decomposition for dynamical characterization and order reduction of mechanical systems: an overview. *Nonlinear Dynamics*, 41(1-3):147–169, 2005.

[46] Clarence W Rowley. Model reduction for fluids, using balanced proper orthogonal decomposition. *International Journal of Bifurcation and Chaos*, 15(03):997–1013, 2005.

[47] Eric A Sobie. Parameter sensitivity analysis in electrophysiological models using multivariable regression. *Biophysical Journal*, 96(4):1264–1274, 2009.

[48] Amrita X Sarkar and Eric A Sobie. Quantification of repolarization reserve to understand interpatient variability in the response to proarrhythmic drugs: a computational analysis. *Heart Rhythm*, 8(11):1749–1755, 2011.

[49] Amrita X Sarkar, David J Christini, and Eric A Sobie. Exploiting mathematical models to illuminate electrophysiological variability between individuals. *The Journal of Physiology*, 590(11):2555–2567, 2012.

[50] Jingqi QX Gong and Eric A Sobie. Population-based mechanistic modeling allows for quantitative predictions of drug responses across cell types. *NPJ Systems Biology and Applications*, 4(1):11, 2018.